

# Three-dimensional Gradient Index Optics Fabricated in Diffusive Photopolymers

by

Chunfang Ye

B.A., Zhejiang University, 2004

M.S., Zhejiang University, 2006

A thesis submitted to the

Faculty of the Graduate School of the

University of Colorado in partial fulfillment

of the requirement for the degree of

Doctor of Philosophy

Department of Electrical, Computer and Energy Engineering

2012

This thesis entitled:  
Three-dimensional Gradient Index Optics Fabricated in Diffusive Photopolymers  
written by Chunfang Ye  
has been approved for the Department of Electrical, Computer and Energy Engineering

---

Robert R. McLeod

---

Carol Cogswell

*Date*\_\_\_\_\_

The final copy of this thesis has been examined by the signatories, and we  
Find that both the content and the form meet acceptable presentation standards  
Of scholarly work in the above mentioned discipline.

Ye, Chunfang (Ph. D., Electrical, Computer, and Energy Engineering)

Three-dimensional Gradient Index Optics Fabricated in Diffusive Photopolymers

Thesis directed by Associate Professor Robert R. McLeod

This thesis demonstrates three-dimensional gradient index (GRIN) optics fabricated in two diffusive photopolymers. These polymer optical components have localized gradient index structures, which are self-developed in diffusive photopolymers by introducing localized illuminations. Based on the sizes of the formed index structures, the photopolymer optics studied in this thesis fall into two categories: GRIN lens based optics and waveguide based optics. GRIN lenses and lens arrays with parabolic index profiles are created through Gaussian beam exposure, while GRIN lenses with arbitrary index profiles are created through a dual-axis galvo scanning system. Waveguide based optics, which include uniform waveguides, waveguide tapers, waveguides through thin optics and  $90^\circ$  sharp waveguide bends, are fabricated through direct-write lithography.

Several quantitative characterization methods for the fabricated polymer optics are described. The index profiles of the GRIN lens based optics are quantitatively measured by a modified scanning transmission phase microscope and a Shack-Hartmann wavefront sensor. Three-dimensional mode profile characterization of the polymer waveguides is carried out through a novel polymer sample preparation procedure and an active mode imaging system. A single mode performance is confirmed for the fabricated waveguides. A loss measurement for the waveguides is also accomplished.

An index formation model is developed for a diffusive polymer developed by Dr. McLeod's group, which provides a fundamental guidance for fabricating custom-design index structures in the polymer. A hybrid GRIN axicon lens is fabricated to significantly extend the depth of focus in an endoscopy OCT application. Potential applications of the fabricated polymer

optics include hybrid integrated optical circuits. The diffusive photopolymer with self-development characteristics provides a platform to integrate various optoelectronic subcomponents in integrated optical circuits.

## Acknowledgement

I am deeply indebted to my advisor, Bob McLeod for being a continuing source of tremendous support and invaluable advices, which greatly enhanced my personal and professional growth during my PhD years. Bob has not only inculcated me with the love for knowledge but also imbued me with confidence in writing and presentation, which are particularly important for me, an international student. Working with Bob has always been fun, exciting and rewarding.

I would like to thank all other members, both past and present, of the McLeod Research Group, especially Amy Sullivan, Matt Grabowski, Eric Moore, Mark Ayers, Keith Kamysiak, Ben Kowalski, Adam Urness, Michael Cole, Marty Baylor, Darren Forman, Patrick Wagner, Martha Bodine, David Glugla, Callie Fielder and Jacob Friedlein for all their help and support all the way. I thank Keith Kamysiak for developing the direct-write lithography platform with amazing accuracy and stability, which I used to fabricate the waveguide-based optics in my thesis. Adam Urness kindly let me use his UV lamp setup to cure my samples. Ben Kowalski provided many great discussions which shed insights into the index formation model. Michael Cole developed the new polymer and has been so knowledgeable and patiently to taught me the chemistry of the diffusive photopolymers.

I would like to thank my committee members: Prof. Zoya Popvic, Prof. Rafael Piestun, Prof. Carol Cogswell and Prof. H. Jerry Qi. Among them, I would like to pay special thanks to Carol Cogswell. Carol has been warm-hearted, encouraging and supportive all the time. I am very grateful for all her kind help throughout my entire journey to the PhD degree – from accepting me into to the program, to serving as my first-year academic advisor and to providing numerous and meticulous comments for the first draft of my dissertation.

I would also like to acknowledge the financial support. I have been the fortunate recipient of the fellowship from CDM Optics, Inc. My thesis work has been supported by the two NSF grants ECS 0636650 and IIP-0750506, a NIH grant and a NSF STTR grant IIP-0822695.

Finally, I would like to thank my family and friend. My husband, Yacheng Sun, has always stood by me through good times and bad. I enjoyed all his love and encouragement that accompanied me throughout the long journey.

# Content

Acknowledgement.....	v
Content .....	vii
List of Tables.....	x
List of Figures .....	xi
Chapter 1 Introduction.....	1
1.1. Hybrid integrated optical circuit .....	1
1.2. Hybrid integrated optical circuits in diffusive photopolymers.....	3
1.3. Three-dimensional diffusive photopolymer optics .....	6
1.4. Introduction to diffusive photopolymers.....	8
1.5. Outline of the thesis.....	14
Chapter 2 GRIN Micro Lens and Lens Array Fabricated in the HDS 3000 Polymer .....	16
2.1. Introduction .....	16
2.2. Diffusive photopolymer sample .....	21
2.3. GRIN lens fabrication method .....	23
2.4. GRIN lens characterization methods.....	27
2.4.1. A modified differential transmission phase microscope.....	29
2.4.2. Quantitatively measured index profiles .....	35
2.4.3. Imaging the focal spots of fabricated GRIN lens.....	38
2.5. Fabrication of GRIN lenses with a specified parabolic profile .....	40
2.6. Application and Conclusion .....	46
Chapter 3 GRIN Lens with Arbitrary Index Profiles Fabricated in the LBR Polymer .....	50
3.1. Introduction .....	50
3.2. Light Blue Russet photopolymers .....	53
3.2.1. Formulation of the LBR polymer .....	53
3.2.2. The absorption of the LBR polymer .....	54
3.2.3. Pre-cure energy dose to clear out oxygen .....	57
3.2.4. Bulk refractive index and dispersion .....	60

3.3	Index formation model for the LBR polymer.....	62
3.3.1.	Experiment design .....	64
3.3.2.	Peak index change vs. exposure dose .....	66
3.3.3.	Monomer conversion vs. photoinitiator consumption .....	67
3.3.4.	Index shapes of the Gaussian exposures .....	72
3.3.5.	Conclusions for the index formation study .....	76
3.4.	Fabrication of programmable GRIN lenses.....	77
3.4.1.	The galvo scanning system .....	77
3.4.2.	Examples of fabricated programmable GRIN lens .....	81
3.5.	Quantitative index measurement with a Shack-Hartmann wavefront sensor. ....	83
3.5.1.	Design of the testing setup .....	83
3.5.2.	Examples of the measurement results.....	84
3.6.	Conclusion .....	86
Chapter 4	Hybrid GRIN Axicon Lens Fabricated in the LBR Polymer.....	89
4.1.	Introduction .....	89
4.2.	Introduction to axicon lenses .....	91
4.3.	Design of the hybrid polymer GRIN axicon lens .....	92
4.3.1.	Specifics of the hybrid GRIN axicon lens .....	93
4.3.2.	Design of the GRIN axicon lens .....	94
4.3.3.	Index profile optimization of the polymer GRIN phase plate .....	100
4.4.	Fabrication of the hybrid GRIN axicon lens .....	106
4.4.1.	Fabrication procedure .....	107
4.4.2.	Material shrinkage .....	113
4.4.3.	Oxygen termination effect during the index development .....	117
4.5.	Experiment results .....	118
4.5.1.	Index profile of the GRIN phase plate .....	118
4.5.2.	DOF of the hybrid GRIN axicon lens .....	120
4.6.	Conclusions .....	122
Chapter 5	Uniform and Tapered Single-Mode 3D Waveguides .....	125
5.1	Introduction .....	125



5.2	Diffusive photopolymer samples .....	128
5.3	Fabrication of 3D waveguides in diffusive photopolymers .....	132
5.3.1.	Parallel lithography to fabricate 3D waveguides .....	135
5.3.2.	Taper control .....	137
5.4	Pseudo-cutback method for 3D mode characterization.....	139
5.4.1.	Pseudo-cutback sample preparation method.....	139
5.4.2.	Active mode imaging system.....	141
5.4.3.	Verification of single mode performance .....	143
5.4.4.	Mode profile test results.....	145
5.5	Loss measurement for uniform single-mode polymer waveguides .....	148
5.6	Two extensions of uniform single mode waveguides .....	149
5.6.1.	Waveguides through thin optics.....	151
5.6.2.	Sharp waveguide bends.....	154
5.7	Conclusions .....	160
Chapter 6 Conclusion and Future Work.....		161
6.1.	Summary.....	161
6.2.	Future research directions.....	164
6.2.1.	Future studies for 3D index structure fabrication .....	164
6.2.2.	Future studies for characterizing and engineering polymer materials .....	167
Appendix A .....		169
Appendix B.....		173
Appendix C.....		178
Bibliography.....		183

## **List of Tables**

Table 3.1: Formulation of the Light Blue Russet polymer .....	54
Table 3.2: List of symbols and their units in absorption calculation .....	55
Table 3.3: Summary for the experiment design.....	66
Table 3.4: Polymer chain length and TPO consumption to clear oxygen for the four samples.....	71
Table 3.5: The list of parameters of the index measurement setup .....	84
Table 4.1: Specifications of the hybrid GRIN axicon lens .....	94
Table 5.1: Comparison of perpendicular writing and parallel writing for waveguide fabrication .....	135
Table 5.2: Experiment results of mode profiles and loss measurement for waveguides through thin glass with different thickness .....	153

## List of Figures

Figure 1.1. Process steps illustrated for a single subcomponent of a hybrid integrated circuit. ....	3
Figure 1.2. Preliminary demonstration of proposed hybridization method. (a) shows the fiber mounting by encapsulation in 0.7 mm thick photopolymer. The waveguide which bends in 3D is dimly visible via refraction of the light source in the background. (b) is a preliminary result of the proposed lithography platform to show a waveguide written directly up to the fiber core. ....	5
Figure 1.3. Four types of polymer GRIN optics that provide various interconnections for hybrid integrated optical applications. (a) shows a polymer GRIN lens to collimate the light out of a single mode waveguide in order to go through thick subcomponents. (b) shows waveguide tapers for mode transformation. (c) shows a single mode uniform waveguide through thin transmissive optics. (4) shows a 90 <sup>0</sup> sharp waveguide bend. ....	7
Figure 2.1. Comparison of the two types of micro lenses: (a) conventional lenses have a surface shape and a constant refractive index; (b) radial gradient index lenses have two flat surfaces, while the refractive index is continuously varying.....	17
Figure 2.2. The geometry for the polymer slide sample: a photopolymer layer with a thickness of 1mm is sandwiched by two pieces of microscope glass slides with a thickness of 1mm. ....	22
Figure 2.3. Demonstration of the flatness of polymer slide samples fabricated using the ZeroWave <sup>TM</sup> technique. (a) is the photo of a slide sample. (b) shows the optical phase of the slide sample measured by an interferometer.....	22
Figure 2.4. Optical layout for the direct write lithography system, consisting of a frequency doubled Nd:YAG laser, a spatial filter, a collimation lens, a shutter and a focusing lens. ....	23

Figure 2.5. Demonstration of Gaussian beam width $2w(z)$ as a function of the axial distance $z$ , with a beam waist of $2w_0$ and a Rayleigh range of $Z_R$ .....	25
Figure 2.6. Fabrication of a GRIN lens array through a step-and-repeat process. ....	26
Figure 2.7. DIC images of two fabricated GRIN lens arrays with different lens sizes and periods. (a) shows a GRIN lens array with an exposure power of $7\mu w$ , an exposure time of 10s, an exposure beam diameter of $100\mu m$ and a period of $200\mu m$ . (b) shows a GRIN lens array with an exposure power of $7\mu w$ , an exposure time of 10s, an exposure beam diameter of $40\mu m$ and a period of $50\mu m$ . ....	27
Figure 2.8. Optical layout for the direct-write lithography system and the integrated differential transmission microscope used to measure the resulting index profiles. ....	30
Figure 2.9. Simulation of the quantitative phase estimation: (a) object with Gaussian index profile; (b) index gradient in x direction; (c) index gradient in y direction; (d) estimated index profile for the object. ....	32
Figure 2.10. The beam propagation simulation results for the index gradient estimation of GRIN lens with different thickness. (a) is the comparison of actual and estimated gradient for the GRIN lens with thickness of $100\mu m$ , $1200\mu m$ and $8mm$ respectively. (b) is the RMS error between the actual and the estimated gradient with different sample thicknesses. ....	35
Figure 2.11. Quantitative measurement results of a GRIN lens with an exposure power of $30\mu w$ , a beam diameter of $290\mu m$ and an exposure time of 5s: (a) raw scanning data from PSD x channel; (b) raw scanning data from PSD y channel; (c) measured index profile in gray scale; (d) measured index profile in mesh grid; (e) horizontal (x) and vertical (y) line plots through the center of the measured index profile and a parabolic fit (dashed blue curve). ....	37
Figure 2.12. Quantitatively measured index profiles of a GRIN lens array with an exposure power of $7\mu w$ , an exposure time of 10s, an exposure beam diameter of $100\mu m$ and a period of $200\mu m$ . ....	38

Figure 2.13. Experimental setup for imaging the focal spot of the GRIN lens arrays.....	39
Figure 2.14. Imaged focal spots of fabricated GRIN lens with writing condition: (a) an exposure power of $7\mu\text{w}$ , an exposure time of 10s, an exposure beam diameter of $100\mu\text{m}$ and a period of $200\mu\text{m}$ ; (b) an exposure power of $7\mu\text{w}$ , an exposure time of 20s, an exposure beam diameter of $200\mu\text{m}$ and a period of $500\mu\text{m}$ . ....	40
Figure 2.15. The measured peak index changes from three sets of GRIN lens arrays, which are fitted into a simplified index formation model.....	43
Figure 2.16. Comparison of experimentally measured index profile and calculated index profile from the derived model. Shown here is the cross section of the index profile of the GRIN lens with an exposure power of $30\mu\text{w}$ , a beam diameter of $290\mu\text{m}$ and an exposure time of 5s. ....	46
Figure 2.17. Demonstration of the function of a GRIN lens pair in a hybrid integrated optical circuit the first GRIN lens couples the light out of the guide so that the light can go through a thick micro optics; then the second GRIN lens couples the light back into the guide.....	47
Figure 2.18. Simulation demonstration of the photopolymer GRIN lenses used in the integrated optics to expand the beam: (a) the index profile of the sample; (b) the absolute value of the E field through the FFT beam propagation simulation; (c) the absolute value of the E field at the input and output planes. ....	48
Figure 2.19. Demonstration of the wafer level fabrication of GRIN lens devices. ....	49
Figure 3.1. Diagram of Beer-Lambert absorption of a light beam as it travels through a material with length of $l$ and molar concentration of $[c]$ . ....	56
Figure 3.2. Material absorptions vs. initiator concentrations. The dots are measured absorption and the line is the linear fitting.....	57
Figure 3.3. The photoinitiator bleaching curve for the LBR polymer. ....	59

Figure 3.4. The measure bulk index of refraction of the BR polymer with monomer concentration of 0%, 5% and 10% respectively. The line is linear fitting from the measured three bulk indices.....	61
Figure 3.5. The bulk index of the matrix polymer measured at the wavelength of 410nm, 532nm, 633nm, 832nm, 1302nm and 1553nm respectively. The curve line is a power fitting for these six data points.....	62
Figure 3.6. The measured on-axis index change vs. on axis exposure dose for the four samples. Each symbol represents the on-axis index contrast of a different GRIN lens.	67
Figure 3.7. Measured relationship between index change and photoinitiator consumption. The symbols are the measured on-axis index change of the GRIN lenses in the four samples respectively. The lines are linear fits. ....	68
Figure 3.8. Demonstration of the linear relationship of the monomer conversion and the TPO consumption. The dark dash line shows where monomer conversion is 1. The lines are the linear fits with the fitting equation next to each line.....	70
Figure 3.9. Measured index profile calculated via an azimuthal average of the measured 2D index profile of each lens. Parts (a)-(d) show the index profiles for the labeled cases and also the Gaussian intensity profile (the green dash line), normalized to the peak index change. Note that the index scales are not the same for all cases.....	72
Figure 3.10. Demonstration of the normalized monomer concentration after the photo cleaved radicals react with monomers and turn monomers into polymers, thus carving a hole in the monomer concentration. Here two monomer concentrations are shown for oxygen and no oxygen presence situations respectively. The oxygen threshold effect causes a sharper monomer gradient, thus increasing the monomer diffusion speed. ....	73
Figure 3.11. The depletion of TPO in the polymer as the expose dose is increasing.....	74
Figure 3.12. Comparison of the normalized index profiles and the normalized TPO consumption distributions for three group of GRIN lenses. Each group has four lenes that	

exposed at the same on axis exposure dose, but for different conditions: pre-cured oven baked, not pre-cure oven baked, pre-cured room temperature, not pre-cured room temperature respectively. The solid blue curves are the normalized measured index profiles and the dash pink curves are the normalized calculated TPO consumption distributions..... 75

Figure 3.13. Comparison of the index profiles in the four samples with same expose doses. (a) shows the normalized measured index profiles with on axis dose of 1,222 mJ/cm<sup>2</sup>. (b) shows the normalized measured index profiles with on axis dose of 2,445 mJ/cm<sup>2</sup>..... 76

Figure 3.14. The optical layout of the galvo scanning system..... 79

Figure 3.15. The system block diagram to show how the galvo scanning system works. .... 80

Figure 3.16. The expose pattern with a 9×9 matrix of dots with different exposure dose in the LBR polymer. (a) represents the exposure pattern designed in MATLAB. The circled 8 dots is a binary code used uniquely for each sample. (b) is the DIC phase image of the index profile of the exposed structure in the sample with a thickness of 200μm. The sample is not pre-cured. The last two arrays of dots are almost invisible due to the oxygen threshold effect..... 82

Figure 3.17. The exposed square pattern in the LBR polymer. (a) represents the exposure pattern designed in MATLAB. (b) is the DIC phase image of the index profile of the exposed structure in the sample with a thickness of 200μm..... 82

Figure 3.18. The exposed double parabolic pattern in the LBR polymer. (a) represents the exposure pattern designed in MATLAB. (b) is the DIC phase image of the index profile of the exposed structure in the sample with a thickness of 200μm. .... 83

Figure 3.19. The optical layout of the setup for testing the index profile of fabricated GRIN lenses using a Shack-Hartmann wavefront sensor. .... 84

Figure 3.20. Confirmation of the accuracy of the (a) is the measured wavefront slope of the off-the-shelf plano-convex singlet lens. (b) is the reconstructed wavefront surface of the lens. (c) is the comparison between measured optical path delay profile and the calculated one from the surface profile..... 85

Figure 3.21. One example of measured index profile the fabricated GRIN lens by the galvo scanning system. The thickness of the sample is 1mm and the sample is not pre-cured. (a) is the rendered exposure pattern for a double parabolic lens. (b) is the measured optical path delay (OPD) from the Shack-Hartman sensor. (c) is the calculated index profile based on the measured OPD and the thickness of the GRIN lens. (d) is the x-cross section of the exposure pattern and the measured index profile. .... 86

Figure 3.22. Demonstration of the fan-out waveguide array that can be fabricated using the galvo scanning system through a layer-by-layer exposure. (a) is the simulated index profile of the fan-out waveguide array. (b) is the simulated exposure pattern that the galvo scanner drew for the first layer, where  $z=0\mu\text{m}$ . The colorbar indicates the normalized exposure dose. (c) is the simulated exposure pattern that the galvo scanner drew for the last layer, where  $z = 4000\mu\text{m}$ . .... 88

Figure 4.1. The optical layout of the endoscope OCT probe..... 93

Figure 4.2. Parameters used to derive the index profile of a thin GRIN axicon..... 95

Figure 4.3. The index profile of the derived thin-lens GRIN axicon to meet the specifics ..... 97

Figure 4.4. The simulated intensity distribution of the thin-lens GRIN axicon lens. (a) shows the GRIN axicon lens focusing the incident Gaussian beam  $\sim 1\text{mm}$  away from the back of the lens while (b) is the intensity distribution in the focus region. .... 98

Figure 4.5. Demonstration of the design of the hybrid GRIN axicon lens. .... 99



Figure 4.6. Simulation of the index profile optimization of the GRIN phase plate through a MATLAB simulation program. (a) is the index distribution setup for the simulation. (b) is the simulated intensity distribution of the hybrid GRIN axicon lens.....	102
Figure 4.7. The simulated intensity distribution at the focused region of the hybrid GRIN axicon lens .....	103
Figure 4.8. Demonstration the four requirements to defined the DOF.....	104
Figure 4.9. The region that is defined as the DOF. The dip at $\sim 1950\mu\text{m}$ is due to the slight oscillation for meeting the transverse resolution shown in Fig. 4.8-(a).....	105
Figure 4.10. Demonstrate the direct search results for optimized the index profile of the GRIN phase plate.....	105
Figure 4.11. Index profile for the GRIN phase plate design. The blue dash line is the optimized index profile of the GRIN phase plate from the MATLAB simulation. The red solid line is the designed index profile for the galvo scanner to fabricate in the polymer sample. ....	106
Figure 4.12. The designed lens geometry of the hybrid GRIN axicon lens. (a) is the three-dimensional cartoon of the lens. (b) is the photo of the hybrid GRIN axicon lens I've made compared to the one cent coin. (c) shows the cross section of the lens.....	107
Figure 4.13. The photo of a wafer sample I've made with 16 polymer tubes. ....	108
Figure 4.14. The optical layout of the galvo scanning system, which is used to fabricate the GRIN polymer phase plates. ....	109
Figure 4.15. The optical layout of the stage to assemble the GRIN phase plate with the GRIN rod lens through an active alignment procedure. The inset shows part of the actual experimental setup to assemble the phase plate with the GRIN rod lens. The phase plate and the GRIN rod lens are hold by two custom-made plastic scaffolds respectively. Each plastic scaffold is mounted to a 5D stage.....	111

Figure 4.16. Demonstration of the sample geometries during each step of the 8-step fabrication procedure .....	112
Figure 4.17. Stress testing results of the polymer samples in aluminum tubes with thickness of 1mm, 2mm and 3mm. The images are captured by a bright field microscope with two crossed polarizers. The upper row images are taken <i>before</i> the samples are flood cured. The lower row images are taken <i>after</i> the samples are flood cured.....	114
Figure 4.18. The measured uniformity of the polymer tube sample. (a) shows the sample geometry. (b) is the two dimensional plot of the measured OPD. (c) is the x cross section of the measured OPD. (d) is the y cross section of the measured OPD.....	115
Figure 4.19. The deformed polymer surface due to material shrinkage in the tube sample without glass slides on both sides. (a) shows the sample geometry. (b) is the two dimensional plot of the measured OPD. (c) is the x cross section of the measured OPD. (d) is the y cross section of the measured OPD. ....	116
Figure 4.20. The measured index profiles of a individually packaged polymer tube sample: (a) when the windows was delaminated from the polymer; (b) after the windows were reattached to polymer. The missing part on the down-right corner is due to a small air bubble trapped in the polymer. ....	117
Figure 4.21. The measured index profile for the GRIN phase plate with oxygen termination effect around the edge. (a) is the measured two-dimensional index plot. (b) is the cross section of the measured index compared to the exposure dose distribution....	118
Figure 4.22. The measured index profile of the GRIN phase plate I made. (a) is the exposure does pattern. (b) is the measured two-dimensional index plot. (c) is the comparison between the cross section of the index structure and the exposure dose pattern. ....	119
Figure 4.23. The index profile of the GRIN phase plate compared at Step 4 and Step 7 validates the fabrication procedure. (a) is the measured index profile plot from Step 4; (b)	

is the measured index profile plot from Step 7; (c) is the cross-section index profile comparison between Step 4 and Step 7..... 120

Figure 4.24. The measured PSFs of the hybrid GRIN axicon lens from the beam profiler through the focus region. The color bar stands for the intensity scale. .... 121

Figure 4.25. The main lobe diameters over the focus region for the hybrid GRIN axicon lens I have made..... 122

Figure 4.26. The measured PSFs of the glass GRIN rod lens from the beam profiler through the focus region. The color bar stands for the intensity scale. .... 122

Figure 4.27. The measured index profile yields a better fitting with the photoinitiator consumption distribution than the exposure dose pattern. (a) is comparison between the measured index profile and the exposure dose. (b) is comparison between the measured index profile and the normalized photoinitiator consumption..... 123

Figure 5.1. Two sample formation geometries used in 3D waveguides fabrication and testing. (a) Cuvette sample: photopolymer material HDS 3000 with half photoinitiator is casted into a glass cuvette with size of 5mm×10mm×50mm. (b) Slide sample: photopolymer material is casted into a 1mm polymer layers between two pieces of glass. The polymer layer later is delaminated from the glass and stacked together to form an optical-quality thick sample for 3D characterization of the waveguides..... 130

Figure 5.2. DIC microscope images of waveguides with the different power modulation curves. The photopolymer used for these two waveguides is the LBR polymer with 0.2% photoinitiators, which is discussed in chapter 3. (a) The writing power is 10.1  $\mu\text{W}$  at the front surface, modified by power profiles  $T_{\text{Eff}} = 0.75$ . The writing velocity is 1mm/s. (b) the writing power is 10.1  $\mu\text{W}$  at the front surface, modified by power profiles  $T_{\text{Eff}} = 0.70$ . The writing velocity is 1mm/s. .... 131

Figure 5.3. DIC microscope images of waveguide arrays that show destructive effects due to dust or impurities in the material. (a) The scatter pattern recorded in a waveguide

grating with period of  $50\mu\text{m}$  (b) The filaments formed in a waveguide grating with period of  $50\mu\text{m}$ ..... 132

Figure 5.4. Waveguide fabrication by direct-write lithography through parallel writing or perpendicular writing..... 133

Figure 5.5. The calculated index cross section of waveguides fabricated by (a) parallel writing and (b) perpendicular writing respectively..... 134

Figure 5.6. Optical layout of the parallel direct-write lithography system. The logarithmic neutral density filter modulates the laser with large dynamic range naturally matched to the exponential Beer Lambert absorption. .... 136

Figure 5.7. Pseudo-cutback method developed for polymers that cannot be cut or polished. Step 1: Cast individual polymer layers. Step 2: Laminate the layers into a thick polymer sample. Step 3: Write guides through the laminated polymer sample. The material transmittance (dashed line), the incident power curve (dash-dot line) and power at the focus (solid line) along the depth are also shown. Step 4: Separate the stack sample the individual layers. Step 5: Test individual layers. .... 140

Figure 5.8. Optical layout of the active mode imaging system for waveguide characterization. A typical measured profile from a single-mode guide is shown in the inset, which is nearly perfect Gaussian in shape..... 141

Figure 5.9. A typical user interface of the beam profiler for mode profile measurement. .... 143

Figure 5.10. Verification of single-mode performance. (a) - (c) are the test geometries for  $x$ ,  $y$  and  $z$  direction respectively. (d) - (f) are the measured and theoretically calculated coupling efficiencies as a function of offset in the  $x$ ,  $y$  and  $z$  direction respectively. Disagreement at  $z > 0$  may be due to uncorrected spherical aberration. .... 145

Figure 5.11. 3D characterization of tapered and untapered buried waveguides. The test procedure shown in Fig. 5.10 verifies that the waveguides are single mode at all points.

The error bars are one standard deviation of seven samples at each point, demonstrating the repeatability of the process. Dotted lines are parabolic fits to show trends. Accurate data for several points could not be taken because the coupling between incident laser mode and the guided mode plummets in the weakly guiding limit so that the mode could not be captured on the beam profiler. .... 146

Figure 5.12. Experimental layout and results of loss measurement for the uniform single-mode waveguides. (a) is modified cutback method for the loss measurement. Couple the incident laser beam into the waveguide and capture the maximum power in the guided mode on the mode profiler. By comparing the power in the guided mode to the measured power when the incident laser beam is focused at the front surface mirror, the material absorption and loss at the reflection surfaces are calibrated out. (b) Loss versus guide length..... 148

Figure 5.13. Sample geometry for direct-writing a waveguide through thin optics..... 151

Figure 5.14. Demonstration of the light guided in the waveguide through thin glass. (a) The incident laser focus diffracts without waveguide. (b) The incident laser focus couples into the waveguide. .... 152

Figure 5.15. The coupling loss through the thin glass due to the shife in z..... 153

Figure 5.16. The comparison of the measured coupling loss to the theoretical calculated ones through thin glasses at the thickness 30 $\mu$ m, 50 $\mu$ m and 100 $\mu$ m. A polynomial fitting is applied to both the measured and theoretical calculated coupling losses. .... 154

Figure 5.17. Sample geometry for 90<sup>0</sup> sharp waveguide bend: (a) waveguide bends fabrication through parallel writing and (b) waveguide bends characterization through the active mode imaging. .... 156

Figure 5.18. Demonstration of the deviation of the polymer sample from a perfect isosceles right the triangle.  $\Delta\theta_1$  shows the deviation of the angle between the diagonal plane of the sample and the x-y plane from 45<sup>0</sup>.  $\Delta\theta_2$  is the angle that diagonal plane of the sample deviates from perpendicular to x-z plane. S1 is the x-y plane, S2 is he y-z

plane, and S3 is the diagonal plane of the triangle sample. Guide 1 is the front portion of the waveguide bend, while Guide 2 is the back portion of the waveguide bend. .... 157

Figure 5.19. Demonstration of the waveguide coupling loss, which is due to angular misalignment in (a) y-z plane and (b) x-y plane. .... 159

Figure 6.1. Process for on-chip rib waveguide to off-chip fiber connector packaging. (a): The chip is hard-mounted within a package which includes a thin (~25 micron) window centered on an external fiber connector. (b): The edge of the chip is encapsulated with polymer which fills the chip-window gap. (c): The optical bonder, working through the package window, identifies the waveguide and window center coordinates. (d): The written waveguide tapers for asymmetry and mode-mismatch of the waveguide and bends from the uncontrolled position of the chip to the center of the connector ferrule. A fiber later inserted into the connector is efficiently connected to the waveguide. .... 165

Figure 6.2. A 1550 nm mode-locked laser that is implemented (a) in fiber and (b) in a hybrid optical integrated circuit via 3D-routed waveguides in an encapsulating photopolymer. Note the 90° bends implemented with embedded prisms, the integrated fiber connection and complete hybridization on VLSI. .... 166

Figure A.1. Theory of operation of a duolateral isotropic position sensitive detector [186]. (a) shows the layout and working principle of an isotropic PSD. (b) shows the photocurrent that flows in a duo-lateral PSD. .... 170

Figure A.2. Calibration of the ON-TRAK PSD detector model PSM2-45 for (a) the x channel and (b) the y channel. .... 171

Figure A.3. Validation of the differential transmission phase microscope metrology by measuring an off-the-shelf plano-convex singlet lenses. (a) Measured shape profile of the lens. (b) Comparison of the x cross section of the measured lens shape to the actual one, indicating an experimental error of about 1% .... 172

Figure B.1. The output powers from the laser diode vs. driving currents. .... 173

Figure B.2. The laser modulation voltage vs. target power command in the parameter file. The laser modulation voltage saturates at 4.34V.....	174
Figure B.3. The modulation pulse width vs. time duration command in the vector file. .....	175
Figure B.4. The calibration pattern. The dark spot is the exposure laser focus spot position. The dark line traces the movement of the laser focus spot. The color bar represents the exposure dose distribution. ....	176
Figure B.5. The measured phase image from a DIC microscope for the calibration square pattern. ....	177
Figure C.1. The basic elements of a Shack-Hartmann sensor. ....	178
Figure C.2. The data flow diagram for the wavefront analysis. ....	179

## Chapter 1

# Introduction

This thesis demonstrates three-dimensional gradient index (GRIN) optics fabricated in diffusive photopolymers. These polymer optical components have localized index structures, which are self-developed in diffusive photopolymers by introducing localized illuminations.

Based on the sizes of the formed index structures, the photopolymer optics studied in this thesis fall into two categories: GRIN lens based optics and waveguide based optics. GRIN lenses and lens arrays with parabolic index profiles are created through Gaussian beam exposure, while GRIN lenses with arbitrary index profiles are created through a dual-axis galvo scanning system. Waveguide based optics, which include uniform waveguides, waveguide tapers, waveguides through thin optics and  $90^\circ$  sharp waveguide bends, are fabricated through direct-write lithography.

These diffusive polymer components can be potentially applied to hybrid integrated optical circuits. The diffusive photopolymer with self-development characteristics provides a platform to incorporate various optoelectronic subcomponents in integrated optical circuits.

### 1.1 Hybrid integrated optical circuit

Integrated optical circuits have a number of benefits over standard electronic circuits and conventional free space optical systems. Optical circuits are capable of handling a larger bandwidth and are immune from electromagnetic interference. A conventional free optical system is composed of large discrete elements, and requires alignment of each element generally on a stable optical table. Since the integrated optical circuits turn a table size optical system into a chip, it is of smaller size, lighter weight, and greater stability.



However, unlike purely electronic circuits, the majority of optical systems demand multiple material components. These materials include drawn glass fiber, lithographically patterned semiconductors, deposited dielectric films, grown crystals, replicated diffractive elements and ground lenses [1]. Such material diversity cannot be grown or doped from a single semiconductor process. Thus optical systems are inherently heterogeneous, which necessitates hybridization of integrated optical circuits.

However, integrating various optoelectronic elements in the optical circuits faces two major challenges. The first challenge is to develop a material platform that is suitable for hybridization. Research in silicon photonics has demonstrated that many optical functions can be performed with a single material. For example, it suffices to use silicon for fabricating detectors and planar waveguides. However, keeping the breadth of functionality requires the system to be capable of incorporating the full variety of materials used in tabletop optical systems. The second challenge arises from optical interconnection, which includes (1) on-chip interconnection to connect various optoelectronic elements; (2) on-chip interconnection to guide the light through the optoelectronic elements that can be up to cm scale and back into the waveguide circuit with tolerable loss and (3) off-chip interconnection to connect the chip to the outside world generally through fibers.

Current available integration methods cannot sufficiently tackle these two challenges. Hybridization solutions from the integrated microelectronics field such as flip-chip bonding [1] are inappropriate for optical interconnects due to the sub-micron alignment tolerances required to match optical wavefronts. Since most optical subcomponents involve at least one cleaving, sawing or a polishing step, the dimensions of each individual hybrid subcomponent typically vary by many micrometers. Therefore, each device requires a customized alignment, excluding the use of lithographically-defined optical interconnects such as planar lightwave circuits (PLCs) [2,3] or lithographically-defined alignment features such as silicon optical benches [4,5].

This need for device-to-device customization explains the current approach for optical fabrication which requires manual active alignment of optical components followed by epoxy to a machined metal scaffold. This approach was used by Galileo and van Leeuwenhoek several hundred years ago and has advanced very little since then. The resulting device is expensive due to the intensive manual labor, large due to the scaffold, delicate due to the nanometer tolerances held only by adhesive and limited to small quantities due to active alignment. These features are acceptable in high-value applications but not in high-volume applications which demand the opposite characteristics.

To overcome the above-mentioned limitations for current approaches, I investigate a novel optoelectronic lithography platform that uses diffusive photopolymer as an optically-addressable encapsulant in which embedded micro-optical components are interconnected by waveguides directly written into the photopolymer via 3D direct-write lithography. The details for the proposed lithography platform are discussed in the next section. The diffusive photopolymer is introduced in Sec 1.4.

## 1.2 Hybrid integrated optical circuits in diffusive photopolymers

The proposed lithography platform can potentially fabricate hybrid integrated optical circuits in five main steps, shown in Fig. 1.1 below.

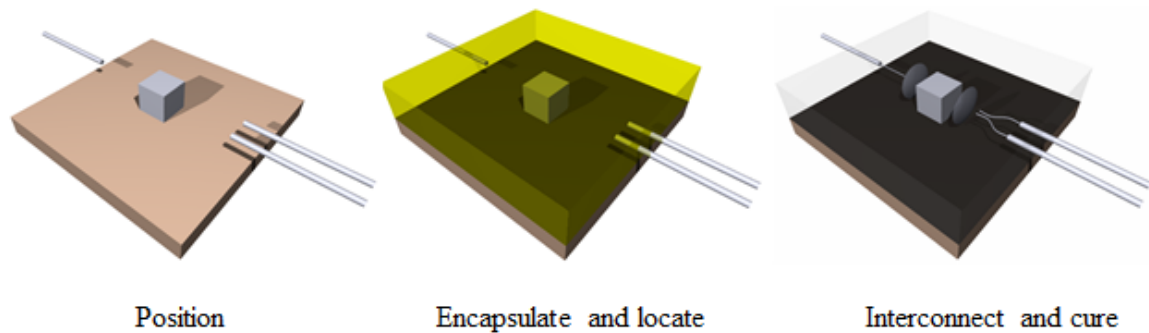


Figure 1.1. Process steps illustrated for a single subcomponent of a hybrid integrated circuit.

*Position:* Hybrids such as fibers, laser diodes, detectors, thin film filters, etc. are first loosely positioned on a substrate.

*Encapsulate:* The liquid polymer is then cast over the assembly. A unique property of the diffusive polymer is its very low shrinkage and shrinkage stress as it thermally cures into a solid at room temperature. The polymer naturally adheres to glass, plastic and dielectric surfaces and thus encapsulates and hermetically seals all of the subcomponents.

*Locate:* The locations and tolerances of the parts are now detected with a scanning confocal microscope [6] and/or a scanning transmission microscope [7] that operate in the red, which is outside the sensitivity band of the polymer material. The system controller records these fabrication and location deviations and adjusts the interconnection design accordingly.

*Interconnect:* The writing beam of moderate numerical aperture (0.1 to 0.6) and very low power ( $\mu\text{W}$ ) is scanned in three dimensions to selectively write optical index features. The index response in the polymer is localized at the focus of the beam in response to the intensity profile. The introduced index structure in the diffusive polymer material can be controlled both by materials formulation and lithography hardware configurations.

*Cure:* Finally, uniform incoherent exposure bleaches the writing dye and fully cures the polymer making the part optically clear and insensitive to further exposure.

The proposed materials and lithography platform have applications in a broad range of markets. By encapsulating arbitrary hybrids, virtually any optical or optoelectronic component can be integrated into a guided-wave microcircuit. By aligning the waveguides in 3D to these encapsulated parts, the system avoids all physical active alignment, one of the major cost and reliability constraints of nearly all optical devices. For example, the cost of fiber pigtailling a laser diode is typically 50% of the total cost and is the source of 80% of device failures [8]. The high sensitivity of the materials enables CW lasers that are inexpensive and naturally write smooth waveguides for low scattering loss. The single, maskless process step enables low cost at low

volumes, which is essential for most optical circuit applications today. These applications include telecommunications, signal processing, medical devices, biological and chemical sensing systems.

Previous graduate students have already demonstrated the 3D direct-write lithography platform [9] and a polymer waveguide to interconnect two fibers [10], shown in Fig. 1.2. My thesis work has extended the existing work in three ways. First, this thesis extends the GRIN optics that are fabricated in the diffusive polymers to single mode low loss waveguides, waveguide tapers,  $90^\circ$  sharp waveguide bends, GRIN lenses and lens arrays. Second, this thesis presents the methods that quantitatively characterize the index profile and performance of the fabricated GRIN polymer elements. Third, I studied the index formation in a diffusive photopolymer, which provides fundamental guidance to fabricate GRIN polymer optics with high fidelity. The next section will briefly demonstrate the GRIN photopolymer optics that I have made.

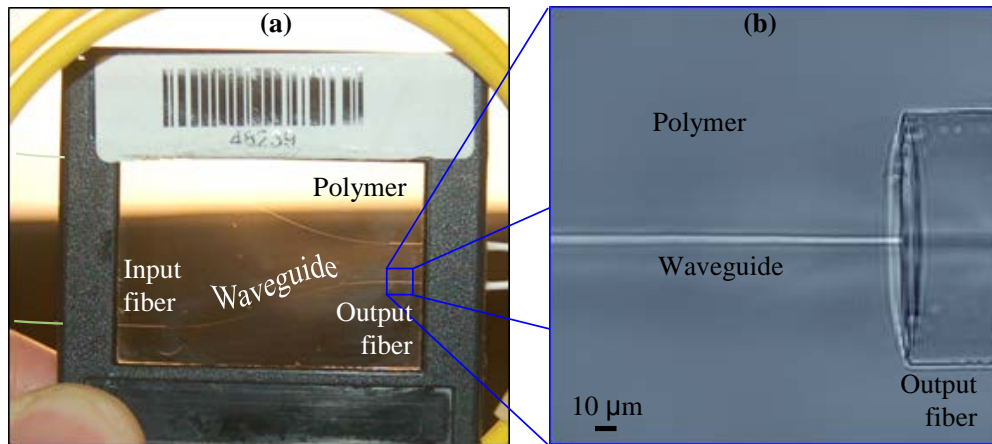


Figure 1.2. Preliminary demonstration of proposed hybridization method. (a) shows the fiber mounting by encapsulation in 0.7 mm thick photopolymer. The waveguide which bends in 3D is dimly visible via refraction of the light source in the background. (b) is a preliminary result of the proposed lithography platform to show a waveguide written directly up to the fiber core.

### 1.3 Three-dimensional diffusive photopolymer optics

Previous work has demonstrated 3D waveguides fabricated in the diffusive photopolymers, which potentially provide the interconnection between the encapsulated optoelectronic components. However, guiding the light through optical-electronic components with various thicknesses, off-chip interconnection and others are the remaining problems. First of all, the light is not guided in optical-electronic components. Secondly, the mode diameter is approximately several micrometers for single mode waveguides at the visible spectrum. Thus, the light diffracts through the optical-electronic component and only a small portion will couple back to the waveguide circuit. For example, a photorefractive crystal or a gain medium in a laser system has an optical path length of about 1cm. After the guided mode diffracts through a 1cm unguided region, less than 1% of the original light couples back into the waveguide circuit. The off-chip interconnection generally requires an adiabatic guided mode conversion to match the mode size of the on-chip waveguide and the off-chip fiber.

This thesis demonstrates several types of 3D GRIN optics I have made in diffusive polymers to provide various interconnection needs for hybrid integrated optical application. These polymer elements include GRIN lenses, single mode waveguide tapers, single mode uniform waveguides through thin transmission optics and  $90^\circ$  sharp waveguide bends. The potential functions of these polymer elements in a hybrid integrated optical circuit are shown in Fig. 1.3. GRIN lenses with parabolic index profile can provide a mode expansion ratio up to 1:100. Thus, the light out of the single mode waveguide is now collimated by the GRIN lens to go through optics with thickness up to cm. Then another GRIN lens focuses the collimated light back to the single mode waveguide circuit. Single mode waveguide tapers can provide mode expansion ratios typically around 1:2 to 1:5, which are especially useful for coupling between waveguides with different mode sizes and off-chip interconnection between the waveguide and the optical fiber in order to reduce the coupling loss.

Waveguides fabricated by parallel direct-write lithography, which will be discussed in chapter 5, can naturally go through thin transmission optical elements or bounce back at the reflective optical elements to form sharp waveguide bends. Thus single mode uniform can directly connect thin films with tolerable coupling loss, since the thickness of thin film filters that are used in hybrid integrated optical system are typically at the order of tens of micrometers. Sharp waveguide bends make the optical circuit more compact and integrate reflective optics into the optical waveguide circuits.

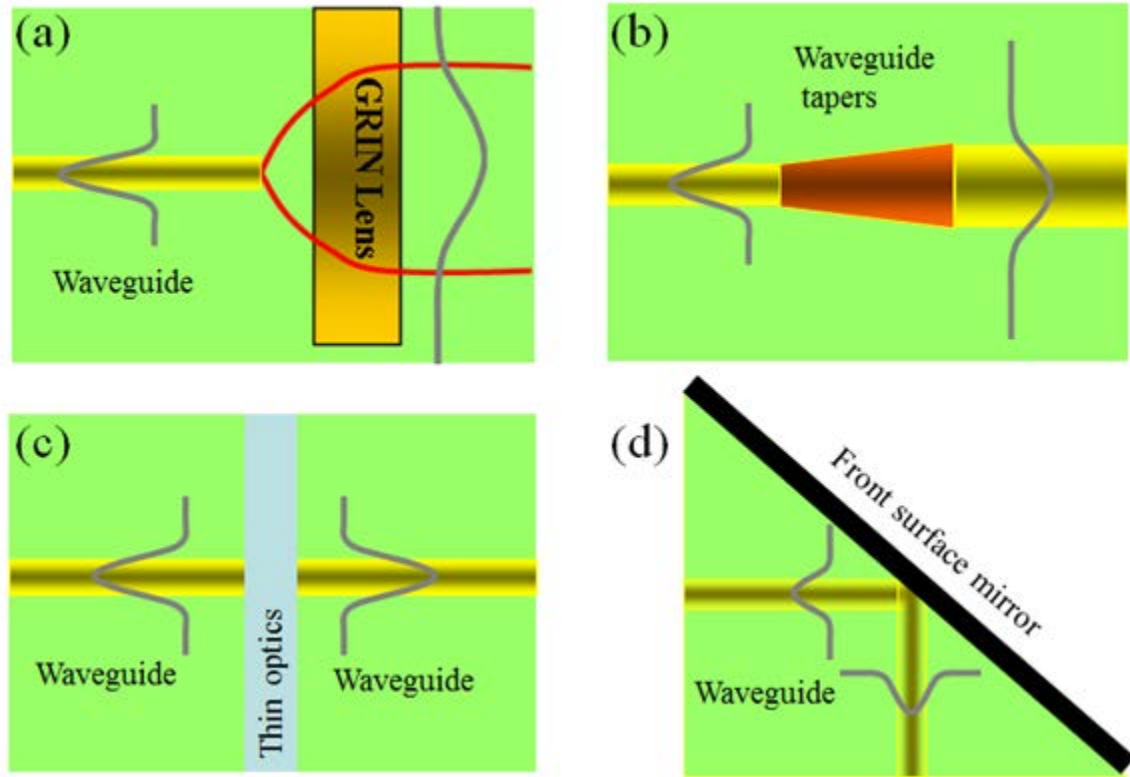


Figure 1.3. Four types of polymer GRIN optics that provide various interconnections for hybrid integrated optical applications. (a) shows a polymer GRIN lens to collimate the light out of a single mode waveguide in order to go through thick subcomponents. (b) shows waveguide tapers for mode transformation. (c) shows a single mode uniform waveguide through thin transmissive optics. (4) shows a  $90^\circ$  sharp waveguide bend.

Furthermore, this thesis will demonstrate the ability to fabricate arbitrary index structure in the diffusive photopolymer, and with high fidelity. This capability enables customized low-volume GRIN optics to be produced in a rapid and cost-effective way. Although fully

hybridizing the integrated optical circuits is still at its nascent stage, the research demonstrated in this thesis is a meaningful step forward by building up the tool box to fabricate a hybrid integrated optical circuit.

#### **1.4 Introduction to diffusive photopolymers**

This section will briefly discuss the characteristics of the diffusive photopolymers used in this thesis. A simplified index formation model is demonstrated to help readers to gain a better understanding of the diffusive polymers. Diffusive photopolymers, also referred to as volume photopolymers, are originally an active research area in applications involving holographic data storage. Dupont introduced [ 11 ] and commercialized photopolymer films intended for holography with thickness up to 100 $\mu$ m in the 1970's[12,13]. Such photopolymers self-develop index change by diffusion and were primarily utilized for display holography. Other U.S. and Asian chemical companies, including Polaroid [14] (now Dow Corning [15]), also developed similar materials for the display, security and storage markets. In 1993, Bell Laboratories initiated an effort to develop an improved material that would meet the stringent demands by high-density holographic data storage. This improved photopolymer, named *Tapestry*<sup>TM</sup> [ 16 ], has a fundamental advantage thanks to a two-chemistry strategy that enables the host matrix and the photo-active response to be independently controlled. Benefits of *Tapestry*<sup>TM</sup> photopolymers include unmatched dynamic range, high photosensitivity, dimensional stability, optical clarity, manufacturability, large (cm) thickness, and environmental as well as thermal stability. In this thesis, I used two types of diffusive photopolymers, both of which are based on *Tapestry*<sup>TM</sup>. The first is the *Tapestry*<sup>TM</sup> HDS 3000 polymer from InPhase Technologies, a local company that was spun off from Bell Laboratories. The second one is created in our group using *Tapestry* as a model, and named as *Russet*. This non-commercial formulation enabled us to study the material characteristics as a function of its formulation. The material is sensitive to 405 nm and has very low absorption as is needed for thick (many mm) optics, thus the specific formulation used in this

thesis is referred to as *Light Blue Russet* (LBR). I conducted a preliminary material study of this LBR polymer, which is demonstrated in chapter 3.

These two diffusive photopolymers are flexible solids. Their active components consist of (1) an initiator that absorbs a fraction of the incident light to form radicals or other initiating species and (2) a monomer that polymerizes by reacting with this photo-initiator. Therefore, a localized illumination is used to create high molecular-weight polymers in the illuminated region via the consumption of low molecular-weight monomer units. This local depletion of monomers causes monomers to diffuse into the exposed region, resulting in an area of increased density and refractive index. After this mass-transport has locally increased the refractive index, a uniform optical exposure is used to consume all remaining initiators and monomers, making the polymer chemically and optically inert.

The unique properties of the diffusive photopolymers make them appealing for hybrid integrated optics application because of the following reasons. Firstly, the diffusive photopolymers initially are liquid and can encapsulate various optoelectronic components. The polymers then harden at room temperature, permanently fixing the positions of the components. A step-growth polymerization is used to reduce shrinkage stress the matrix solidification. Secondly, unlike traditional photopolymers such as photoresists, the index structure formation process in diffusive photopolymers does not require any thermal or wet processing [13-14,]. A necessary step for making structures in photoresists is material removal via solvent wash and wet processing also makes photoresists inappropriate for the fabrication of 3D index structures, since the solvent access is not possible. Thirdly, one photo-absorption mechanism makes the diffusive photopolymers highly sensitive to incident light, allowing index structures to be written using low power, continuous wave and thus inexpensive lasers. Furthermore, these photopolymer materials are themselves inexpensive and can be engineered to have low optical absorption and scatter after flood cured.



A final advantage of the diffusive photopolymer is its tunability. For example, the material can be made more sensitive by increasing the initiator concentration or choosing an initiator with higher absorption. Increasing the monomer concentration or using monomers with higher index of refraction can lead to higher index change. Functionality or stiffness of the matrix monomer impacts modulus and diffusion time. Therefore, the material formulation can be altered accordingly to suit different applications. While this flexibility is useful, in order to optimize photopolymer material's performance, a quantitative model about the index structure formation is needed, which is described next.

Here, a simplified index formation model is presented, which describes the functional dependence of recorded index structures on the optical exposure pattern within the photopolymer sample. This model is important for all applications in volume photopolymers, especially for hybrid integrated optics applications, where precise index structures are required to produce desired functionality in integrated optical components.

There are three main steps involved in the index formation process in the diffusive photopolymers: initiation, polymerization and termination. Here, the three main steps are assumed to be well separated, which means that the initiation rate is much higher than polymerization rate and polymerization rate is much higher than the monomer diffusion rate. In the simplified model, it is also assumed that none of active species are diminished, which implies the concentration of active species is assumed to be constant. A more complete model that removes these assumptions is presented in chapter 3. The details regarding the index formation process are shown next.

*Initiation* When a volume photopolymer sample is illuminated, a photoinitiator molecule PI absorbs a photon and then cleaves into a pair of radical  $R^\bullet$ , expressed as



These primary radicals,  $R^\bullet$ , react with a monomer functional group  $M$  to produce propagating radicals  $M^\bullet$



*Polymerization* The polymerization process then proceeds via chain growth with successive addition of monomer units, which can be generally expressed as



*Termination* The polymerization reaction propagates until the reaction terminates. The termination process can generally be classified into two mechanisms: bimolecular termination and unimolecular termination.

In bimolecular termination, two radical centers annihilate each other and transform into inactive polymers. Such a transformation process can take two likely routes: either by coupling, resulting in a single dead polymer chain, or the two chains can be terminated by the process of disproportionation, resulting in two unlinked dead polymer chains. These two possibilities can be summarized by two equations shown in Eq. 1.4. The important feature of bimolecular termination is that its rate depends on the square of the radical density since it involves two radicals.



In contrast, in unimolecular termination, the propagating radical center is terminated by a quenching molecule to stop the polymerization reaction; alternatively, radicals are trapped that causes active radicals to cease participation in the polymerization reaction; or, mathematically,



The kinetics of bimolecular versus unimolecular termination yield very different relationships between index contrast and exposure intensity. To see that this is the case, consider the rates at

which the initiation, polymerization and termination steps occur. For initiation via photo-dissociation of initiator molecules, the initiation rate  $R_i$  will be given by

$$R_i = 2\eta I_0, \quad (1.6)$$

where  $I_0$  is the intensity distribution of the localized illumination, the parameter  $\eta$  is the quantum yield, indicating the number of initiated polymer chains per photon. The factor of 2 indicates that each cleaved photoinitiator molecule produces a pair of radicals.

The polymerization step involves the reaction of a monomer molecule with a radical center, and as such, the polymerization rate  $R_p$  will be proportional to the concentrations of radicals and monomer

$$R_p = k_p [M^\bullet][M], \quad (1.7)$$

where  $k_p$  is the kinetic rate constant of the polymerization reaction,  $[M^\bullet]$  is the propagating radical concentration, and  $[M]$  is the monomer concentration. First, restricting to the case of just bimolecular radical termination, where each termination event involves two propagating radical centers, the termination rate  $R_t$  can be expressed as,

$$R_t = 2k_t [M^\bullet]^2. \quad (1.8)$$

In the steady state, the initiation rate equals the termination rate ( $R_i = R_t$ ). This results in a radical concentration given by

$$[M^\bullet] = \sqrt{\frac{\phi}{k_t} I_0}. \quad (1.9)$$

Substituting  $[M^\bullet]$  with Eq. 1.9 in Eq. 1.7, the overall polymerization rate is

$$R_p = k_p [M] \sqrt{\frac{\phi}{k_t} I_0}. \quad (1.10)$$

Thus, the polymerization rate is proportional to the square root of the incident irradiance for the case of bimolecular termination. It is typical to assume a constant polymerization rate and a

resulting index contrast proportional to monomer consumption and I will validate this assumption in chapter 3. This assumption leads to an index change  $\delta n$  given by

$$\delta n \propto R_p t, \quad (1.11)$$

where  $t$  is the duration of the optical exposure. Thus, for the case of bimolecular termination,

$$\delta n \propto \sqrt{I_0} t. \quad (1.12)$$

This result, well known in the polymer literature, says that monomer conversion and thus index change is proportional to the square root of intensity due to bimolecular termination. This would result in index structures that are not copies of incident intensity and to an apparent reduction in sensitivity as intensity is increased.

Now, the index change dependence on exposure intensity for unimolecular termination is derived in the same way. The termination rate for pure unimolecular termination is given by

$$R_t = k_Q [M^\bullet][Q], \quad (1.13)$$

where  $[Q]$  is the concentration of the inhibiting species and  $k_Q$  is the kinetic constant for the inhibition reaction. In this case, the steady state solution yields

$$[M^\bullet] = \frac{2\phi}{k_Q [Q]} I_0 \quad (1.14)$$

and the polymerization rate is governed by

$$R_p = \frac{2\phi k_p [M]}{k_Q [Q]} I_0. \quad (1.15)$$

So in the case where the dominant termination pathway is unimolecular, the polymerization rate is directly proportional to the incident irradiance, expressed as

$$\delta n \propto R_p T \propto I_0 t. \quad (1.16)$$

In most radical photopolymer systems, termination is a mixture of unimolecular and bimolecular mechanisms. The polymerization rate in these cases is accurately described as  $I^\alpha t$ ,

where  $I$  is the writing beam intensity,  $t$  is the exposure time and  $\alpha$  is between  $\frac{1}{2}$  (pure bimolecular) and 1 (pure unimolecular) termination. Note that, in the case that  $\alpha$  does not equal 1, the relevant dose for the material cannot be described by  $\text{mJ}/\text{cm}^2$  but instead by independently characterized as intensity for a specific time. This model is simple; yet it is able to capture the key chemical reactions that occurred in the polymer to form the index structure. On the other hand, real-world applications of diffusive polymers require a generic and corresponding more complicated index formation model, due to the two assumptions made by this simplified model. I will present a more sophisticated index formation model in chapter 3, which is developed in collaboration with two other graduate students in Prof. Robert R. McLeod's group.

## 1.5 Outline of the thesis

The purpose of this thesis is four-fold. First, I demonstrate how to fabricate three-dimensional gradient index (GRIN) optics in two diffusive photopolymers. Second, I present the methods that quantitatively characterize the index profiles of the polymer optics. Third, I discuss some of the potential applications of GRIN optics. Fourth, I will show an index formation model for the LBR polymer, which provides a fundamental guidance for fabricating polymer optics with arbitrary index profiles.

More specifically, chapter 2 shows GRIN lenses and lens arrays formed in the *Tapestry*<sup>TM</sup> HDS 3000 photopolymer, which is photoinitiated by a defocused laser beam with a wavelength of 532nm. A modified scanning phase microscope [7] is used to quantitatively measure the index profile of the fabricated GRIN lenses. The measured index profiles of lenses created under Gaussian exposures turn out to fit well with parabolic shapes, which are the standard index profiles of commercial GRIN lenses. Chapter 3 introduces a more general method to make GRIN lenses with arbitrary index profiles in a diffusive photopolymer initiated at a wavelength of 405nm. A preliminary study of this LBR polymer is also discussed in this chapter. A dual-axis galvo scanning system is implemented to draw two-dimensional exposure dose distributions, thus

forming arbitrary index changes in the diffusive photopolymer. The index profiles of the fabricated lenses are characterized in transmission by a Shack-Hatmann wavefront sensor. Chapter 4 gives an example of the application of GRIN lenses with arbitrary index profiles: a hybrid GRIN axicon lens to increase the depth of focus (DOF) for an endoscope optical coherent tomography application. The hybrid GRIN axicon consists of a GRIN phase plate, which is made in the LBR polymer and a commercial GRIN rod lens. An 8-step fabrication procedure is established to solve problems that emerged during the polymer packaging and index formation process. Chapter 5 presents single-mode uniform and parabolically tapered three-dimensional waveguides that are fabricated via direct-write lithography in the *Tapestry*<sup>TM</sup> HDS 3000 photopolymer. Modulation of the writing power is demonstrated to compensate for Beer-Lambert absorption in the single-photon initiator, and to provide precise control of modal tapers. A laminated sample preparation is introduced to enable full 3D characterization of these modal tapers. The propagation loss measurement of the uniform waveguides is also described. Finally, two extensions of uniform 3D waveguides are discussed, namely waveguides through thin optics and sharp waveguide bends. Chapter 6 summarizes this thesis and discusses future work.

## Chapter 2

# GRIN Micro Lens and Lens Array Fabrication in the HDS 3000 Polymer

### 2.1 Introduction

This chapter introduces a new method of making GRIN micro lenses and GRIN lens arrays in the HDS 3000 photopolymer. At its core, this method exposes the photopolymer under a low-power CW laser, leading to the following advantages. First, the index profile of the GRIN lens can be controlled by changing the size, power of the laser beam and the exposure time. Second, the GRIN lens arrays are fabricated by a simple step-and-repeat process, where the lens position and properties can be flexibly changed on demand. I used a modified scanning transmission microscope [7] to quantitatively measure the index profile of the fabricated GRIN lens. Third, this differential transmission phase microscope is conveniently integrated into the lens exposure system which facilitates monitoring of index formation during the fabrication. In the following, I review the strengths and weaknesses of the existing techniques in order to demonstrate the intended contribution of the newly-developed technique.

Micro lenses and lens arrays are important photonic and optoelectronic devices with a wide range of applications in fiber optic communication [17,18], imaging systems [19], biomedical devices [20,21], lithography [22], among others [23]. Broadly speaking, refractive micro lenses fall into two main types, namely conventional surface shape lenses and gradient index lenses, based on their underlying working principles. A conventional micro lens has a homogeneous refractive index and uses surface curvatures to perform its function as shown in Fig. 2.1-(a). In contrast, a GRIN micro lens generally has two flat end surfaces, and the continuous variation in the index of refraction in the material enables the lens function. Currently, there are

three primary types of index gradients: axial gradient, spherical gradient and radial gradient. In axial gradient, the index of refraction varies in a continuous way along the optical axis but is invariant transverse to this axis. In spherical gradient, the index of refraction is centro-symmetric, i.e., the surfaces with constant index are spheres. The refractive index of radial gradient lenses varies continuously outward from the optical axis. In this chapter I focused on lens with a radial gradient index, shown in Fig. 2.1-(b), whose index is highest in the center of the lens and gradually decreases away from the center of the lens. I will discuss the fabrication method for GRIN lenses with arbitrary index profiles in a new diffusive photopolymer in chapter 3.

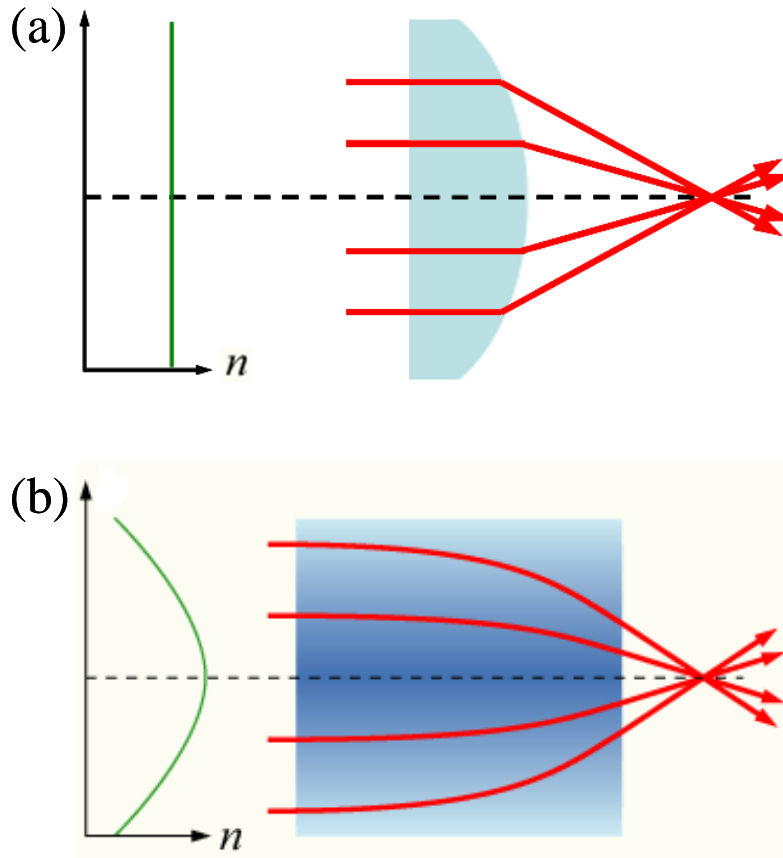


Figure 2.1. Comparison of the two types of micro lenses: (a) conventional lenses have a surface shape and a constant refractive index; (b) radial gradient index lenses have two flat surfaces, while the refractive index is continuously varying.

Compared to conventional surface lenses, GRIN lenses have several advantages. The flat surfaces of GRIN lenses simplify the mounting of the lens, making them more attractive for



photocopiers, scanners and telecom components [24], where many very small lenses need to be mounted together. The flat surfaces also allow a GRIN lens to be easily fused to an optical fiber [25,26] to collimate the light out of the fiber. Finally, gradient index can be applied to conventional surface lenses in order to enhance the focusing power, correct aberration and provide additional freedom of optimizing the lens [27,28].

Several methods have been developed to fabricate GRIN lenses [29], such as neutron irradiation [30], chemical vapor deposition (CVD) [31], ion exchange [32], ion stuffing [33] and polymerization. Each of these existing techniques has its upsides and downsides. The index of refraction of boron glass such as BK7 glass can be locally altered under neutron irradiation by changing the boron concentration. The variation in the index of refraction is approximately linear to the neutron irradiation dose. The downside of the neutron irradiation technique is that a large amount of neutrons is needed to cause the index change; and there is a possibility that the index change is not permanent. The CVD technique deposits layer by layer of glass materials with different index of refractions onto a surface to produce a cumulative refractive change. Each layer creates a step index of refraction. The CVD technique has been widely applied in manufacturing preforms for gradient-index fibers. When the fiber is drawn, the layers become thinner than the wavelength of light. Therefore the gradient index appears to be continuous. However, this CVD technique has limitations for large-geometry lenses due to the step index formation through the layer by layer depositing process.

The ion exchange and diffusion technologies are widely used in current mass manufacturing. Ions from a bath of salt such as lithium bromide diffuse into a glass and exchange with ions in the glass such as sodium ions. A one-for-one exchange of ions with different density results in a gradient index of refraction in the glass. The ion exchange technique can make lenses with a diameter range of 0.5 ~ 10 mm. However the nature of diffusion limits the index profiles formed to be either Gaussian, Lorentzian or linear.

In ion stuffing, a special glass is heated for phase separation. One of these phases dissolves out of the glass in an acid solution. Then the glass is exposed to an ion or molecule bath. As the ions or the molecules diffuse into the material, a gradient index of refraction is formed. The glass is then re-condensed by heating, and the index-of-refraction profile is finalized. Similar to the ion exchange technique, only limited types of profiles can be created using ion stuffing. Furthermore, a major challenge of this technique is that few glasses can phase separate. Furthermore, an uneven phase separation results in uneven index gradient. GRIN lens rods fabricated in polymers through thermal treatment [34] or UV irradiation [35] also have been reported.

To summarize, all the techniques discussed above have a complex control procedure and, with only a few exceptions, are not able to fabricate GRIN lens arrays. To my best knowledge, there are two techniques for fabricating GRIN lens arrays. The first combines ion exchange with high precision structuring of metal masks [36]. This technique involves two steps: the first step uses ion exchange through a precisely designed titanium mask to form a phase distribution that represents the mask; and the second step involves post heating process or field assist ion exchange by applying an electrical field to smooth out the phase distribution. Unfortunately, the index profile created by this technique is not uniform through the thickness. The second method is a stack-and-draw technique [37]. This technique starts with stacking two types of glass rods with different refractive indices together to create an initial preform; the initial preform is then processed to generate an intermediate perform in a way similar to making photonic crystal fibers [38] but with a larger size; finally, a set of intermediate preforms are stacked together to form an index structure, e.g. lens arrays. The final index profiles depend on the index contrast and distribution of the two different types of glass rods. This stack-and-draw technique is capable of making GRIN elements with arbitrary index profiles. However, this technique has two major limitations: (1) the index distribution is not continuous, which is problematic especially for large-

size elements; (2) the glass rods with different refractive index must be thermally and mechanically matched in order to reduce the internal stress.

In light of the problems of fabricating GRIN lenses using existing methods, researchers have turned to alternative micro-fabrication technologies to manufacture refractive micro lens arrays. These micro lens array fabrication technologies include photolithography [39], excimer laser ablation [40], two-photon polymerization [41], thermal reflow/resist-melting [42], UV laser irradiation of doped PMMA [43], photosensitization [44], drop-on-demand ink-jet printing [45], embossing [46] and stamping [47,48]. These techniques, however, are not without weaknesses. Photolithography, excimer laser ablation, two-photo polymerization and stamping techniques are capable of fabricating micro lens arrays with arbitrary lens shapes. However, photolithography involves gray-scale masks, a layer-by-layer process and multiple post-process steps. The excimer laser ablation and two-photo polymerization are slow and requires large laser energy. The stamping method requires precise molds, making this technique economical only for large volume production. The drop-on-demand printing, UV laser irradiation, and photosensitization methods can potentially be fast; however the underlying physical principle of these methods is to use the surface tension of liquid droplets or melted solids to form spherical or semispherical lenses, which limits their flexibility to fabricate lenses of arbitrary shape.

This chapter and chapter 3 propose and demonstrate new forms of lenslet and lenslet array fabrication techniques that overcome the above-mentioned limitations. The proposed new techniques excel in its ability to print complex parts with a large degree of control over the lens parameters. Specifically, the method demonstrated in this chapter makes polymer GRIN lenses and GRIN lens arrays by exposing diffusive photopolymers to a low-power CW laser. Initiators absorb the incident light to start polymer chain growth and monomer diffusion, resulting in a permanent volume index change which is approximately proportional to the light intensity [49]. This produces GRIN lenses in a single, simple step with no wet chemical processing. It is similar

to waveguides written by a tightly focused laser [50], but in this case the large spot size induces slow diffusion and thus avoids the complexity of self-trapping. There are several promising features for this fabrication method: GRIN lenses fabricated with this method can be integrated with other polymer optics (i.e. photopolymer waveguides [9]); it enables the researcher to control the index profile of the GRIN lens; and the cost of fabrication equipment and individual parts is low.

I also used a modified scanning transmission phase microscope [7] to quantitatively measure the index profile of the fabricated GRIN lenses, which is easily integrated with the GRIN lens fabrication platform. This testing system scans the fabricated GRIN lens, acquiring data that are proportional to the derivative of the index profile of the lens. A post-processing algorithm can then be employed to calculate the quantitative index profile.

## 2.2 Diffusive photopolymer sample

The diffusive photopolymer used in this chapter is *Tapestry*<sup>TM</sup> HDS 3000 provided by InPhase Technologies. This photopolymer was originally optimized for holographic data storage and thus exhibits shrinkage of less than 0.1%. The InPhase *Tapestry*<sup>TM</sup> HDS 3000 material is phase-uniform and scatters less than  $10^{-6}$  per steradian, making it an extraordinary high-quality optical material. The *Tapestry*<sup>TM</sup> diffusive photopolymers are flexible solids with active components consisting of an initiator that absorbs a fraction of the incident light to form radicals and a monomer that polymerizes by reaction with this photo-initiator. A localized illumination therefore creates high molecular-weight polymer in the illuminated region via the consumption of low molecular-weight monomer units. This local depletion of monomer causes monomer diffusion into the exposed region, resulting in an area of increased density and refractive index.

The sample geometry used to fabricate GRIN lens and lens array is illustrated in Fig. 2.2. The polymer layer is sandwiched by two pieces of glass slides with thickness of 1mm. The thickness of the polymer layer is controlled by spacers. These samples are fabricated via a simple

pour-and-set casting process, and do not require the spinning process. A packaging method patented by Inphase Technologies Inc. as ZeroWave™ process [51] is used to form polymer slide samples within  $\lambda/4$  flatness, using low-cost, unpolished glass, shown in Fig. 2.3.

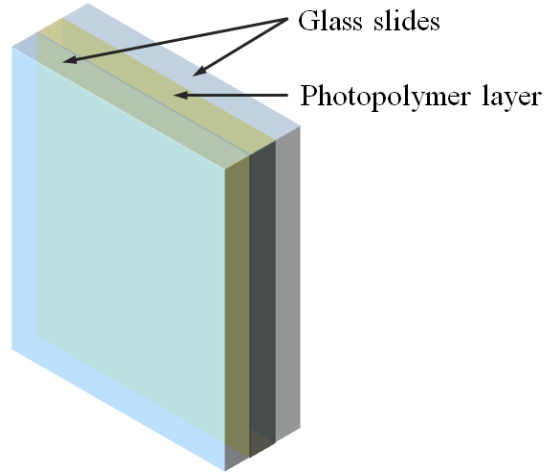


Figure 2.2. The geometry for the polymer slide sample: a photopolymer layer with a thickness of 1mm is sandwiched by two pieces of microscope glass slides with a thickness of 1mm.

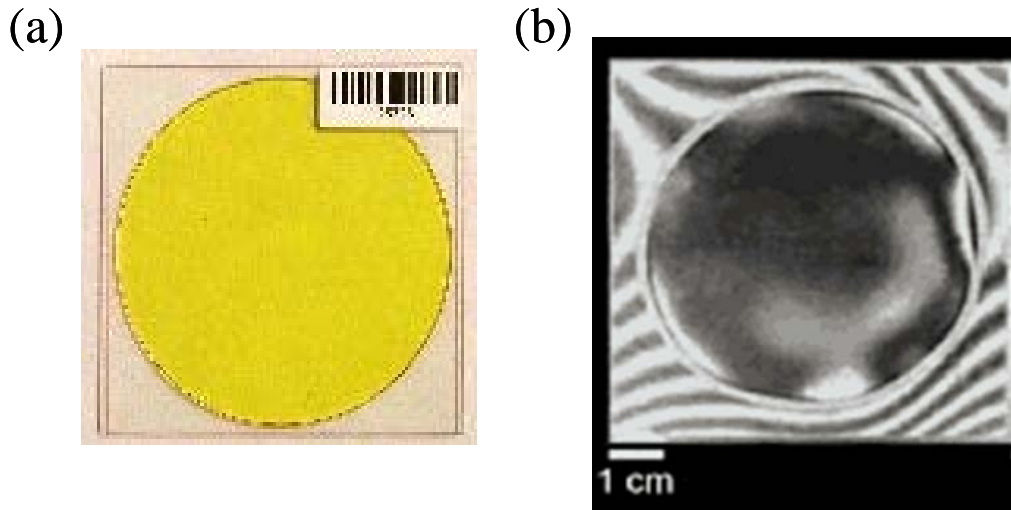


Figure 2.3. Demonstration of the flatness of polymer slide samples fabricated using the ZeroWave™ technique. (a) is the photo of a slide sample. (b) shows the optical phase of the slide sample measured by an interferometer.

### 2.3 GRIN lens fabrication method

Arbitrary index structures can be achieved by creating arbitrary analog intensity patterns, because locally introduced index change in a diffusive photopolymer is dependent on the exposure light intensity. Two methods are generally used to form arbitrary intensity patterns: analog spatial light modulators and rapid scanning modulated laser beam. I will discuss the rapid scanning modulated laser beam method in chapter 3. Here I used a simple method that enables a large variety of high quality lenses to be fabricated with a simple exposure geometry.

This method uses a focused Gaussian beam at variable distances to the sample to change the exposure scales. The optical setup for the GRIN lens exposure is shown in Fig. 2.4. As the HDS 3000 photopolymer is photo-initiated with 532 nm light, a frequency-doubled Nd:YAG laser with wavelength of 532nm is used as the write beam. This laser beam, controlled by a Vincent Associates mechanical shutter, is focused at some distance in front of the sample. The polymer sample is mounted on a high-precision 5D stage. The  $x$ ,  $y$ ,  $z$  part motions are implemented with Newport PM500 stages controlled by a PM500-C6 driver and custom designed LabView software. Two rotation axes, used primarily to orient the part perpendicular to the incident laser beam, are motorized via Newport TRA12CC actuators controlled by a Newport EPS7000.

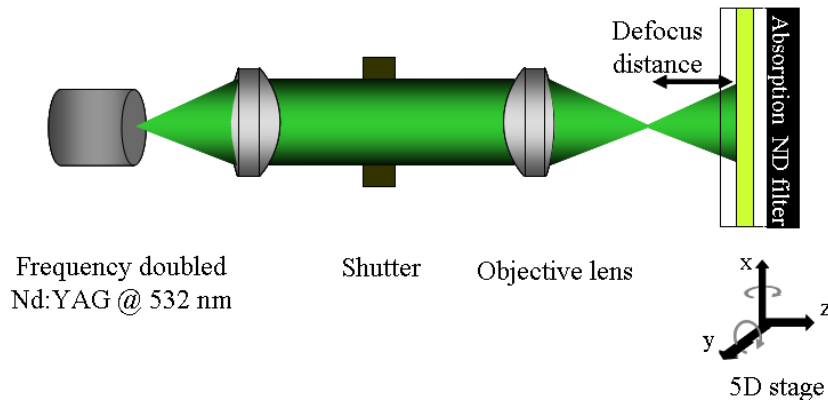


Figure 2.4. Optical layout for the direct write lithography system, consisting of a frequency doubled Nd:YAG laser, a spatial filter, a collimation lens, a shutter and a focusing lens.

The one-photon initiation and self-developing index through monomer diffusion make this polymer attractive for 3D micro fabrications. However, these advantages also come at a cost: they make the polymer very sensitive to any modulation to the exposure beam intensity distribution. The glass slides in the photopolymer slide sample are not antireflection coated. Thus, about 4% of the incident beam intensity reflects at the back glass/air boundary. Another 4% of the reflected beam intensity reflects at the front air/glass. As the writing laser beam is highly coherent, the reflected beams interfere with the incident beam, thus modulating the light intensity distribution with an interference pattern in the polymer layer. Such intensity modulation deteriorates the quality of GRIN lens fabricated. Furthermore, impurities in the photopolymer sample, such as dust, air bubbles or undissolved monomers, and spots or dust on the optical elements near the polymer sample, introduce scatter patterns in the polymer sample.

In order to significantly reduce these undesirable high frequency light modulations, I employed two methods. To suppress reflections, an absorbing ND filter with an optical density of 3 was attached to the back glass surface with index matching oil (Type A microscope immersion oil). To suppress interference patterns due to reflections outside of the part, I oscillated the slide sample in z direction with an oscillation distance of 200 $\mu$ m and an oscillation speed of 10mm/s during exposure of the GRIN lens to effectively wash out residual interference patterns. These two methods significantly reduce the interference pattern recorded in the exposed index structures.

Next I discuss the way to fabricate a large variety of high quality lenses. As discussed in Chapter 1, in the simplest model, the index change is proportional to  $I^\alpha t$ , where  $I$  is the writing beam intensity,  $t$  is the exposure time and  $\alpha$  is between 1/2 for pure bimolecular termination and 1 for pure unimolecular termination.

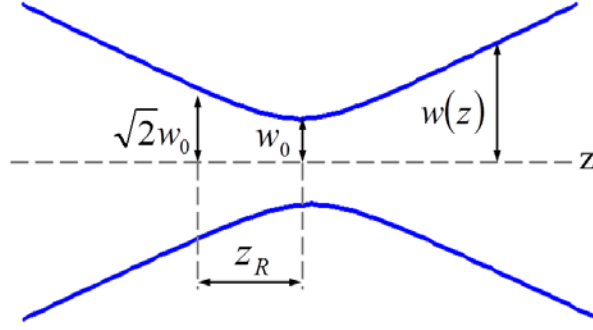


Figure 2.5. Demonstration of Gaussian beam width  $2w(z)$  as a function of the axial distance  $z$ , with a beam waist of  $2w_0$  and a Rayleigh range of  $Z_R$ .

The intensity of the defocused Gaussian beam (shown in Fig. 2.5) in the polymer sample is expressed as

$$I(r, z) = \frac{2P_0}{\pi w^2(z)} \exp\left[-\frac{2r^2}{w^2(z)}\right], \quad (2.1)$$

where  $z$  is the defocus distance,  $P_0$  is the incident laser power and  $w(z) = w_0 \sqrt{1 + \left(\frac{z}{Z_R}\right)^2}$ , where

$w_0$  and  $2Z_R$  are the radius and Rayleigh range of the focused laser beam.

Therefore, the introduced index profile of the out-focus Gaussian beam exposure in the photopolymer sample, assuming index response is proportional to steady-state polymerization rate, is

$$\delta n(r, z) \propto \left(\frac{2P_0}{\pi w^2(z)}\right)^\alpha t \exp\left[-\frac{2r^2}{(w(z)/\sqrt{\alpha})^2}\right]. \quad (2.2)$$

Equation 2.2 shows that the formed index profile of the GRIN lens depends on the incident exposure power  $P_0$ , exposure beam radius  $w(z)$  at the defocus distance  $z$  and exposure time  $t$ . I can use these three parameters to fabricate GRIN lenses with different index profiles. The exposure beam size at the sample is conveniently controlled by changing the defocus distance  $z$ . The incident exposure power  $P_0$  can be manually adjusted through a pair of a half-wave plate and



a polarized beam splitter, or automatically controlled by a continuous variable ND filter via a LabVIEW program. The exposure time  $t$  is controlled by the shutter via the LabVIEW program. These variables are sufficient to explore a wide range of GRIN lenses in single convenient exposure geometry.

I used a simple step-and-repeat process to create GRIN lens arrays in the diffusive photopolymers. Similar to the single polymer GRIN lens fabrication, a glass/polymer/glass sample with polymer thickness of 1mm is mounted to the direct-write lithography stage, shown in Fig. 2.4. A lens array is formed by a sequential multi-exposure, shown in Fig. 2.6. After the system is properly setup, I only need to repeatedly (1) open the shutter to expose GRIN lens A; (2) close the shutter and move the sample through the computer control to the desired location and (3) open the shutter to expose GRIN lens B to fabricate the GRIN lens array.

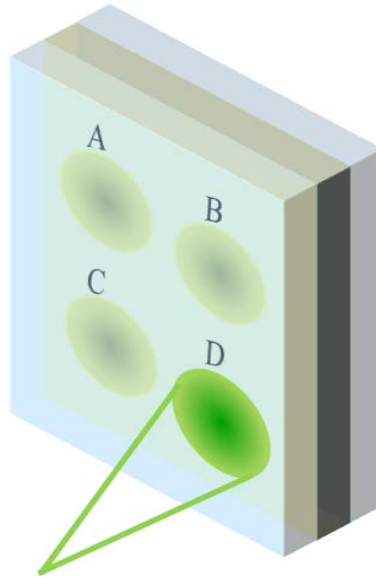


Figure 2.6. Fabrication of a GRIN lens array through a step-and-repeat process.

This step-and-repeat process of GRIN lens array fabrication method is convenient, because the lens position and properties can be changed on demand. For example, a GRIN lens array with the required fill factor can be conveniently fabricated. Differential interference contrast

(DIC) microscope images of two fabricated GRIN lens arrays with different sizes and periods are shown in Fig. 2.7.

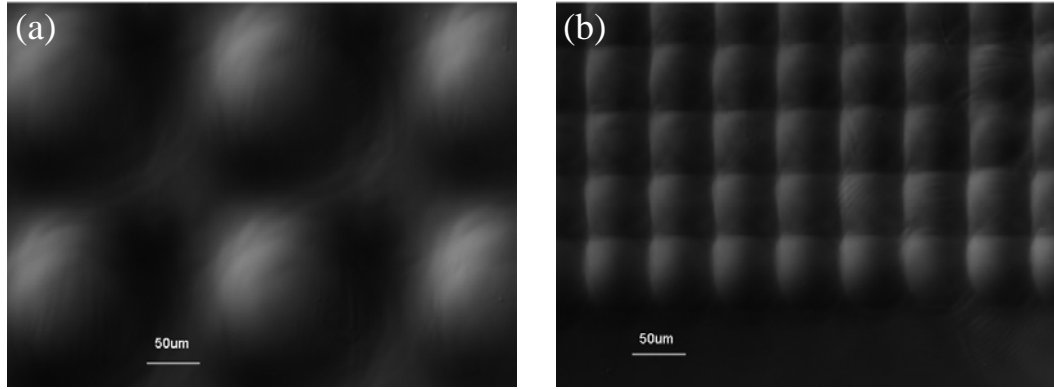


Figure 2.7. DIC images of two fabricated GRIN lens arrays with different lens sizes and periods. (a) shows a GRIN lens array with an exposure power of  $7\mu\text{w}$ , an exposure time of 10s, an exposure beam diameter of  $100\mu\text{m}$  and a period of  $200\mu\text{m}$ . (b) shows a GRIN lens array with an exposure power of  $7\mu\text{w}$ , an exposure time of 10s, an exposure beam diameter of  $40\mu\text{m}$  and a period of  $50\mu\text{m}$ .

## 2.4 GRIN lens characterization methods

So far, I have demonstrated that the direct-write lithography is capable of fabricating GRIN lenses and lens arrays in the HDS 3000 diffusive photopolymer. The qualitative index profiles of these lenses can be acquired through a DIC microscope. However in order to make controllable GRIN lenses, quantitative index measurements of the fabricated GRIN lenses are necessary. These measurements allow me to predict the characteristics of the GRIN lenses I have made. More importantly, the precise index measurement for each GRIN lens provides the insight into the index change formation model for the polymer, making it possible to design exposure condition to fabricate custom-designed GRIN lenses.

Several methods, such as phase microscopy, interferometry, optical diffraction tomography, raster scanning of surface reflectivity and near field pattern methods [52,53], have been developed to measure GRIN structures. These methods differ in whether the transverse field, the scattered field, or the reflected field of the micrometer scale index structure is collected to measure the index distribution. Phase imaging microscopes, such as DIC microscopy [54],

typically offer a qualitative index picture. Quantitative implementations of phase microscopy have been reported, but are limited to thin objects [55]. Interferometry is widely used to precisely characterize phase objects. However, the GRIN lenses I made have strong index structures that are not equivalent to thin objects with the same projected optical path length. Thus any simple projection method, such as interferometry, will not yield the index profile. Also, interferometry has difficulty to measure small (diameter below 1mm) phase objects. Scanning reflectometry [56] measures the reflectivity distribution of the end surface of the GRIN lens, which are directly related to the refractive index profile of the sample. In order to only collect the reflectivity information at the surface of the index object, two types of techniques have been developed by two graduate students in Prof. Robert R. McLeod's group respectively: one through confocal filtering [57] and the other through optical frequency domain reflectometry (OFDR) [58]. These two can achieve an index precision on the order of  $10^{-4}$ . However the reflection method can only provide the index distribution at the sample surfaces. Also, laser instability, noise in the detection system and imperfections in sample surfaces are problematic for these reflection methods [59,60].

Optical diffraction tomography can potentially provide 3D index distribution of the index structure by measuring the fields diffracted from the object at a number of incident probe beam angles and back propagating the fields to reconstruct the scattering object[ 61 ]. Normally, diffraction tomography requires information about the phase of the scattered fields, which significantly complicates both the experimental setup and the numerical reconstruction. Also, the scattered field generally is so weak that it is difficult to separate the measured scatter field from the background noise. A novel technique has been reported to solve these two problems for measuring index profile of waveguides [9]. However, the fundamental limitation of this method is that it is only valid for weak scatter objects with a phase delay of less than one wavelength. Therefore, the optical diffraction tomography unfortunately does not apply to the GRIN lenses we fabricated.

I modified a quantitative index measurement technique previously developed in our group [7] to characterize the fabricated GRIN lenses and lens arrays. This method uses a position sensitive detector (PSD) to acquire data that are proportional to the first derivative of the index profile of the lens. Then a post-processing algorithm is employed to calculate the quantitative index profile. I call this method differential transmission phase microscope in this thesis. This microscope is readily integrated into the GRIN lens fabrication platform.

#### 2.4.1 A modified differential transmission phase microscope

The differential transmission phase microscope to quantitatively measure the index profiles of the fabricated GRIN lenses is shown in Fig. 2.8. This differential transmission phase microscope is easily integrated into the exposure hardware. After the sample is exposed to the writing beam and a localized index structure has developed by polymerization and monomer diffusion, the system is switched to the differential transmission microscope using a longer wavelength laser to which the polymer is significantly less photosensitive. This allows the diffusion-driven index development to be monitored before the final step of flood curing the polymer.

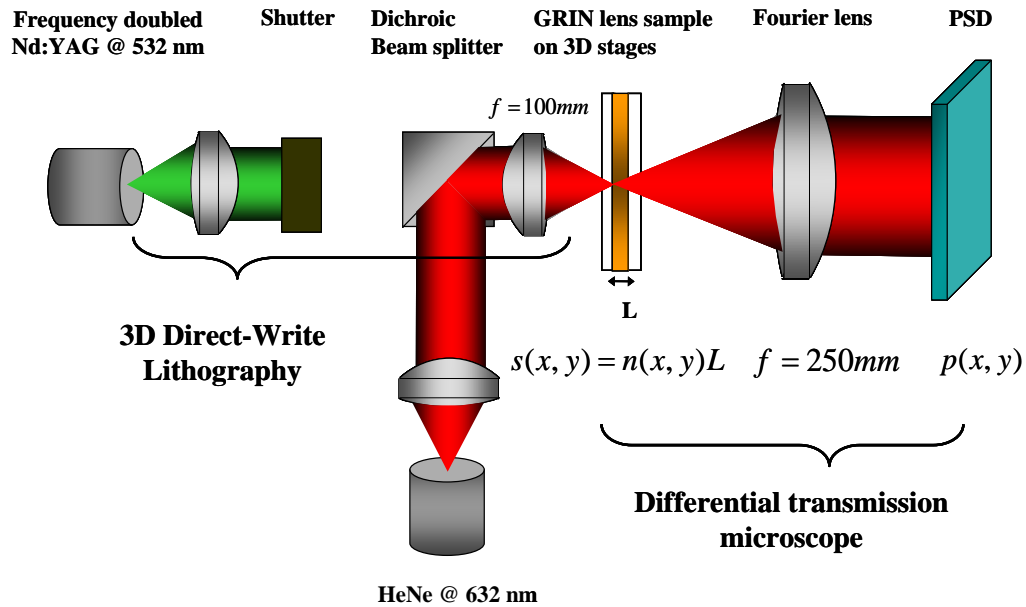


Figure 2.8. Optical layout for the direct-write lithography system and the integrated differential transmission microscope used to measure the resulting index profiles.

In the differential transmission microscope, the collimated HeNe laser beam is focused onto the photopolymer sample with a spot size of 20  $\mu\text{m}$ . The focused beam is deflected by an angle of  $ds/dx$  in the  $x$  direction and  $ds/dy$  in the  $y$  direction, where  $s = n(x,y)L$  is the optical path delay of the lens,  $n(x,y)$  is the index profile of the lens and the  $L$  is thickness of the lens. Upon emerging from the sample, this deflected beam is Fourier transformed before it arrives at the ON-TRAK model PSM2-45 position sensitive detector (PSD). With appropriate calibration, this measures the  $x$  and  $y$  positions of the centroid of the power on the PSD, whose coordinates are given by

$$\begin{aligned} p_x(x, y) &= \frac{ds(x, y)}{dx} f \\ p_y(x, y) &= \frac{ds(x, y)}{dy} f \end{aligned} \quad (2.3)$$

where  $p_x(x,y)$  and  $p_y(x,y)$  are the data from the  $x$  and  $y$  channels of PSD respectively,  $f$  is the focal length of the Fourier lens. Based on the Fourier transform relationship

$$\begin{aligned} P_x(k_x, k_y) &= jk_y f S(k_x, k_y) \\ P_y(k_x, k_y) &= jk_x f S(k_x, k_y) \end{aligned} \quad (2.4)$$

we get the amplitude transfer function

$$\begin{aligned} H_{xPSD}(k_x, k_y) &= jk_y f \\ H_{yPSD}(k_x, k_y) &= jk_x f \end{aligned} \quad (2.5)$$

where  $S(k_x, k_y)$ ,  $P_x(k_x, k_y)$  and  $P_y(k_x, k_y)$  are the Fourier transforms of  $s(x,y)$ ,  $p_x(x,y)$  and  $p_y(x,y)$  respectively. As a result, the estimates of the index profile transform from each channel can be calculated as

$$\begin{aligned}
S_x(k_x, k_y) &= \frac{P_x(k_x, k_y)}{H_{xPSD}(k_x, k_y)} \\
S_y(k_x, k_y) &= \frac{P_y(k_x, k_y)}{H_{yPSD}(k_x, k_y)} .
\end{aligned} \tag{2.6}$$

The two estimates are combined in the Fourier domain in a manner that maximizes the signal-to-noise ratio[7]

$$S(k_x, k_y) = \frac{\left| H_{xPSD}(\vec{k}) \right|^2}{\left| H_{xPSD}(\vec{k}) \right|^2 + \left| H_{yPSD}(\vec{k}) \right|^2} S_x(k_x, k_y) + \frac{\left| H_{yPSD}(\vec{k}) \right|^2}{\left| H_{xPSD}(\vec{k}) \right|^2 + \left| H_{yPSD}(\vec{k}) \right|^2} S_y(k_x, k_y) . \tag{2.7}$$

Therefore, the index profile in the Fourier domain is

$$n(k_x, k_y) = \frac{-j}{fL} \left[ \frac{k_x}{(k_x^2 + k_y^2)} P_x(k_x, k_y) + \frac{k_y}{(k_x^2 + k_y^2)} P_y(k_x, k_y) \right] . \tag{2.8}$$

Then by Fourier transforming back to the spatial domain, we get the measured index profile of the lens from the PSD data.

Here, I performed a numerical simulation to demonstrate this index profile estimation process for a phase object with Gaussian index profile. The results are shown in Fig. 2.9-(a). The gradient of the phase object in x and y directions computed using Eq. 2.1 are shown in Fig. 2.9-(b) and Fig. 2.9-(c) respectively. The estimated quantitative phase object from the inverse Fourier transform of Eq. 2.8 is shown in Fig. 2.9-(d).

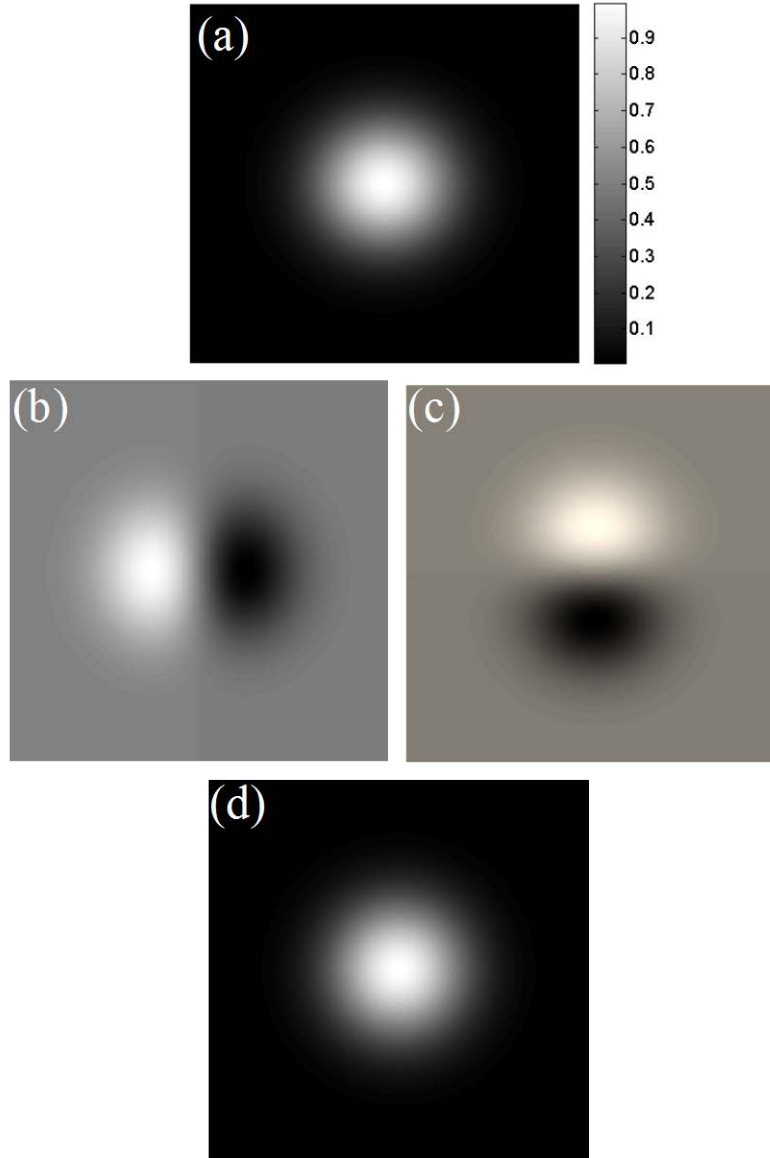


Figure 2.9. Simulation of the quantitative phase estimation: (a) object with Gaussian index profile; (b) index gradient in x direction; (c) index gradient in y direction; (d) estimated index profile for the object.

The validity of this differential transmission phase microscope testing method hinges on the assumption that the acquired raw data from the PSD precisely represent the phase gradient of the test object. This assumption may not hold if the probe beam size and the thickness of the GRIN lens testing sample are not chosen properly. This raster scan phase measurement method basically divides the GRIN lens into a number of small sub areas. Thus the spatial resolution of

the testing system is the sample size. Since I use the focused laser beam into the GRIN lens sample as the probe beam, the laser beam focus spot size ( $2w_0$ ) determines both the sample size and thickness of the sample. The thickness of the GRIN lens sample should be within the Rayleigh range of the laser focus and the sample size is twice size of the laser spot. Ideally I'd like to have small focus spot size and a thin sample in order to increase the spatial resolution. However a thinner sample leads to lower phase resolution, defined as the minimum detectable phase gradient of each sampling size, which can be expressed as  $\left(\frac{dn}{dx}\right)_{\min} = \frac{b_x}{Lf}$ , where  $b_x$  is the resolution of the PSD in the x direction (the resolution is the same in the y direction),  $L$  is the thickness of the GRIN lens sample, and  $f$  is the focal length of the Fourier lens. Furthermore, the sample thickness is also restricted by the maximum phase gradient of each sampling area, express as  $\left(\frac{dn}{dx}\right)_{\max} L = 2w_0$ . It means that the probe beam should not be significantly deflected to the adjacent sample area by the GRIN profile. Therefore, given the probe beam size and our prior knowledge of the GRIN lenses under test, such as the range of the peak index change and size, I expect there to be a proper range for the sample thickness. I carried out a beam propagation simulation method to find out such range for choosing the sample thickness.

In the experimental measurement setup, the probe beam focus spot in GRIN lens is 20μm and sampling step is 40μm for both x and y directions. The tested resolution of the PSD I used is 10um [62]. The focal length of the Fourier lens is 250mm. In the beam propagation simulation, I only studied index gradient along the x coordinate. The index profile of the GRIN lens is a Gaussian profile with a radius of 250um and a peak index change of  $5 \times 10^{-3}$ . A Gaussian spot with  $2w_0 = 20 \mu\text{m}$  propagates though the each sub sampling area of GRIN lens and then continuously propagates in air for a distance of 250mm. The sampling step is 40 μm. The location shift of the Gaussian spot at the output plane compared with the input plane, together with the resolution of PSD, provides the simulated phase gradient for each sampling step. Then the index



gradient is estimated by dividing the phase gradient by the thickness of the GRIN lens. The thickness of GRIN lens varied in the simulation, and the estimated index gradient for each sample thickness is achieved. Examples of the estimated index gradient with sample thickness of 100  $\mu\text{m}$ , 1200  $\mu\text{m}$  and 8000  $\mu\text{m}$  are shown in Fig. 2.10-(a). From this figure, we see that when the sample is too thin, e.g. 100  $\mu\text{m}$ , some of the phase gradient signals are buried in the PSD noise. On the other hand, when the sample is too thick, the measured index gradient deviates from the actual one, because the probe beam is significantly deflected by the index profile in the GRIN lens. The root mean square (RMS) errors of the estimated index gradients from the actual ones for the simulated sample with different sample thickness is shown in Fig. 2.10-(b). This figure indicates that for the GRIN lens with an index change around  $10^{-3}$  over 100  $\mu\text{m}$ , the proper sample thickness is in the range of 500  $\mu\text{m}$  to 2000  $\mu\text{m}$ . The HDS 3000 photopolymer I used for GRIN lens fabrication has the peak index change at the order of  $10^{-3}$  and the diameters of GRIN lenses are approximately one to couple hundred micrometers. All GRIN lenses were fabricated in slide samples with thickness of 1mm, which is within the optimum sample thickness.

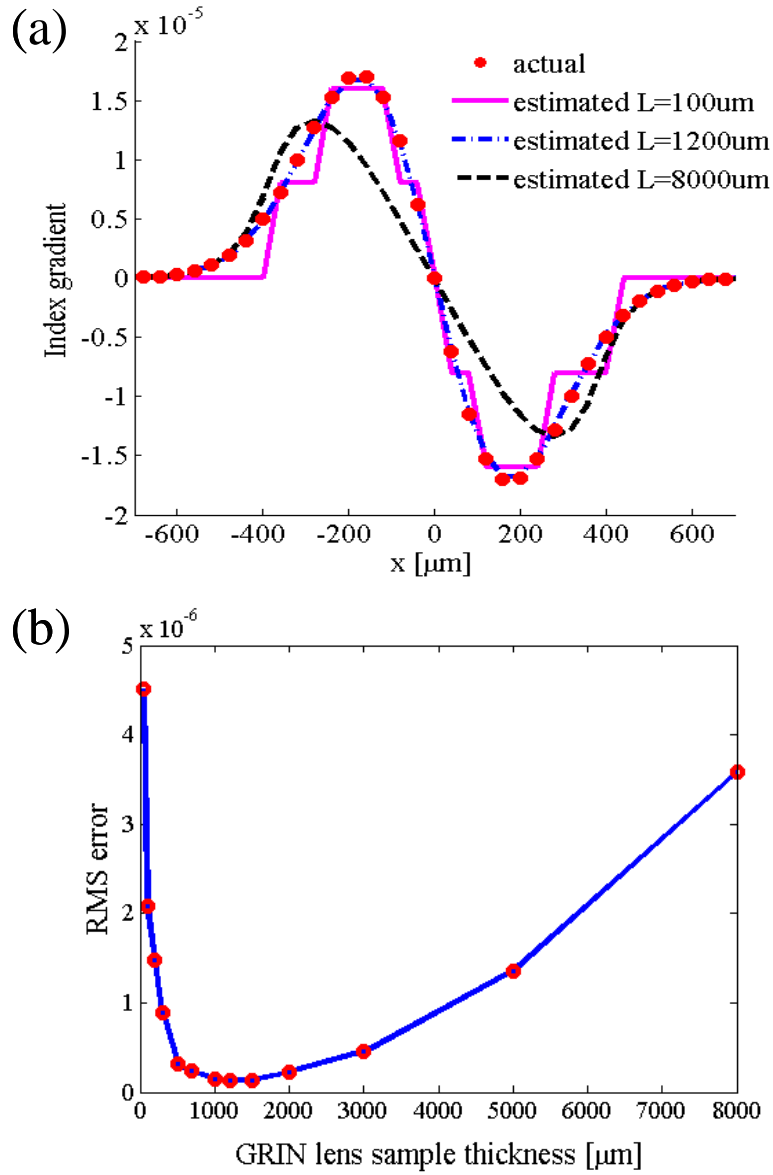


Figure 2.10. The beam propagation simulation results for the index gradient estimation of GRIN lens with different thickness. (a) is the comparison of actual and estimated gradient for the GRIN lens with thickness of  $100\mu\text{m}$ ,  $1200\mu\text{m}$  and  $8\text{mm}$  respectively. (b) is the RMS error between the actual and the estimated gradient with different sample thicknesses.

#### 2.4.2 Quantitatively measured index profiles

The 1 mm thick photopolymer is sandwiched between two 1 mm thick glass slides to create a part that is optically flat initially. The exposure power, exposure beam diameter and

exposure time at the sample are in the range of 5 $\mu$ W to 30 $\mu$ W, 20 $\mu$ m to 1000 $\mu$ m and 1s to 30s respectively to fabricate structures with peak index change on the order of  $10^{-3}$ . After exposure, the samples are kept in the dark for several days to finish the monomer diffusion. Finally, incoherent light is used to flood cure the entire sample, which consumes all of the remaining photoinitiators and polymerizes the remaining monomers. This makes the index structure permanent and the polymer insensitive to light.

One example of quantitatively measured index profile of GRIN lenses I fabricated is shown in Fig. 2.11. The GRIN lens was fabricated by exposure to the green laser beam with an exposure power of 30uW and an exposure beam diameter of 145 $\mu$ m for 5s. Figure 2.11-(a) and Fig. 2.11-(b) are the raw data from the PSD x and y channels respectively. By employing the data processing algorithm discussed in Section 2.4.1, I calculated the index profile of the fabricated GRIN lens with peak index change  $\Delta n = 2.9 \times 10^{-3}$ . Figure 2.11-(c) shows  $x$  and  $y$  cross sections with a parabolic fit to the measured index profiles. The accuracy of the measurements using the modified differential transmission phase microscope is characterized by testing several off-the-shelf plano-convex singlet lenses, shown in Appendix A.

The numerical aperture (NA) of a parabolic GRIN lens is given by  $NA = \sqrt{(n_0 + \Delta n)^2 - n_0^2}$  [63], where  $n_0 = 1.481$  is the bulk refractive index, yielding  $NA = 0.093$  and the corresponding focal length of the GRIN lens with a thickness of 1 mm is approximately 4.5 mm. Similar calculations using the measured index profiles of GRIN lenses with the exposure power, exposure beam diameter and exposure time in the range of 5 $\mu$ W to 30 $\mu$ W, 20 $\mu$ m to 1000 $\mu$ m and 1s to 30s, demonstrate the feasibility of creating GRIN lenses with NA between 0.05 and 0.13 and diameter from 40 to 1000  $\mu$ m.

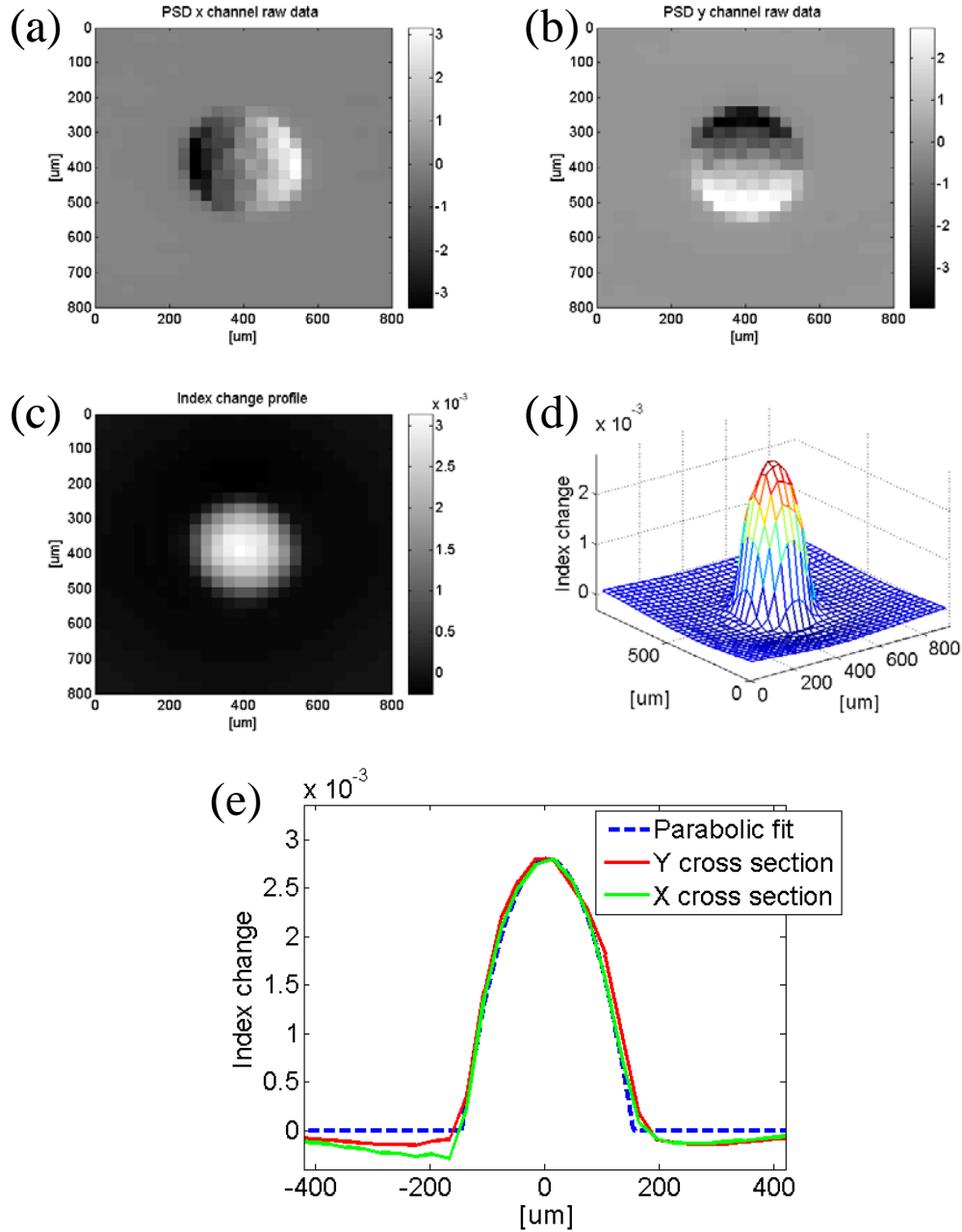


Figure 2.11. Quantitative measurement results of a GRIN lens with an exposure power of  $30\mu\text{W}$ , a beam diameter of  $290\mu\text{m}$  and an exposure time of 5s: (a) raw scanning data from PSD x channel; (b) raw scanning data from PSD y channel; (c) measured index profile in gray scale; (d) measured index profile in mesh grid; (e) horizontal (x) and vertical (y) line plots through the center of the measured index profile and a parabolic fit (dashed blue curve).

As discussed in Sec. 2.3, the direct-write GRIN lens fabrication process can be repeated with a motion stage under the computer control. Figure 2.12 shows the measured index profile of

a GRIN lens array I made using the differential transmission phase microscope. I used the parabolic fit to get the diameter and peak index change of every GRIN lens in this  $3 \times 2$  GRIN lens array. The mean of the measured lens diameter is  $129.3 \mu\text{m}$  with a standard deviation of 2.5% of the mean, while the mean of the measured peak index change is  $2.1 \times 10^{-3}$  with a standard deviation of 6.0% of the mean, indicating the repeatability of the GRIN lens fabrication and testing method.

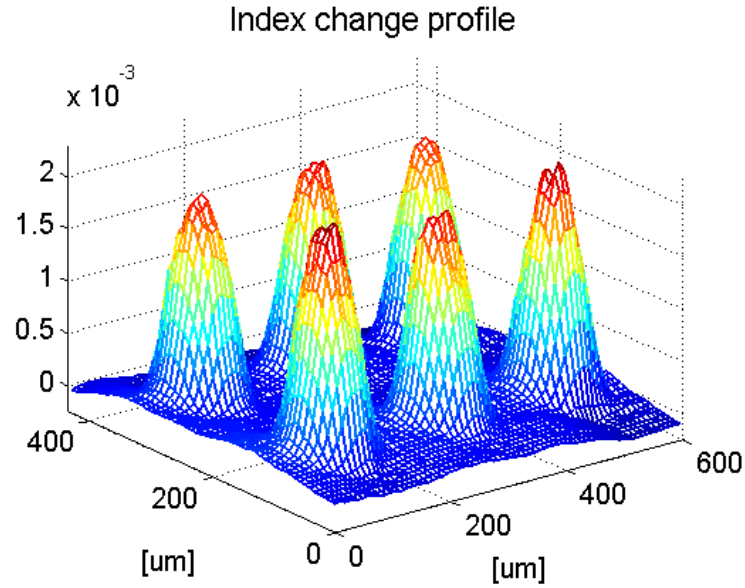


Figure 2.12. Quantitatively measured index profiles of a GRIN lens array with an exposure power of  $7 \mu\text{W}$ , an exposure time of 10s, an exposure beam diameter of  $100 \mu\text{m}$  and a period of  $200 \mu\text{m}$ .

#### 2.4.3 Imaging the focal spots of fabricated GRIN lens

Another typical method used to characterize the fabricated GRIN lens is to test the quality of focused spots by the GRIN lenses. The experiment setup is shown in Fig. 2.13. A spatially filtered and collimated He-Ne laser beam is shined into the fabricated GRIN lens arrays and the focal spots of the GRIN lens arrays were imaged to a digital camera.

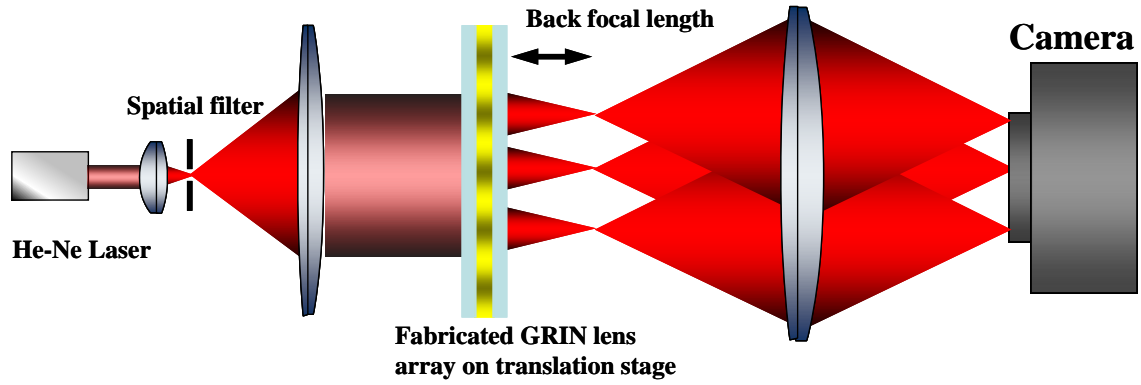


Figure 2.13. Experimental setup for imaging the focal spot of the GRIN lens arrays.

The camera is focused first on the back surface of the sample, then on the spot focal plane in order to measure the back focus distance of the GRIN lenses. Fig. 2.14 shows the imaged focal spots for GRIN lens arrays at different writing conditions. The GRIN lens arrays in Fig. 2.14-(a) are exposed under the power of  $7\mu\text{W}$ , the exposure time of 10s, the exposure beam diameter of  $100\mu\text{m}$  and a period of  $200\mu\text{m}$  and the measured back focal length is  $\sim 1.466\text{ mm}$ . The GRIN lens arrays in Fig. 2.14-(b) are exposed under the power of  $7\mu\text{W}$ , the exposure time of 10s, the exposure time of 20s, the exposure beam diameter of  $200\mu\text{m}$  and a period of  $500\mu\text{m}$  and the measured back focal length is  $\sim 3.321\text{mm}$ . The full width half maximum (FWHM) of the four focal spots in Fig. 2.14-(b) is measured to be  $9.8 \pm 5\mu\text{m}$ , while the calculated focus spot diameter at the diffraction limit condition is  $10.5\mu\text{m}$ , which is the FWHM of the Airy disk. The FWHM of the Airy disk is expressed as  $\lambda F\#$ , where  $\lambda$  is the wavelength of the probe beam and  $F\#$  is defined as the focal length over the diameter of the GRIN lens. Here the diameter of the GRIN lens is assumed to be the same as the exposure beam diameter of  $200\mu\text{m}$ . This indicates that the performance is approximately diffraction-limited.

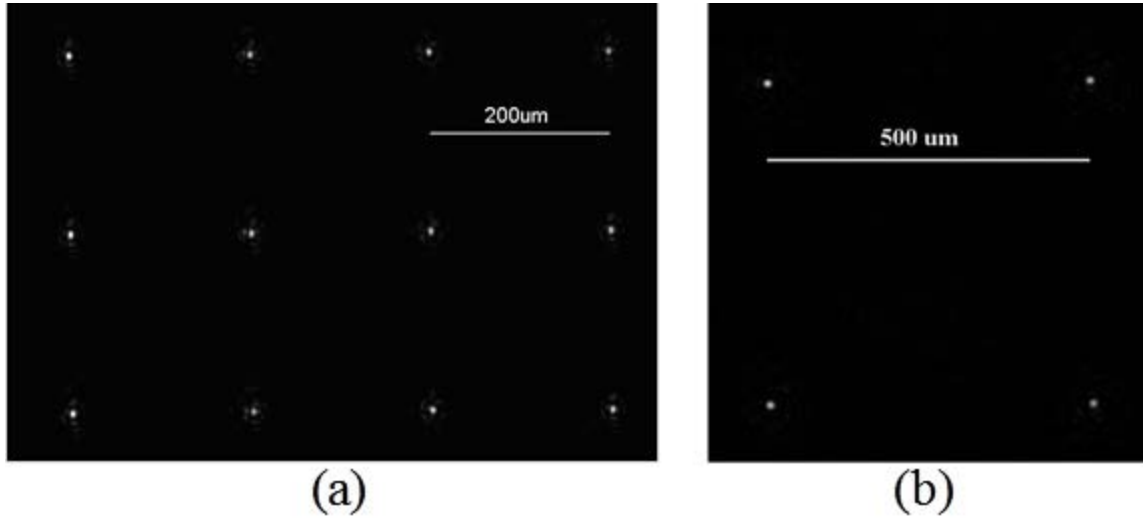


Figure 2.14. Imaged focal spots of fabricated GRIN lens with writing condition: (a) an exposure power of  $7\mu\text{w}$ , an exposure time of 10s, an exposure beam diameter of  $100\mu\text{m}$  and a period of  $200\mu\text{m}$ ; (b) an exposure power of  $7\mu\text{w}$ , an exposure time of 20s, an exposure beam diameter of  $200\mu\text{m}$  and a period of  $500\mu\text{m}$ .

## 2.5 Fabrication of GRIN lenses with a specified parabolic profile

So far I have shown our abilities to fabricate GRIN lenses and lens arrays in the HDS 3000 photopolymer and to quantitatively measure the index profiles of these lenses, which fit parabolic curves well. The inverse process, which is to fabricate a GRIN lens given its index profile, is more challenging and important for practical applications. In order to solve this inverse problem, it is necessary to understand how the material responds to the incident laser beam. Diffusive photopolymers were originally designed for holographic data storage and material modeling research has been done on holographic grating formation [64,65]. However, index formation modeling has not been carried out for large scale index formation, such as GRIN lenses. Here, I derived a simplified index formation model for large structures such as GRIN lens. This model takes into account the inhibition period at the beginning of the exposure due to oxygen and uses a simple saturation model to account for limited total index change. In chapter 3, this model is further refined by identifying and modeling the specific chemical species which causes this saturation.

A localized index change in the volume polymer is formed by polymerization and monomer diffusion. When a defocused laser beam is incident onto the polymer slide sample, photoinitiators absorb the incident light and cleave into initiating radicals. These primary radicals combine with nearby available monomers to start polymer chain growth. Such polymerization turns the low molecular weight monomers into high molecular weight polymers, which drives monomer diffusion into the exposed area. Thus the locally introduced index change roughly represents the light pattern. However, oxygen molecules in the polymer have two possible effects for the index structure formation [66]. The first is the *quenching* effect during the photoinitiating. When an initiator absorbs a photon promoting it to its excited state, an oxygen molecule can steal the energy from the excited initiator, preventing this excited initiator from becoming radicals. Quenching thus reduces the quantum yield of the photoinitiating process. The second is the *termination* effect during the polymerization. Oxygen molecules react with primary radicals and growing polymer radicals to form peroxy radicals, which are three orders of magnitude less active [67], thus terminating the polymerization process. Therefore, an effective exposure dose,  $D_{thres}$ , is needed to consume all the oxygen in the exposed area before the polymerization will start to proceed. As discussed previously in chapter 1, I can then assume that the index structure is proportional to polymerization rate which varies as  $I^\alpha t$ , where  $I$  is the writing beam intensity,  $t$  is the exposure time and  $\alpha$  is a fit parameter that describes the termination kinetics, which can range from  $\frac{1}{2}$  for pure bimolecular termination to 1 for unimolecular termination. This indicates that higher exposure does lead to stronger index change until a maximum index change of  $\Delta n$  is reached, when the exposed area runs out of active species, e.g. radicals or monomers. I call such exposure dose saturation dose,  $D_{sat}$ . By incorporating the oxygen threshold effect and saturation effect, the introduced index change profile vs. the incident exposure dose can therefore be expressed as



$$\delta n = \Delta n \frac{I^\alpha t - D_{thres}}{(I^\alpha t - D_{thres}) + D_{sat}}, \quad (2.9)$$

where  $\Delta n$  is the maximum index change that the material can achieve,  $I$  is the incident light intensity and  $t$  is the exposure time.

The four parameters  $\Delta n$ ,  $\alpha$ ,  $D_{thres}$  and  $D_{sat}$  in this simplified index formation model can be derived from fits to quantitatively measured index profiles of three arrays of GRIN lenses I made. A polymer slide sample with a thickness of 1mm is exposed under a laser beam with  $w_0$  of 145  $\mu\text{m}$ . This sample is not pre-cured to clear out oxygen. The exposure power and exposure time are varied to form three arrays of GRIN lenses. Each array has 10 GRIN lenses with the same exposure power, but different exposure times of 0.5s, 1s, 1.5s, 2s, 2.5s, 3s, 3.5s, 4s, 4.5s and 5s, respectively. Exposure powers for the three arrays are 20 $\mu\text{w}$ , 30 $\mu\text{w}$  and 30 $\mu\text{w}$ , respectively. The index profiles of these GRIN lenses were measured using the differential transmission phase microscope discussed in Sec. 2. 4.1. The peak index changes of GRIN lenses are shown in Fig. 2.15.

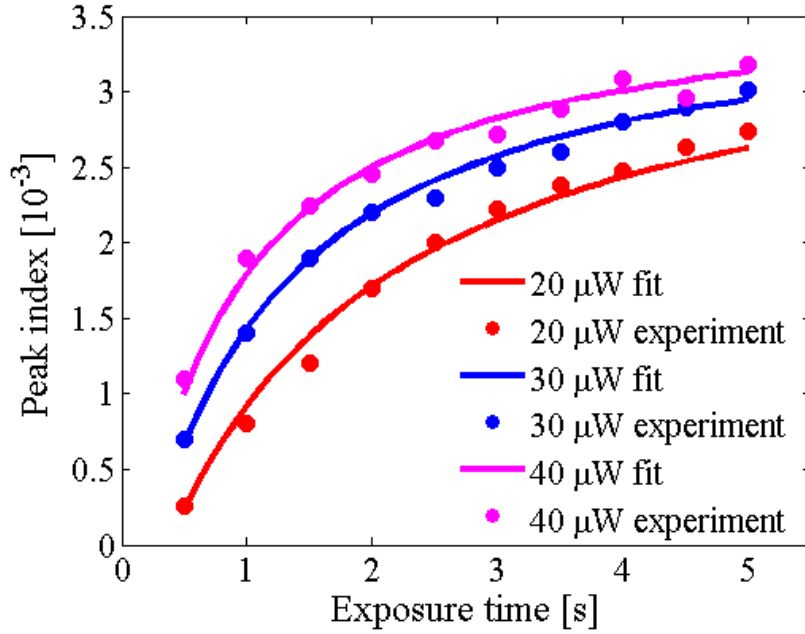


Figure 2.15. The measured peak index changes from three sets of GRIN lens arrays, which are fitted into a simplified index formation model.

The peak index changes of the three GRIN lens show saturation at large exposure times and similar shapes, indicating a single model may predict this behavior. These three sets of peak index changes vs. exposure times are then fit to Eq. 2.9 using a nonlinear fitting MATLAB function, *nlinfit*. The fit curves are shown in Fig. 2.15. From the nonlinear fitting, the maximum index change  $\Delta n$  is 0.0037, the oxygen threshold dose  $D_{thres}$  is 35mJ/cm<sup>2</sup>, and the saturation energy dose  $D_{sat}$  is 176mJ/cm<sup>2</sup> and the kinetic parameter  $\alpha$  is 1.1. The index formation model therefore becomes

$$\delta n = 0.0037 \frac{I^{1.1}t - 35}{(I^{1.1}t - 35) + 176}. \quad (2.10)$$

The interesting part about this index formation model is that the kinetic parameter  $\alpha$  is 1.1, which indicates that the HDS 3000 polymer has a close to linear ( $\alpha = 1$ ) response to the incident light. Such linear response is potentially caused by oxygen inhibition and dark polymerization. Dark polymerization here is defined as the continuous polymerization after the polymer is left in

the dark for the monomer diffusion. As discussed in chapter 1, for a radical initiation polymer with purely bimolecular termination, when radicals combine with radicals to terminate the polymerization process, the introduced index structure is the square root of the incident irradiance pattern. When the polymer exhibits purely unimolecular termination, when radicals combine with inhibitors, the index structure replicates the incident irradiance pattern. The oxygen molecules in the polymer function as inhibitors, therefore the existence of oxygen in polymer pushes the kinetic parameter  $\alpha$  towards 1. Previous study of waveguide fabrication with a high-intensity focused laser in the same polymer showed that the kinetic parameter  $\alpha$  is approximate 0.8 [Error! Bookmark not defined.]. For the waveguide with the size around of  $5\mu\text{m}$ , it only takes about milliseconds for the oxygen to diffuse from the unexposed region to the center of the exposed region, thus shutting down the dark polymerization. However, for a GRIN lens with the size of hundreds microns, it takes tens of seconds for the oxygen to diffuse to the center of the GRIN lens. Thus, while oxygen has already shut down the dark polymerization at the edge, the dark polymerization is still going on at the center of the lens. Therefore, the center gains extra index change than the periphery. A more sophisticated modeling and detailed quantitative study of the oxygen effect for the index formation is demonstrated in chapter 3. A conclusion that can be drawn at this point, however, is that these experiments do not show the sublinear ( $\alpha < 1$ ) behavior common to nearly all radical photopolymers. This will also be studied again in Chapter 3 where I find, for a second material in this diffusive polymer class, that  $\alpha \approx 1$ .

The maximum peak-to-valley index change  $\Delta n$  can also be derived from  $M/\#$ , which is a parameter that succinctly characterizes the dynamic range performance of a holographic recording material [68]. For a set of  $M$  overlapped, multiplexed holograms of equal strength, the diffraction efficiency is defined to be  $(M/M\#)^2$ .  $M/\#$  can be found from the Kogelnik diffraction formula to be  $M/\# = \pi L \Delta n / \lambda$ , where  $L$  is the material thickness and  $\lambda$  is the wavelength of the exposure beam. Experimentally,  $M/\#$  is measured by summing the square roots of the diffraction

efficiencies of a set of angle multiplexed holograms. The recording exposure schedule is adjusted to consume all the photoactive species in the recording media, and thus yields holograms with nearly equal diffraction efficiency. The  $M\#$  for the HDS 3000 photopolymer is 4 for  $L= 200$  microns. Therefore the  $\Delta n$  of HDS 3000 is 0.0034 at a wavelength of 532nm. The maximum achievable index change from Eq. 2.10 is 0.0037, which agrees with the holographic measurement to within 10%. Given that the GRIN lenses have  $\sim 300$  micron scale compared to the  $\sim 300$  nm scale of the holograms and that the GRIN lenses consume all of the dynamic range in single exposure in comparison to many weak holograms, this agreement is quite good. Importantly, it suggests that material parameters may be acquired at one scale or exposure condition and applied with moderate accuracy to vastly different scales and recording conditions. The complete material response model developed in chapter 3 for GRIN lenses is thus potentially applicable to holographic recordings at nm scales which are much more difficult to characterize.

I also applied the model of Eq. 2.10, derived only from the peak index change, to predict the profile of a lens given the Gaussian incident intensity profile. The measured and calculated index profiles from the model are shown in Fig. 2.16. The experimental data is congruent with the theoretical prediction, with the exception that a ‘dip’ is observed in the tail of the experimental index profile. Such local difference is likely due to insufficient monomer diffusion time. The Gaussian, when truncated by  $O_2$  threshold, yields a generally parabolic shape. Since the Gaussian exposure is convenient and the parabolic index profile is a standard GRIN profile, this motivates why Gaussian exposure is actually a useful way of making lenses.

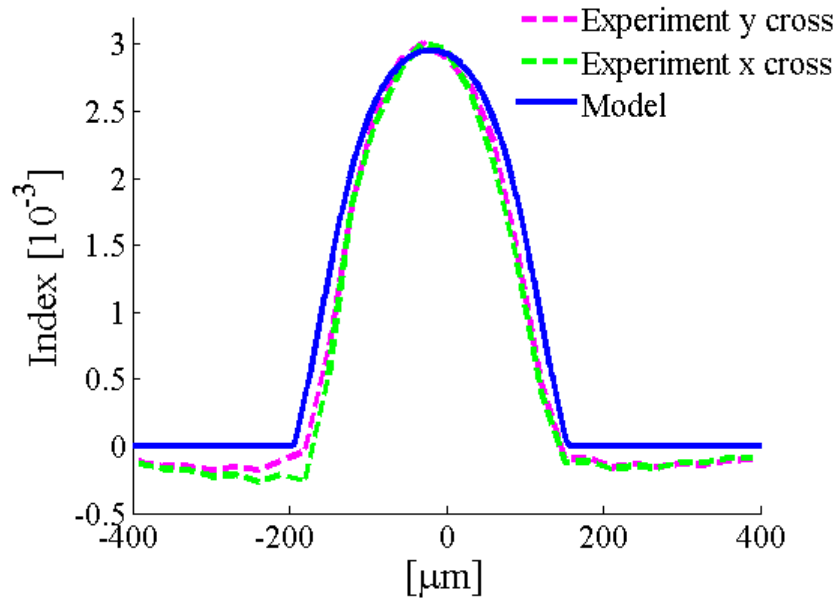


Figure 2.16. Comparison of experimentally measured index profile and calculated index profile from the derived model. Shown here is the cross section of the index profile of the GRIN lens with an exposure power of  $30\mu\text{w}$ , a beam diameter of  $290\mu\text{m}$  and an exposure time of 5s.

## 2.6 Application and Conclusion

GRIN lenses and lens arrays fabricated in the diffusive photopolymer have a great potential for applications in hybrid integrated optical circuits. As discussed in chapter 1, one main challenge for hybrid integrated optical circuits is guiding the light out of a single-mode (SM) waveguide or fiber through an optoelectronic component and back into a SM waveguide or fiber without significant loss. The mode size of a SM guide at visible wavelengths is about several micrometers. When the mode propagates out the guide, it diffracts immediately. When this diffracting light goes through an optoelectronic component with thickness that can be up to a centimeter, such as electronic an optical (EO) modulators, photorefractive crystals etc., only a tiny fraction of light couples back to the waveguide. A GRIN lens pair can solve this problem, shown in Fig. 2.17. A GRIN lens couples the light out of the guide into a collimated beam,

allowing it to pass through the micro optics with a minimal loss. Then another GRIN lens focuses the beam back into the guide with a high efficiency.

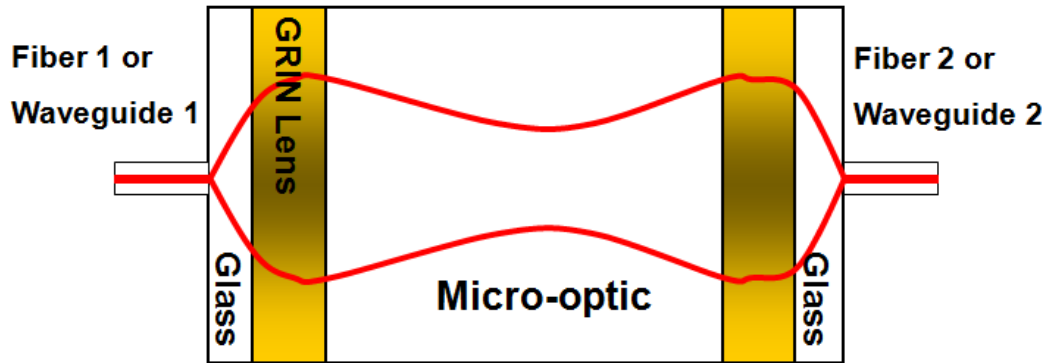


Figure 2.17. Demonstration of the function of a GRIN lens pair in a hybrid integrated optical circuit the first GRIN lens couples the light out of the guide so that the light can go through a thick micro optics; then the second GRIN lens couples the light back into the guide.

To demonstrate this application, I did a beam propagation simulation where the GRIN lens is used to collimate and then refocus a beam passing through an optical element with a thickness of 25mm. Two pieces of glass with thickness of 1.5mm are the entrance and exit windows. The thickness of the GRIN lenses is 2mm. Figure 2.18-(a) shows the index distribution of the simulation setup. The index profile of the GRIN lenses is modeled using the parabolic fitting curve from the measured index profile of the GRIN lens shown in Fig. 2.18-(e). A  $TEM_{00}$  beam with a radius  $\omega_0 = 5\mu\text{m}$  at the wavelength of 632 nm is incident at the entrance face. Figure 2.18-(b) shows the amplitude of the electric field of the fast Fourier transform (FFT) beam propagation simulation. One can see the GRIN lens collimates the light out of the SM waveguide and the other GRIN lens refocus the beam after passing through the thick optical element. The coupling efficiency from the simulation is over 95% based on the overlap integral of the electrical fields at the input and output planes.

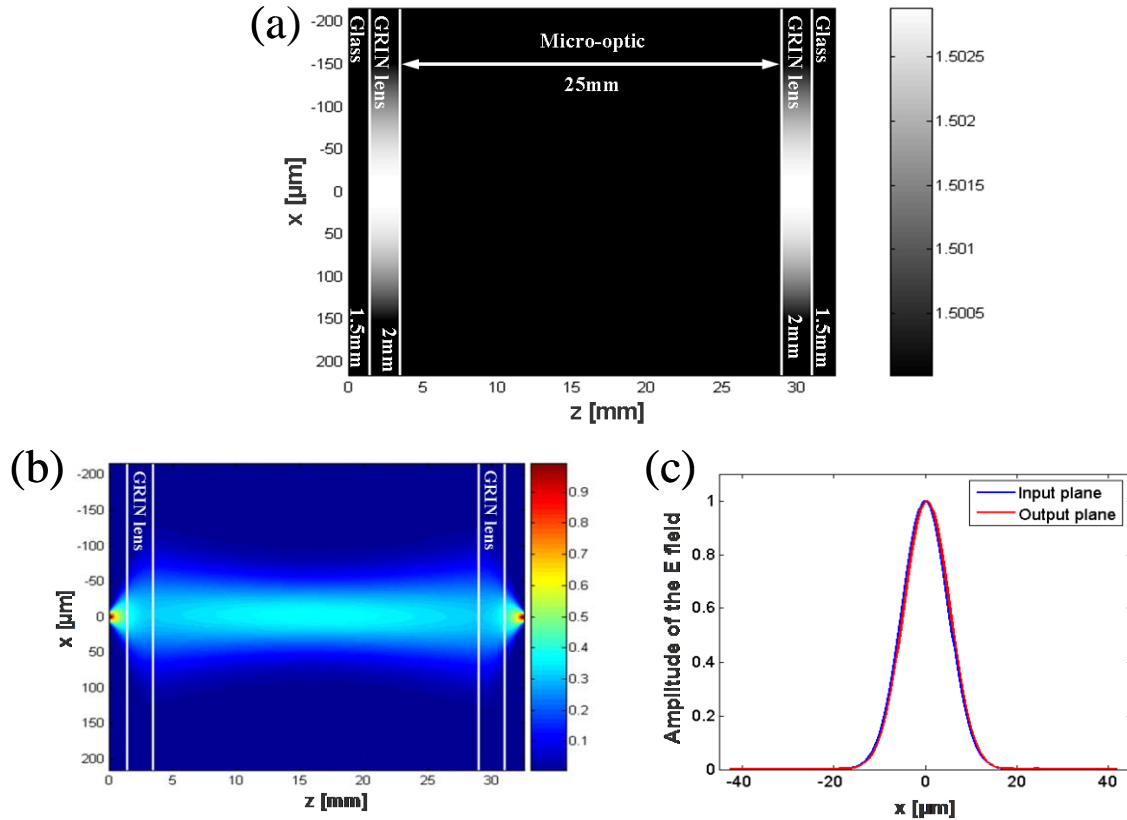


Figure 2.18. Simulation demonstration of the photopolymer GRIN lenses used in the integrated optics to expand the beam: (a) the index profile of the sample; (b) the absolute value of the E field through the FFT beam propagation simulation; (c) the absolute value of the E field at the input and output planes.

This GRIN lens pair can also be integrated with thin film filters, such as thin film polarizers or narrow band filters, to form useful optoelectronic devices for telecommunication applications. These devices can be fabricated in high volume utilizing wafer level procedures, significantly reducing the cost. For example, a thin film filter can be sandwiched by two layers of photopolymer. Then two pieces of cover glass can be used to provide protection windows, shown in Fig 2.19. GRIN lens array pairs can then be fabricated by sequentially exposing under a collimated laser beam. Finally, the wafer can be diced into many individual functional optoelectronic components.

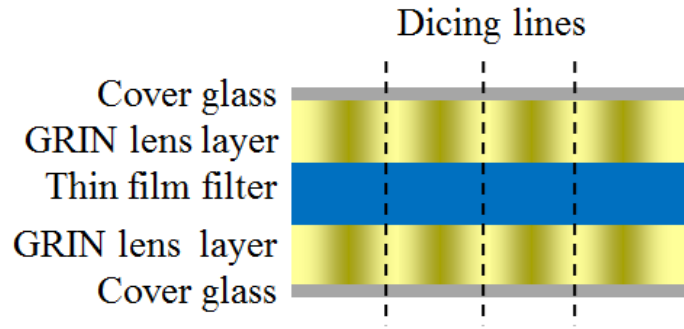


Figure 2.19. Demonstration of the wafer level fabrication of GRIN lens devices.

In summary, this chapter has presented a new fabrication method for GRIN lenses and GRIN lens arrays in diffusive photopolymers exposed with a low-power CW laser. A quantitative testing method was employed to test the fabricated lenses; with a demonstrated experimental error of about 1%. Parabolic fits to the measured index profiles demonstrate the capability to create GRIN lenses with NA between 0.05 and 0.13 and diameter from 40 to 1000  $\mu\text{m}$ . The lithography method uses simple, inexpensive hardware with integrated metrology. The materials are cost efficient and self-develop with no wet chemical processing. The combination provides a simple and direct control over lens index profiles via optical exposure patterning, which makes this method attractive for rapid prototyping of GRIN lenses and GRIN lens arrays.

With the index profile formulation model, exposure conditions and development time can be chosen to fabricate desired GRIN lenses with index profiles that fit parabolic curves. Existing holographic photopolymers optimized for low shrinkage of  $\sim 0.1\%$  have  $M/\#$  as high as  $\sim 40$  in one mm of material [16]. These holographic photopolymers can achieve a peak-to-valley index change of roughly 0.01 in the visible. Materials with ten times the index change are reasonable, although shrinkage will almost certainly be greater [16]. In the thin, paraxial limit, this range of index change enables lenses with a NA up to 0.5 at diameters up to 1 mm.



## Chapter 3

# GRIN Lens with Arbitrary Index Profiles Fabrication in the LBR Polymer

### 3.1 Introduction

I have elaborated in chapter 2 a new method for fabricating GRIN micro lenses and lens arrays. This method exposes a diffusive photopolymer to Gaussian laser beams at a wavelength of 532nm such that the index profiles turn out to be parabolic. I demonstrate in this chapter a more general method with arbitrary index profiles in a diffusive photopolymer initiated at a wavelength of 405nm. A preliminary study of a new diffusive polymer, *Light Blue Russet*, is discussed in this chapter. In sum, this study includes the material absorption, energy dose to clear out oxygen and an index-formation model. I use a galvo scanning system to draw two-dimensional exposure dose distributions, thereby forming arbitrary index changes in the diffusive photopolymer. The index profiles of the fabricated lenses are characterized in transmission by a Shack-Hartmann wavefront sensor (SHWFS).

There is a correspondence between the index change, locally introduced in a diffusive photopolymer, and the exposure light intensity at an appropriate wavelength. To the extent that this relationship can be inverted, we can create a desired index pattern by an appropriate exposure light intensity distribution. The straightforward way of implementation is to project a gray-scale transmission optical mask, which defines the exposure light pattern, onto the photosensitive materials. A true gray-scale mask can be fabricated in a high-energy, beam-sensitive glass by changing the glass transmission with a laser beam or an electron beam [69,70]. This mask is continuous; but expensive to make. A more cost-effective and popular alternative approach is to use a commercial binary chrome mask to mimic a gray-scale light distribution for fabricate index

structures [71,72]. Different light transmission levels are created by modulating the size and the distribution of transparent holes in the chromium mask [73]. Afterwards, the transmitted light distribution is projected to form corresponding structure in photosensitive resin. The size of the transparent holes, also referred to as the pixel size of the mask, should be below the resolution limit of the exposure tool. The number of gray levels achievable is also dependent on the resolution and magnification of the projection lithography system, the minimum pixel size and increment between subsequent pixel sizes used to create the gray-scale mask. Furthermore, the sharp edge of binary mask may introduce diffraction. Alternatively, an inexpensive optical mask can be made using a high resolution film inkjet printer [74,75]. This technique modulates the ink dot density on a transparent film to produce the different transmission levels. These methods with optical masks suffer the same major drawback: they require different static masks for different structures, which is costly and time consuming.

To circumvent this drawback, spatial light modulators have been developed to generate dynamic masks that are capable of modulating the exposure light intensity distribution electronically, avoiding physically replacing the mask for each exposure. There are two main types of commercial spatial light modulators: liquid crystal display (LCD) and digital micromirror device (DMD). Liquid crystal display is an array of liquid crystal pixels. By controlling the orientation of the liquid crystal molecules at the level of individual pixels, each pixel can be set either at a transparent state or an opaque state. The LCD based commercial SLMs can contain as much as  $1280 \times 1024$  pixels, with a typical pixel size of  $17\text{-}30\mu\text{m}$  [76]. This commercial LCD modulator functions a convenient dynamic pattern generator, and have been used in projection micro-stereolithography [77]. However, LCDs have some intrinsic disadvantages [76]: (1) low fill factor; (2) low switching speed ( $\sim 20\text{ms}$ ); (3) low contrast/dynamic range of the transmitted pattern and (4) high UV absorption during the ON mode.

In order to address these limitations in the LCD based modulators, an alternative technology, called DMD has been developed in Texas Instruments. DMD is a semiconductor based array of fast, reflective digital light switches that exercise precise control of a light source [78]. Micromirrors on the DMD have two stable states: one indicates light on and the other indicates the light off. The grayscale modulation of the incident light is achieved by a binary pulse width modulation technique [79], which turns light on and off rapidly by the beam-steering action of the micromirrors. The mechanical switching time for the micromirror is  $\sim 15\mu\text{s}$  [80]. This opto-mechanic and electro-mechanic technique makes the DMD modulator more compact; have a full fill factor and a high dynamic range. However the LCD and DMD modulators have the following limitations: (1) can only make rectangular grid of features; (2) edges of pixels must be spatially filtered, reducing effective resolution; (3) maximum of  $\sim 1$  megapixel set by chip fabrication; (4) typically only 8 bits of grey scale; (5) quite expensive.

Here, I use a galvo scanning system to introduce a two-dimensional dose distribution at a high speed. Even though the exposure is sequential, if it is significantly faster than the time scale of polymerization in the material, then it is effectively instantaneous. It takes the galvo scanner less than a second to draw an exposure pattern, while the polymerization time of the material is over tens of seconds. Therefore, it is analogous to an instantaneous exposure to the material instead of a sequential exposure. The dose and XY locations of the “pixels” of the scanner system can be analog, while the SLMs and chrome masks are digital, such that the sizes of their pixel size limit the resolution. This rapid scanning modulated laser focus method provides convenient way to fabricate arbitrary index structures in the diffusive photopolymer.

The outline for the rest of the chapter is as follows. Section 3.2 introduces a new diffusive photopolymer called *Light Blue Russet* (LBR). A series of studies about this new photopolymer, including absorption, bulk index of refraction and pre-cure energy dose are conducted. Section 3.3 demonstrates an index formation study in the LBR polymer. Section 3.4 describes a galvo

scanning system to fabricate programmable GRIN lenses in the new diffusive photopolymer. Section 3.5 presents a quantitative index profile measurement method using a Shack-Hatmann wavefront sensor. Section 3.6 discusses the advantages and limitations of the programmable index structure fabrication method using the galvo scanning.

### 3.2 Light Blue Russet photopolymers

One of the advantages of the diffusive photopolymer is its incredible tunability. For example, increasing the initiator concentration can increase the sensitivity of the material. Increasing the monomer concentration or using monomers with higher index of refraction can achieve a higher peak index change. Therefore we can alter the material formulation accordingly to suit different applications. However we lose this tunability because the InPhase *Tapestry*<sup>TM</sup> HDS 3000 polymer is a commercial polymer. We do not know the formulation in detail and we cannot readily change it. Another drawback for the *Tapestry*<sup>TM</sup> HDS 3000 polymer is its complicated photoinitiation kinetics due to the particular photoinitiator, Irgacure 784, which is used because of the low energy 532 photos [81]. Two absorptive intermediate photoproducts are generated during photoinitiation, temporarily increasing the absorptivity of the material and thus making it difficult to understand this polymer material. In order to avoid these drawbacks, we propose to use a new photopolymer in this chapter. This new polymer is created in our group using *Tapestry*<sup>TM</sup> polymer as a model, and named as *Russet*. The material is sensitive to 405 nm and has very low absorption as is needed for thick (many mm) optics, thus the specific formulation discussed here is referred to as *Light Blue Russet*.

#### 3.2.1 Formulation of the LBR polymer

Similar to the InPhase HDS 3000 photopolymer, the LBR polymer comprises two independent and compatible polymerizable systems: one forms a solid yet permeable matrix polymer that functions as a mechanical scaffold; and another serves as the active components

consisting of initiators that absorb a fraction of the incident light to form radicals and monomers that polymerize by reacting with radicals. The detailed LBR formulation is shown in Table 3.1. Polyester block polyether and desmodur 3900 are the two components that thermally polymerized to form the matrix polymer. The catalyst, dibutyltin dilaurate with a purity of 95%, accelerates this thermal polymerization process to be within 24 hours at room temperature. When premixed with the matrix polymer components, the active components, namely photo initiators and monomers, are uniformly distributed in the spongy matrix polymer. Butyl phthalate is used as a plasticizer, which increases the flexibility and permeability of the matrix polymer so that the active components are free to diffuse in the polymer matrix.

Table 3.1: Formulation of the Light Blue Russet polymer

Chemical component	Chemical function	wt %
Diphenyle(2,4,6-trimethylbenzoyl) phosphine oxide (TPO)	Photo initiator	0.067
Tribromophenyl Acrylate	Monomer	6.00
Butyl phthalate 99%	Plasticizer	0.50
Polyester Block Polyether	Matrix polymer component 1	55.61
Desmodur 3900	Matrix polymer component 2	37.81
Dibutyltin Dilaureate, 95%	Catalyst	0.01

### 3.2.2 The absorption of the LBR polymer

The photoinitiators absorb part of incident light energy to generate radicals, which initiate polymerization. The absorption of the diffusive polymer depends on the molar absorptivity and concentration of the photoinitiator. Generally, higher concentration of the photoinitiators provides greater absorption and thus greater sensitivity of the material. However, higher concentration of the photoinitiators results in less uniformity of initiation in depth due to the Beer-Lambert absorption of the material. Also, there must be sufficient initiator concentration to meet the

stoichiometric needs of the formulation. Therefore, applications with thick optical materials lead to the use of initiators on the tail of their absorption bands so that the materials have low total absorption at the required concentration.

In this section, I calculate the absorption of the LBR polymer based on the molar absorptivity and molar concentration of the photoinitiator (TPO). Then, I experimentally measure the absorptions of the polymer with different photoinitiator concentrations. Here, I define several parameters associated with the absorption of material. These parameters include absorbance, molar absorptivity, molar concentration, path length of light through the material and transmission. The symbols and units for each term are shown in Table 3.2.

Table 3.2: List of symbols and their units in absorption calculation

	Symbol	Unit
Absorbance	$A$	Unitless
Molar absorptivity	$\epsilon$	[L/(mol.cm)]
Molar concentration	$[c]$	[mol/L]
Path length of light through material	$l$	[cm]
Transmittance	$T$	Unitless

Based on Beer-Lambert law, the transmittance of a polymer sample can be expressed as

$$T = \frac{I_1}{I_0} = 10^{-A} \quad (3.1)$$

where  $A$  is the absorbance of the material,  $I_0$  and  $I_1$  are the intensities of the incident light and the transmitted light respectively, as shown in Fig. 3.1. The absorbance of the LBR polymer sample depends on the molar absorptivity of TPO, the path length of light through the sample and the concentration of TPO through the relationship  $A = \epsilon[c]l$ .

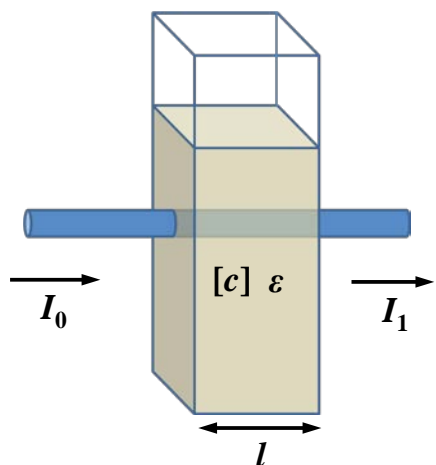


Figure 3.1. Diagram of Beer-Lambert absorption of a light beam as it travels through a material with length of  $l$  and molar concentration of  $[c]$ .

The molar absorptivity, also referred to as molar absorption coefficient or molar extinction coefficient, is a measure of how strongly chemical species absorb light at a given wavelength. The molar absorptivity is an intrinsic property of the material. The molar absorptivity of the TPO at 405nm is about 240 L/mol.cm [82]. The molecular weight of TPO is 348.37g/mol [83]. The weight concentration of the TPO in the LBR formulation is 0.067%. The density of the LBR polymer is tested to be 1.189g/mL. The molar concentration of TPO in LBR formulation can be calculated be  $2.3 \times 10^{-3}$  mol/L. Given the path length of the light through the material is 1cm, the absorbance  $A = 0.576$ , the transmittance is calculated to be  $T = 10^{-A} = 0.266$ . Since the absorption of the material equals  $1-T$ , the Beer-Lambert absorption of the LBR is calculated to be 0.73 for the light through a 1cm material sample.

Next, I measured the absorption at 405 nm of four polymer samples with TPO concentrations of 0%, 0.07%, 0.1% respectively. The measured absorptions are shown in Fig. 3.2. By linear fitting, the relationship of the absorption vs. the TPO concentration is  $y = 49.126[TPO] + 0.024$ , where  $y$  is the absorption through 1mm material and  $[TPO]$  is the TPO molar concentration. The  $y$  intercept indicates that the scatter of the matrix polymer is around 0.09dB/cm. Given the molar concentration of TPO in LBR formulation is  $2.3 \times 10^{-3}$  mol/L, the

absorption through 1mm LBR polymer is  $49.126 \times 0.0023 = 0.113$ , which excludes the matrix scatter. Thus absorption through 1cm LBR polymer is 0.70, which is accurate to the second decimal point, compared with theoretical calculated absorption 0.73 through 1cm LBR polymer. Now I can calculate the exposure dose versus depth, initiator consumption and radical generation rate, given the published values of the quantum yield. I first calculate the energy dose needed to consume the oxygen in the LBR polymers in next section.

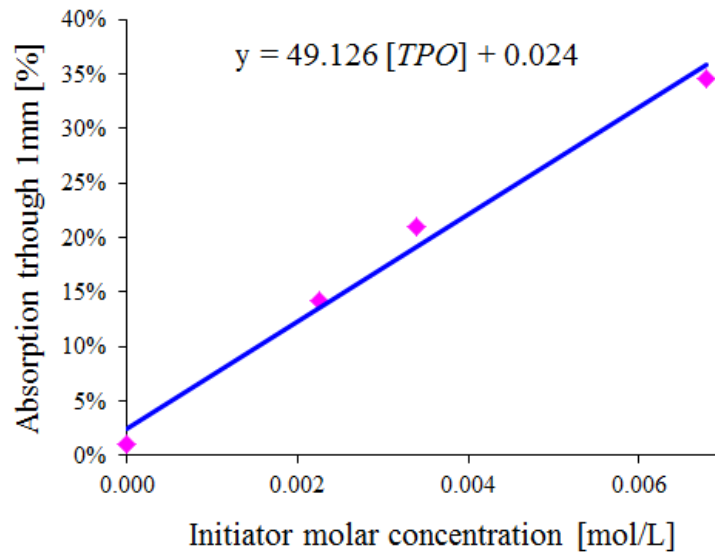


Figure 3.2. Material absorptions vs. initiator concentrations. The dots are measured absorption and the line is the linear fitting.

### 3.2.3 Pre-cure energy dose to clear out oxygen

Oxygen molecules in the polymer have two possible effects for the index change formation [84]. The first is the quenching effect during the photoinitiating. More specifically, when an initiator absorbs a photon and moves to its excited state, oxygen molecule steals the energy from the excited initiator, preventing the excited initiators to become radicals. Quenching reduces the quantum yield of the photoinitiating process. The second effect is the termination effect during the polymerization: oxygen molecules react with primary radicals and growing polymer radicals to form peroxy radicals, which are three orders of magnitude less active [85], thus terminating the polymerization process.



These effects due to the presence of oxygen can be avoided by a pre-cure procedure that consumes all the oxygen before the sample is used to index structure fabrication. This pre-cure process places the polymer under a uniform and incoherent light at the wavelength of 405nm to generate just enough radicals through photoinitiator depletion, to scavenge oxygen in the polymer.

Here, I first discuss the TPO bleaching process, as the amount of radicals generated is the amount of TPO consumed with a quantum yield. The rate of TPO bleaching can be express as

$$\frac{d}{dt}[TPO] = -k_{I-PI} I_0 [TPO], \quad (3.2)$$

where  $[TPO]$  is the molar concentration of photoinitiators with a unit of mol/L,  $k_{I-PI}$  is the bleaching rate constant,  $I_0$  is the exposure beam intensity and  $t$  is the exposure duration time. The left side of this equation describes the amount of photons absorbed per volume per second in the polymer, assuming that every photon absorbed initiate a TPO molecule. Thus the right side of the equation can be expressed as

$$K_{I-PI} I_0 [TPO] = \frac{I_0 (1-T)/l}{N_A E_{photon}}, \quad (3.3)$$

where  $E_{photon}$  is the photon energy,  $1-T$  is the absorption of the TPO,  $l$  is sample thickness, and  $N_A$  is the Avogadro constant, which expresses the number of photons per mole and is valued at  $6.022 \times 10^{23}$ . The photon energy equals  $h\nu$ , where  $h$  is Planck constant  $6.626 \times 10^{-34}$  J.s and  $\nu$  is the frequency of the 405 light. Given the transmittance  $T = 10^{-\varepsilon[TPO]l} = e^{-\text{Ln}(10)\varepsilon[TPO]l}$ , Eq. 3.3 becomes

$$\frac{d}{dt}[TPO] = \frac{I_0 (1 - e^{-\text{Ln}(10)\varepsilon[TPO]l})/l}{N_A h \nu}. \quad (3.4)$$

Taylor expanding  $e^{-\text{Ln}(10)\varepsilon[TPO]l}$  and assuming the absorbance of the material is small,  $k_{I-PI}$ , becomes a constant, expressed as

$$K_{I-PI} = \frac{\text{Ln}(10)\varepsilon}{N_A h \nu}. \quad (3.5)$$

Substitute  $k_{I-PI}$  with Eq. 3.5 in Eq. 3.2, a dynamic relationship between the TPO bleaching and exposure dose is derived, expressed as

$$[TPO] = [TPO_0] e^{-\frac{\text{Ln}(10)\varepsilon}{N_A h \nu} I_0 t} = [TPO_0] e^{-\frac{\text{Ln}(10)\varepsilon}{N_A h \nu} D_{\text{expose}}}. \quad (3.6)$$

where  $D_{\text{expose}}$  is the expose dose. This exponentially decay of TPO is shown Fig. 3.3.

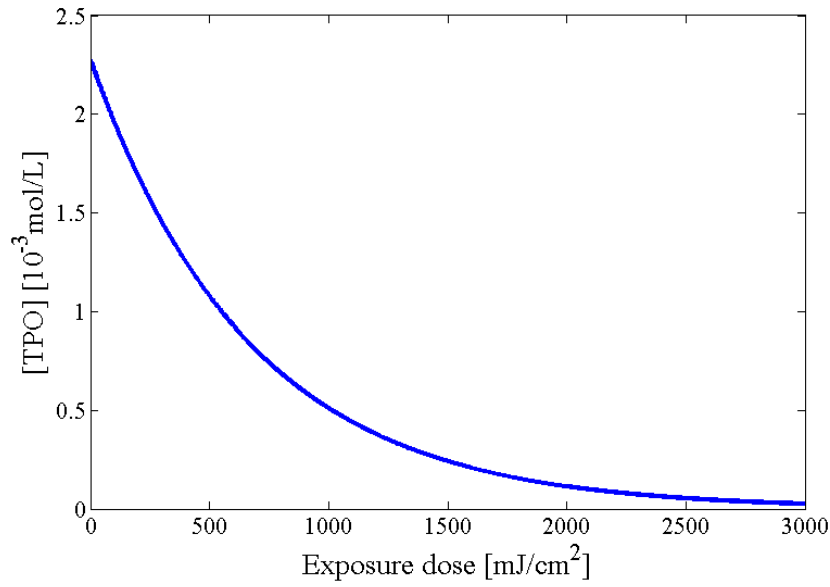


Figure 3.3. The photoinitiator bleaching curve for the LBR polymer.

This initiator bleaching provides a convenient way to calculate the pre-cure dose. The equilibrium dissolved oxygen concentration in acrylates is reported to be  $\sim 10^{-3}$  mol/L [86]. The quantum yield of generating radicals through consuming TPO is reported to be around 0.8 [87]. Therefore, the amount of TPO that needs to be consumed for clear outting oxygen is approximately  $1.25 \times 10^{-3}$  mol/L, resulting in a pre-cure dose of 517 mJ/cm<sup>2</sup>.

The pre-cure dose is also experimentally measured by exposing a LBR polymer slide sample with polymer thickness of 1mm to a set of exposure doses and monitoring the index development. Index change starts to show up when the exposure dose is approximately

900mJ/cm<sup>2</sup>. The difference between the calculation and the experimental measurement is due to the approximation of Eq. 3.4. This approximation achieves a constant  $k_{I-PI}$ , thus yielding an exponentially decayed initiator concentration during the bleaching process, which is intuitive to describe the initiator bleaching process. However the approximation does introduce calculation error, especially when the absorption of the polymer is not small. Numerically solving Eq. 3.4, the pre-cure dose is calculated to be 780mJ/cm<sup>2</sup>, yielding a 15% error compared to the measured pre-cure dose, which is reasonable, given that reported dissolved oxygen concentration and quantum yield in literature are used in the calculation. I use the experimentally measured 900mJ/cm<sup>2</sup> as the pre-cure dose to clear out oxygen for the LBR polymers in this chapter and chapter 4.

#### 3.2.4 Bulk refractive index and dispersion

The bulk refraction index of the polymer material depends on the refractive indices and the concentrations of the matrix polymers and the monomers. Given the refractive index of the monomer is higher than the matrix polymer, a higher monomer concentration in the formulation leads to a higher bulk refractive index of the polymer material based on the refractive index mixture rules [88]. In order to derive the relationship between the bulk refractive index and the monomer concentration, the LBR polymer samples with different monomer concentration are made. After the samples are uniformly flood cured, the bulk refractive indices of the samples are measured.

The bulk index of refraction is measured with a Metricon prism coupler model 2010/M. The photopolymer sample is clamped against the prism. The angle of the laser beam incident at the prism and polymer interface is varied, while the reflectivity is captured by a detector. Given the refractive index of the polymer sample is higher than the refractive index of the prism, total internal reflection occurs when the angle reaches the critical angle. The refractive index of the polymer is determined by the critical angle, expressed as  $n = n_1 \sin \theta_c$ , where  $n$  is the refractive

index of the sample under test,  $n_1$  is the refractive index of the prism and  $\theta_c$  is the measured critical angle. The measured bulk refractive indices of the LBR polymers at wavelength of 633nm with different monomer concentration are shown in Fig. 3.4.

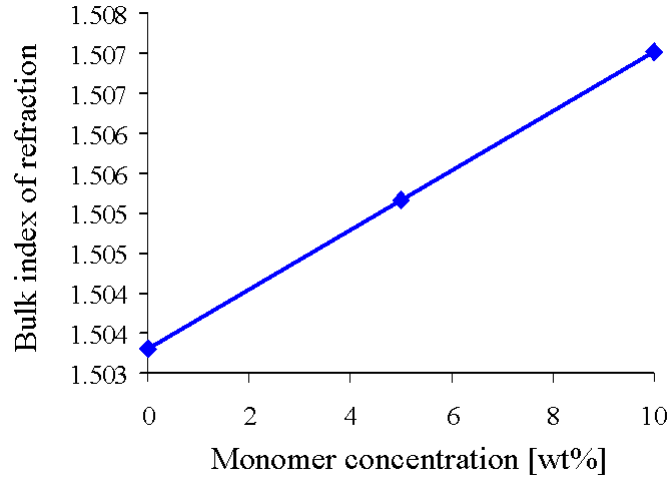


Figure 3.4. The measure bulk index of refraction of the BR polymer with monomer concentration of 0%, 5% and 10% respectively. The line is linear fitting from the measured three bulk indices.

By linearly fitting the data, we can write down the equation that conveniently calculates the bulk index change based on the monomer concentration as follows

$$n_{633}([m]) = 0.000371[m] + 1.5033, \quad (3.7)$$

where  $n_{633}$  is the bulk index of refraction at the wavelength of 633nm and  $[m]$  is the wt% of monomer concentration. The y intercept indicates that the bulk index of pure the polymer matrix is 1.5033. The maximum localized index change than can be achieved for the LBR polymer with 6 wt% monomer concentration is about  $2.2 \times 10^{-3}$ . This conclusion is based on the assumption that the polymerization process and monomer diffusion are well separated. That means the monomers diffuse into the exposed region after the polymerization has finished. Section 3.3 will demonstrate that I measured a peak index change of  $2.2 \times 10^{-3}$  for large structures in the LBR polymer where the monomer diffusion is expected to be slow. However, the peak index changes are measured to

be more than twice of  $2.2 \times 10^{-3}$  when the LBR polymer sample is baked in oven after exposure at  $60^\circ\text{C}$  to increase the monomer diffusion speed. An index formation model is developed in next section to reveal the underling chemical reactions to cause this difference.

The dispersion of the matrix polymer is also characterized by measuring the bulk refractive indices at different wavelength for the matrix only sample, shown in Fig. 3.5. By power fitting the measured data points, the dispersion of the LBR polymer is found to be:

$$n(\lambda) = 1.489 + \frac{5897}{\lambda^2} - \frac{1.286 \times 10^8}{\lambda^4}. \quad (3.8)$$

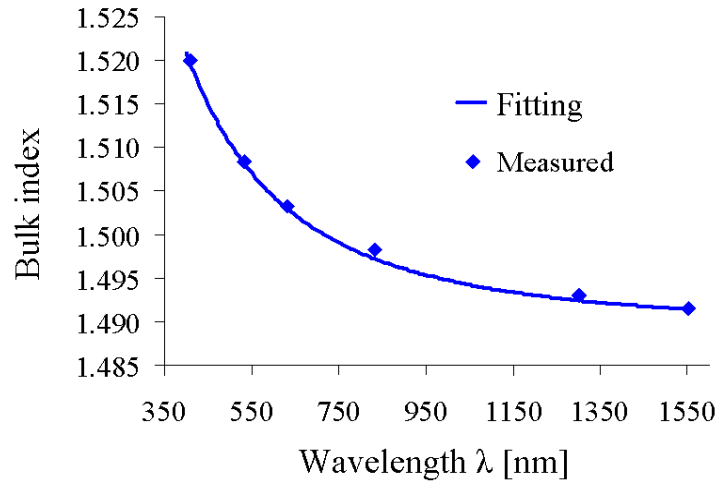


Figure 3.5. The bulk index of the matrix polymer measured at the wavelength of 410nm, 532nm, 633nm, 832nm, 1302nm and 1553nm respectively. The curve line is a power fitting for these six data points.

### 3.3 Index formation model for the LBR polymer

In this section, I derive an index formation model by studying the locally introduced index structures with a spatial scale of couple hundred micrometers in the LBR polymer. As discussed in chapter 1, in the simplest model, the index change is proportional to  $I^\alpha t$ , where  $I$  is the exposure beam intensity,  $t$  is the exposure time and  $\alpha$  is a single fit parameter. In chapter 2, I develop an index formation model for the HDS 3000 polymer, which includes the oxygen inhibition effect and an *ad hoc* mechanism of saturation with no explanation of what caused this.

Here, I extended the model in the following ways for the LBR polymer. First, index development at high temperature ( $60^{\circ}\text{C}$ ) will be shown to increase index contrast by a significant factor. Second, quantitative local index measurement will be converted to local monomer conversion. This measurement is not possible with standard chemical reaction testing methods, such as Fourier transform infrared spectroscopy (FTIR) [89], since over 90% of the LBR formulation is the matrix polymer. Third, the exposure dose will be converted into the initiator consumption, through the published quantum yield and the primary radical generation. This will be shown to be the source of the observed saturation.

These advances will enable the following conclusions. First conclusion is that a previously-unknown thermal initiation mechanism occurs at  $60^{\circ}\text{C}$ , reinforcing the exposure pattern without changing its shape. Second conclusion is that at room temperature and at the spatial scales investigated, polymerization and diffusion occur sequentially, limiting maximum monomer conversion to 100% of the formula concentration. Third conclusion is that the monomer diffusion is accelerated relative to polymerization at  $60^{\circ}\text{C}$  such that polymerization can continue in the dark, fed by diffused monomers. This enables the local polymer concentration to be several times greater than the formula concentration of the monomer. Fourth conclusion is that at the investigated scales, oxygen acts as a local threshold with minimal non-local behavior due to diffusion. Last conclusion is that the parameter  $\alpha$  is found to be close to 1, indicating limited radical-radical termination events in contrast to typical radical polymerization mechanisms.

In summary, the index formation model captures a quantitative description of the roles of oxygen, monomers and initiators under four different conditions (pre-cured and not, room temperature and  $60^{\circ}\text{C}$  development). This model is shown in the following section to enable accurate design of experimental conditions to yield a desired index structure.

### 3.3.1 Experiment design

The experimental design philosophy is to capture as many factors that affect the index formation in the LBR polymer as possible. In order to capture effects of the exposure dose, oxygen and development temperature on the index formation separately, four LBR polymer slide samples are used and are divided into two groups. The two samples in one group are pre-cured under a uniform incoherent UV lamp at the wavelength of 405nm with an exposure dose of  $900\text{mJ}/\text{cm}^2$  to clear out the oxygen for the entire polymer sample. The two samples in the other group are not pre-cured. The reason to pre-cure just one group is to confirm the oxygen inhibition for localized index formation in the LBR polymer. The oxygen inhibition has been demonstrated experimentally in the *Tapestry*<sup>TM</sup> HDS 3000 polymer. Then each polymer slide sample is exposed to a Gaussian beam with  $2w_0$  of  $635\mu\text{m}$  to form a set of GRIN lenses with different exposure durations. Previous experiment in the HDS 3000 polymer has demonstrated that a two-dimensional Gaussian beam exposure forms a circularly symmetrical GRIN lens, whose peak index change occurred at the center.

Originally, baking the sample during the index formation is used to increase the monomer diffusion, thus lower the development time required. The rule of thumb is that increasing the temperature by every  $10^\circ\text{C}$  doubles the monomer diffusion speed. After the exposure, one sample of each group is left in the room temperature, and the other sample of each group is left in the oven at  $60^\circ\text{C}$ . The baking temperature of  $60^\circ\text{C}$  is carried over from the previous experiment for the *Tapestry*<sup>TM</sup> HDS 3000 polymer, which becomes thermally unstable above approximately  $70^\circ\text{C}$ . The experiment design for the index exposure and development is summarized in Table 3.3.

After the index structures in the samples are fully developed, the index profiles of GRIN lenses in these four samples are measured using a Shack-Hartmann wavefront sensor setup described in Sec. 3.5. Next, I convert the experimentally measured index changes into the actual chemical reactions in the polymer step by step, to derive the index formation model. First, I

derive an index formation model from the on axis index changes of the four groups of exposed GRIN lenses. Then I show that the model established using just the peak response predicts the complete profile of the lens to a reasonable accuracy.



Table 3.3: Summary for the experiment design

	Pre-cure	Development temperature
Sample 1	Yes	Oven 60 <sup>0</sup> C
Sample 2	No	Oven 60 <sup>0</sup> C
Sample 3	Yes	Room Temperature
Sample 4	No	Room Temperature

### 3.3.2 Peak index change vs. exposure dose

The curves of the measured peak index change in each GRIN lens vs. on axis exposure dose are shown in Fig. 3.6. These four curves reveal several patterns: (1) the curves for peak index change vs. on axis exposure dose corresponding to the two samples without pre-cured are shifted to the right with an exposure dose approximately 1000mJ/cm<sup>2</sup>, confirming the oxygen threshold effect in the LBR polymer; (2) baking the sample immediately after the exposure can boost the maximum achievable index change by at least two times, which suggests a previously unknown reaction may have happened; (3) in the low exposure dose range, the index has a linear relationship with the exposure dose, indicating that the unimolecular termination dominates; (4) the peak index changes tend to saturate in the large exposure dose regions. Such saturation can be potentially attributed to exhaustion of photoinitiators or monomers. Next I first convert the exposure dose into photoinitiator consumption and then convert the on-axis index change into the on-axis monomer conversion, to explain the underlying chemical reactions that cause these patterns.

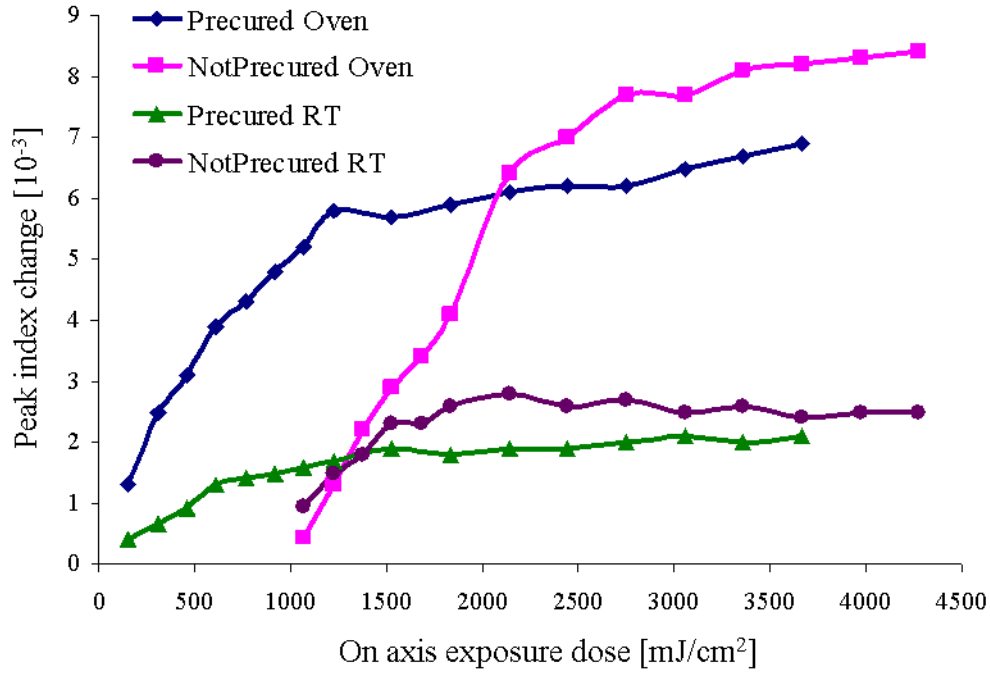


Figure 3.6. The measured on-axis index change vs. on axis exposure dose for the four samples. Each symbol represents the on-axis index contrast of a different GRIN lens.

### 3.3.3 Monomer conversion vs. photoinitiator consumption

The initiator concentration decreases due to photolysis during the exposure, reducing the material sensitivity. Therefore, I converted the dose into initiator consumption in order to express the initiation in more natural units. This conversion is calculated by solving Eq. 3.7, the similar way to calculate the pre-cure dose for clearing out oxygen, which is discussed in Sec. 3.2.3. Figure 3.7 illustrates the peak index change against TPO consumption.

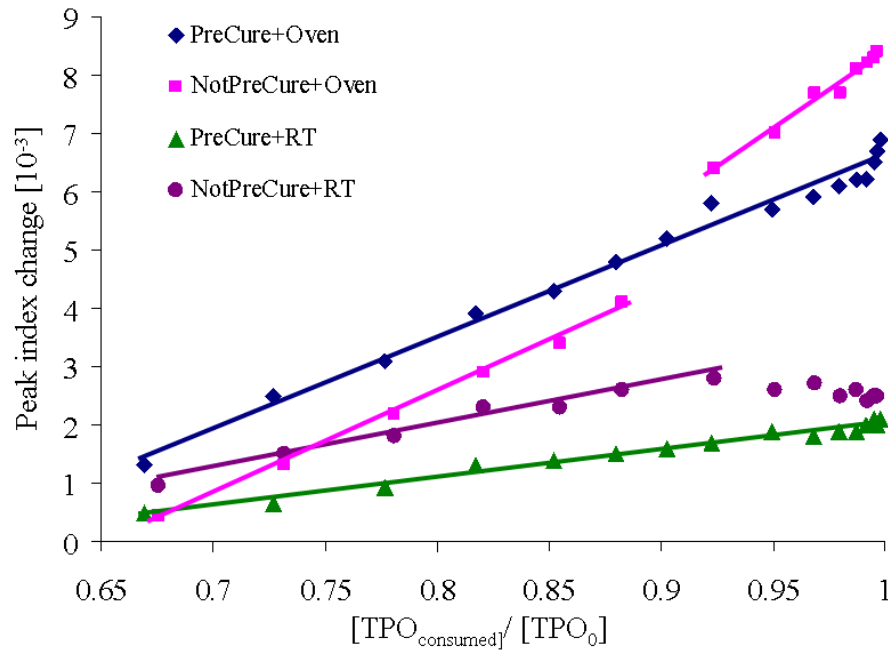


Figure 3.7. Measured relationship between index change and photoinitiator consumption. The symbols are the measured on-axis index change of the GRIN lenses in the four samples respectively. The lines are linear fits.

It is apparent that for all four exposure and development conditions, the on-axis index change increases linearly with the photoinitiator (TPO) consumption. Also the on-axis index change tends to saturate when the TPO is completely consumed. As discussed in Sec. 3.2.4, the localized index change is proportional to polymer formed at the exposed region, assuming that diffusion completely replaces any monomer consumed. Thus, the peak index change can be transformed into the monomer conversion using the Eq. 3.7.

Now I have turned the experimental measured relationship (exposure dose vs. index response) into a relationship between two chemical components in the polymers, shown in Fig. 3.8. For the LBR polymer, when the normalized conversion of monomers is 1, it means that all the formulary monomers (6wt%) are transformed into polymers in the exposed region when the index development has completely finished. When the normalized conversion of monomer is  $> 1$ , it indicates that more than 6wt% monomers are polymerized, which happens through continuous

polymerization with monomers that diffuse from the outside of the exposed region into the exposed region. Such continuous polymerization when the sample is left in the dark to develop index change is defined in this thesis as dark polymerization. Thus, conversion of monomers for the four cases will provide information about the time sequence of the chemical reactions (photoinitiation, polymerization and monomer diffusion) for these four cases.

All GRIN lenses in the group which is pre-cured and developed in room temperature have monomer conversion under 1. This indicates the process does not overlap in time for the pre-cured and developed in room temperature sample. That is, initiation causes polymerization which then terminates, followed by diffusion. All other three samples have lenses with monomer conversion  $>1$ , indicating that some polymerization of diffusing monomer took place. The on-axis monomer conversion for the lenses in the not pre-cured and developed in room temperature sample, is slight above 1 when the TPO consumption is over 0.85 and the monomer conversion is saturated towards 1 when the TPO consumption is reaching 1. This is potentially due to the increased monomer diffusion speed caused by sharper monomer concentration gradient due to oxygen threshold effect, which I will discuss in detail in Sec. 3.3.4.

The two oven baked samples show monomer conversions much higher than the samples left in room temperature for the on-axis exposure regions, indicating something significant happens in the baking process. First, the baking process is expected to significantly increase the monomer diffusion speed, thus the diffused monomers continuously feed the polymer gain growth in the exposed region when the polymerization is not terminated, resulting a monomer conversion  $> 1$ . Second, a previously-unknown thermal initiation during the baking process is discovered in my experiment and validated in a separate experiment by Dr. Michael C. Cole, a research associate in our group. As mentioned in Sec. 3.2.3, when a LBR polymer is exposed to a 405nm light beam, the radicals generated by cleaving the TPO molecules first react with oxygen to form peroxy radicals. These peroxy radicals are stable in room temperature, but can be

thermally initiated when the temperature is above  $\sim 55^{\circ}\text{C}$  to initiate polymerization process. Thus baking process not only increases the monomer diffusion speed but also brings in a thermal initiation to boost the index change.

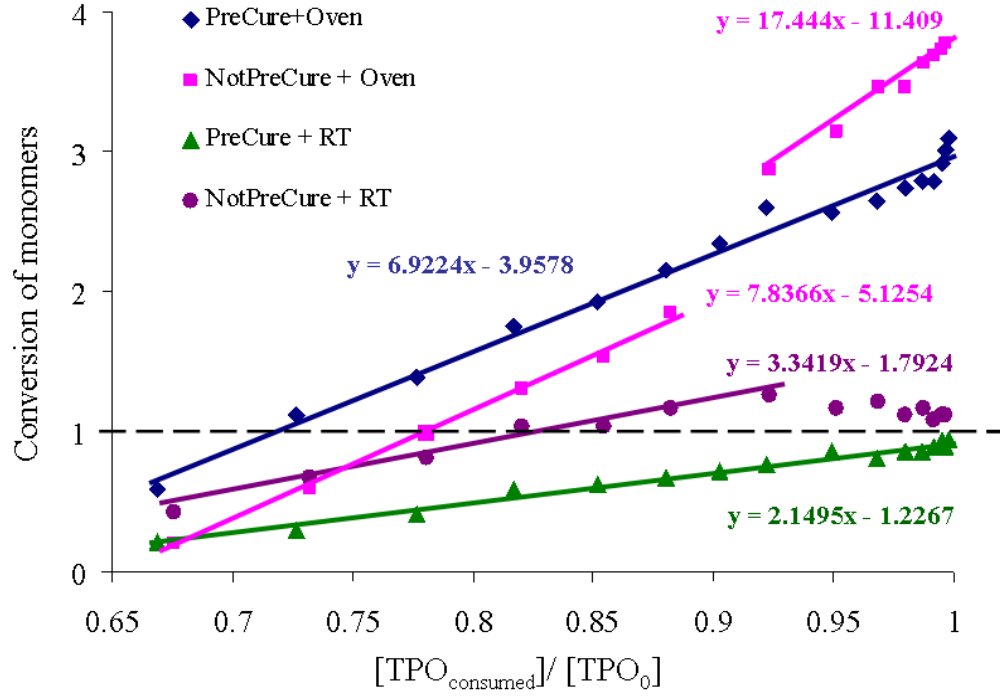


Figure 3.8. Demonstration of the linear relationship of the monomer conversion and the TPO consumption. The dark dash line shows where monomer conversion is 1. The lines are the linear fits with the fitting equation next to each line.

All the four monomer plots of conversion vs. TPO consumption are apparently show a linear relationship between the monomer conversion and the TPO consumption. Thus I used a line fit to fit all the four plots, shown in Fig. 3.8. The linear fit can be express as

$$[p]/[M_0] = a_1 ([TPO_{consumed}]/[TPO_0] - [TPO_{threshold}]/[TPO_0]), \quad (3.9)$$

where  $[p]$  is molar concentration of monomers that are polymerized into polymers,  $[M_0]$  is the formulary molar concentration of the writing monomer,  $a_1$  is the slope of the linear fit,  $[TPO_0]$  is the formulary molar concentration of the initiator,  $[TPO_{consumed}]$  is the molar concentration of the

initiators that are totally consumed during the exposure and  $[TPO_{threshold}]$  is the molar concentration of the initiators that are consumed to clear out the oxygen.

I extracted two interesting parameters from Eq. 3.6. First, the slope of each line can be used to estimate the average polymer chain length, which is defined as the number of monomers per polymer chain. The polymer chain length is difficult to be measured experimentally. The calculated polymer chain length for each sample is shown in Table 3.4. The line fits also indicate that in the same sample, the average polymer gain length in on-axis region of each formed GRIN lenses is almost the same, despite the differences in the exposure dose for each GRIN lens. Second, the x intercept of each line fits is the TPO consumption to clear out oxygen, shown in Table 3.4. The averaged TPO consumption to clear oxygen is  $0.58 \pm 0.06$  of the total TPO. The pre-cure dose we used is  $900 \text{ mJ/cm}^2$ , which consumes 0.60 of total TPO. Thus, the fitted TPO consumption to clear oxygen in the LBR photopolymer has  $< 10\%$  error with the experimentally measured TPO consumption for pre-curing the sample.

You may also notice that the linear fit for the GRIN lens array that is not pre-cured and is oven baked is broken and shifted when the TPO consumption is over 0.9, which indicates a potential new chemical reaction. But with the current data I could not come up a clear explanation for it. Extra data are needed to shed insights into the new chemical mechanism.

Table 3.4: Polymer chain length and TPO consumption to clear oxygen for the four samples

	Slope	Average polymer chain length [monomers/chain]	$[TPO_{consumed}]/TPO_0$ to clear oxygen
Pre-cure RT	2.1495	96	0.57
Not Pre-cure RT	3.3419	150	0.54
Pre-cure Oven	6.9224	310	0.57
Not Pre-cure Oven	7.8366	351	0.65

### 3.3.4 Index shapes of the Gaussian exposures

So far, I have discussed the index formation based on the relationship between on-axis index changes and the on-axis TPO consumptions. The experiments measured the index profile of each GRIN lens in the four samples, not just the peak, thus there is considerably more data available. Here, I show that the model established using just the peak response predicts the complete profile of the lens to a reasonable accuracy.

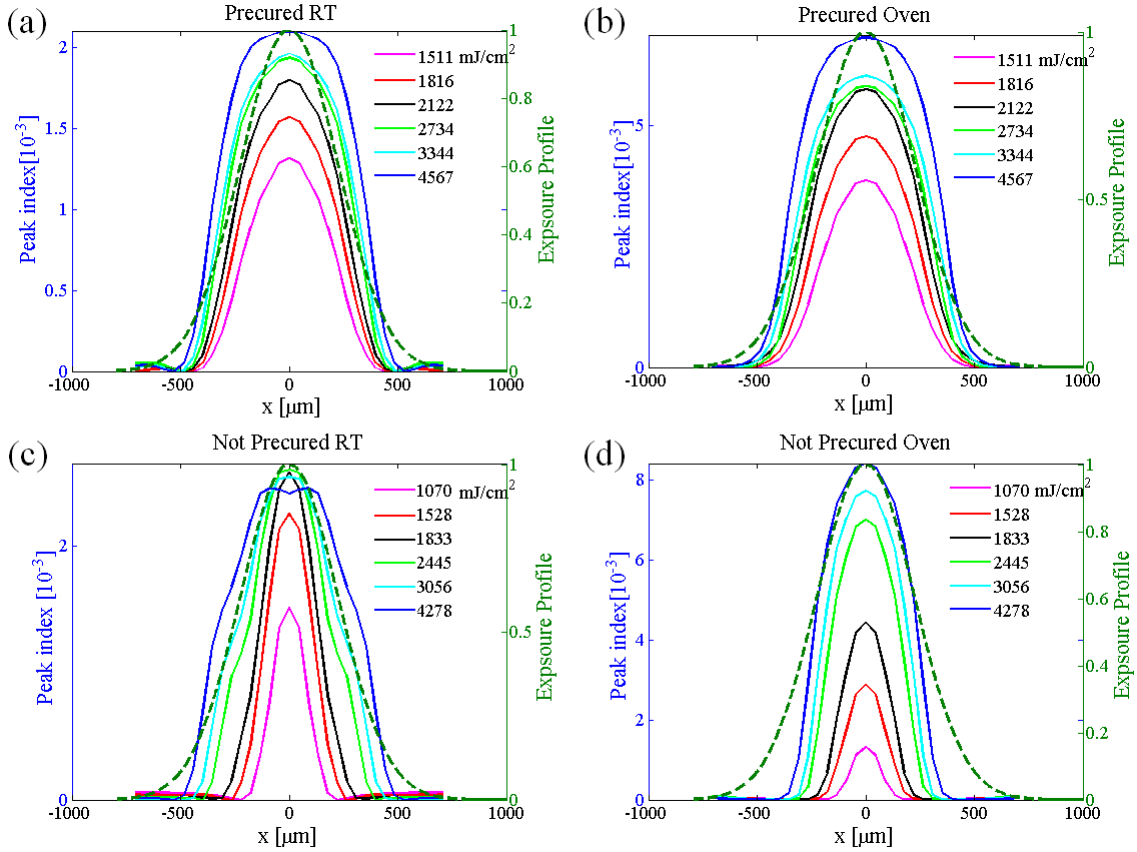


Figure 3.9. Measured index profile calculated via an azimuthal average of the measured 2D index profile of each lens. Parts (a)-(d) show the index profiles for the labeled cases and also the Gaussian intensity profile (the green dash line), normalized to the peak index change. Note that the index scales are not the same for all cases.

The index profiles of GRIN lenses in the four samples are shown in Fig. 3.9. First, comparing the index shapes of the not pre-cured sample to the pre-cured sample for both the oven baked and room temperature cases demonstrates that oxygen narrows the index structures by

locally inhibiting the polymerization under a threshold dose. In the sample that is not pre-cured and developed in room temperature sample, shoulders show up in the index profiles with large exposure doses. A potential explanation for the shoulder to emerge is the increased monomer diffusion speed due to sharper monomer concentration gradient caused by the oxygen threshold effect, shown in Fig. 3.10.

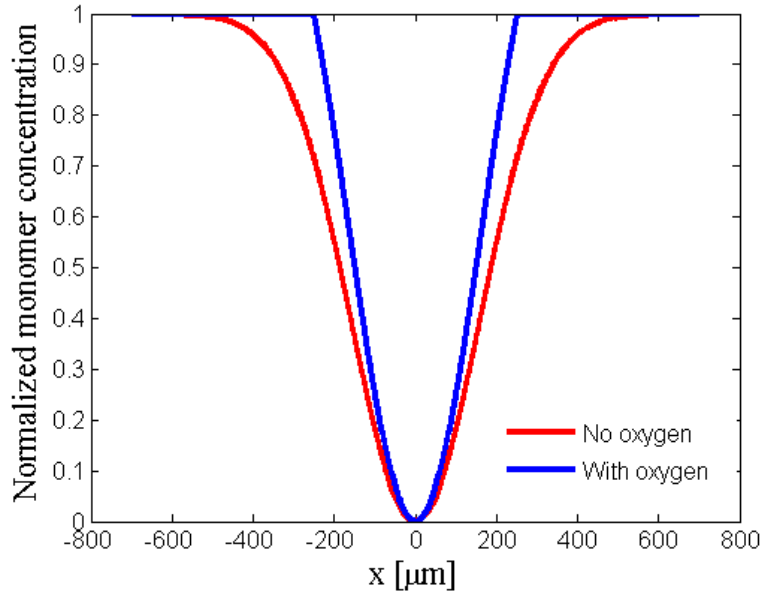


Figure 3.10. Demonstration of the normalized monomer concentration after the photo cleaved radicals react with monomers and turn monomers into polymers, thus carving a hole in the monomer concentration. Here two monomer concentrations are shown for oxygen and no oxygen presence situations respectively. The oxygen threshold effect causes a sharper monomer gradient, thus increasing the monomer diffusion speed.

Another trend of the index shapes in Fig. 3.8 is when the exposure dose increases, the introduced index profile are broader, compared to the Gaussian exposure intensity distribution. This may due to a saturation effect as was shown earlier in Fig. 3.6. Next, I identify which specie is being depleted and leads to this saturation. Given the TPO concentration in the LBR polymer before any exposure is only 0.067wt%, I believe that the TPO depletion is the main factor for the broadening effect. The TPO consumption vs. exposure dose is shown in Fig. 3.11, which is calculated through numerically solving Eq. 3.4.



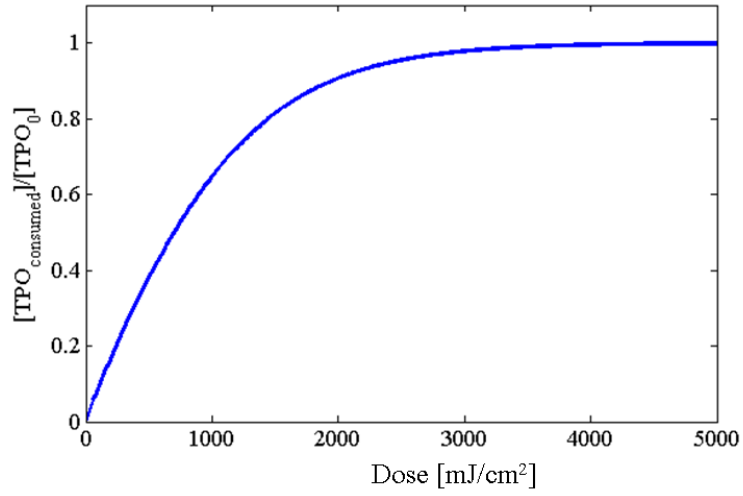


Figure 3.11. The depletion of TPO in the polymer as the expose dose is increasing.

Now, I have converted the exposure dose distributions of the GRIN lenses in the four samples to the normalized TPO consumption distributions, and compared the normalized TPO consumption distributions to the normalized index profiles of each corresponding lens, shown in Fig. 3.12. The normalized index profiles match well with the normalized TPO consumption curves, except for the shoulder regions in case that was not pre-cured and left in room temperature. This confirms that the TPO consumption distributions, instead of the expose dose patterns, determine the index profiles. Thus, when I design the exposure condition to fabricate arbitrary index structure, the TPO consumption distribution that replicates the required index profile should be used to calculate the exposure dose pattern.

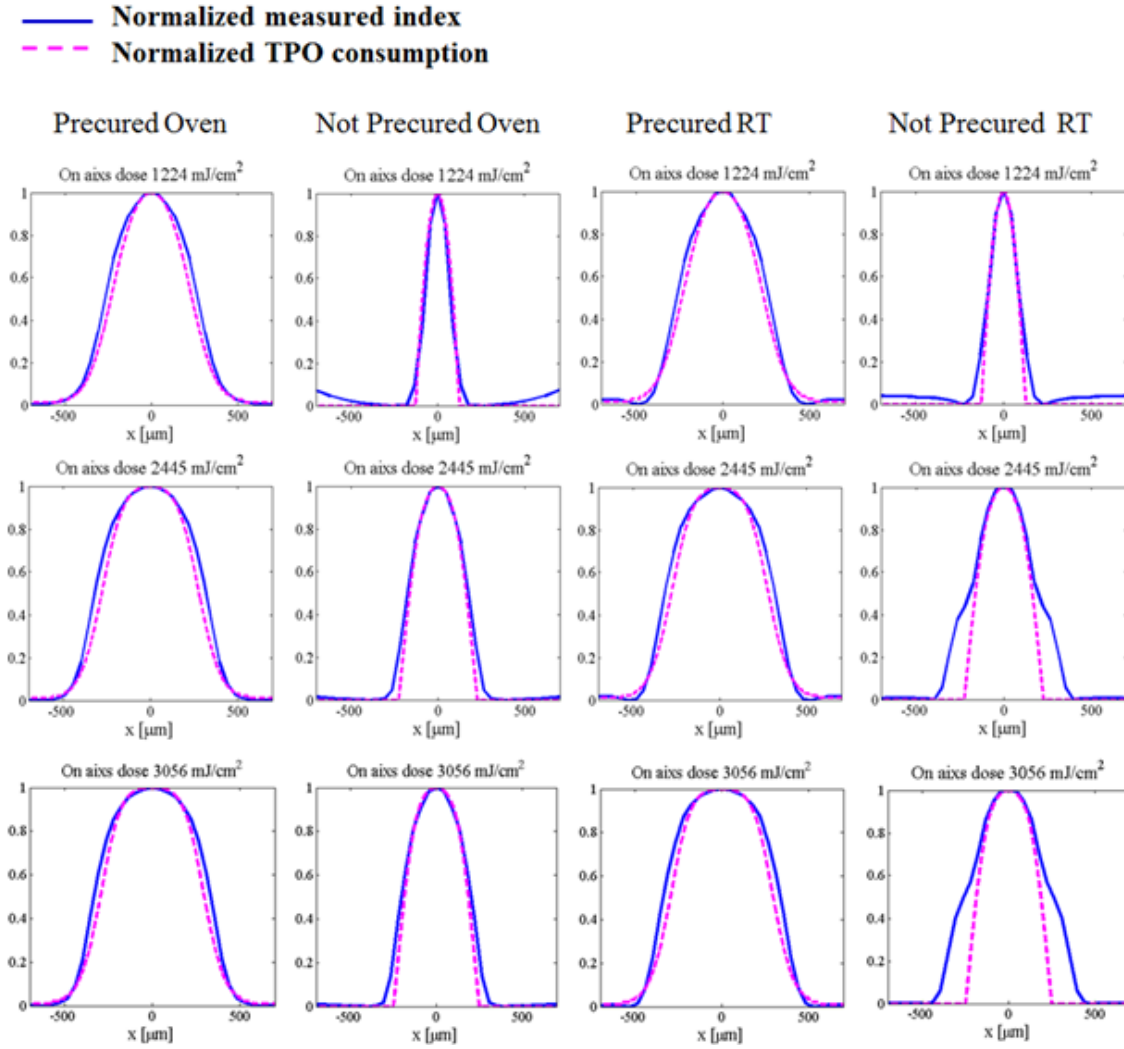


Figure 3.12. Comparison of the normalized index profiles and the normalized TPO consumption distributions for three group of GRIN lenses. Each group has four lenes that exposed at the same on axis exposure dose, but for different condistions: pre-cured oven baked, not pre-cure oven baked, pre-cured room temperature, not pre-cured room temperature respectively. The solid blue curves are the normalized measured index profiles and the dash pink curves are the normalized calualted TPO consumption distributions.

I also noticed that the index profiles of the lenses that are developed in room temperature are similar to those that are developed in oven at 60<sup>0</sup>C, given the on-axis exposure dose is the same for each comparison. The difference is that the peak index changes are much higher for lenses left in oven. This indicates the baking process can significantly boost the index change without distorting the index shapes. This pattern is confirmed through the comparison of the

measured index profiles with the same on axis exposure dose, shown in Fig. 3.13. This finding is exciting. First, this is the evidence for the thermal initiation happened during the baking process. Second, baking at 60°C after exposure provides two advantages: (1) reducing the required development time, since high temperature increase the monomer diffusion speed; (2) the thermal initiation reinforcing the exposure pattern.

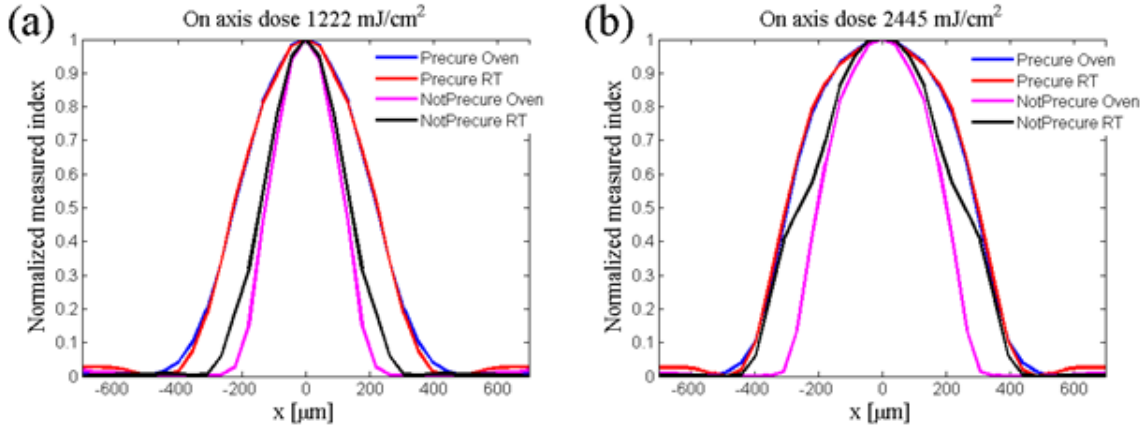


Figure 3.13. Comparison of the index profiles in the four samples with same expose doses. (a) shows the normalized measured index profiles with on axis dose of 1,222 mJ/cm<sup>2</sup>. (b) shows the normalized measured index profiles with on axis dose of 2,445 mJ/cm<sup>2</sup>

### 3.3.5 Conclusions for the index formation study

The index formation study reveals several useful characteristics of the LBR polymer. First, the profile of the introduced index structures is determined linearly by the photoinitiator consumption distribution. Second, oxygen narrows structures by locally suppressing polymerization below a threshold dose. No significant diffusion of oxygen is observed at these size and time scales, which simplifies the design of structures using this effect. Third, baking the sample at 60°C after exposure increases the index change without changing the index shape, which provides a convenient way to fabricate high index structures with controlled profiles. And last, the index change is linear to radical generation, which is not typical of most radical systems that undergo bimolecular termination and sublinear initiation kinetics. This linear response also simplifies design.

This index formation model provides a guidance to design the fabrication process to make arbitrary index structures in the LBR polymer. Exposure condition, oxygen and the development temperature are the design variables I can use to form required index structure. However, the oxygen concentration is hard to control. Thus it is better to clear out oxygen through the pre-cure process before making any index structure. To design the exposure condition, I need to first ensure that a TPO consumption distribution is determined to replicate the required index profile. Then, I convert the TPO consumption distribution into the corresponding exposure dose pattern.

### **3.4 Fabrication of programmable GRIN lenses**

This section elaborates a method to fabricate GRIN lenses with programmable index profiles in diffusive polymers. This method uses a galvo scanning system to introduce arbitrary index structures in polymers. The galvanometer scanner draws a two-dimensional image in the polymer sample that describes the exposure energy dose distribution.

#### **3.4.1 The galvo scanning system**

The optical layout of the galvo scanning system is shown in Fig. 3.14. This galvo scanning system was originally developed under a capstone project by several senior undergraduate students. Later on, a confocal microscope with a HeNe laser as the probe beam was added to locate the polymer sample, which is discussed in detail in chapter 4. The laser beam from a pigtailed laser diode, Thorlabs LP405-SF10, is collimated using an adjustable aspheric collimator, Thorlabs CFC-5X-A. This collimator has a focal length of 4.6mm. The collimated laser beam goes through a Thorlabs dual-axis galvo scanner GVS001, and then is focused by an objective lens into the polymer sample. The polymer sample is mounted onto a three dimensional stage. The dual-axis galvo scanner consists of two galvanometer-based scanning motors and two optical mirrors. The mirrors are mounted on the shaft for x, y axis respectively. GRIN lenses with

any arbitrary index profile can be fabricated by mapping out the exposure dose distributions at the polymer sample using this dual-axis galvo scanner. The collimator is chosen based on the specifics of the pigtail diode laser and the dual-axis galvo scanner. A single mode fiber, Thorlabs SM405-HP, is used to spatially filter the diode laser beam. The mode field diameter of the fiber is 2.9  $\mu\text{m}$  at the wavelength of 405nm.

The focal length of the collimator for the pigtailed laser diode is chosen so that the repeatability of the scanner must be small in comparison to the laser spot size in order to reliably position the writing spot. Given the focal length of the writing objective lens, the maximum variance of the exposure spot at the polymer sample is

$$\delta x_{spot} = 2f_{obj} \delta\theta, \quad (3.10)$$

where  $\delta\theta$  is the repeatability of the dual-axis galvo scanner, which is 15  $\mu\text{rad}$  for the Thorlabs dual-axis galvo scanner. The laser focus spot size at the polymer sample plane is

$$w_{spot} = \frac{\lambda}{\pi NA_{obj}} = \frac{\lambda}{\pi (w_{col}/f_{obj})}. \quad (3.11)$$

Consider the requirement for the accuracy of locating the laser spot at the polymer sample, which is

$$\frac{\delta x_{spot}}{2w_{spot}} = \frac{\pi w_{col}}{\lambda} \delta\theta < \frac{1}{10}. \quad (3.12)$$

From the above inequality we get the upper limit of the collimated beam size, which is

$$w_{col} < \frac{1}{10} \frac{\lambda}{\pi \delta\theta} = 860 \mu\text{m}. \quad (3.13)$$

Given that  $w_{col} = \frac{\lambda f_{col}}{\pi w_0}$ ,  $2w_0$  is about 2.9 $\mu\text{m}$ , the focal length of the collimation lens  $f_{col}$  should

be less than 9 mm. The focal length of the collimator is chosen to be 4.6mm.

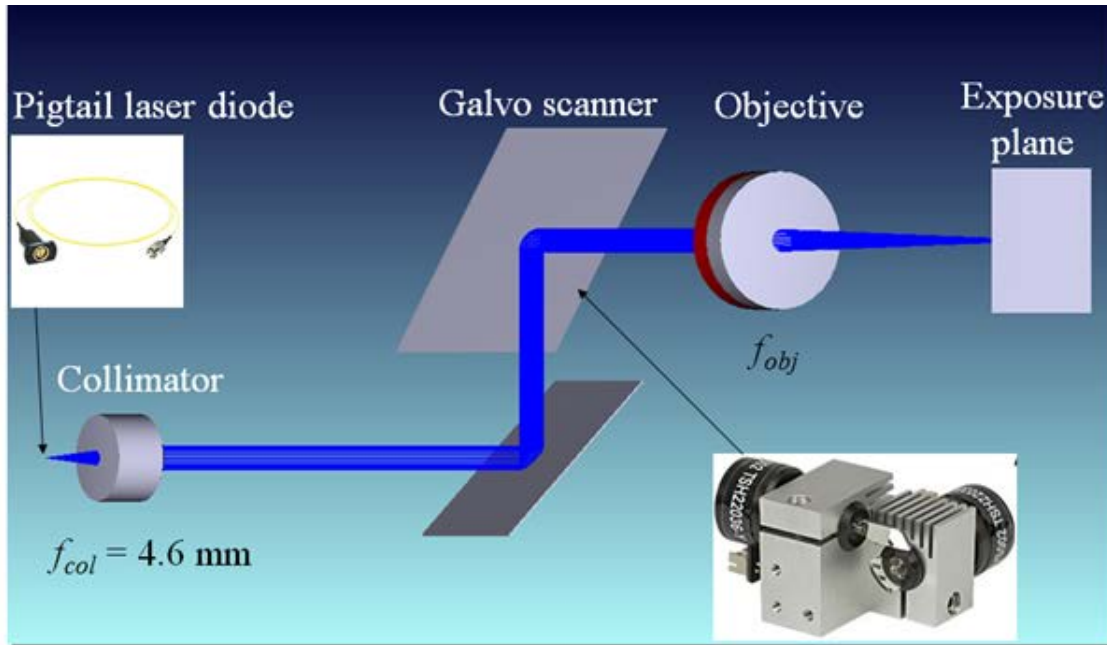


Figure 3.14. The optical layout of the galvo scanning system.

A custom designed circuit is used to control the galvo scanning system. The system block diagram is shown in Fig. 3.15. A microcontroller unit (MCU), TI MSP430 F5436, is used to communicate between the user and the optical system. A parameter file and a vector file are downloaded onto the MCU by a RS232 UART, which connects the external PC to the MCU. The parameter file sets the key control parameters for the system, such as the output power of the diode laser, the drawing mode, and so on. The vector files consists of  $x$ ,  $y$  axis coordinates and laser “on” time spans of the sequential exposure spots, which are designed to draw any arbitrary index structure in the polymer sample. The  $x$ ,  $y$  coordinates, which are integers from 0 to  $2^{16}-1$ , are converted into analog voltage signals that drive the galvanometer based mirrors. In order to gain the ability to translate and scale the optical field produced by the galvo scanner, a basic summer and inverter op-amp circuit is placed in series after the digital to analog convert (DAC) output. At the same time, the signal that controls the laser output power and duration is converted into an analog voltage and sent to the laser diode controller, ILX Lightwave LDC-3724B. Therefore the galvo system is capable of drawing arbitrary two-dimensional energy dose

distributions at the exposure plane by designing the parameter and vector files. Three-dimensional energy dose distribution can also be realized by synchronizing the z-coordinate of the translation stage and the vector commands for different layers. Because the locally introduced index change in the diffusive polymers is determined by the exposure dose distribution, any arbitrary index structure can be fabricated by programming the parameter and vector files. The dose distribution at the exposure plane can be captured by a camera and displayed on a computer. The calibration procedure for this galvo scanning system is shown in Appendix A.

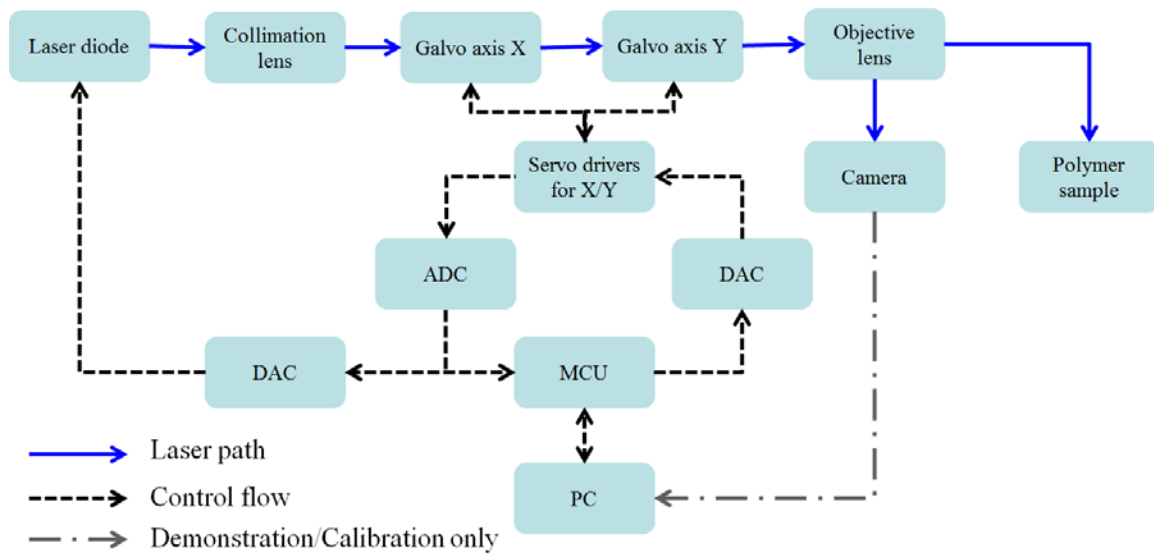


Figure 3.15. The system block diagram to show how the galvo scanning system works.

The main drawback of this galvo scanning system is the limitation of the scan speed. This system works with a step-and-hold mode: steer the laser focus spot to one location; turn on the diode laser for a short time span; then steer the laser focus to next location. This work mode fundamentally limits the scan speed. It takes 300  $\mu\text{s}$  for the galvo mirror to move and stabilize for small angle scanning, compared to the minimum laser on/off cycle time of 1.2  $\mu\text{s}$ . Therefore the amount of time required to draw an index structure is determined by the amount of scan points needed. For example, for an index structure that needs 1000 scan points and the average laser on duration for each scan point is 100  $\mu\text{s}$ , the minimum time required is 400ms.

Also the internal memory of the MCU only accepts the vector file that contains less than 2000 scan points. This limitation can be easily overcome by using an external memory. The focus spot at the polymer sample is

$$w_{spot} = \frac{\lambda f_{obj}}{\pi w_{col}}. \quad (3.14)$$

The distance for two adjacent scan spots is set to be  $0.8w_{spot}$  so that the adjacent scan spots overlap smoothly. Therefore the focal length of the writing objective lens is determined by the size of the index structure, in order to maintain the number of scan points needed around 2000.

### 3.4.2 Examples of fabricated programmable GRIN lens

So far, I have demonstrated the galvo scanning system and the procedure to calibrate the system in order to design the vector file for any arbitrary index structure. Next, I show this capability using several examples of two-dimensional programmable index structures.

The first example is a  $9 \times 9$  matrix of dots with different exposure dose through a raster scanning mode, shown in Fig. 3.16-(a). The four corner spots indicate the workable scanning area. The eight dots after the up-left corner is a binary code for each sample, shown in the white circle. Here, the binary code is set to be 104. The black spots are the location for each scan spot. The black line is the trace of the laser focus movement. This exposure pattern is through a raster scanning mode. The color scale demonstrates the exposure dose distribution. The introduced index structure is qualitatively imaged under a DIC microscope, shown in Fig. 3.16-(b).



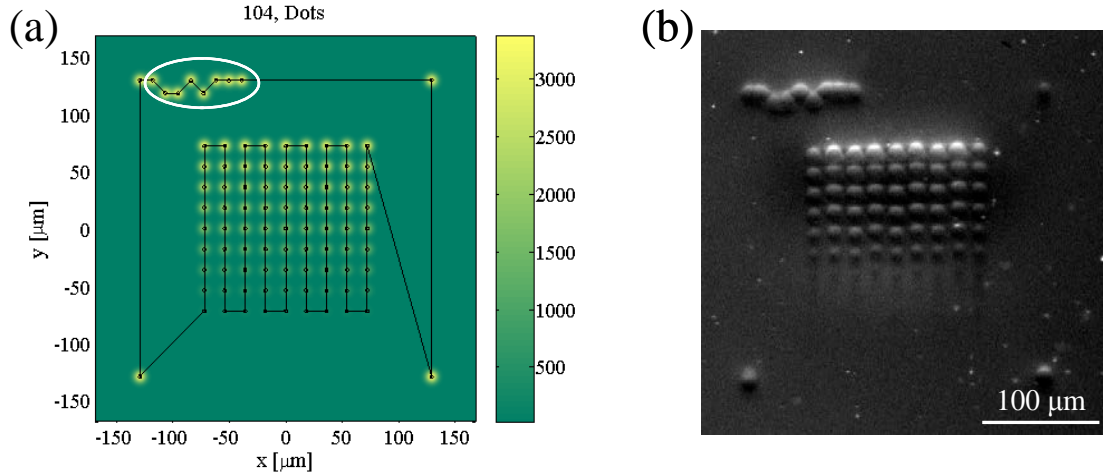


Figure 3.16. The expose pattern with a  $9 \times 9$  matrix of dots with different exposure dose in the LBR polymer. (a) represents the exposure pattern designed in MATLAB. The circled 8 dots is a binnary code used uniquely for each sample. (b) is the DIC phase image of the index profile of the exposed structure in the sample with a thickness of  $200\mu\text{m}$ . The sample is not pre-cured. The last two arrays of dots are almost invisible due to the oxygen threshold effect.

I used a spiral scanning mode, especially for circularly symmetric index pattern. Two examples are shown here, one is a square index pattern and the other is a double parabolic index pattern, shown in Fig. 3.17 and Fig. 3.18 respectively.

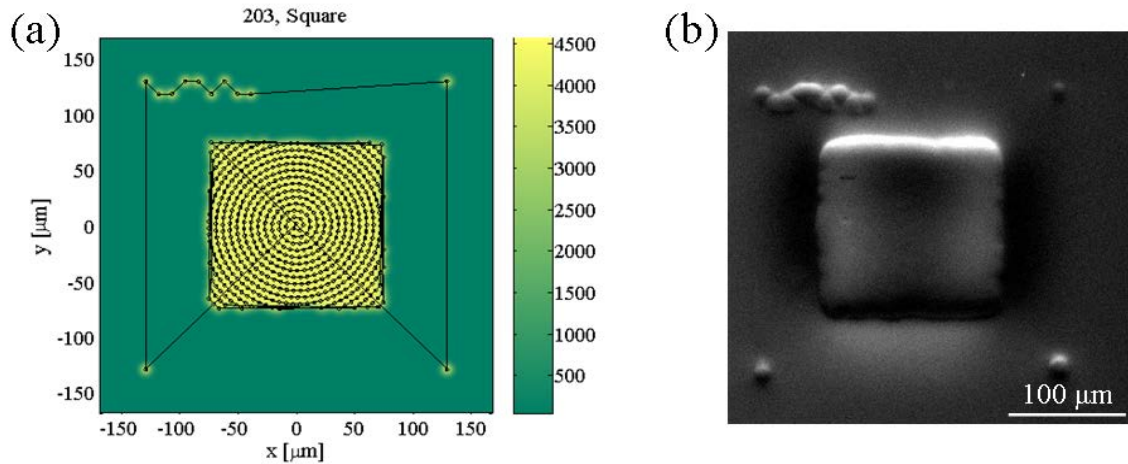


Figure 3.17. The exposed square pattern in the LBR polymer. (a) represents the exposure pattern designed in MATLAB. (b) is the DIC phase image of the index profile of the exposed structure in the sample with a thickness of  $200\mu\text{m}$ .

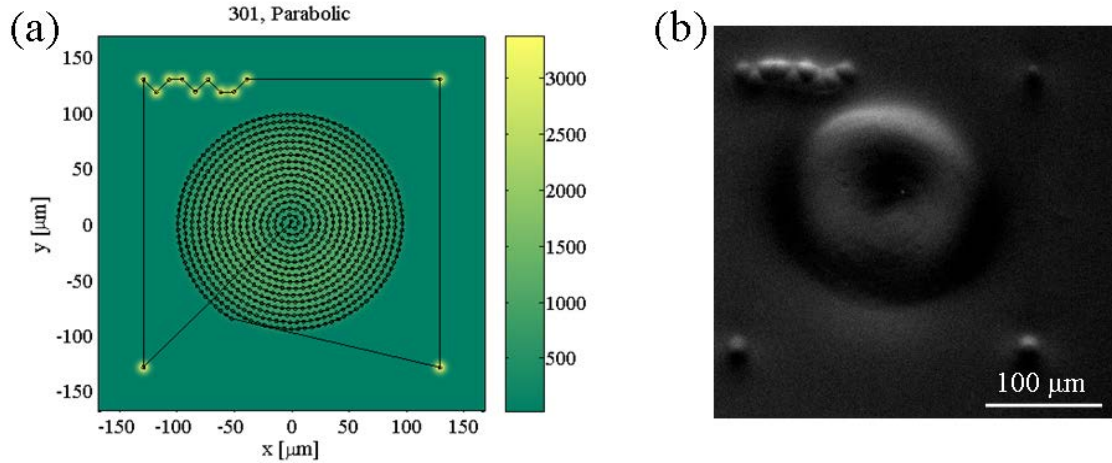


Figure 3.18. The exposed double parabolic pattern in the LBR polymer. (a) represents the exposure pattern designed in MATLAB. (b) is the DIC phase image of the index profile of the exposed structure in the sample with a thickness of 200μm.

### 3.5 Quantitative index measurement with a Shack-Hartmann wavefront sensor

I introduced a modified transmission scanning phase microscope in chapter 2 to quantitatively measure the index profile of the GRIN lens. This phase microscope is naturally integrated into the fabrication setup for convenient process monitoring. However, this testing method is slow due to its raster scanning nature. Here I use a Shack-Hartmann wavefront sensor to quantitatively characterize the index profile of the arbitrary structures. The Shack-Hartmann wavefront sensor is convenient to use and provides a two dimensional index profile within a second. A brief introduction to the Shack-Hartmann wavefront sensor is shown in Appendix B.

#### 3.5.1 Design of the testing setup

The setup to make transmission measurement for the index profile of the fabricated GRIN lenses is shown in Fig. 3.19. The main elements includes (1) a laser source that is spatially filtered and collimated to illuminate the GRIN lens under test, (2) a reimaging component and (3) a Shark-Hartmann wavefront sensor. The magnification of the reimaging component is chosen to match the sizes of the lens and the sensor. The specifics of the test setup are listed in Table 3.5.

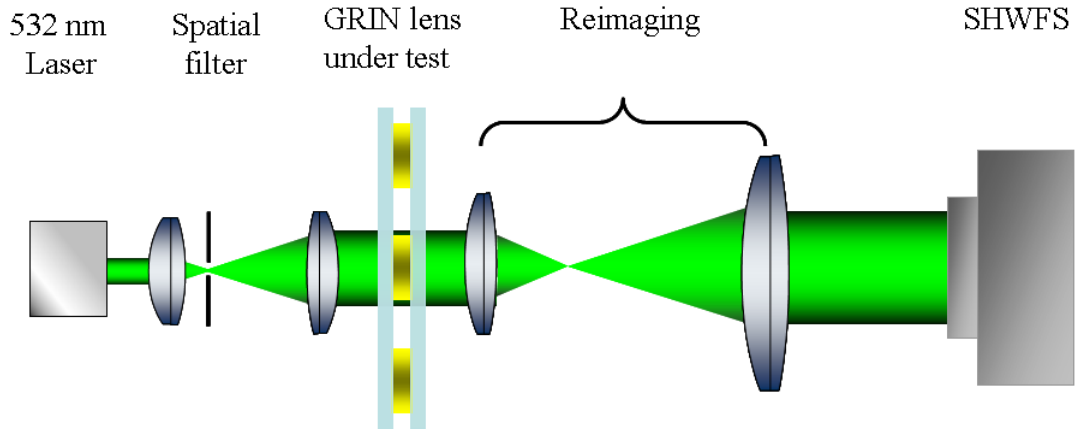


Figure 3.19. The optical layout of the setup for testing the index profile of fabricated GRIN lenses using a Shack-Hartmann wavefront sensor.

Table 3.5: The list of parameters of the index measurement setup

Parameter	Symbol	Value
Magnification of the testing system	M	2.5
Lenslet focal length [mm]	L	4.579
Lenslet diameter [mm]	d	0.108
Number of lenslet in x direction	$N_x$	62
Number of lenslet in y direction	$N_y$	49
Pixel size [ $\mu\text{m}$ ]	p	5.2
Number of pixels of CCD in x direction		1280
Number of pixels of CCD in y direction		1024

### 3.5.2 Examples of the measurement results

Here I show two examples of the measurement results using the wavefront sensor setup. First, I validated this testing by measuring an off-the-shelf plano-convex singlet lens. The measured optical path delay (OPD) profile fits the known surface profile with an error of 5%. The off-the-shelf singlet lens is Newport KPX211AR.14, with a focal length of 500mm. The measured wavefront slope distribution and wavefront profile are shown in Fig. 3.20. The comparison of the measured optical path delay profile with the calculated one from the surface profile is shown in Fig. 3.20-(c).

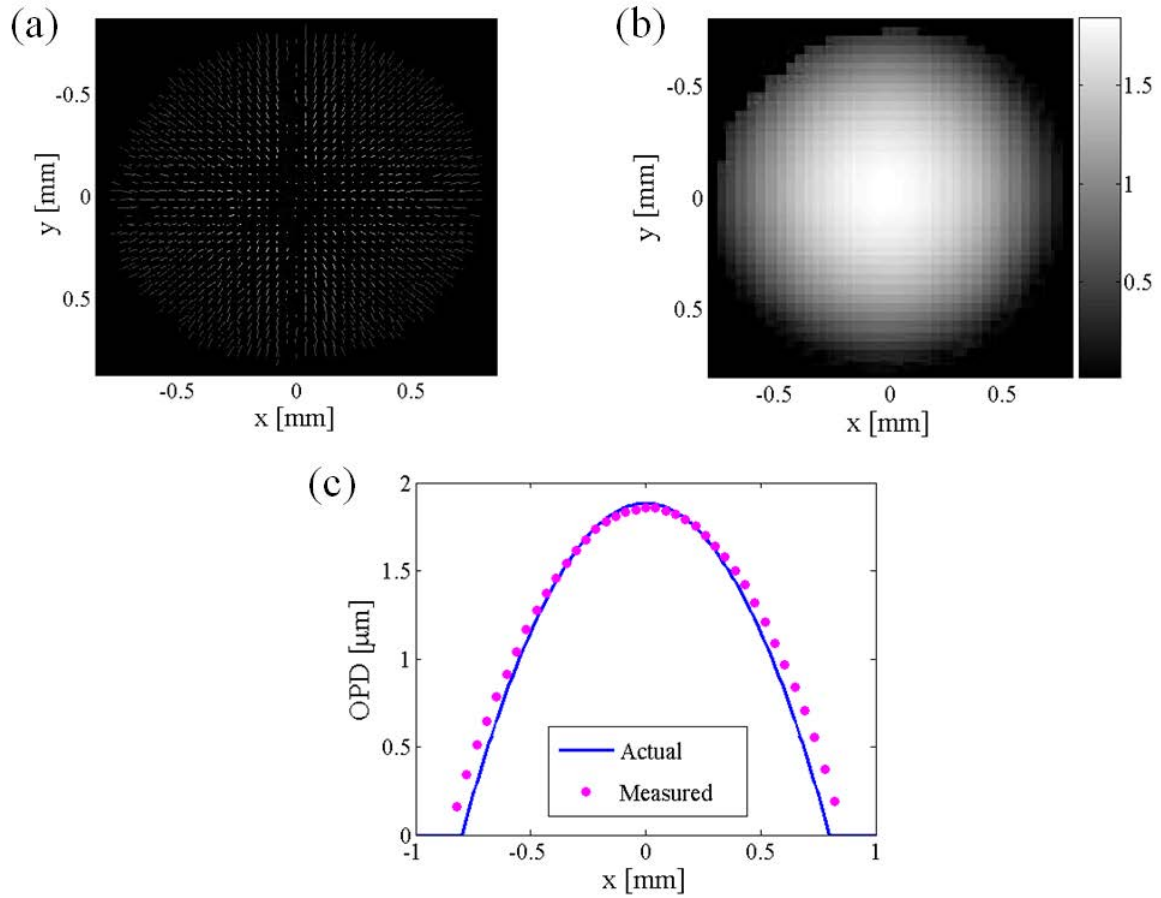


Figure 3.20. Confirmation of the accuracy of the (a) is the measured wavefront slope of the off-the-shelf plano-convex singlet lens. (b) is the reconstructed wavefront surface of the lens. (c) is the comparison between measured optical path delay profile and the calculated one from the surface profile.

Here, I show one example for the measured index profile of fabricated GRIN lens using the galvo scanning system is shown in Fig. 3.21. The wavefront sensor measures the relative optical path delay (OPD) due to the index variance or thickness variance in the sample. Given that thickness of the GRIN lens sample is uniform and assume that the index profile of the fabricated GRIN lenses is uniform in depth, the index profile equals the measured OPD divided by the thickness of the lens.

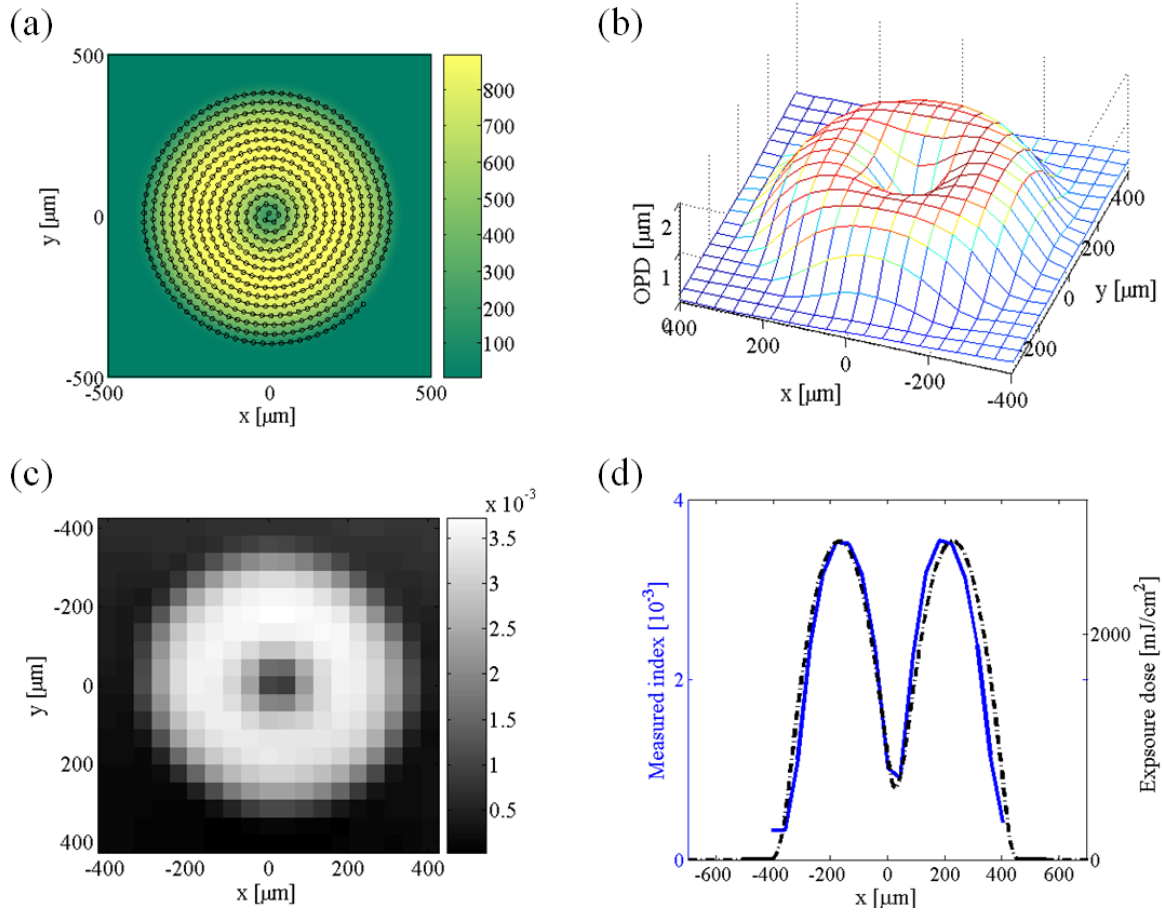


Figure 3.21. One example of measured index profile the fabricated GRIN lens by the galvo scanning system. The thickness of the sample is 1mm and the sample is not pre-cured. (a) is the rendered exposure pattern for a double parabolic lens. (b) is the measured optical path delay (OPD) from the Shack-Hartman sensor. (c) is the calculated index profile based on the measured OPD and the thickness of the GRIN lens. (d) is the x-cross section of the exposure pattern and the measured index profile.

### 3.6 Conclusion

This chapter demonstrated our ability to fabricate GRIN structures with arbitrary index profiles in the new LBR polymer. First, I have derived an index formation model in the LBR polymer based on index structures with size of hundred micrometers formed in the polymer. The index formation model shows that the introduced index structures is determined linearly by the photoinitiator consumption distribution and an oven baking process after the exposure reinforces

the exposure pattern without changing the index shape. This index formation model simplifies the design of the fabrication process to make arbitrary index structures in the LBR polymer.

Second, I have demonstrated in this chapter a method to fabricate GRIN lenses with programmable index profiles using a galvo scanning system and a quantitative index measurement using a Shack-Hartman wavefront sensor. The galvo scanner draws a two dimensional dose distribution in the polymers sequentially. This method can also be used to fabricate three dimensional structures through layer-by-layer exposure by moving the sample in z direction. Although the scanning speed of the galvo scanner may limit the scanning spots for each GRIN structure, this method is more convenient than static masks and cheaper than DMD modulators. Furthermore, the galvo scanner can be used at some special applications that other method may have difficulties.

One exemplar context is to fabricate a fan-out waveguide array by a layer-by-layer exposure using the galvo scanner, shown in Fig. 3.22. Since the intensity distribution of each scanning spot is a smooth Gaussian shape. Similar to the parallel direct-write waveguide fabrication discussed in chapter 5, the Gaussian laser spot in the galvo scanning system can introduces symmetric waveguides. Except that the parallel direct-write draws each waveguide separately, while the galvo scanner draws the waveguide array at the same time through layer-by-layer exposure. The thickness of each layer (the movement in z direction for each layer) should be within a Rayleigh range to produce a smooth transition between two layers. Generally, the size of a single-mode waveguide is around several microns, while the pixel size of DMD modulator is normally over  $15\mu\text{m}$ . It is difficult for the DMD modulator to fabricate structures that have such fine resolution over large area.

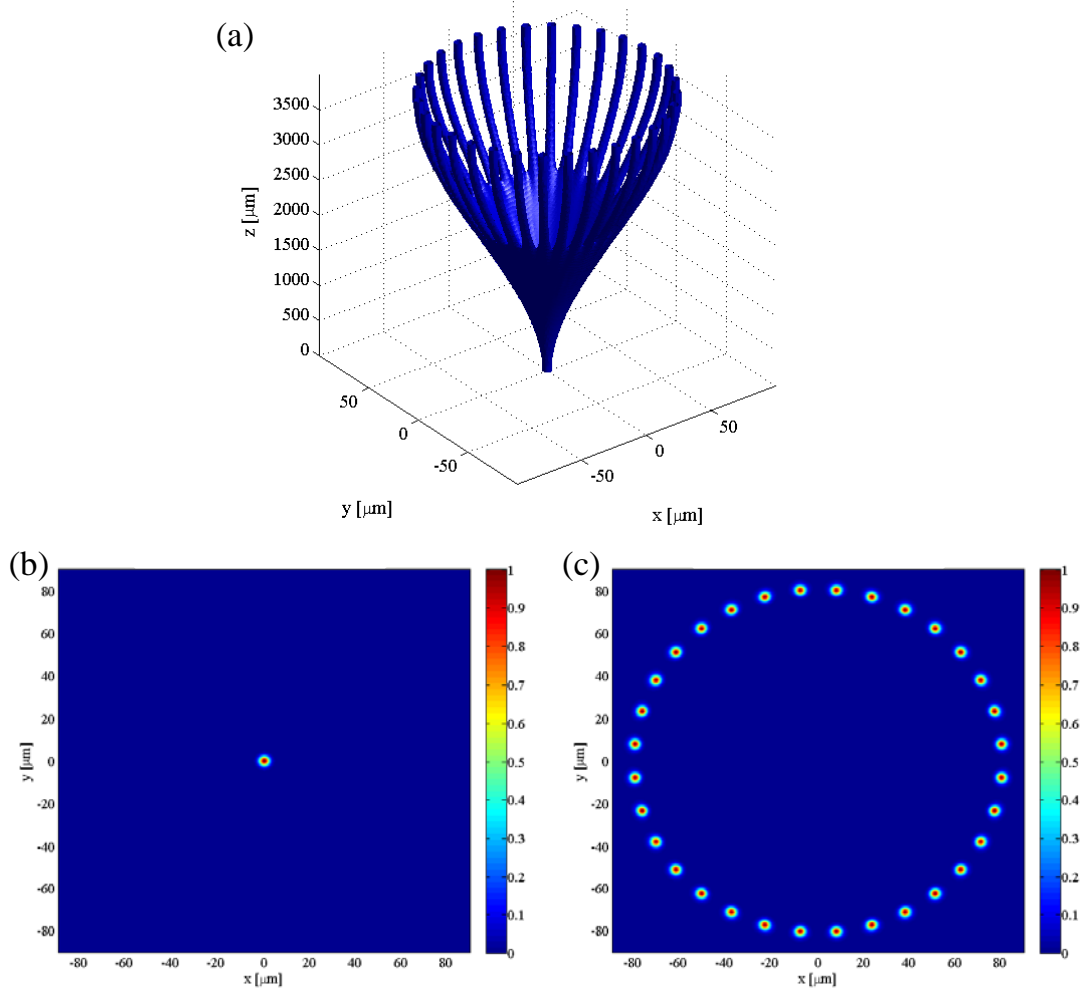


Figure 3.22. Demonstration of the fan-out waveguide array that can be fabricated using the galvo scanning system through a layer-by-layer exposure. (a) is the simulated index profile of the fan-out waveguide array. (b) is the simulated exposure pattern that the galvo scanner drew for the first layer, where  $z=0\mu\text{m}$ . The colorbar indicates the normalized exposure dose. (c) is the simulated exposure pattern that the galvo scanner drew for the last layer, where  $z = 4000\mu\text{m}$ .

# Hybrid GRIN Axicon Lens Fabricated in the LBR Polymer

### 4.1 Introduction

This chapter demonstrates a potential application of a hybrid GRIN axicon lens in endoscope micro-optical coherent tomography ( $\mu$ OCT) [90]. This hybrid GRIN axicon lens significantly increases the depth of focus (DOF) by combining a GRIN phase plate with a commercial glass GRIN rod lens to form a quasi-diffraction-free beam and an off-the-shelf glass GRIN rod lens to provide the primary focal power. The GRIN phase plate is fabricated by a rapid galvo scanning system in the LBR polymer, which is discussed in chapter 3. Two main challenges arise during the fabrication of the hybrid GRIN axicon lens. The first challenge is to design a GRIN phase plate that meets the optical performance requirements. The second challenge is to package the flexible diffusive photopolymer under a size restriction and fabricate the designed index structure in the polymer. A radial BPM program is implemented in MATLAB to optimize the index profile of the phase plate. An 8-step fabrication procedure is developed to overcome the package and fabrication challenge.

The OCT technique was invented in 1991[91] in order to provide non-invasive, high resolution, cross-sectional images for biological tissues. Unlike conventional optical imaging systems where the axial and transverse resolutions are correlated, the axial and transverse resolutions of OCTs are independently determined. More specifically, the transverse resolution of OCTs is determined by the numerical aperture (NA) of imaging lens in the sampling arm, while the axial resolution is determined by the coherence length of the light source. Broadband light sources are generally used in OCT to improve the axial resolution [92].



However the trade-off between transverse resolution and the DOF still exists as long as conventional optical elements are used. The transverse resolution is proportional to  $1/NA$ . Increasing the NA of the imaging system will increase the transverse resolution. However the DOF, defined by the full width at half-maximum (FWHM) of the modulus of the axial amplitude distribution, is proportional to  $1/NA^2$ . That means increasing the transverse resolution will degrade the DOF quickly. In practice, a large DOF is preferred and sometimes necessary in OCT applications, especially in endoscopic applications [93]. Dynamic focus compensation [3], also referred to as a zone-focusing and image-fusion technique, has been reported to overcome the limitation of a short DOF. However, this technique can only be used in low frame rate OCTs [94], which is not preferred for *vivo* imaging applications. Also, dynamic focusing lenses are bulky and cannot be used when physical space is restricted, such as in the case of endoscopic OCTs. Therefore, development of improved DOF techniques is currently an active area for the OCT research.

Several methods have been proposed in literature to improve the DOF to be used in the imaging systems. These methods include apodization and chromatic dispersion technique [90], binary-phase spatial filters [95], wavefront coding technique [96,97] and axicon lenses [98,99,100]. All the existing methods are not without their own limitations. Apodization techniques sacrifice the illumination efficiency, since part of the incident light is blocked. The wavefront coding technique, on the other hand, needs a post imaging process to computationally regain the transverse resolution across the extended DOF. Thus, this method cannot meet the frame rate requirement for *in vivo* bio-imaging. The axicon lens is so far the most effective one. This chapter will demonstrate a hybrid GRIN axicon that is fabricated in the LBR photopolymer to extend the DOF for the  $\mu$ OCT application.

The outline for the rest of the chapter is as follows. Section 4.2 introduces the axicon lenses, including the main types, fabrication methods and applications of axicon lenses. Section

4.3 describes the design process for the hybrid GRIN axicon lens. Section 4.4 elaborates the package and fabrication procedure for the hybrid GRIN axicon lens. Section 4.5 shows the test results of the hybrid GRIN axicon lens. Section 4.6 discusses the ways to improve the design and fabrication of the hybrid GRIN axicon and concludes this chapter.

## **4.2 Introduction to axicon lenses**

The axicon was introduced by John McLeod in 1954 to describe the optical element that images a point source into a line focus [101]. Later non-diffraction beams [102,103], reported by Durnin et al. enhance the researcher's interests into axicon lenses. Because of such unusual properties, axicons have been found to be very useful in many applications. Axicon is initially used in precision alignment [104], which still remains the most important application. Axicons form a long and narrow light segment along the optical axis, which serves as a reference line, providing alignment accuracy on the order of  $10^{-6}$  [105]. Other important applications include scanning optical systems, such as the supermarket bar code reader [106], laser machining [107,108], optical trapping [109,110] and nonlinear optics [111]. In the past decade, axicons have been applied to high resolution biomedical imaging to significantly extend the depth of focus [96-98,112]. From the literature, axicon lenses generally can extend the depth of focus by about 10 times over conventional systems. Researchers have already reported  $1.5\mu\text{m}$  resolution across a  $200\mu\text{m}$  DOF using an axicon lens [98].

Based on the surface profile, axicons generally can be divided into two types: linear axicons and logarithmic axicons. Linear axicons have a conical surface, such as a classical conical prism. A conical mirror is a reflection version of the classic conical prism. Logarithmic axicons have a profile of a logarithmic-curved surface [113-114]. Linear axicons provide a constant central-core width while the axis intensity is varied linearly. The logarithmic axicons provide a constant axial intensity [114, 115,116], which is very useful for optical scanning and light sectioning.

The traditional conical prisms are made through standard glass lens fabrication. Linear axicons can also be fabricated into a Fresnel surface [117, 118]. Fiber-tip axicon microlenses can be fabricated by a selective chemical etching process [119,120]. A logarithmic axicon is more difficult and more expensive to make than a linear axicon, because it is a challenge to precisely control the logarithmic surface during the fabrication. The first logarithmic axicon that is experimentally demonstrated is a holographic version [115]. Micro logarithmic axicon lens is fabricated through a femtosecond laser nanofabrication via two-photon polymerization of resins [113] and CW laser effusion [121].

The axicons described above are all fabricated in a single material and generally are surface lenses. Next, I will introduce a hybrid version of GRIN axicon lens that has similar characteristics of a linear surface axicon lens. The classical axicon prisms produce extended focus that begins at the back surface of the axicon. In OCT applications, it needs to produce a line focus that is shifted away from the back surface. The hybrid GRIN axicon I've made forms an extended DOF that is shifted 2mm away from the back surface of the lens. This hybrid GRIN axicon lens consists of two parts: a GRIN polymer phase plate and a commercial glass GRIN rod lens. The nominal focus of the GRIN rod lens provides the focal shift and the GRIN phase plate provides the extended DOF. This GRIN version of axicon lenses is easier for alignment and is cost efficient.

### **4.3 Design of the hybrid polymer GRIN axicon lens**

The hybrid polymer GRIN axicon lens I've made is applied to an endoscope Fourier domain  $\mu$ OCT[90]. This  $\mu$ OCT probe is used to image the subcellular structures of human coronary atherosclerosis. The optical layout of this endoscope OCT probe is shown in Fig. 4.1. The light is out of the single mode fiber and is collimated by a glass GRIN collimator. The hybrid GRIN axicon accepts the collimated light to form an extended DOF for imaging. By rotating the

prism reflector in the probe while pulling the probe through the coronary artery, a three-dimensional spiral image about the inside wall of the artery is formed.

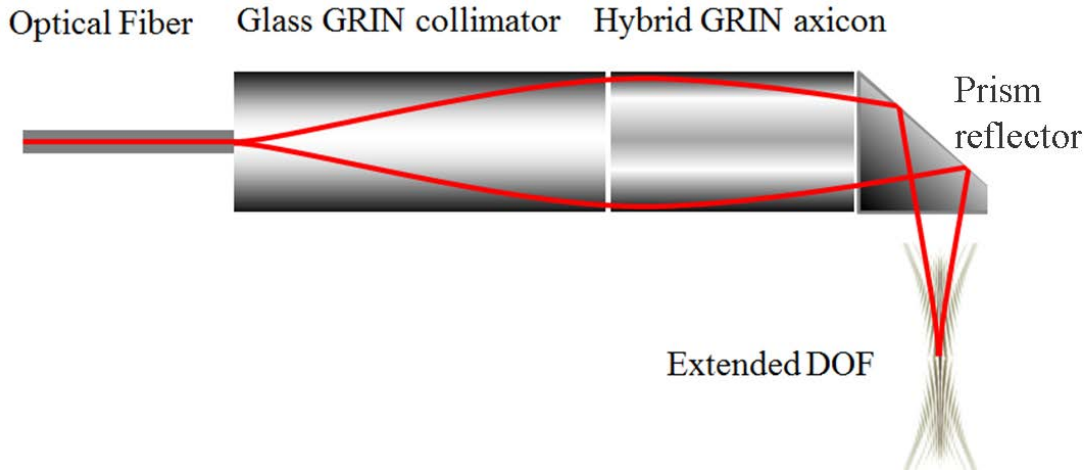


Figure 4.1. The optical layout of the endoscope OCT probe.

#### 4.3.1 Specifics of the hybrid GRIN axicon lens

We collaborate with a research group in Massachusetts general hospital (MGH) to make this OCT probe. Our responsibility is to make the hybrid GRIN axicon lens. The MGH research group will use the hybrid GRIN axicon to make the OCT probe and test its performance. The design specifications for this GRIN axicon lens are listed in Table 4.1. For a conventional optical system, given the transverse resolution  $2w_0$ , the depth of focus is  $\Delta f = \pi w_0^2 / \lambda$ , where  $\lambda$  is the wavelength of the light source. Thus, with the wavelength of 800nm and  $2w_0 = 2\mu\text{m}$ , the depth of focus  $\Delta f$  is about  $4\mu\text{m}$ . Therefore, this GRIN axicon needs to extend the depth of focus by 100 times, which is a huge challenge.

Table 4.1: Specifications of the hybrid GRIN axicon lens

Transverse resolution	2 $\mu$ m
Back focal position	2mm
Depth of focus ( $\Delta f$ )	400 $\mu$ m
Clear aperture	1mm
Length	< 9mm
Single pass transmission 600-1000 nm*	>70%

#### 4.3.2 Design of the GRIN axicon lens

In this section, I first demonstrate a thin-lens version of the GRIN axicon design. Then I move to a hybrid version. The first step in the design process of a GRIN axicon is to determine the refractive index profile necessary for a radial gradient lens to produce an extended DOF. The object distance is infinite for the design. Also, the GRIN axicon offsets the line focus from the back surface. The index profile is derived with geometrical optics and an optical path length (OPL) argument. This method is demonstrated by Charman to determine the index profile for concentric varifocal lenses [122]. The same method has also been reported by Fisher to determine index profile of a GRIN axicon [123]. The thin-lens design procedure demonstrated here is based on Fisher's method.

---

\* The single pass transmission > 70% here means that less than 30% off the incident collimated Gaussian beam is chopped off by the hybrid GRIN axicon lens.

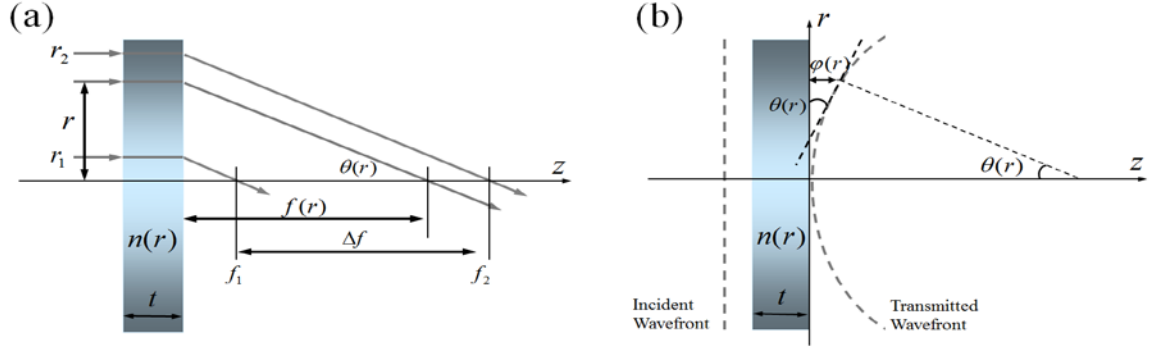


Figure 4.2. Parameters used to derive the index profile of a thin GRIN axicon.

The GRIN axicon lens has a planar surface with a radial gradient index profile. When the incident light is collimated and perpendicular to the GRIN lens, by geometrical ray tracing, the back focal length is proportional to the incident ray height, shown in Fig. 4.2. Thus, the back focal length can be expressed as,

$$f(r) = f_1 + \frac{r - r_1}{r_2 - r_1} \Delta f \quad (4.1)$$

where  $r$  is the radial ray position,  $r_{1,2}$  is the minimum and maximum incident ray heights allowed,  $f_{1,2}$  is the back focal length for the ray height of  $r_{1,2}$ ,  $\Delta f$  is the depth of focus that is equal to  $f_2 - f_1$ , and  $n(r)$  is the radial gradient index profile.

Assuming the GRIN axicon is a thin lens, the incident light experiences a negligible beam displacement through the lens. This assumption allows the index profile of the lens to be determined by the optical path argument. The radial ray position at the emerging wave front is then considered equal to the input position, expressed as  $n(0)t = n(r)t + \phi(r)$ , where  $\phi(r)$  is the wavefront displacement at the radial ray position  $r$ ,  $t$  is the thickness of the lens. Therefore the index profile of the lens is

$$n(r) = n_0 - \frac{\phi(r)}{t}, \quad (4.2)$$

where  $n_0$  is the index of refraction at the center of the lens. The slope of the transmitted wavefront is given by

$$\tan(\theta) = -\frac{d\varphi(r)}{dr}. \quad (4.3)$$

Given the geometrical ray angle is equal to the slope of the wavefront normal, and assuming the wavefront displacement  $\varphi(r)$  is much smaller than the back focal length  $f(r)$ , the slope of the transmitted wavefront is

$$\tan(\theta) = -\frac{d\varphi(r)}{dr} = \frac{r}{f(r)}. \quad (4.4)$$

The wavefront displacement  $\varphi(r)$  is determined to be

$$\varphi(r) = \int_{r_1}^{r_2} \frac{r}{f(r)} dr. \quad (4.5)$$

Replacing  $f(r)$  with Eq. 4.1, the wavefront slope can be expressed as

$$\varphi(r) = \frac{r_2 - r_1}{\Delta f} r - \left( f_1 - \frac{r_1}{r_2 - r_1} \Delta f \right) \left( \frac{r_2 - r_1}{\Delta f} \right)^2 \ln \left[ f_1 + \frac{\Delta f}{r_2 - r_1} (r_2 - r_1) \right] \Bigg|_{r_1}^{r_2}. \quad (4.6)$$

Substituting  $\varphi(r)$  with Eq. 4.2 in Eq. 4.6, and assuming no central obscuration,  $r_1 = 0$ , the index profile can be simplified to be

$$n(r) = n_0 - \frac{r_2}{t(\Delta f)^2} \left[ r \Delta f - r_2 f_1 \ln \left( 1 + \frac{r \Delta f}{r_2 f_1} \right) \right]. \quad (4.7)$$

To illustrate this thin-lens design, I discussed two special cases from Eq. 4.7. The first case is when the design is reduced to be a unifocal lens and the index profile is

$$\lim_{\Delta f \rightarrow 0} n(r) = n_0 - \frac{1}{2t f_1} r^2. \quad (4.8)$$

In this case, the lens has a quadratic radial-gradient index profile and a back focal length of  $f_1$ .

The other case is when the focus begins at the back surface of the lens, and the index profile is

$$\lim_{f_1 \rightarrow 0} n(r) = n_0 - \frac{r_2}{t \Delta f} r. \quad (4.9)$$

In this case, the index profile has a linear form, which is similar to a classic conical axicon prism.

Now I use this thin-lens design method to calculate the index profile of the GRIN axicon that meets the specs in Table 4.1. The thickness of the GRIN axicon is chosen to be  $t = 5\text{mm}$ . The bulk index of refraction of the LBR is approximately 1.5. Other parameters are:  $f_1 = 1.8\text{mm}$ ,  $\Delta f = 400\mu\text{m}$  and the  $r_1=0$ ,  $r_2 = 500\mu\text{m}$ . The calculated index profile based on the thin-lens design from Eq. 4.7 is shown in Fig. 4.3.

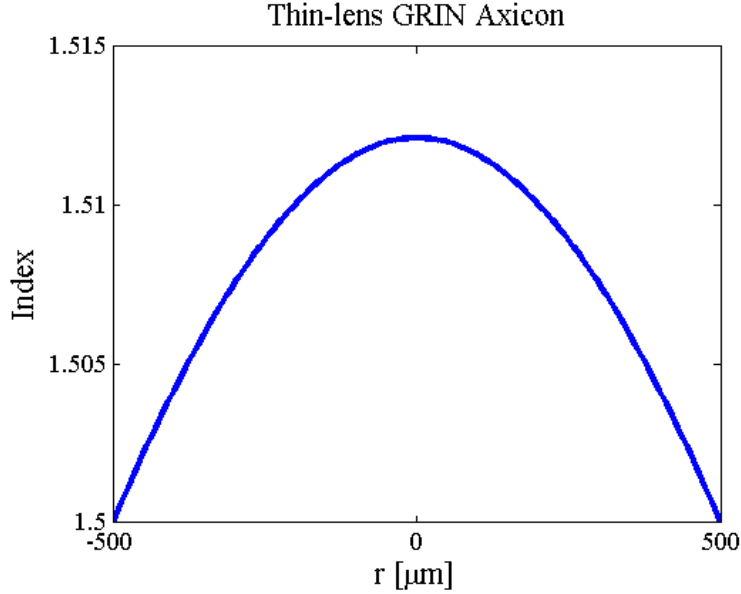


Figure 4.3. The index profile of the derived thin-lens GRIN axicon to meet the specifics

The calculated peak index change required for the GRIN axicon lens is 0.012. However the maximum index change that can be potentially achieved in the LBR polymer is about 0.008 based on the material characterization that is discussed in chapter 3. Also, since the calculated GRIN axicon is a lens with a large index change and a thickness of 5mm, it might invalidate the thin-lens assumption. A radial beam propagation method is implemented in MATLAB to simulate the performance of the GRIN axicon with the index profile shown in Fig. 4.4. The back focal distance from the simulated intensity distribution is  $\sim 1\text{mm}$ . The DOF from the simulation that meets the required specs is about  $\sim 120\mu\text{m}$ . The way to calculate the DOF will describe in detail in Sec. 4.3.3.



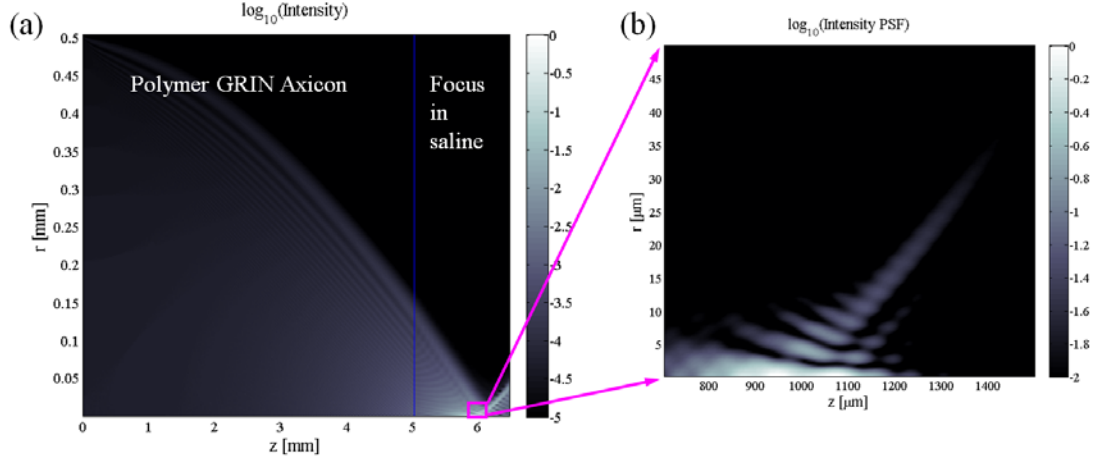


Figure 4.4. The simulated intensity distribution of the thin-lens GRIN axicon lens. (a) shows the GRIN axicon lens focusing the incident Gaussian beam  $\sim 1$ mm away from the back of the lens while (b) is the intensity distribution in the focus region.

In summary, the thin-lens design method is not proper for designing the index profile of the GRIN axicon because the index change from the thin-lens design exceeds the material capability. Furthermore, the derived GRIN axicon does not meet the design specifications and invalidates the thin-lens assumption.

However the calculated index profile from this thin-lens design method does provide the inspiration for a hybrid design of the GRIN axicon. The reader might already notice that the index profile of the thin-lens GRIN axicon looks very close to a parabolic curve. Using a series expansion, Eq. 4.7 can be expressed as

$$n(r) = n_0 - \frac{1}{2tf_1}r^2 + \frac{\Delta f}{2r_2^2tf_1^2}r^3 - \frac{\Delta f^2}{4r_2^2tf_1^3}r^4 + \dots \quad (4.10)$$

The first two terms on the right hand of Eq. 4.10 are the same as the right hand of Eq. 4.8. These two terms describe the primary focal power of the lens that provides the offset of the focal region from the back surface. The remaining terms can be treated as phase aberration for the parabolic lens. Similar to theory of using an aberrated lens system [124], this phase aberration extends the DOF. Therefore I can design a hybrid GRIN axicon lens by utilizing an off-the-shelf GRIN rod

lens to provide the primary focal power and a polymer GRIN phase plate to extend the DOF, shown in Fig. 4.5.

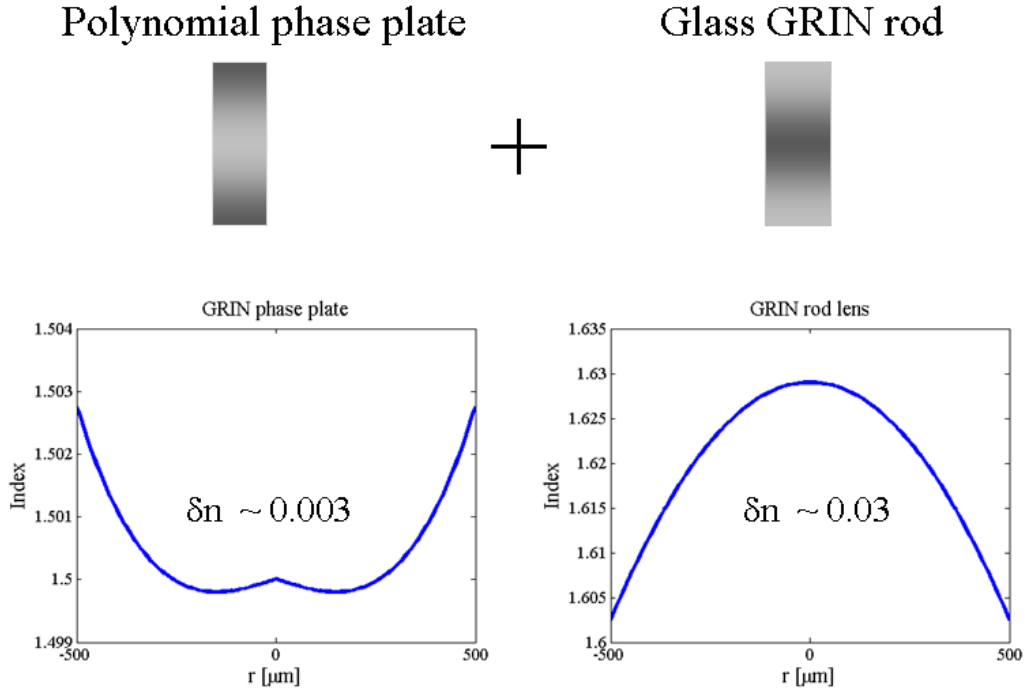


Figure 4.5. Demonstration of the design of the hybrid GRIN axicon lens.

The commercial GRIN rod lens used here is from Edmund optics, part# NT64-525. The index profile of this GRIN rod lens is

$$n = 1.629 - 0.107r^2 + 4.4 \times 10^{-3}r^4, \quad (4.11)$$

where  $r$  is measured in millimeter. The polynomial index profile of the GRIN phase plate is expressed as

$$n = n_0 + n_1r + n_2r^2 + n_3r^3, \quad (4.12)$$

where  $n_0$  is the bulk refractive index of the LBR polymer with a value of approximately 1.5.

Through an optimization process, the index profile of the polymer phase plate becomes

$$n = 1.5 - 0.002r + 0.03r^3, \quad (4.13)$$

where  $r$  has a unit of minimeter. The index profile optimization of the polymer phase plate will be discussed in Sec. 4.3.3. The optimized index profile of the phase plate is shown in Fig. 4.5. Now the peak index change of the polymer GRIN phase plate is only 0.003, which is in the linear index formation region from the material modeling in chapter 3.

### 4.3.3 Index profile optimization of the polymer GRIN phase plate

This section will demonstrate a radial BPM program that is implemented in MATLAB to optimize the index profile of the phase plate. The three parameters  $n_1$ ,  $n_2$  and  $n_3$  in Eq. 4.12 are varied while the simulated point spread functions across the focus region from the BPM program are characterized to calculate the DOF. The goal of the optimization is to find the largest DOF in the three-dimensional search space defined by parameters  $n_1$ ,  $n_2$  and  $n_3$ .

The depth of focus is defined as the axial extent of the focus region that meets four requirements: (1) The transverse resolution is less than 2  $\mu\text{m}$ ; (2) The fractional encircled power is more than 4.5%. The fractional encircled power is the ratio of the power carried by the central lobe within the  $1/e^2$  beam radius to the total power of the Bessel field; (3) The intensity drops less than -20 dB compared with the peak intensity before the focal position and the intensity drops less than -6dB compared with the peak intensity after the focal position; (4) The ratio of the peak intensity between the first side lobe and the main lobe at 800 nm is less than 0.17.

Professional optical design software, such as Zemax, is typically used to optimize optical systems. However the polynomial index profile of this phase plate requires a custom-made Zemax dll file. Also, the Zemax cannot evaluate the given specifications for calculate the DOF. Finally, I show that the DOF is an ill-conditioned merit function in that it is discontinuous in the search variables  $n_1$ ,  $n_2$  and  $n_3$ . This defeats the deterministic gradient optimization methods built into Zemax. In summary, the GRIN axicon design problem is not well-matched to commercial ray-tracing optimization software such as Zemax.

Thus I used a radial BPM program written in MATLAB to simulate the performance of the hybrid GRIN axicon lens. The simulation space is shown in Fig. 4.6-(a). The phase plate has a thickness of 2mm and a third-order polynomial index profile. The window has a thickness of 0.5 mm and uniform index of refraction of 1.515. The GRIN rod lens has a thickness of 2.5mm and an index profile from Eq. 4.11. The tissue-filled region behind the OCT endoscope probe is modeled as a saline solution with a refractive index of 1.33.

Since the index distributions of the phase plate and the GRIN rod lens are all circularly symmetric, a Fourier split-step BPM program implemented in polar coordinates is used to optimize the index profile of the phase plate to gain the maximum DOF. This radial BPM method use Hankel transforms of zero order based on a Fourier-Bessel series expansion [125]. Figure 4.6-(b) shows the intensity of the Gaussian beam that propagates through the index distribution setup shown in Fig. 4.6-(a). The radius of the Gaussian beam is chosen so that 70% of the beam intensity will pass through the clear aperture of 1mm. This truncated Gaussian beam goes through the polymer GRIN phase plate, the window and the GRIN rod lens to focus in the saline solution 2mm from the back surface of the GRIN rod lens.

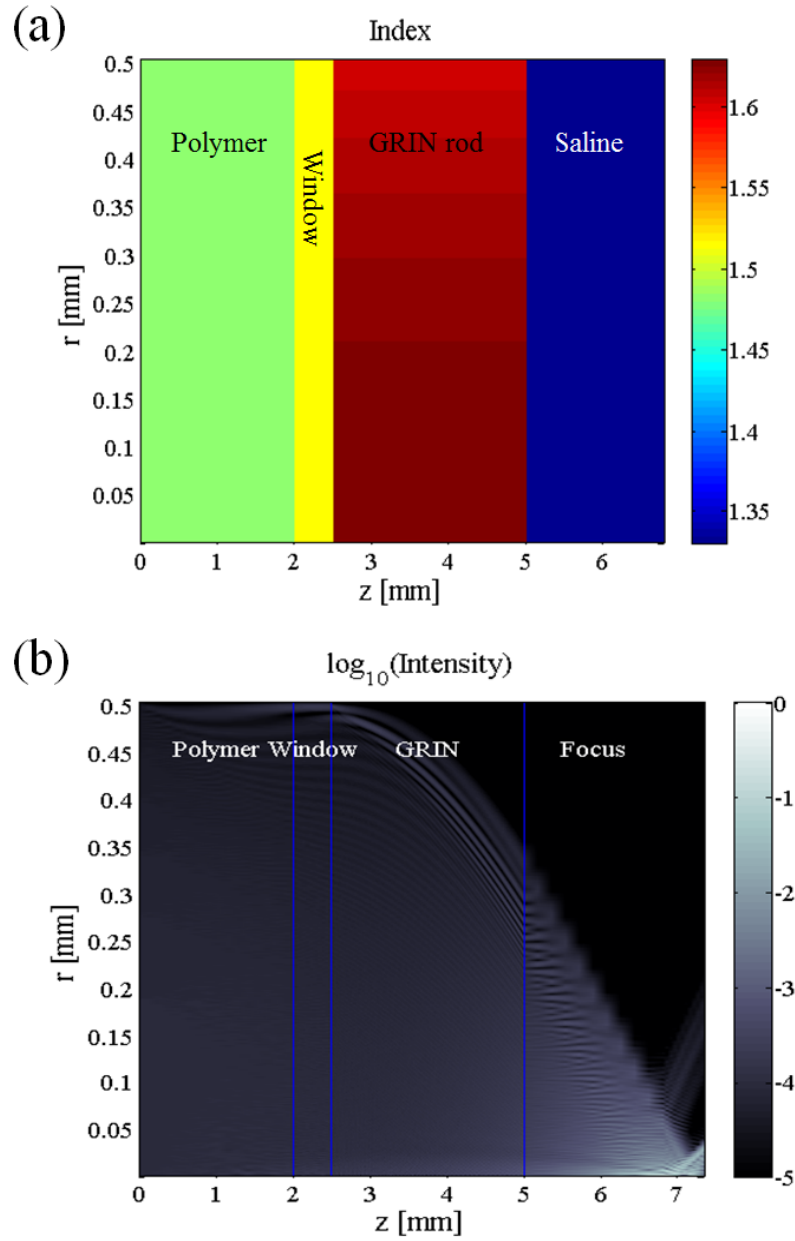


Figure 4.6. Simulation of the index profile optimization of the GRIN phase plate through a MATLAB simulation program. (a) is the index distribution setup for the simulation. (b) is the simulated intensity distribution of the hybrid GRIN axicon lens.

Now zoom in the focus region to see the point spread function characteristics, show in Fig. 4.7.  $Z$  is the back focus distance across the focus region. The DOF is calculated based on the intensity distribution cross the focus region.

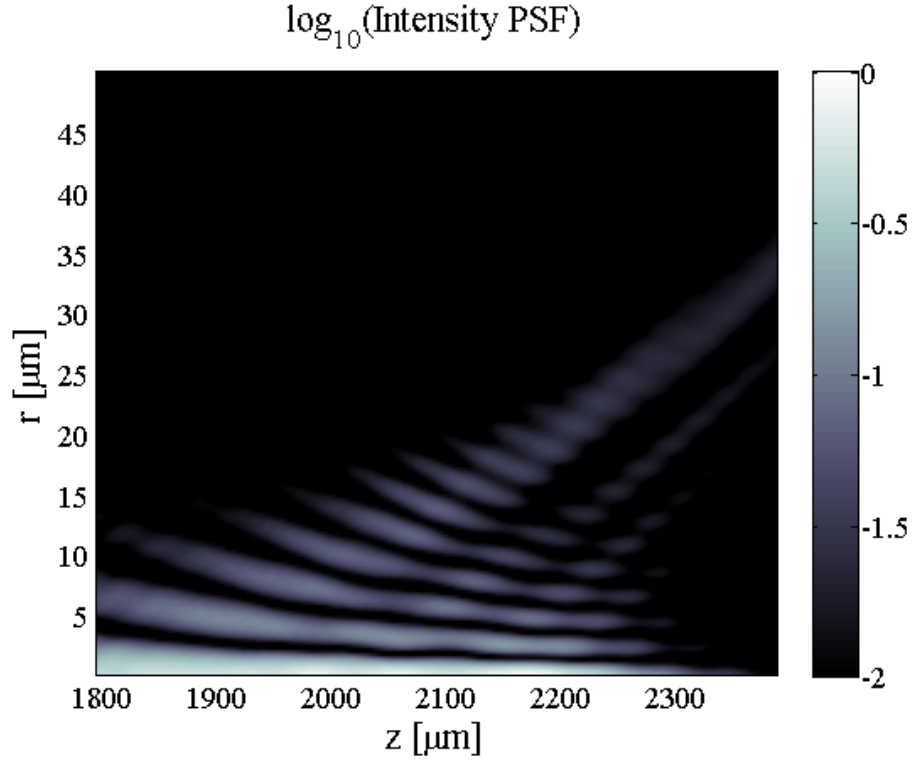


Figure 4.7. The simulated intensity distribution at the focused region of the hybrid GRIN axicon lens

As discussed before, the DOF is defined as the length, in  $z$ , where the focus region meets the four requirements. I marked the focus regions that meet each of the four requirements respectively, shown in Fig. 4.8. The red region in Fig 4.8-(a) is the focus region that has a transverse resolution less than  $2\mu\text{m}$ . The transverse resolution is defined as the FWHM of the main lobe of the intensity distribution in the focus region. The green region in Fig. 4.8-(b) is the focus region that meets the fractional encircled power specification. The pink region in Fig 4.8-(c) is the focus region that meets the on axis peak intensity requirement. The blue region in Fig. 4.8-(d) is the focus region that meets the side lobe ratio requirement.

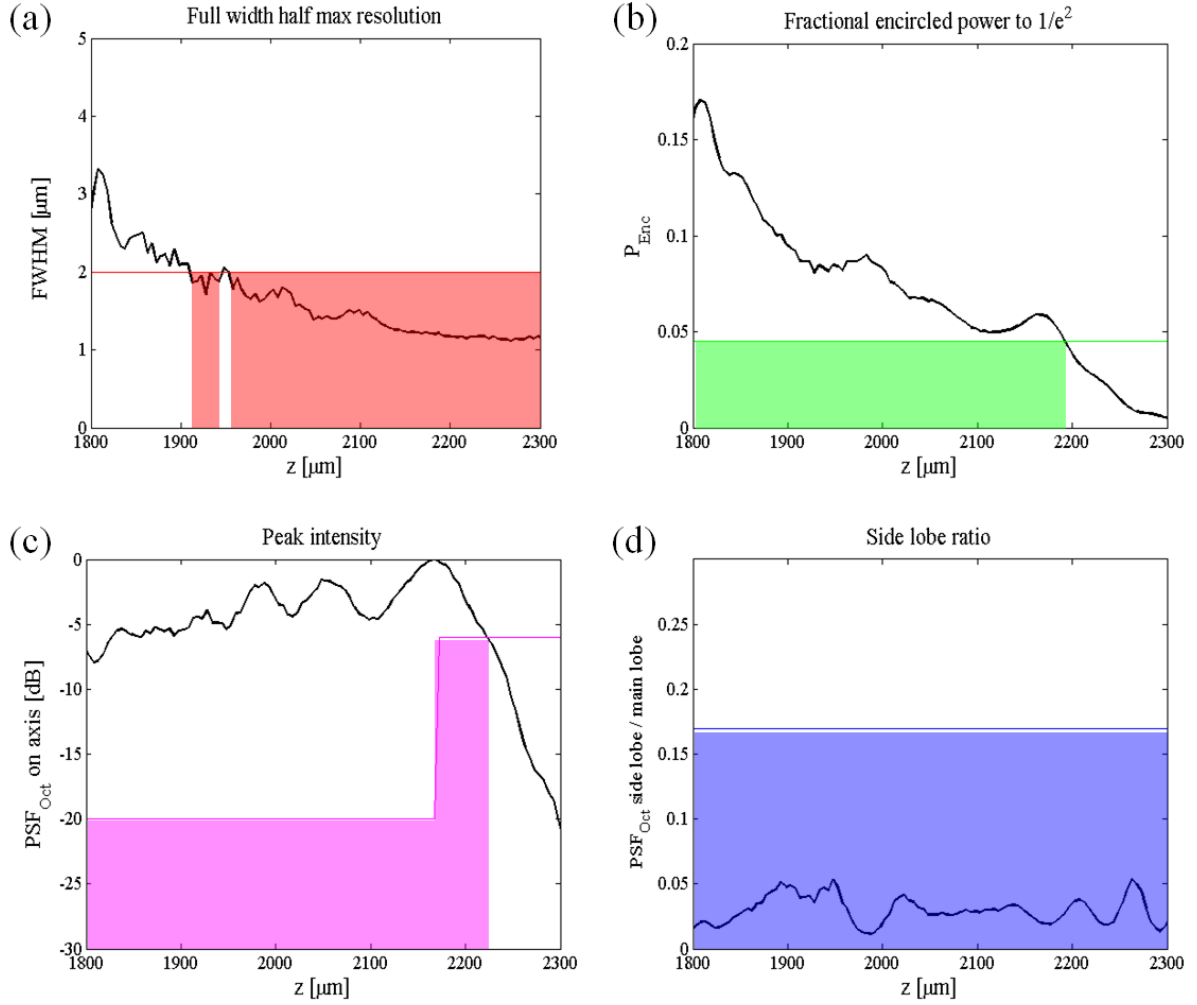


Figure 4.8. Demonstration the four requirements to defined the DOF.

The DOF of the simulated lens is shown in Fig. 4.9, which meets all the four requirements. As can be seen in Fig. 4.8-(a), small oscillations in the point spread functions (PSFs) cause the DOF to be discontinuous in lens specs, defeating deterministic optimizers. Thus, a direct search method is used to calculate the DOF while varying the parameters  $n_1$ ,  $n_2$  and  $n_3$  in Eq. 4.12.

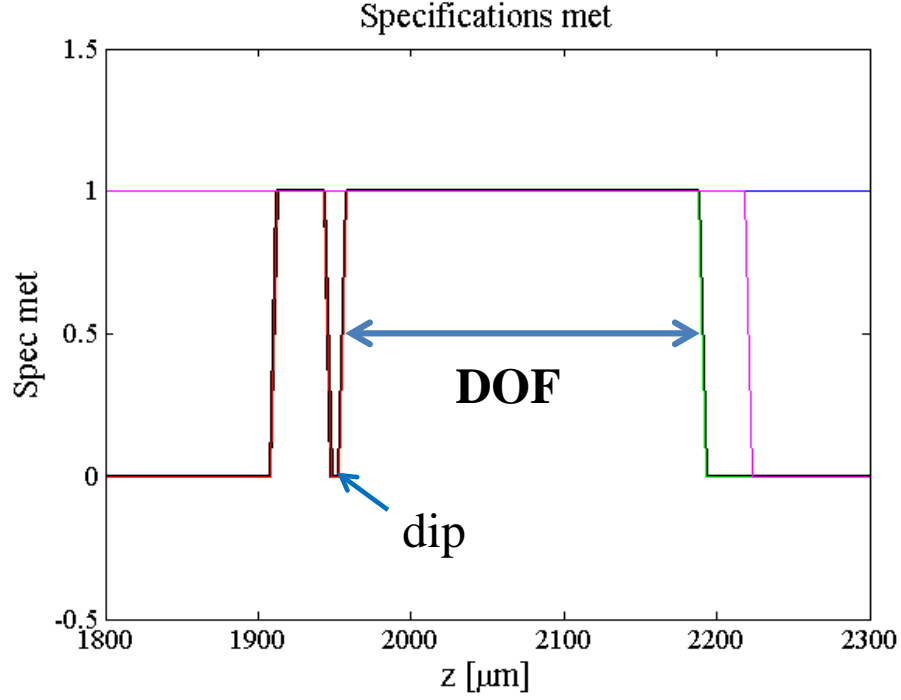


Figure 4.9. The region that is defined as the DOF. The dip at  $\sim 1950\mu\text{m}$  is due to the slight oscillation for meeting the transverse resolution shown in Fig. 4.8-(a).

The direct searching results are shown in Fig. 4.10. Several restrictions are placed during the direct searching: (1) the allowed peak index change is less than 0.005; (2) all the thicknesses are fixed; (3) the polynomial index curve is only to third orders. These restrictions reduce the researching time but limiting the searching space.

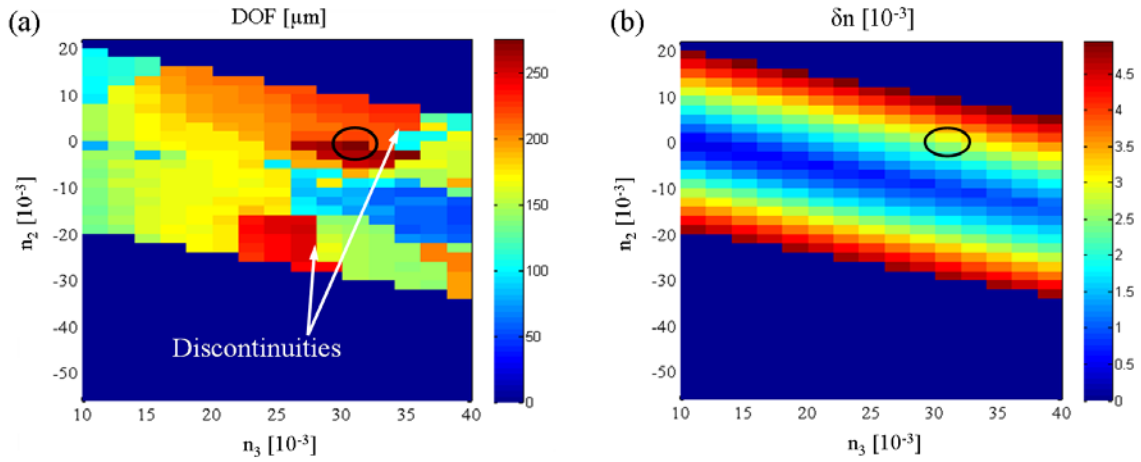


Figure 4.10. Demonstrate the direct search results for optimized the index profile of the GRIN phase plate.



The best result is the circled one with the DOF of  $\sim 275\mu\text{m}$  and the peak index of 0.003. The optimized index profile is shown in Fig. 4.11. I brought the edge of the optimized index profile down in order to practically make this index structure in the diffusive polymers. Next section, I will show the procedure to fabricate the polymer GRIN phase plate and assemble with the GRIN rod lens to form the hybrid GRIN axicon lens.

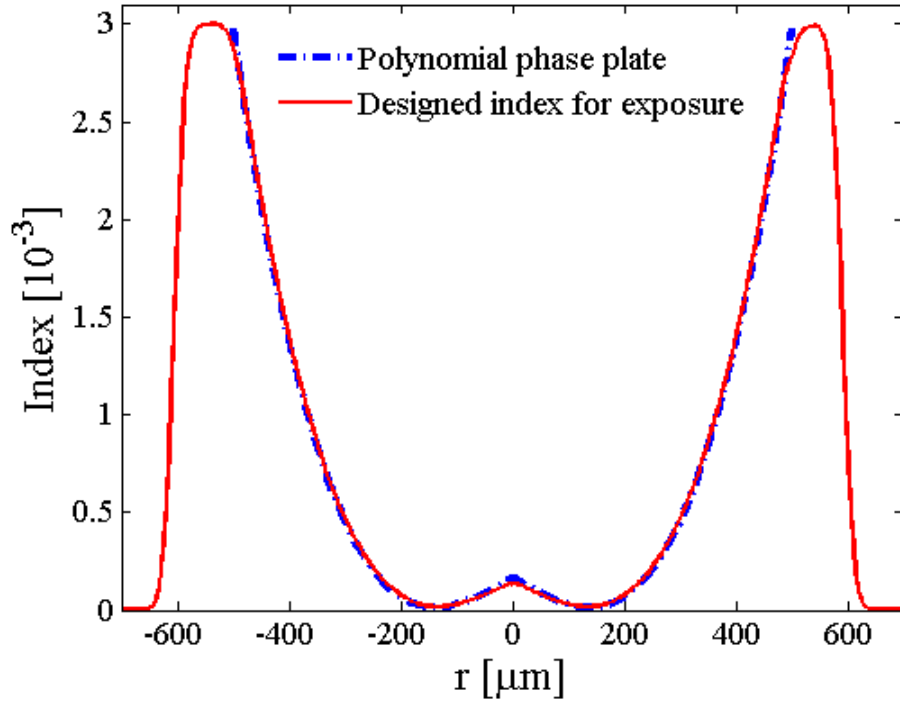


Figure 4.11. Index profile for the GRIN phase plate design. The blue dash line is the optimized index profile of the GRIN phase plate from the MATLAB simulation. The red solid line is the designed index profile for the galvo scanner to fabricate in the polymer sample.

#### 4.4 Fabrication of the hybrid GRIN axicon lens

So far, I have demonstrated the design process for the hybrid GRIN axicon lens in the last section. The required index profile for GRIN phase plate is shown in Fig. 4.11. How to fabricate this hybrid GRIN axicon lens is the remaining challenge. In this section, I first elaborate the packaging and fabrication procedure. Then I explain why I used this procedure, which includes a

discussion of the problems that emerged during the package and fabrication process and the corresponding solutions.

#### 4.4.1 Fabrication procedure

The lens geometry of the hybrid GRIN axicon I've made is shown in Fig. 4.12. The polymer material is cast into an aluminum tube with an inside diameter of 1.5mm. Two glass windows with thickness of 0.5mm are attached to the aluminum tube using the polymer itself as the adhesive. After the index structure is formed in the polymer and the index profile is quantitatively measured, a commercial GRIN rod lens, NT64-525 from Edmund Optics, is attached to the GRIN phase plate with a UV-cured polymer. This GRIN rod lens is polished from the length of 4.34mm down to 2.5mm.

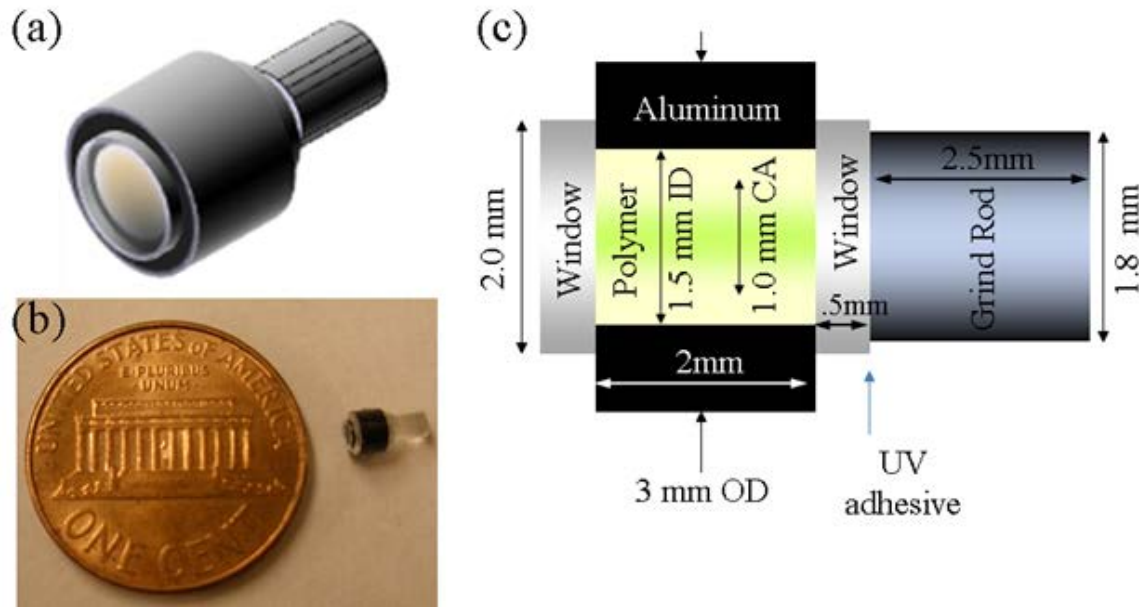


Figure 4.12. The designed lens geometry of the hybrid GRIN axicon lens. (a) is the three-dimensional cartoon of the lens. (b) is the photo of the hybrid GRIN axicon lens I've made compared to the one cent coin. (c) shows the cross section of the lens.

The fabrication procedure can be divided into 8 main steps, outlined below:

**Step 1** Insert the aluminum tubes into a plastic sheet with holes. The diameter of holes in the plastic sheet is 3.1mm, while the outside diameter of the metal tubes is 3mm. The

thickness of the plastic sheets and tubes is 2mm. Then, cast the polymers into the tubes. Two microscope slides are attached to both sides of the plastic sheet. In this way, the polymer tube samples are assembled into a wafer, shown in Fig. 4.13. This polymer tube wafer provides three advantages: (1) it avoids delamination and oxygen termination of the polymerization during the baking process; (2) it is efficient in that many phase plates are fabricated at once; (3) it reduces bubbles trapped in the polymers.

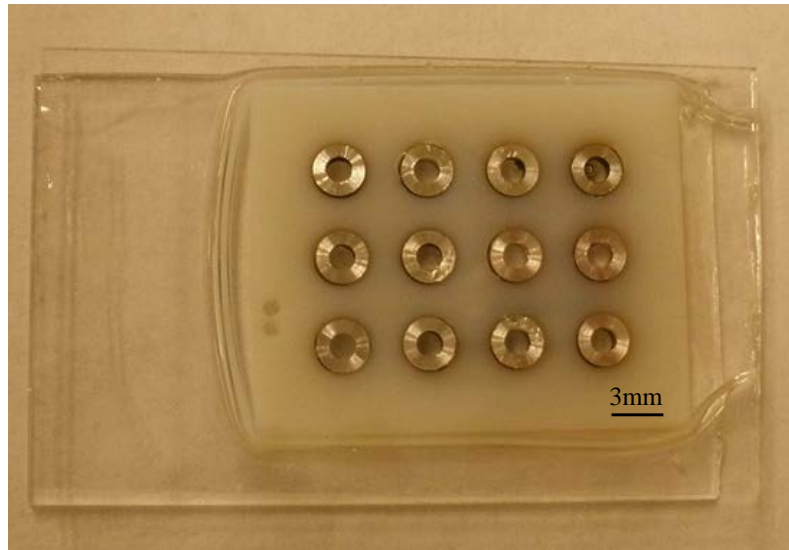


Figure 4.13. The photo of a wafer sample I've made with 16 polymer tubes.

**Step 2,** The whole wafer sample is pre-cured under a uniform, incoherent light at the wavelength of 405nm with a dose of  $900\text{mJ}/\text{cm}^2$  to get rid of oxygen in the polymer. Next, the GRIN phase plates are exposed into the polymer tubes by using the rapid galvo scanning system that is shown in Fig. 4.14. Since the LBR photopolymer is insensitive to the red light, a He-Ne laser is used as the probe beam for a confocal detector setup. This scanning confocal detector locates the front air/glass and back glass/air surfaces and the center of the polymer tube. Then the rapid galvo scanner draws a 2D exposure dose distribution in the polymer tube to form the index change of the designed GRIN phase plate.

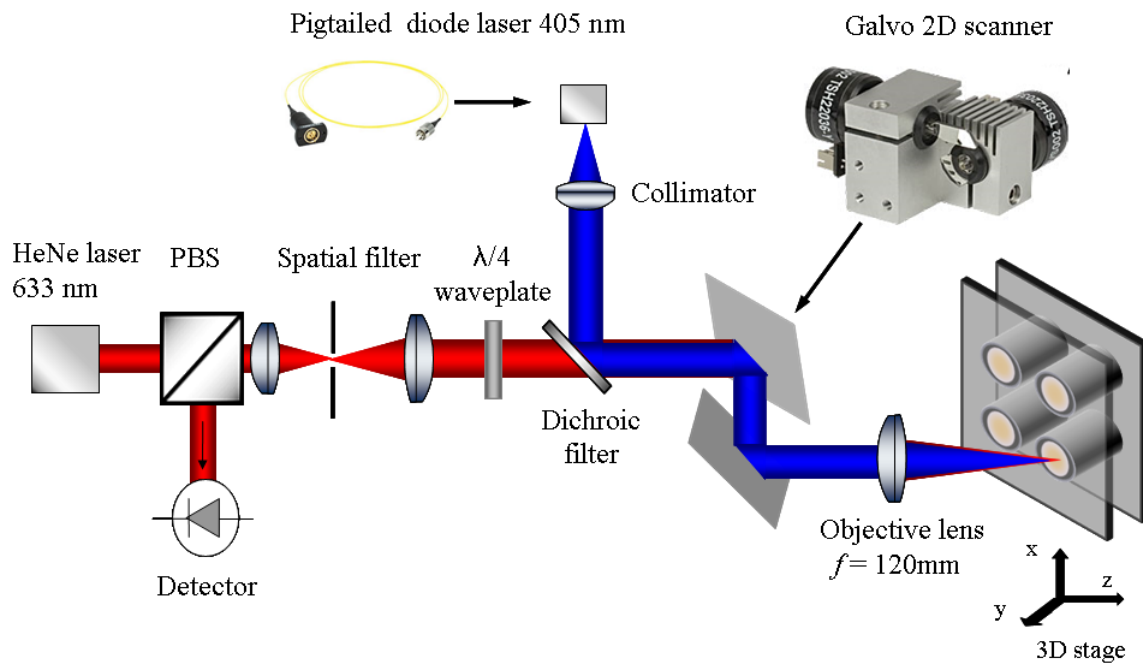


Figure 4.14. The optical layout of the galvo scanning system, which is used to fabricate the GRIN polymer phase plates.

**Step 3,** The exposed wafer is baked in the oven at constant temperature  $60^{\circ}\text{C}$  for several days.

This baking process provides two benefits: (1) it increases the monomer diffusion speed, thus reduces the required develop time; (2) it can increase the index change by about 2 times compared to samples developed at room temperature, which is demonstrated in Sec 3.3 in chapter 3. This baking process in fact is required to get the peak index change of 0.003. The maximum achievable index change without the baking process in the LBR polymer is approximately  $2.2 \times 10^{-3}$ .

**Step 4,** Test the index profiles of the GRIN phase plates in the wafer using a Shack-Hartman wavefront sensor setup discussed in Sec. 3.5 in chapter 3.

**Step 5,** Disassemble the wafer sample into individual polymer tubes. First, heat the wafer sample in the oven to  $80^{\circ}\text{C}$  to loosen the bonding between the polymer and the glass

slides. Then delaminate the two microscope slides from the wafer sample. Finally, disassemble the individual tube from the plastic sheet.

**Step 6,** Attach two windows with thickness of 0.5mm and diameter of 1.5mm to each polymer tube. After the microscope slides are delaminated from the polymer tube surfaces, a concave curve is formed due to the polymer material shrinkage. I will discuss the material shrinkage in Sec. 4.4.2. Therefore, two windows will be applied to each side of the polymer tube. I use the matrix only formulation of the LBR as the adhesive, which is index matched.

**Step 7,** Measure the index profile of individual GRIN phase plate under the Shack-Hartman wavefront sensor setup. This step shows that the effective index profile of the phase plate is the same as the one measured in Step 4.

**Step 8,** Attach the off-the-shelf GRIN rod lens to the GRIN phase plate to form the hybrid GRIN axicon lens through an active alignment process, shown in Fig. 4.15. The GRIN phase plate and the GRIN rod lens are amounted to two 5 dimensional stages respectively. A 532nm laser beam is spatial filtered and collimated. The GRIN phase plate and the GRIN rod lens accept the collimated beam and focus it ~2mm away from the back of the GRON rod lens. The PSFs through the focus region are then magnified by the 40x microscope objective and captured by the beam profiler.

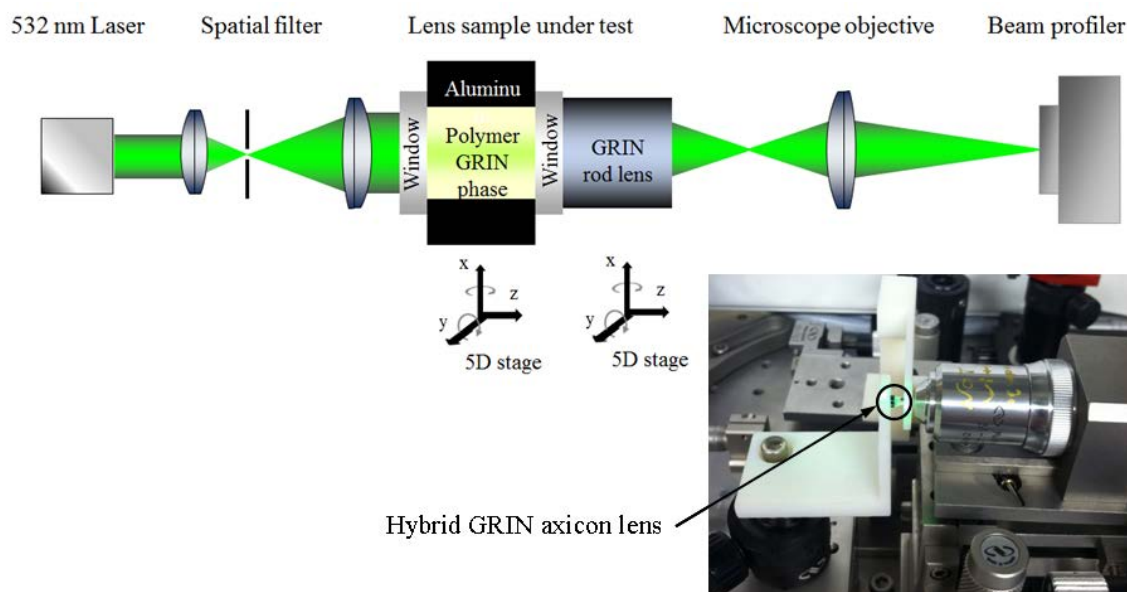


Figure 4.15. The optical layout of the stage to assemble the GRIN phase plate with the GRIN rod lens through an active alignment procedure. The inset shows part of the actual experimental setup to assemble the phase plate with the GRIN rod lens. The phase plate and the GRIN rod lens are hold by two custom-made plastic scaffolds respectively. Each plastic scaffold is mounted to a 5D stage.

The sample geometries during each step of the fabrication procedure are shown in Fig. 4.16. The reader may wonder why I did not use the sample geometry in Step 7 to start with. In that case, disassembling the wafer and attaching the windows to the polymer tube steps can be avoided, simplifying the fabrication process. In fact, originally the GRIN phase plates were fabricated individually by casting polymers into each metal tube with two windows on both sides. However, during the polymer packaging and index structure development process, I found several problems, which lead to establish the 8-step fabrication procedure. Firstly, it is not easy to package the polymer tube sample individually, because both the tube and windows are small. Secondly, it is more likely to trap bubbles in the polymer tube during the individual sample packaging process than the wafer making process. Thus the yield for the individual sample packaging is much lower. More importantly, during the baking process, the windows are likely to delaminate from the polymer. This delamination leads to two problems, material shrinkage and oxygen diffusion into the polymer which terminates the polymerization, limiting the index change.

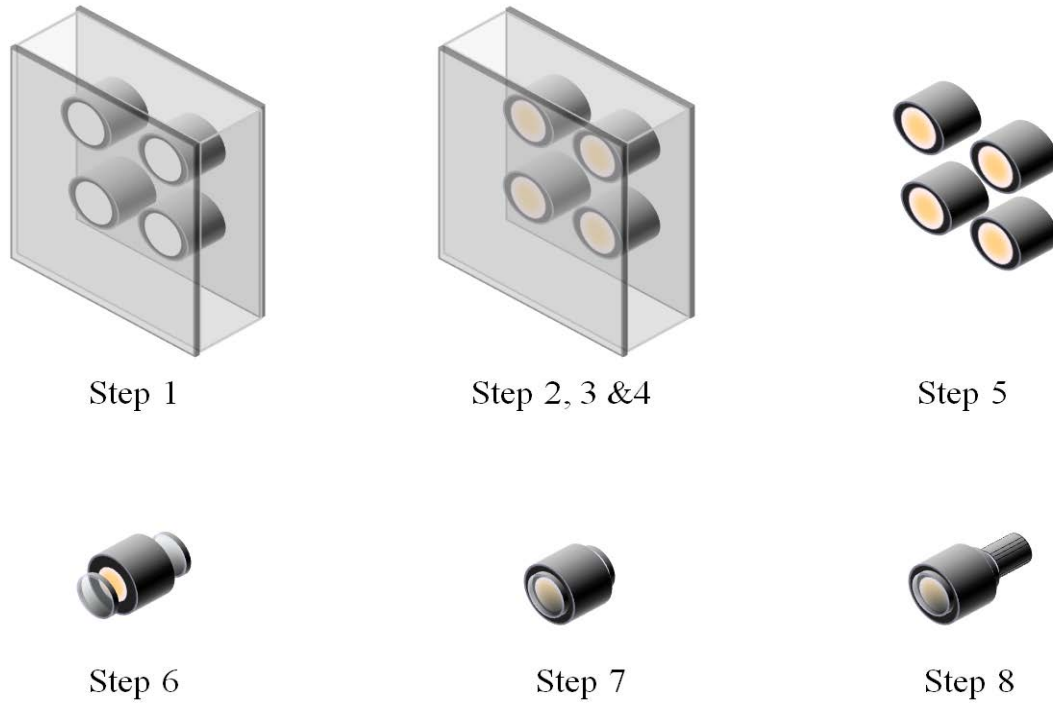


Figure 4.16. Demonstration of the sample geometries during each step of the 8-step fabrication procedure

Baking the sample helps to speed up the monomer diffusion process. At room temperature the measured monomer diffusion constant in LBR is about  $0.05\mu\text{m}^2/\text{sec}$ , which is calculated through the equation  $2\sqrt{v_{\text{diffusion}}t} = L_{\text{diffusion}}$ , where  $v_{\text{diffusion}}$  is the monomer diffusion constant,  $t$  is the diffusion time, and  $L_{\text{diffusion}}$  is the monomer diffusion length. Given the radius of the fabricated GRIN phase plate is about 0.6mm, it takes about 20 days for the monomers to diffuse from the outside of the exposed region to the center of the exposed region. To accelerate this process, I placed the sample in the oven at  $60^\circ\text{C}$  after exposure, which is estimated to increase significantly the diffusion speed, thus reducing the development time. However, baking the individual polymer tube samples will cause the windows to delaminate from the polymers, due to the difference in the thermal expansion coefficients of the polymer and the aluminum tube. This delamination leads to two major problems during the GRIN phase plate fabrication. The first problem is polymer shrinkage that forms a concave surface, as the polymer now is not bonded to

the window surface. The second problem is the contamination by oxygen from the atmosphere that can freely diffuse into the polymer, which terminates the polymerization process. I will discuss the polymer shrinkage in Sec. 4.4.2 and discuss the oxygen problem in Sec. 4.4.3.

#### 4.4.2 Material shrinkage

Material shrinkage may introduce stress and deformation in the polymer sample. Thus polymer packaging design needs to accommodate these weaknesses of the polymer material. First, stress in the polymer caused by the material shrinkage is qualitatively tested. The polymer is cast into a plastic sheet with holes with diameter of 1mm. The plastic sheet is sandwiched by two standard microscope glass slides. Three polymer samples, with thickness of 1mm, 2mm and 3mm respectively, are tested under a bright field microscope with two crossed polarizers. The microscope images are shown in Fig. 4.17. Low stress is observed in the polymer before the final flood cure step, which implies very low shrinkage stress during the matrix solidification. Some stress is observed after the flood cure step, but the stress is confined to edges with stiff mechanical boundary. Therefore, the inside diameter of the metal tube is chosen to be 1.5mm, which is larger than the size of the index structure of the designed GRIN phase plate. This relative large tube size provides two benefits: (1) avoiding the stress at the stiff mechanical boundary; (2) providing a monomer source to form index structure for the GRIN phase plate.



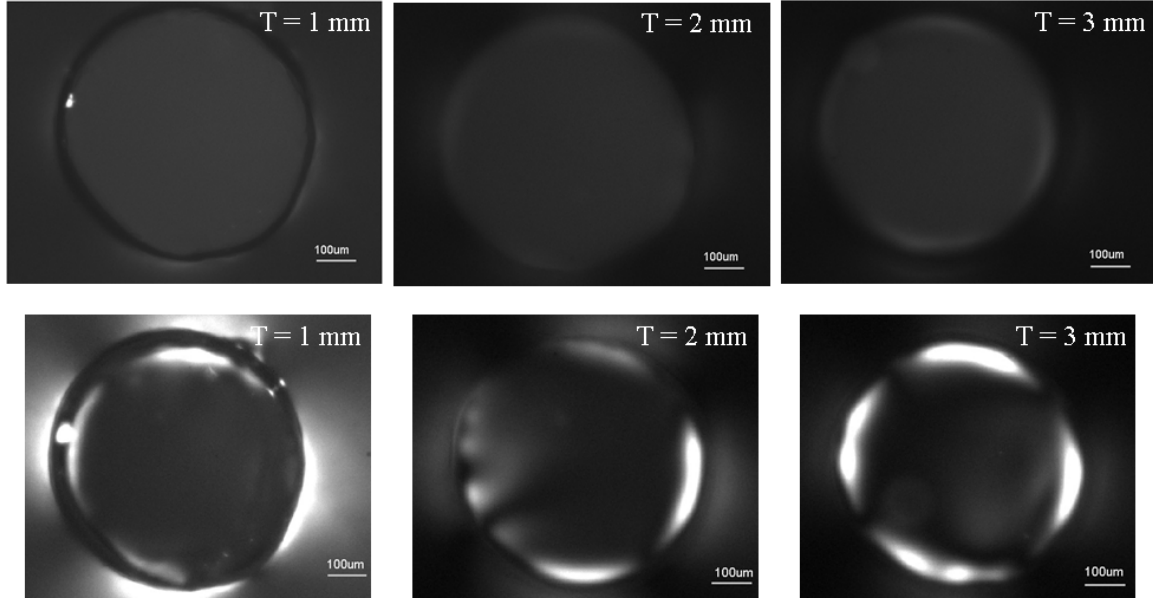


Figure 4.17. Stress testing results of the polymer samples in aluminum tubes with thickness of 1mm, 2mm and 3mm. The images are captured by a bright field microscope with two crossed polarizers. The upper row images are taken *before* the samples are flood cured. The lower row images are taken *after* the samples are flood cured.

Next, the uniformity of the polymer tube sample is quantitatively measured by a Shack-Hartmann wavefront sensor, shown in Fig. 4.18. The polymer thickness of the tube sample is 2mm and the diameter of the polymer is 1.5mm. The maximum measured optical path difference is about  $0.5\mu\text{m}$ , which is equivalent to a peak index change of  $2.5 \times 10^{-4}$ . This optical path length variance in the polymer tube sample may be due to the nonuniformity of the glass slides thickness or stress during the matrix solidification to cause the polymer thickness to be uneven.

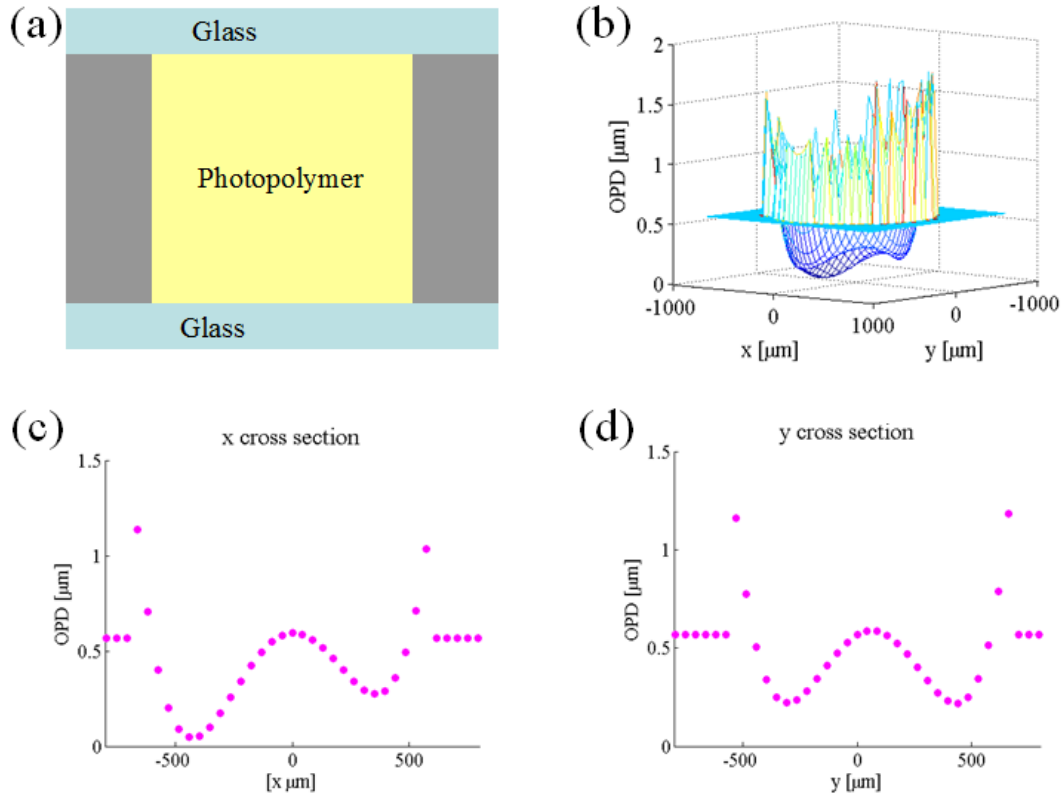


Figure 4.18. The measured uniformity of the polymer tube sample. (a) shows the sample geometry. (b) is the two dimensional plot of the measured OPD. (c) is the x cross section of the measured OPD. (d) is the y cross section of the measured OPD.

Then, I removed the glass slides from the polymer to mimic the delamination during the baking process and to measure the material shrinkage. After the two glass slides are removed, concave surfaces are formed in the polymer sample. The optical path length of the polymer is quantitatively measured using a Shack-Hartmann wavefront sensor. The measured results are shown in Fig. 4.19. Assuming that the density of the polymer is uniform, the volume shrinkage of the polymer in the metal tube is calculated to be  $\sim 0.3\%$ . This estimated shrinkage value is consistent with published values for commercial two-component diffusive photopolymers such as those from InPhase *Tapestry*<sup>TM</sup> polymers [16]. This 0.3% volume shrinkage in the polymer tube sample is equivalent to a peak index change of  $\sim 6 \times 10^{-3}$ , which is two times of the required index

change for the GRIN phase plate. Thus material shrinkage after delamination will destroy the intentionally introduced index structure in the polymer tube sample.

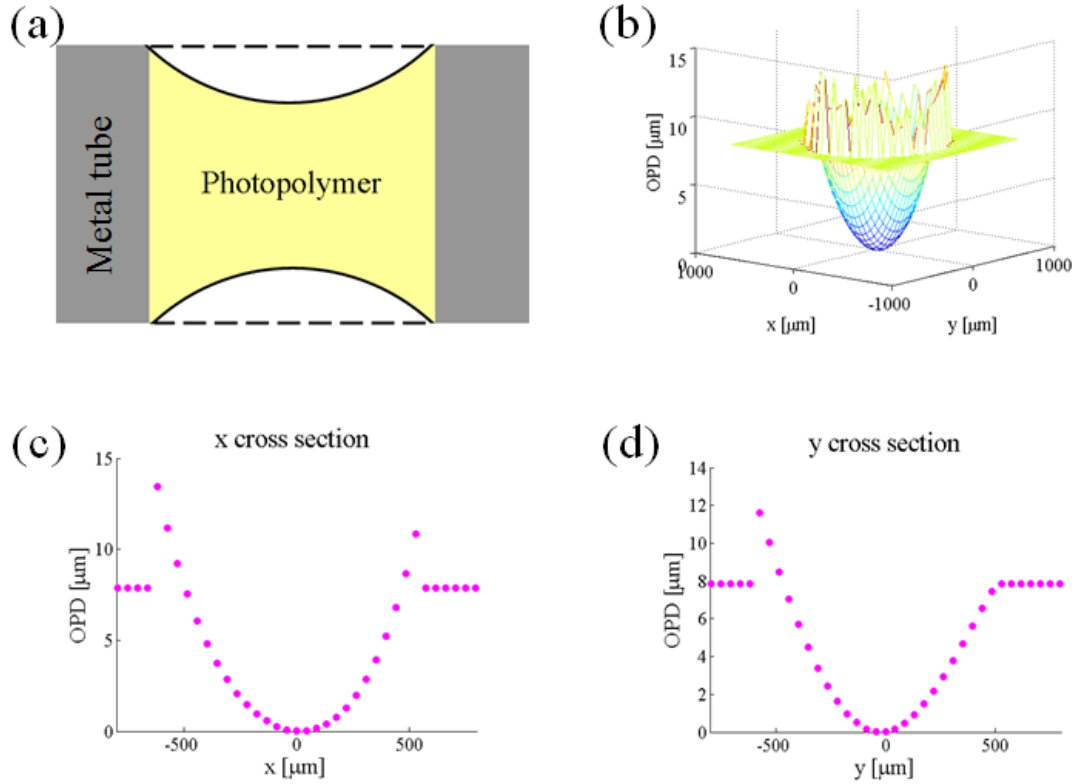


Figure 4.19. The deformed polymer surface due to material shrinkage in the tube sample without glass slides on both sides. (a) shows the sample geometry. (b) is the two dimensional plot of the measured OPD. (c) is the x cross section of the measured OPD. (d) is the y cross section of the measured OPD.

The delamination and material shrinkage problems can be solved by reattaching the glass windows back to the polymer tube sample. In order to index match with the polymer and avoid another flood-cure process, a matrix-only formulation of the LBR polymer is used as an adhesive to reattach the windows to the polymer tube. The measured index profile before and after the window reattachment for an individually packaged polymer tube sample is shown in Fig. 4.20.

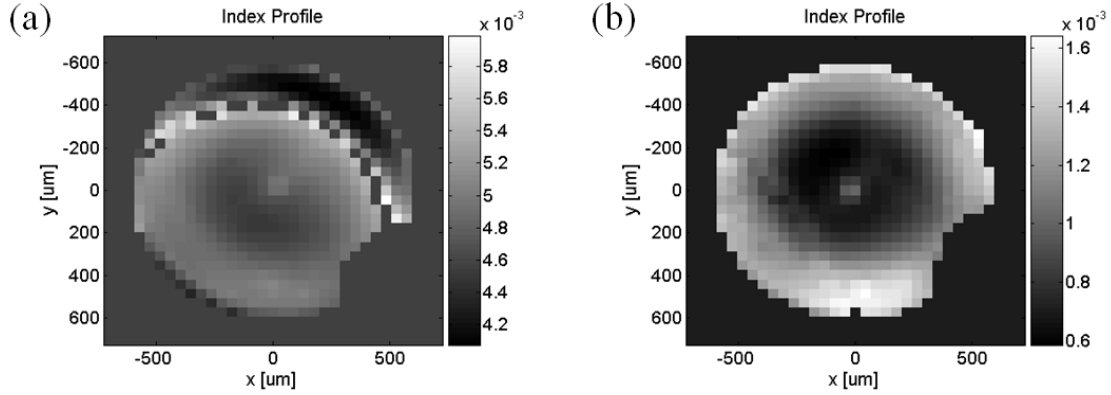


Figure 4.20. The measured index profiles of a individually packaged polymer tube sample: (a) when the windows was delaminated from the polymer; (b) after the windows were reattached to polymer. The missing part on the down-right corner is due to a small air bubble trapped in the polymer.

#### 4.4.3 Oxygen termination effect during the index development

The window delamination during the baking process exposes the polymer to the air. Oxygen in the air diffuses into the polymer and terminates the index development process. Thus the index structure formed in the polymer is no longer what we expect to have. One example of the measured index profile for the GRIN phase plate with this oxygen termination effect is shown in Fig. 4.21. This is an individually packaged polymer metal tube sample. Delamination occurred at the polymer and window intersurface around the metal tube edge. After the index change in the polymer was fully developed, the window was removed and reattached to the polymer. Then the index profile is measured by the Shack-Hartmann wavefront sensor. The peak index change is only half what is expected and the index shape also shows the evidence of the oxygen termination effect around the metal tube edge.

Oxygen termination is also the reason that I switched from a plastic tube to a metal tube. A polymer cylinder can be formed in an acrylic-like plastic tube, which can be conveniently made with a 3D rapid prototyper. However, this plastic stores and transmits atmospheric oxygen. Thus even though the polymer tube sample is pre-cured to clear out the effect of oxygen, the oxygen

that continuously diffuses from the plastic tube shuts down the polymerization and prevent formation of the desired index structure.

Thus, I established the 8-step fabrication procedure to solve the material shrinkage and oxygen problems, in order to form the required index structure in the polymer tube sample.

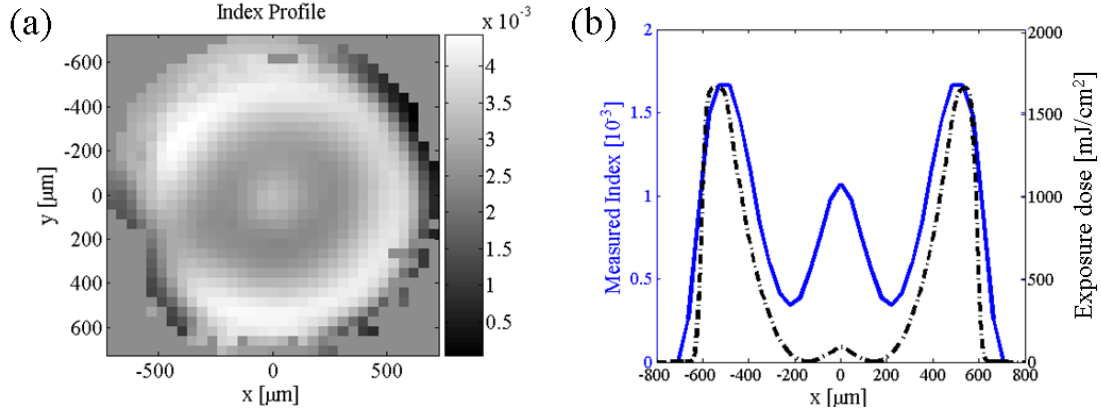


Figure 4.21. The measured index profile for the GRIN phase plate with oxygen termination effect around the edge. (a) is the measured two-dimensional index plot. (b) is the cross section of the measured index compared to the exposure dose distribution.

## 4.5 Experiment results

### 4.5.1 Index profile of the GRIN phase plate

The measured index profile of the GRIN phase plate is shown in Fig. 4.22. It is the experimental result of Step 7 during the fabrication procedure. The exposure dose distribution is designed assuming that the index change responds linearly to the exposure dose. The index profile is calculated from the measured optical path difference, assuming that the index distribution through the entire length of the polymer tube sample is uniform. Given the measured transmission of the LBR polymer is 0.89/mm and the thickness of the polymer tube sample is 2mm, this assumption is reasonable. The measured index profile has a peak index change that meets the design requirement. Also the measured index profile is very close to the exposure dose distribution, except that the center part of the index profile is higher than the expected. The potential reason and the way to fix it will be discussed in Sec. 4.6. This similarity of the measured

index shape to the exposure dose confirms that the total exposure time is sufficiently smaller than the characteristic time of polymerization that the exposure, although sequential, is effectively instantaneous.

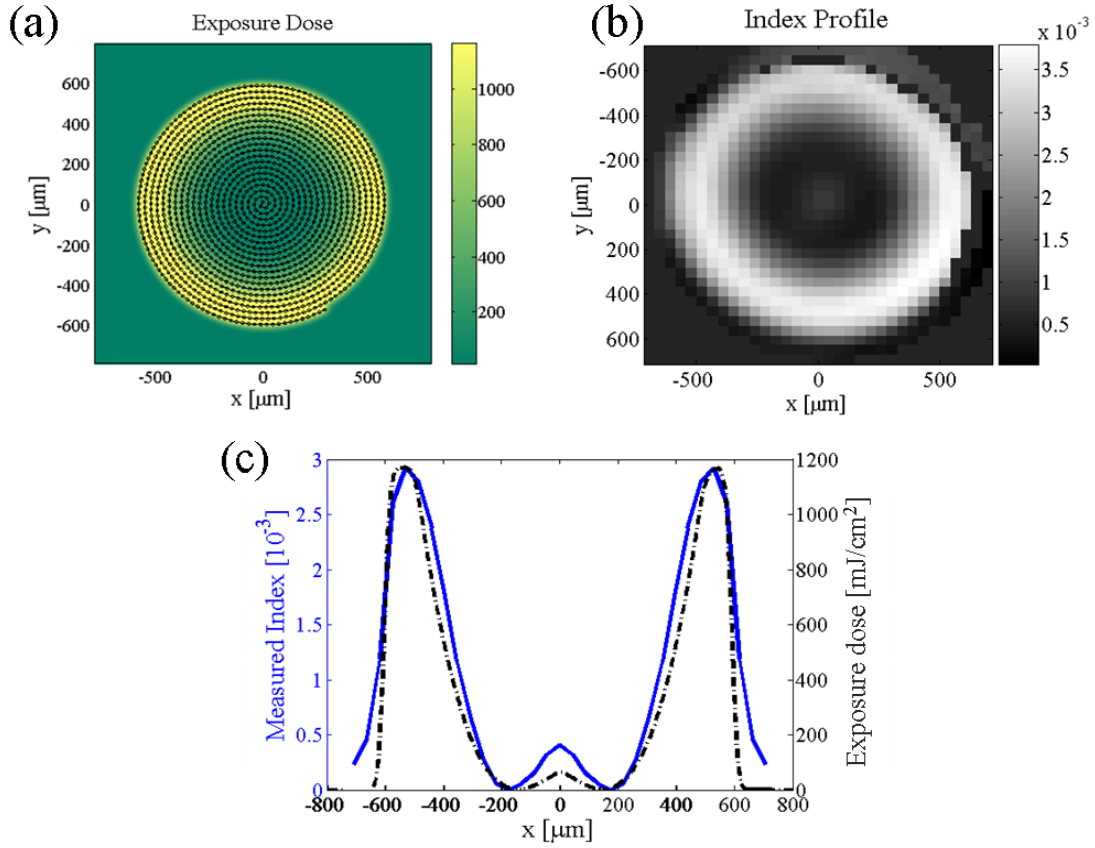


Figure 4.22. The measured index profile of the GRIN phase plate I made. (a) is the exposure dose pattern. (b) is the measured two-dimensional index plot. (c) is the comparison between the cross section of the index structure and the exposure dose pattern.

I also confirmed that the delamination and reattachment of the windows to polymer tube sample has negligible effect on the function of the GRIN phase plate, by comparing the measured index profile from Step 4 to that of Step 7, shown in Fig. 4.23. Thus, it validates the 8-step fabrication procedure.

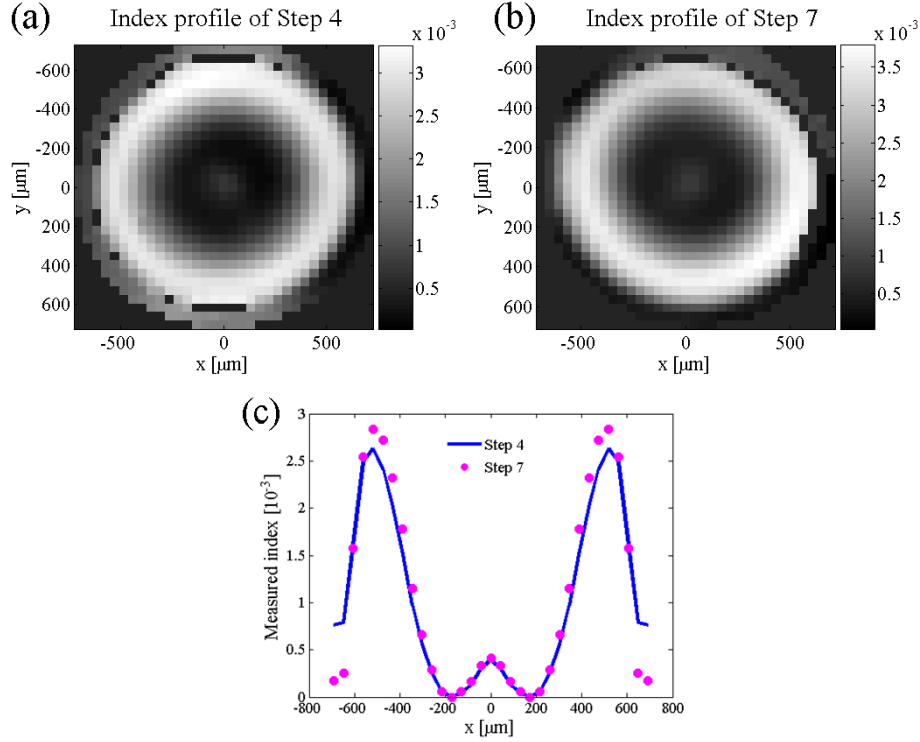


Figure 4.23. The index profile of the GRIN phase plate compared at Step 4 and Step 7 validates the fabrication procedure. (a) is the measured index profile plot from Step 4; (b) is the measured index profile plot from Step 7; (c) is the cross-section index profile comparison between Step 4 and Step 7.

#### 4.5.2 DOF of the hybrid GRIN axicon lens

This section shows a preliminary performance test of the hybrid GRIN axicon lens to extend the DOF. A complete characterization of the hybrid GRIN axicon lens will be carried out at the MGH research group.

After the commercial GRIN rod lens is attached to the GRIN phase plate, the point spread functions through the focus region are captured by a beam profiler. The test setup is shown in Fig. 4.15. The measured PSFs through the focus region are shown in Fig. 4.24. Due to the lack of the required laser source, these PSFs are measured at the wavelength of 532nm. The DOF is calculated based on the main lobe diameters. The main lobe diameters are  $\sim 2\mu\text{m}$  over a focus region of  $300\mu\text{m}$ , shown in Fig. 4.25. On the other hand, the DOF of the commercial GRIN rod

lens only is measured to be  $< 20 \mu\text{m}$ , shown in Fig. 4.26. This demonstrates that the hybrid GRIN axicon lens I have made extends the DOF by more than 10 times.

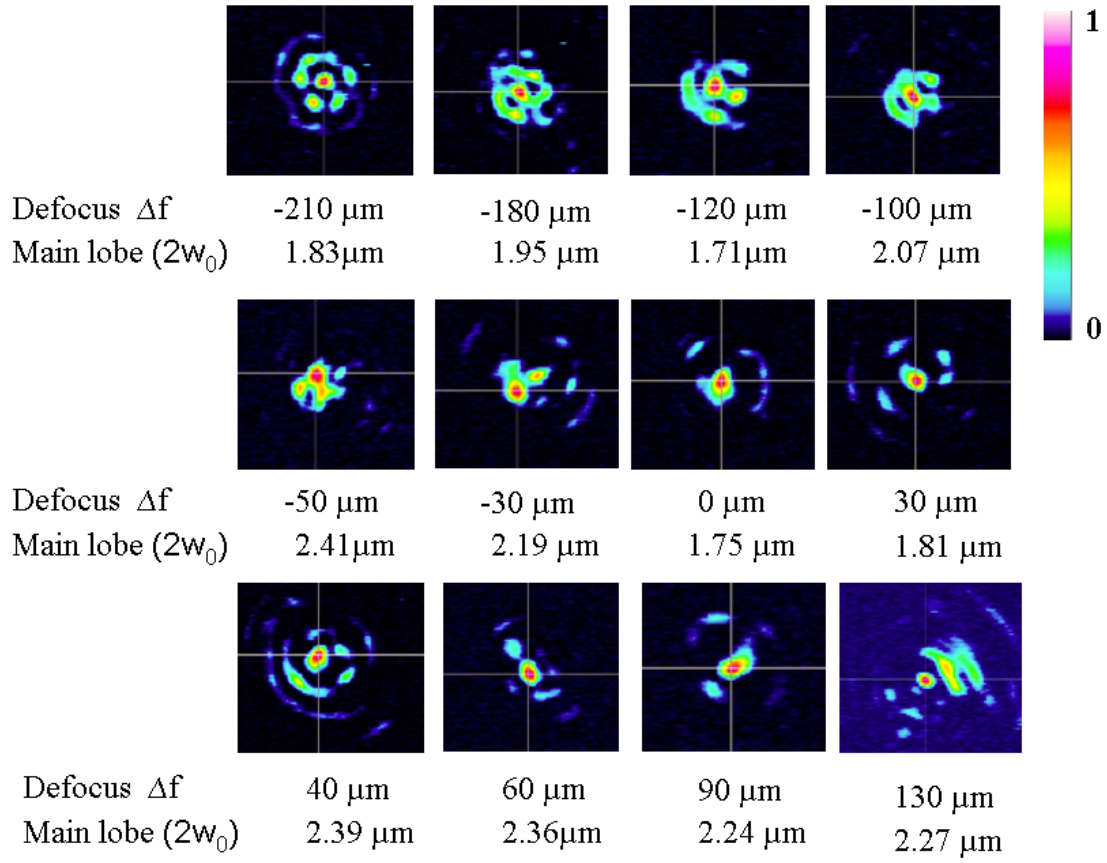


Figure 4.24. The measured PSFs of the hybrid GRIN axicon lens from the beam profiler through the focus region. The color bar stands for the intensity scale.



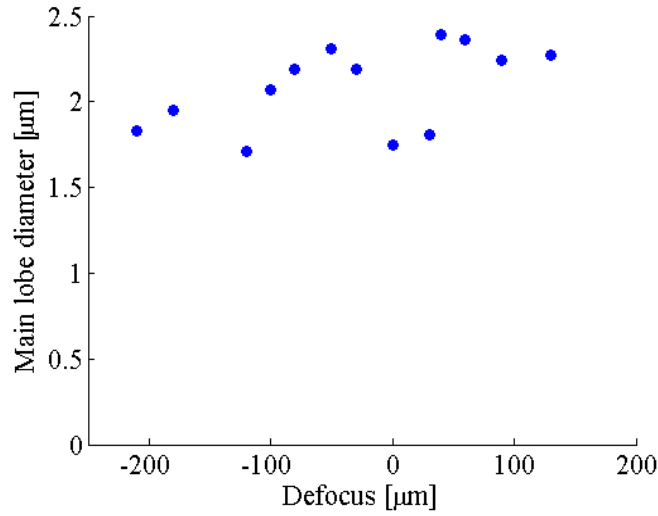


Figure 4.25. The main lobe diameters over the focus region for the hybrid GRIN axicon lens I have made.

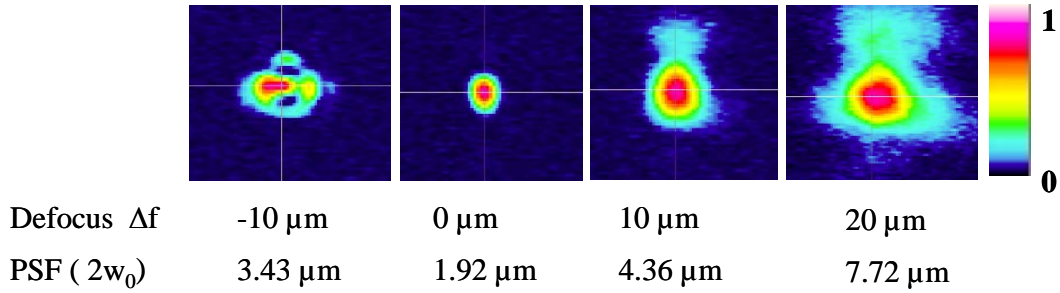


Figure 4.26. The measured PSFs of the glass GRIN rod lens from the beam profiler through the focus region. The color bar stands for the intensity scale.

## 4.6 Conclusions

I have demonstrated the design, fabrication and testing process for a hybrid GRIN axicon lens. This hybrid GRIN axicon includes an off-the-shelf GRIN rod lens to provide the primary optical power to offset the focus and a polymer GRIN phase plate to extend the depth of the focus. A radial BPM MATLAB simulation program is used to directly search for the optimal index profile of the GRIN phase plate. An 8-step fabrication procedure is established to make the designed index in a polymer metal tube sample. This 8-step fabrication procedure solves various problems that emerged during the index fabrication process, such as clearing out oxygen effect

and accommodating material shrinkage. The fabricated index profile of the GRIN phase plate is measured by a Shack-Hartman wavefront sensor.

The introduced index structure in the polymer metal tube sample yields a good fidelity, except that the center part of the lens has a higher index than the designed. I believe that it is caused by the depletion of the photoinitiators during the exposure. Thus, I converted the exposure dose distribution into the photoinitiator consumption distribution and then compared to the measured index profile, shown in Fig. 4.27. The measured index profile yields a better fitting with the photoinitiator consumption distribution than the exposure dose pattern. This is also confirmed by the index formation model I derived in chapter 3. Thus, the index formation model provides the guidance to improve the fidelity of the fabricated index structure as follows: (1) calculate a TPO consumption to replicate the required index profile; (2) convert the TPO consumption distribution into the corresponding the exposure dose pattern; (3) then make the index structure with the designed exposure dose pattern.

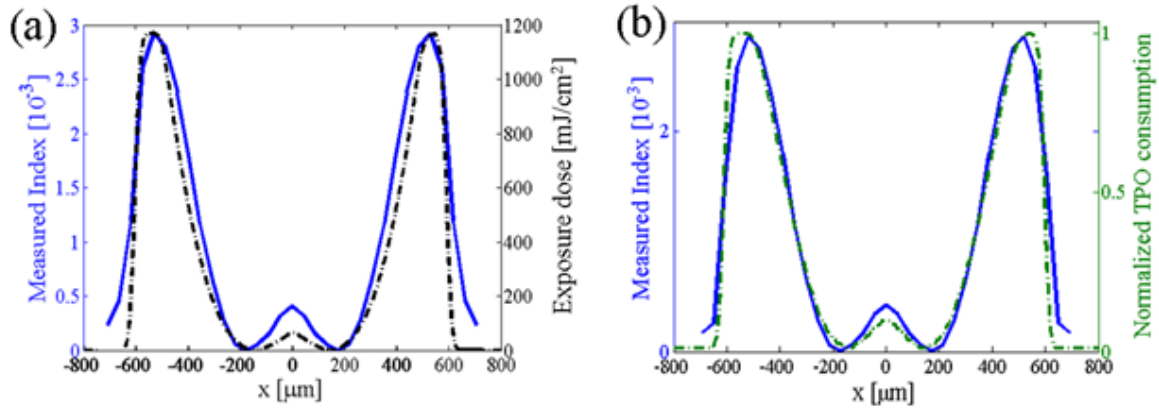


Figure 4.27. The measured index profile yields a better fitting with the photoinitiator consumption distribution than the exposure dose pattern. (a) is comparison between the measured index profile and the exposure dose. (b) is comparison between the measured index profile and the normalized photoinitiator consumption.

A preliminary measurement of the PSFs through focus region demonstrates that the hybrid GRIN axicon lens I've made has a transverse resolution of  $\sim 2 \mu\text{m}$  across a DOF of  $\sim 300 \mu\text{m}$  at the wavelength of 532nm. There is a more than 10 times improvement for the DOF, compared

to the PSFs that are measured for the GRIN rod lens. However, a more rigid procedure is needed to characterize the performance of the hybrid GRIN axicon lens to extend the DOF.

# Uniform and Tapered Single-Mode 3D Waveguides

### 5.1 Introduction

This Chapter demonstrates single-mode uniform and parabolically tapered three-dimensional (3D) waveguides fabricated via direct-write lithography in the *Tapestry*<sup>TM</sup> HDS 3000 photopolymer. Modulation of the writing power is shown to compensate Beer-Lambert absorption in the single-photon initiator and to provide a precise control of modal tapers. A laminated sample preparation is introduced to enable a full 3D characterization of these modal tapers without the need for sample polishing, which is difficult for this class of polymer. The accuracy and repeatability of this modal characterization is shown to allow precise measurement of propagation loss from single samples. These testing procedures are used to demonstrate single-mode waveguides with an excess propagation loss of 0.147 dB/cm and symmetrical tapers up to 1:2.5 using 1.5 microwatts of continuous write power at wavelength of 532 nm. Uniform waveguides through transmissive optics and with reflective optics are also demonstrated.

Traditional optical waveguide circuits are planar devices with uniform thickness and discrete index profiles. In the past decade, there has been growing interest in 3D waveguides whose paths, peak indices and cross section can all be controlled along an arbitrary guide path. These additional degrees of freedom enable novel optical circuits and may provide a platform for the interconnection of fiber and other traditional waveguide devices, including mode transformations.

Current approaches to 3D waveguide fabrication can be characterized by the lithography method (direct write vs. “self-written”) and the material photo-response (multiphoton vs. single

photon). The most common technique is 3D scanning direct-write lithography with a femtosecond laser which undergoes multiphoton absorption at the focus to locally change the index of refraction of glass or polymer[126,127,128]. This method is popular because the lithography approach provides programmable 3D control over the waveguide path and the nonlinear absorption confines the response to the focal region. The primary disadvantages are low fabrication speed enforced by the small multiphoton cross section and difficulty in aligning the waveguides to other devices. The second common approach is to “self-write” waveguides in a one-photon sensitized photopolymer. Here, light from a stationary focus or embedded fiber is introduced directly into the photopolymer, forming a waveguide which propagates into the polymer in a soliton-like fashion [129]. The advantages of this approach are its simplicity and the automatic alignment of the self-written waveguide to an embedded or butt-coupled source. However this technique has limited control over the shape and direction of the resulting waveguides and single-mode operation has not yet been demonstrated over millimeter scale [130,131]. Finally, nearly all studies of 3D waveguides to date have performed limited characterization because the deeply buried, gradient-index guide is not compatible with profilometry, prism coupling or other measurement methods designed for planar devices. This lack of characterization methods is particularly problematic for studies of non-uniform guides such as modal tapers [132,133,134].

In this work, I investigate the use of direct-write lithography, which provides control over the waveguide path and mode, with a one-photon photopolymer, which requires only a low-power continuous laser source. Specifically, I show that direct-write lithography with a  $\mu\text{W}$  laser focused into a one-photon photopolymer can form symmetric, single-mode, 3D waveguides. The power of the writing laser is varied to compensate for absorption and to create precisely controlled modal tapers.

Additionally, I report test procedures for deeply-buried polymer waveguides not compatible with existing measurement techniques. The waveguides written are small (diameter  $< 10\text{ }\mu\text{m}$ ), weak (peak index change  $< 0.01$ ) and deeply embedded in thick (mm) polymers, defeating most index and modal characterization methods. Near-field techniques such as electron microscopy and profilometry can provide precise index shape of ridge planar waveguides, but do not apply to embedded 3D waveguides. Phase microscopy such as differential interference contrast (DIC) microscopy [54] typically offers a qualitative, but not quantitative, index picture. Quantitative phase microscopy has been reported [55], but is limited to physically thin objects. Specialized methods for index profiling of 3D waveguides and fiber cores including modified optical diffraction tomography (ODT) [135], scanning transmission microscopy [7] and reflection scanning [136] do not provide a complete 3D measurement of the guide index. This incomplete characterization prevents the calculation of the critical waveguide properties including mode size, shape and loss.

An alternative is to forgo index measurement and instead to directly measure modal properties along the guide length. The prism-coupling method is commonly used for planar waveguides, but it is not applicable for deeply embedded 3D waveguides. The cutback method allows mode characterization of 3D waveguides including tapers but requires an optical-quality polish after each cut. While appropriate for inorganic glasses and crystals, this polishing step is often impossible for polymers, particularly those with low glass transition temperature as used here. This lack of index or modal test methods for 3D glass and polymer waveguides is reflected in virtually no reported characterization beyond total loss and end-facet mode profile.

Here, I introduce a procedure that enables optical-quality cut-back surfaces in polymers that cannot be cut or polished. Thick, optical-quality materials are first fabricated as laminates of a number of thin polymer layers. After waveguide lithography, the layers are separated and

independently tested for modal properties. This provides complete characterization of modal properties as a function of distance along the guide.

I use this test procedure to show symmetric 3D tapered and untapered polymer waveguides and confirm that they are single mode over a length of 10mm. Precise characterization of the mode profile allows the total measured loss to be separated into coupling and propagation loss. These measurements are used to verify the repeatability of uniform waveguide fabrication which in turn provides an accurate validation of the propagation loss measured via cutback.

The outline for the rest of the chapter is as follows. Section 5.2 introduces and the photopolymer sample preparation for 3D waveguide fabrication. Sec. 5.3 describes a direct-write lithography system that fabricates 3D photopolymer waveguides. A convenient power control method is employed to control waveguide tapers. Section 5.4 introduces a novel polymer sample preparation technique that achieves optical-quality cut-back surfaces in rubbery polymer without actually cutting these polymers. This technique, combined with an active mode imaging system, is demonstrated to precisely characterize the mode profiles along the deeply-buried 3D waveguide. The single-mode waveguide performance is confirmed and various waveguide mode tapers are presented in Sec 5.4. Two types of loss measurement methods are presented in Sec. 5.5. Finally, Section 5.6 discusses two extensions of uniform 3D waveguides, namely waveguide through thin optics and sharp waveguide bends. Section 5.7 summarizes this chapter.

## **5.2 Diffusive photopolymer samples**

Photopolymer offers several advantages over glass as a material platform for optical waveguides including greater optical sensitivity, widely tunable material properties and lower cost. However, polymers used for 3D waveguides must self-develop an index change in response to light, unlike 2D waveguides in which wet chemistry (e.g. solvents) can be used to develop structure [13]. For example, multiphoton absorption writing uses the increased index of the

photopolymerized region at the focus [126,127]. Unfortunately, the structure is only stable so long as one-photon or thermal processes do not cause the large remaining quantity of initiator and monomer to react. Since this assumption is not applicable for one-photon absorbers, an additional process is required to form permanent structures in 3D one-photon polymers.

Diffusive photopolymers were originally developed for holographic data storage (HDS) [137] and have recently been adapted for 3D optical interconnections [130, 134, 138]. As discussed in chapter 1, typical diffusive photopolymers consist of two chemical components: one that forms a solid yet flexible matrix and the photo-active components consisting of an initiator that absorbs a fraction of the incident light to form radicals and a monomer that polymerizes by reacting with this photoinitiator. A localized illumination therefore creates a high molecular-weight polymer within the illuminated region through the consumption of low-molecular-weight monomers. This local depletion of monomers causes monomers to diffuse into the exposed region, resulting in an area of increased density and refractive index. After this mass transport has locally increased the refractive index, a uniform optical exposure is used to consume all the remaining initiators and monomers, rendering the polymer chemically and optically inert.

The diffusive photopolymer used in the work of this chapter is InPhase Technologies *Tapestry*<sup>TM</sup> HDS 3000 polymer, with two modifications. The absorbance of the commercial formulation is optimized for samples with 1-2 mm thickness which would allow only a small amount of the incident light to reach the back of a sample with thickness of 10mm as used later in this chapter. Thus a custom formulation was ordered with ½ density of the normal photo-initiator. The second modification is the use of O<sub>2</sub> as a radical inhibitor. This is present due to diffusion from the atmosphere but can be removed prior to use of these materials via a nitrogen bath or an optical pre-cure process. This process was skipped in the study of this chapter to leave the O<sub>2</sub> in the material. Two sample formation geometries are used in this chapter: slide samples with a thickness of 1mm and rectangular glass cuvette samples, shown in Fig. 5.1.



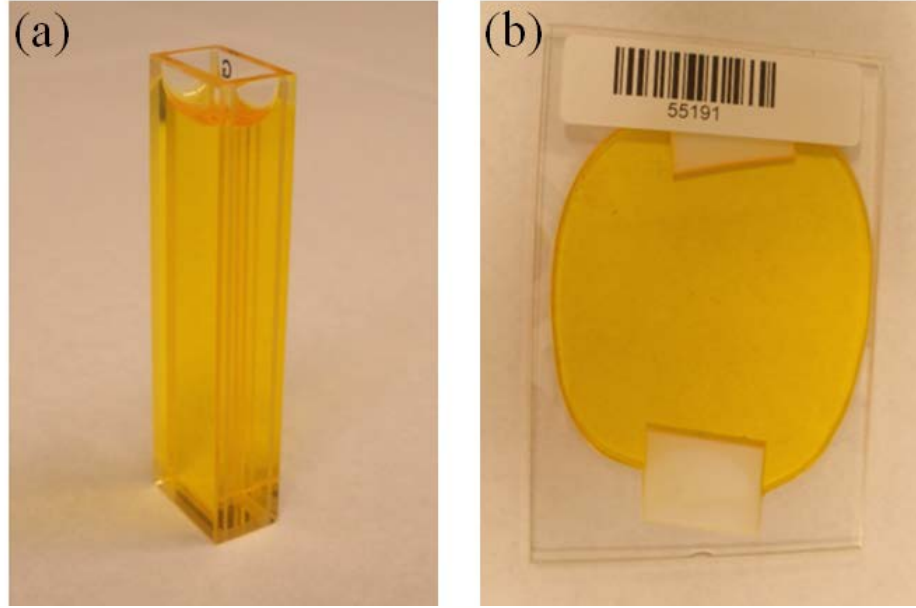


Figure 5.1. Two sample formation geometries used in 3D waveguides fabrication and testing. (a) Cuvette sample: photopolymer material HDS 3000 with half photoinitiator is casted into a glass cuvette with size of 5mm×10mm×50mm. (b) Slide sample: photopolymer material is casted into a 1mm polymer layers between two pieces of glass. The polymer layer later is delaminated from the glass and stacked together to form an optical-quality thick sample for 3D characterization of the waveguides.

The cuvette samples are used for a qualitative study of the taper properties of the 3D waveguides, which helps to narrow down the writing condition for uniform 3D waveguides. 3D waveguide arrays are written into the cuvette samples in the direction with a polymer thickness of 10mm. The Beer-Lambert absorption will naturally taper the waveguides if the incident power is held constant. Therefore, by varying the incident power while writing the waveguide, the taper properties of the 3D waveguides can be controlled. The waveguide fabrication process and the taper control method are demonstrated in detail in Sec. 5.3. After the waveguides are formed in the cuvette sample, the side view of 10mm long 3D waveguide is imaged under a DIC phase microscope. The front, middle and back portions of the waveguides are imaged separately. Two sets of images of waveguides under different exposure condition are shown in Fig. 5.2. By comparing the waveguide widths in the front, middle and back position, a proper power control modulation curve is achieved to fabricate roughly uniform 3D waveguides over 1cm length. For

example, the waveguides with power modulation curve  $T_{Eff} = 0.65$  gain more uniformity than the waveguides with the power curve  $T_{Eff} = 0.70$ , shown in Fig. 5.2. The power modulation is discussed in Sec. 5.3.2.

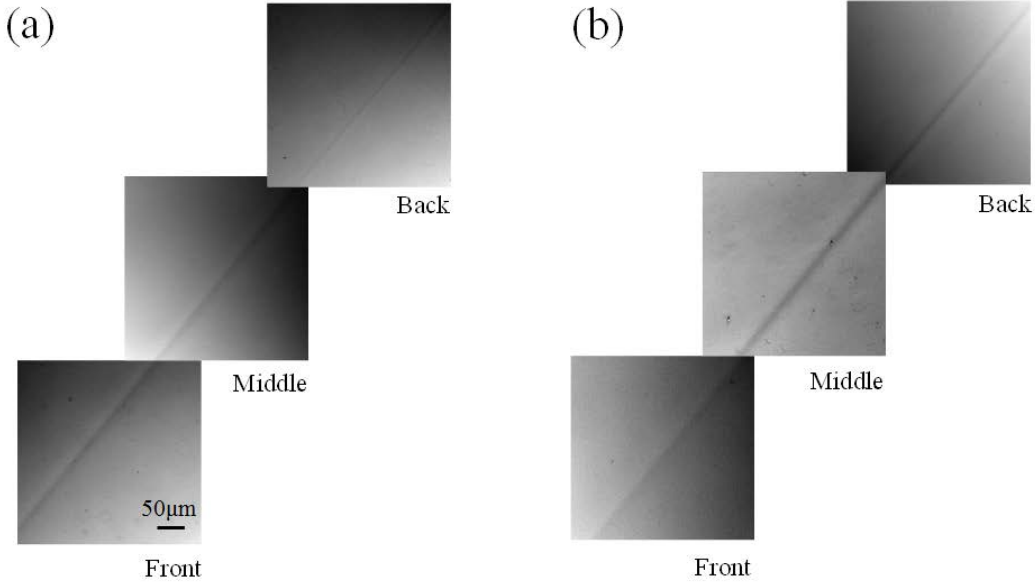


Figure 5.2. DIC microscope images of waveguides with the different power modulation curves. The photopolymer used for these two waveguides is the LBR polymer with 0.2% photoinitiators, which is discussed in chapter 3. (a) The writing power is  $10.1 \mu\text{W}$  at the front surface, modified by power profiles  $T_{Eff} = 0.75$ . The writing velocity is  $1\text{mm/s}$ . (b) the writing power is  $10.1 \mu\text{W}$  at the front surface, modified by power profiles  $T_{Eff} = 0.70$ . The writing velocity is  $1\text{mm/s}$ .

The slide samples are used to build a stacked thick sample for characterizing the mode profile along the 3D waveguide without the need to cutback the waveguide, this method is defined as pseudo-cutback method in this thesis and demonstrated in Sec. 5.4.

The one-photo initiation and self-index-development make the diffusive polymer attractive for 3D waveguide fabrication. For example expensive high power pulse laser is not required. However, these advantages also come at a cost: they make the polymer very sensitive. Any dusts or impurities in the sample or on the optics that is near the sample will produce filaments or scatter patterns in the sample. Examples of such occurrences are shown in Fig. 5.3.

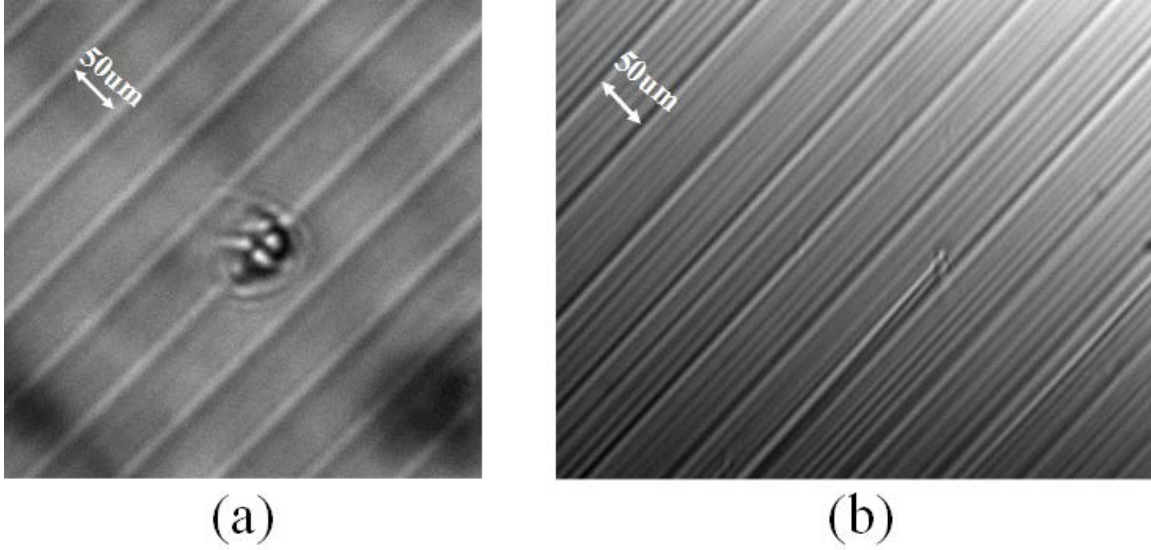


Figure 5.3. DIC microscope images of waveguide arrays that show destructive effects due to dust or impurities in the material. (a) The scatter pattern recorded in a waveguide grating with period of  $50\mu\text{m}$  (b) The filaments formed in a waveguide grating with period of  $50\mu\text{m}$ .

In order to significantly reduce these destructive effects due to existence of dusts, several preventative procedures are employed during the sample preparation and waveguide fabrication process. Firstly, per-clean the cuvettes and glass slides used to make polymer samples. Second, filter the liquid material mixture through a pressure filter with a pore size of  $0.2\ \mu\text{m}$ . Third, a HEPA filter is stored above the direct-write lithography platform to keep the waveguide fabrication platform clean.

### 5.3 Fabrication of 3D waveguides in diffusive photopolymers

3D waveguides are fabricated using a direct-write lithography system, which can be implemented by moving the polymer sample primarily perpendicular or parallel to the optical axis. A laser beam of a wavelength that initiates polymerization is focused into the bulk of a photopolymer slab. By moving the polymer sample perpendicularly or parallel to the optical axis [9], a localized line of index change is created in the material, shown in Fig. 5.4.

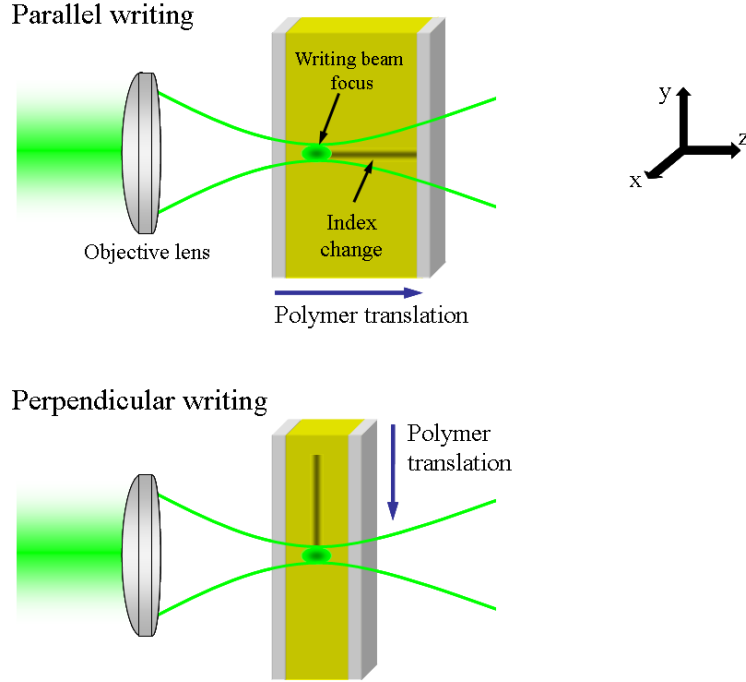


Figure 5.4. Waveguide fabrication by direct-write lithography through parallel writing or perpendicular writing

As discussed in chapter 1, the index change created in the material is proportional to  $I^\alpha t$ , where  $I$  is the writing intensity,  $t$  is the time over which the material is illuminated, and  $\alpha$  is a single fit parameter that describes the termination kinetics. Therefore, when the photopolymer slab is moved at a constant speed of  $v$  and the movement distance is much longer than the Rayleigh range of the writing beam, the introduced index change in the perpendicular writing can be expressed as:

$$\delta n(x, y, z) \propto \int_{-\infty}^{+\infty} I_0^\alpha(x, y + vt, z) dt, \quad (5.1)$$

And for parallel writing, the index change is:

$$\delta n(x, y, z) \propto \int_{-\infty}^{+\infty} I_0^\alpha(x, y, z + vt) dt, \quad (5.2)$$

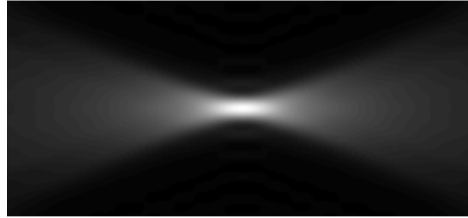
$I_0$  is the incident Gaussian shape irradiance, expressed as

$$I_0(x, y, z) = \frac{2P}{\pi w_0^2 \left[ 1 + \left( \frac{z}{z_0} \right)^2 \right]} \exp \left\{ \frac{-2(x^2 + y^2)}{w_0^2 \left[ 1 + \left( \frac{z}{z_0} \right)^2 \right]} \right\}, \quad (5.3)$$

where  $P$  is the incident power,  $Z_0$  is the Rayleigh range, and  $w_0$  is the  $1/e^2$  intensity radius at the laser focus. Previous research showed that  $\alpha$  is  $\sim 0.75$  for the InPhase HDS 3000 polymer modified for lower absorption by half the usual photoinitiator concentration [9]. Therefore the calculated index cross sections of waveguides fabricated by perpendicular writing and parallel writing are shown in Fig. 5.5.



(a)



(b)

Figure 5.5. The calculated index cross section of waveguides fabricated by (a) parallel writing and (b) perpendicular writing respectively.

These two direct-write waveguide fabrication geometries have their own advantages and disadvantages. Perpendicular writing geometry provides convenience for wiring 3D waveguides over a large area, for example a big photopolymer wafer. However perpendicular writing tends to create asymmetrical guides and weak confinement in the  $z$  direction. Two technologies have developed to potentially correct these issues. Beam shaping has been demonstrated in

multiphoton absorption to create symmetrical waveguides [127,139]. However, beam shaping is much more challenging for the material with linear or sub-linear responses. A two-color irradiation scheme [140] is reported to achieve sub-diffraction spatial control over polymerization. Alternatively, parallel writing automatically creates symmetrical guides from a symmetrical focus. However the length of waveguide that can be written is limited to the working distance of the objective lens. A summary of these two writing geometries is shown in Table 5.1.

Table 5.1: Comparison of perpendicular writing and parallel writing for waveguide fabrication

	Perpendicular Writing	Parallel Writing
Advantages	Wire waveguides over large area	circularly symmetrical guides
Disadvantages	Asymmetrical guides Weak confinement in z direction	Working distance limitation Beer-Lambert absorption

### 5.3.1 Parallel lithography to fabricate 3D waveguides

The index structure written in parallel geometry is cylindrically symmetric and tightly confined, making the parallel writing more applicable for interconnection of hybrid encapsulated components. Therefore the parallel writing geometry is used in this thesis work.

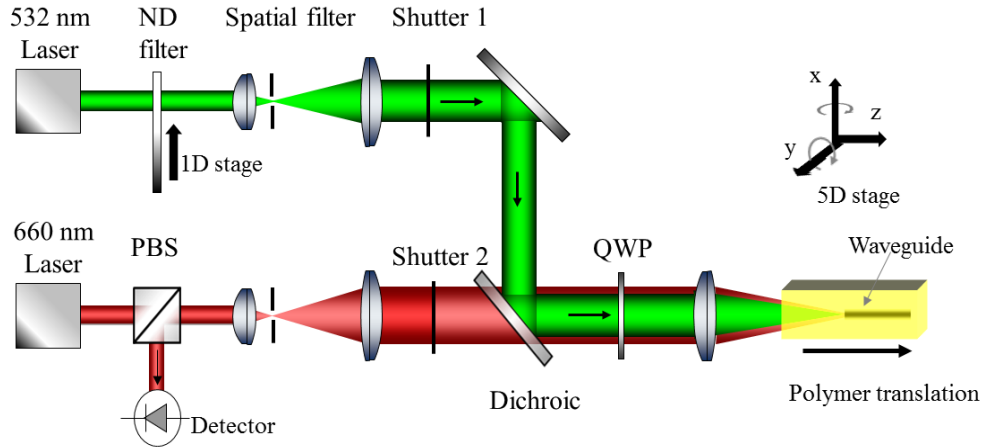


Figure 5.6. Optical layout of the parallel direct-write lithography system. The logarithmic neutral density filter modulates the laser with large dynamic range naturally matched to the exponential Beer Lambert absorption.

The optical layout of the direct-write lithography platform is shown in Fig. 5.6. A 532nm, 50 mW Coherent Compass 315M laser is used as the direct-write laser and a 660 nm, 60 mW Coherent Cube-660-60C laser as the confocal microscope probe laser. The two wavelengths are chosen to be sufficiently separated so that the write laser efficiently initiates polymerization while the longer-wavelength probe laser is only very weakly absorbed by the photoinitiator. However, the two wavelengths must also be sufficiently close so that chromatic aberrations of the common optics are minimized. The unavoidable longitudinal chromatic aberration of the primary objective is compensated by shifting the  $z$  coordinate of the stage between sensing and writing. The Linos achromatic doublet with focal length of 20mm is used as the objective lens. Both lasers are modulated via Vincent Associates mechanical shutters. The confocal microscope is used to locate the position of the polymer sample. Then 3D waveguides are formed by focusing several  $\mu$ W of the CW laser into the moving polymer.

Additionally, the 532 nm power is modulated by a variable ND filter, Thorlabs NDL-10C-4, on a motorized stage synchronized to the sample motion. The stages used for both the 1D ND filter motion and the  $x,y,z$  part motion are Newport PM500s controlled by a PM500-C6 driver

and custom LabView software. Custom hardware and drivers are used to enable 790 Hz position-synchronized measurements in the  $x$  axis. Two rotation axes, used primarily to orient the part, are motorized via Newport TRA12CC actuators controlled by a Newport EPS7000.

### 5.3.2 Taper control

The InPhase HDS 3000 media used for the waveguide fabrication in this chapter contains 0.35% photoinitiator, which results in an absorption of  $\sim 10\%$  per mm. Therefore, although the cm-thick polymer is optically thin, this weak Beer-Lambert absorption naturally tapers the waveguide index if incident power is held constant. The front part of the material, which is closer to the writing objective lens, get higher exposure energy dose than the back part. Therefore, the peak index change of the front part of waveguide is larger and the size of the index profile is wider. These waveguides, with index tapered into two dimensions, are useful in applications involving mode converting, such as coupling the light from a laser diode into an optical fiber[141], interconnecting single-mode fibers to waveguides with much more compact mode profiles[142,143] and etc. However in these applications, the index contrast and subsequently the mode field diameters along the waveguide taper need to be specifically designed and precisely controlled during the fabrication. This section introduces a novel taper control method for the parallel direct-write waveguide fabrication.

As the introduced index contrast of the parallel writing express in Eq.5.2., the taper properties of the waveguide can be controlled in two ways: by varying the writing velocity while holding the incident power constant; and by varying the incident writing power while holding the constant velocity. For control using velocity modulation, the Newport PM500 linear stages in the writing platform have limited options. The only straightforward way to modulate the velocity during waveguide writing is to move the  $z$  stage at a constant rate of acceleration. The maximum acceleration is limited by the moving range and the maximum speed of the stage. Alternatively, the taper can be controlled or eliminated by a logarithmic-variable neutral density (ND) filter,



Thorlabs NDL-10C-4, which is moved synchronously with the sample via Newport PM500 stages. The transmittance along the logarithmic neutral density filter modulates the laser. This modulation offers a large dynamic range and is naturally matched to the exponential Beer Lambert absorption.

Due to the Beer-Lambert absorption, the intensity of laser focus is attenuated exponentially when dragging the laser focus through the material to fabricate a waveguide, more specifically,

$$I(x, y, z) = I_0(x, y, z)T_m^z, \quad (5.4)$$

where  $I_0(x, y, z)$  is the laser focus intensity in the material,  $I_0(x, y, z)$  is the incident laser focus intensity without material absorption and  $T_m$  is the pre-measured material transmittance, and  $z$  is the material depth to the focus in mm.. When the incident laser power is held constant while moving the polymer sample,  $I_0(x, y, z)$  equals  $I_0(x, y, 0)$ , where  $I_0(x, y, 0)$  is the incident laser intensity when the laser focus is at the front surface of the material..  $T_m$  is 0.92/mm for InPhase HDS 3000 polymer with 0.35% photoinitiator concentration. By moving the ND filter in parallel to writing the waveguide, the incident laser intensity is modulated as

$$I_0(x, y, z) = I_0(x, y, 0)T_{Eff}^{-z}, \quad (5.5)$$

where  $T_{Eff}$  is the effective material transmittance.  $T_{Eff}$  depends on the attenuation modulation of ND filter,  $M_{ND}$  and the ratio between the material moving velocity  $v_m$  and the ND filter moving

velocity  $v_{ND}$ , which can be expressed as  $T_{Eff} = \frac{v_m}{M_{ND}v_{ND}}$ . Therefore, by varying the velocity of

the ND filter relative to the velocity of the polymer, the incident writing power can be modulated proportional to  $T_{Eff}^{-z}$ . Beer-Lambert absorption is compensated at the focus when  $T_{Eff}$  equals the pre-exposure transmittance of 1 mm of material.

The intensity of laser focus in the material thus can be expressed as

$$I(x, y, z) = I_0(x, y, 0) \left( \frac{T_{Eff}}{T_m} \right)^{-z}. \quad (5.6)$$

In theory, if one wish to choose the velocity of ND filter movement such that  $T_{Eff}$  equals the pre-measured material transmittance, the index change introduce into the material should be made uniform along the material depth. Alternatively, the index profiles of the waveguide can be tapered up or tapered down when the  $T_{Eff}$  is designed to be smaller or larger than the material transmittance. Therefore, taper properties of the waveguides fabricated in the parallel direct-writing method are precisely controlled.

## 5.4 Pseudo-cutback method for 3D mode characterization

Both tapered and uniform 3D waveguides written into this diffusive photopolymer bulk are difficult to characterize by functions of length, because it is difficult to cut and polish polymer materials particularly the rubbery materials required for diffusion of the monomer. However, this difficulty can be overcome by exploiting the flexible nature of the polymer. A pseudo-cutback sample preparation process is developed, enabling optical quality surfaces along the waveguides for testing without cutting the material. I demonstrate that the mode performances along the waveguides can be characterized using an active mode imaging system. The test results show that I can fabricate SM 3D polymer waveguides, which have a uniform mode profile over 8mm and mode tapers up to 1:2.5.

### 5.4.1 Pseudo-cutback sample preparation method

I utilized the flexible nature of the polymer and develop a sample preparation procedure in order to characterize the waveguide performance as a function of length, shown in Fig. 5.7. The outline of the procedure is as follows. First, the liquid polymer materials are cast between flat glass plates separated by 1mm spacers. Room-temperature thermal polymerization solidifies the material into optical-quality slabs. The polymer slide samples are heated in oven at 60°C in order

to reduce the bonding between the polymers and glass surface, making the separation of the polymer slab from the glass mode much easier. Then bare polymer slabs are laminated together to form multi-mm samples. The coherent confocal microscopy verifies that the laminate boundaries have less than 0.1% reflectivity, indication of intimate contact. Glass microscope slides are then laminated to the front and back to act as optical windows. After waveguides are written and developed, the laminated stack is easily separated into optically-flat sections, avoiding the need to cut or polish the polymer. Since this material preparation process is different from the traditional cutback method, I call it “pseudo-cutback”.

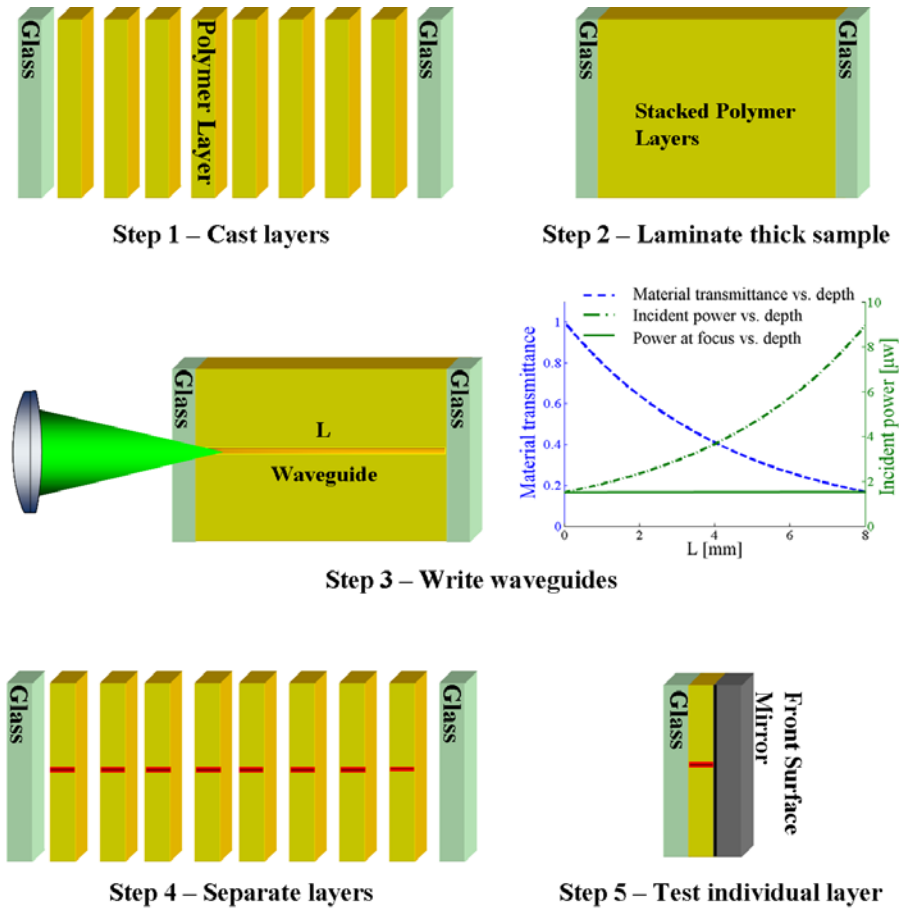


Figure 5.7. Pseudo-cutback method developed for polymers that cannot be cut or polished. Step 1: Cast individual polymer layers. Step 2: Laminate the layers into a thick polymer sample. Step 3: Write guides through the laminated polymer sample. The material transmittance (dashed line), the incident power curve (dash-dot line) and power at the focus (solid line) along the depth are also shown. Step 4: Separate the stack sample the individual layers. Step 5: Test individual layers.

### 5.4.2 Active mode imaging system

I have demonstrated the pseudo-cutback sample preparation method to achieve optical quality surfaces along the waveguide for testing without cutting the material. Here I present an active mode imaging system I have created to test the mode profiles of individual polymer layers, thus characterizing the taper performance of the waveguide. This active mode imaging system is integrated into the waveguide exposure platform, shown in Fig. 5.8. Each polymer layer is laminated to a front-surface metal mirror so that test of the waveguide can be performed in reflection.

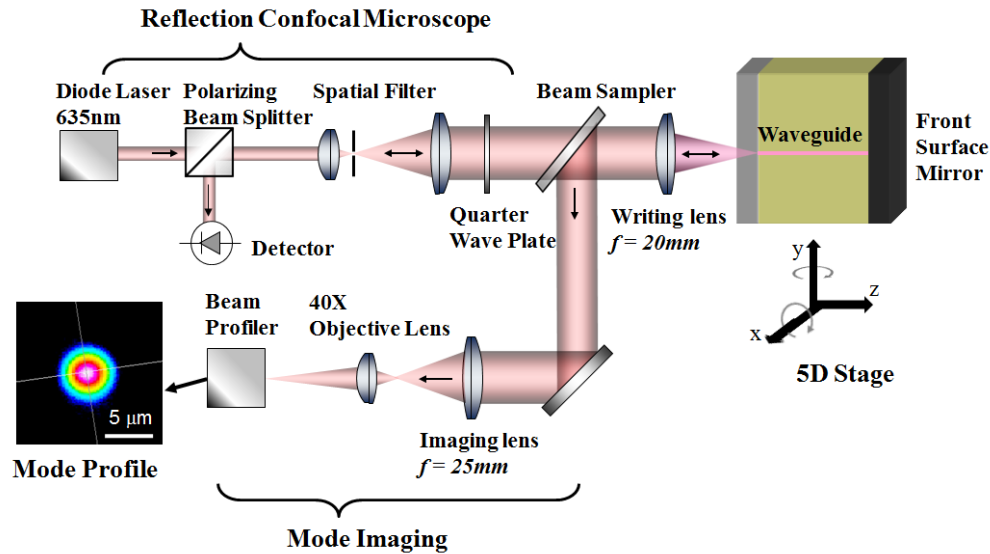


Figure 5.8. Optical layout of the active mode imaging system for waveguide characterization. A typical measured profile from a single-mode guide is shown in the inset, which is nearly perfect Gaussian in shape.

The incident laser focus with  $2.6\mu m$   $1/e^2$  diameter is aligned to the buried waveguide front facet. The incident laser beam is coupled into the fundamental mode of the waveguide. This guided mode propagates through the waveguide, reflects at the front surface mirror, and propagates back through the waveguide. When the guided mode exits the waveguide, it diffracts and is captured by the writing objective lens. Part of the captured beam goes to the confocal filter, while the rest of the beam goes to the mode imaging system. The coupling efficiency of the

incident laser beam into the guided mode is optimized by maximizing the power returned through the confocal filter, which rejects radiation modes and out-of-focus reflections to precisely characterize total round-trip loss. This precise round-trip loss measurement provides a convenient way to characterize the loss performance of the waveguides, which is used in Section 5.5. Without the waveguide, the incident laser beam diffracts through the 1mm polymer slab, reflects at the mirror. At most only 0.02% of incident light couples back to the detector. This reflection test method provides two advantages: (1) the path length is doubled, helping to separate guided from radiation modes; (2) only one alignment is needed, improving the repeatability of coupling loss measurement.

The magnified image of the guided mode is captured by a commercial beam profiler, WinCamD-UCD12 from DataRay Inc. The focal length of the writing objective is 20mm, and the focal length of the imaging lens is 25mm, providing a magnification of 1.25. Then, a 40x objective lens is used to further magnify the imaged mode profile. The total magnification of the mode imaging system is calibrated by using a single mode fiber, or a mirror. The light out of a single mode fiber patch cable, Thorlabs P1-630A-FC-1, at the wavelength of 633nm is imaged into the beam profiler. The mode field diameter at 633nm for the guided mode of the fiber is  $4.3\mu\text{m}$ . The imaged mode field diameter is  $239.3\mu\text{m}$ , yielding a magnification of about 55.7. Alternatively, a collimated laser beam from the diode laser at 635nm is focused at the mirror. This focus spot with a field diameter of  $4.0\mu\text{m}$  is imaged onto the beam profiler with size of  $228.7\mu\text{m}$ , yielding the magnification of about 56.6. I used a magnification of 56, which is the average of these two independent measurements, to calculate the mode size from the magnified images.

A typical user interface of the beam profiler for the measured mode profile is shown in Fig. 5.9. The effective diameter is used for the waveguide mode profile testing. The effective diameter is defined as the radius of a circle with the same size as all pixel areas that have the

intensity over  $1/e^2$  of the peak intensity of the mode profile image. The quality of the measured mode profiles is characterized by ellipticity and the Gaussian fit parameter. The ellipticity is the ratio between the minor diameter and the major diameter. The Gaussian fit parameter is defined as  $1 - \frac{\sum |f_m - f_{fit}|}{\sum f_{fit}}$ , where  $f_m$  is the profile of the measured mode and  $f_{fit}$  is the Gaussian fit profile. This Gaussian fit is based upon a fit algorithm that, while keeping the total area and centroid of the fitted Gaussian curve the same as the measured profile, iteratively adjusts the height and width of the Gaussian until the least squares difference between the actual profile and the Gaussian profile is minimized.

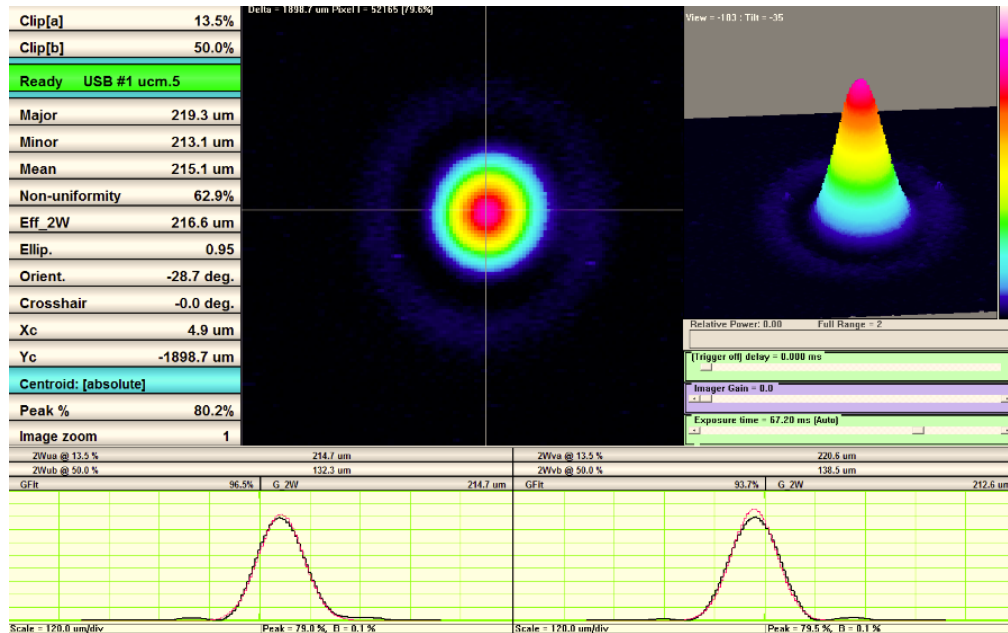


Figure 5.9. A typical user interface of the beam profiler for mode profile measurement.

### 5.4.3 Verification of single mode performance

Next section of this chapter shows that the measured mode profile successfully enables calculation of coupling efficiency, allowing propagation loss to be extracted from total measured loss. However, such success hinges on the premise that the guides support only a single mode. Since the mode image shown in Fig. 5.9 could be the sum of the fundamental and one or more

symmetric higher-order modes, an independent test must be conducted to verify that only a single mode is present. Scanning the incident beam focus across the guide excites the fundamental and possibly higher-order anti-symmetric modes. Coupling efficiency versus offset to these multiple modes will be broader than coupling to a single mode. This latter quantity can be calculated via the overlapping integral of two displaced Gaussian fields as shown in Fig. 5.10-(a) ~ (c). When the incident laser focus mode with radius  $w_1$  scans across the end facet of the buried waveguide, the incident laser mode couples into the waveguide and the confocal return is recorded. If the waveguide supports only a single Gaussian mode of radius  $w_2$ , the coupling efficiency is predicted by the overlap integral of this mode and the offset Gaussian incident focus mode be

$$\eta(\Delta x, \Delta y, \Delta z) = \frac{\left(\frac{w_1 w_2}{w_{0eff}^2}\right)^2}{1 + \left(\frac{\Delta z}{2z_{0eff}}\right)^2} \exp \left[ -\frac{\left(\frac{\Delta x}{w_{0eff}}\right)^2 + \left(\frac{\Delta y}{w_{0eff}}\right)^2}{1 + \left(\frac{\Delta z}{2z_{0eff}}\right)^2} \right], \quad (5.7)$$

where  $w_{0eff} = \sqrt{\frac{w_1^2 + w_2^2}{2}}$  and  $z_{0eff} = \frac{\pi w_{0eff}^2}{\lambda}$ .

I measured the coupling efficiency with the offset only in x, y or z direction respectively. The coupling efficiency is measured via the confocal filter to reject extraneous signals such as surface reflections and radiation modes. As shown in Fig. 5.10-(d)~(f) the measured coupling efficiency agrees well with the theoretical prediction. This confirms that the waveguides support only a single mode.

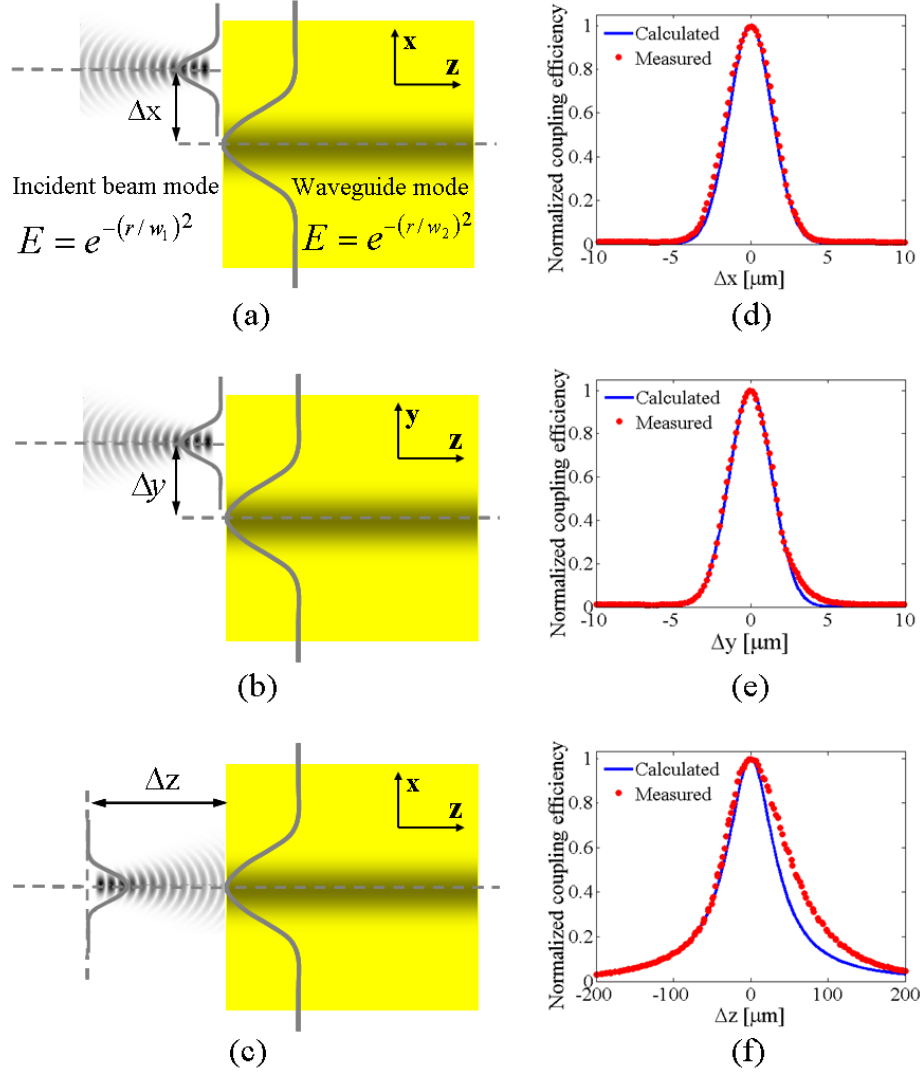


Figure 5.10. Verification of single-mode performance. (a) - (c) are the test geometries for x, y and z direction respectively. (d) - (f) are the measured and theoretically calculated coupling efficiencies as a function of offset in the x, y and z direction respectively. Disagreement at  $z > 0$  may be due to uncorrected spherical aberration.

#### 5.4.4 Mode profile test results

Mode profiles versus thickness for single-mode 3D uniform and tapered waveguides are presented in Fig. 5.11. These waveguides are written at 1mm/s using a focused spot of  $4.36\mu\text{m}$   $1/e^2$  diameter at wavelength of 532nm. The writing power is  $1.5\mu\text{W}$  at the front surface, modified by three power profiles  $T_{Eff}^{-z}$  along the waveguide's depth. One example of these power profiles is shown as the dash-dot line in Fig. 5.7. The power profile with  $T_{Eff} = 0.71$  yields a uniform



waveguide with mode diameters of approximately  $5.2\mu\text{m}$ , while the modes of waveguides written with  $T_{\text{Eff}} = 0.73$  and  $0.75$  are parabolically tapered. The mode profiles are nearly Gaussian (Gaussian fit quality [144]  $\geq 0.92$ ) and symmetric within measurement limits. The narrow error bars in Fig. 5.11 demonstrate the ability to write repeatable uniform and tapered waveguides. I'd like to point out one interesting finding. The pre-measured transmittance of the HDS 3000 polymers with half photoinitiation concentration is  $0.92$ , which is quite different from the effective material transmittance  $T_{\text{Eff}} = 0.71$ . In theory,  $T_{\text{Eff}}$  should equal the pre-measured material transmittance in order to gain uniform index change along the material depth. This mismatch is due to the complicated photoinitiation kinetics [145] of this HDS 3000 polymer. Two absorptive intermediate photoproducts are generated during photoinitiation, temporally increasing the absorptivity of the material and thus making it difficult to characterize this polymer material. This is one of the main reasons that we switch to the LBR polymer to fabricate GRIN structures with arbitrary index profiles, discussed in chapter 3.

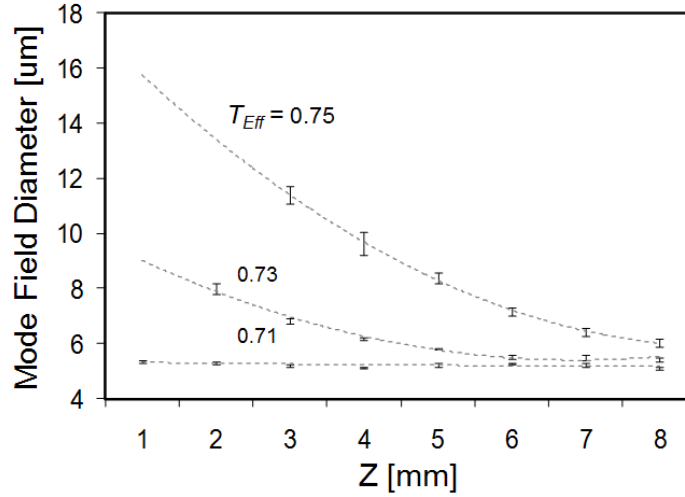


Figure 5.11. 3D characterization of tapered and untapered buried waveguides. The test procedure shown in Fig. 5.10 verifies that the waveguides are single mode at all points. The error bars are one standard deviation of seven samples at each point, demonstrating the repeatability of the process. Dotted lines are parabolic fits to show trends. Accurate data for several points could not be taken because the coupling between incident laser mode and the guided mode plummets in the weakly guiding limit so that the mode could not be captured on the beam profiler.

Given the index profile of a waveguide, the mode profile is uniquely determined but *not* vice versa. The index profile of a waveguide is not uniquely determined by the mode profile. However I can estimate peak index change  $\Delta n$  by assuming the index shape of the waveguide. Since the introduced index structure is proportional to the writing intensity with a single fit parameter, it reasonable to assume a Gaussian-shape index profile for the waveguides. For a single-mode waveguide with a Gaussian-shaped index profile  $n^2(r) = n_0^2 + NA^2 e^{-(r/\rho)^2}$ , the field radius  $r_0$  of the guided mode can be expressed as [146]

$$r_0 = \frac{\sqrt{2}\rho}{\sqrt{(NAk_0\rho - 1)}}^*, \quad (5.8)$$

where  $\rho$  is the radius of the index profile,  $NA$  is the numerical aperture of the mode,  $n_0$  is the bulk refractive index of the waveguide, and  $k_0 = 2\pi / \lambda_0$  is the vacuum wavenumber with  $\lambda_0 = 635$  nm. Sublinear kinetics of radical photoinitiation [147] result in an index change proportional to  $I^\alpha$ , where  $I$  is the writing beam intensity and  $\alpha$  is a single fit parameter [144]. Previous work has shown the sub-linear kinetic parameter  $\alpha$  to be  $\sim 0.75$  for this material [9]. Given  $I(r) = I_0 e^{-2(r/w_0)^2}$ , where  $w_0$  is the  $1/e^2$  radius of the writing beam, the index profile is  $n(r) \propto e^{-2\alpha(r/w_0)^2}$ , resulting  $\rho = w_0 / (\sqrt{2\alpha})$ . Therefore, the calculated  $NA$  for the uniform waveguide shown in Fig. 5.11 is estimated to be 0.12. Since  $NA$  of a single-mode waveguide can be approximated as  $NA = \sqrt{(n_0 + \Delta n)^2 - n_0^2}$ , where  $n_0 = 1.481$ , the estimated peak index change  $\Delta n$  is  $4.64 \times 10^{-3}$ , which is consistent with holographic recordings in the same material [137].

---

\* In the reference [146], the mode field is defined as  $\psi(r) = \psi_0 e^{-\frac{1}{2}(r/r_0)^2}$ , while the mode field in the mode profiler measurement is defined as  $\psi(r) = \psi_0 e^{-(r/r_0)^2}$ .

## 5.5 Loss measurement for uniform single-mode polymer waveguides

This mode characterization along the guide length enables simple and accurate measurement of propagation loss of a single waveguide via calculation and subtraction of coupling loss. To confirm the accuracy of this measurement, I exploit the repeatability demonstrated in Fig. 5.11 to test individual waveguides with different lengths, shown in Fig. 5.12-(a). Uniform waveguides are written with an exposure power of  $1.5 \mu\text{W}$  and power profile  $T_{\text{Eff}} = 0.71$  in three polymer slabs of thickness  $L = 1, 5$ , and  $10 \text{ mm}$ , respectively. Each slab is tested as shown in Fig. 5.8 to obtain a calibrated total round trip loss that only includes the excess propagation loss for length  $2L$  and coupling efficiency, by calibrating out the reflection loss at the front surface mirror and absorption of the material. Excess propagation loss was obtained by fitting the results of four experiments at each length to a line, as by the standard practice of the cutback method, shown in Fig. 5.12- (b). Excess propagation loss of four samples of each length yields  $0.147 \pm 0.009 \text{ dB/cm}$  waveguide loss. The y intercept from the linear fit gives the coupling loss, which equates  $0.393 \pm 0.124 \text{ dB}$ . Coupling loss can also be calculated based on the overlap integral of the incident laser focus and the mode profile of the single mode waveguide. The calculated coupling loss turns out to be  $0.413 \pm 0.056 \text{ dB}$ , which is close to the measured one.

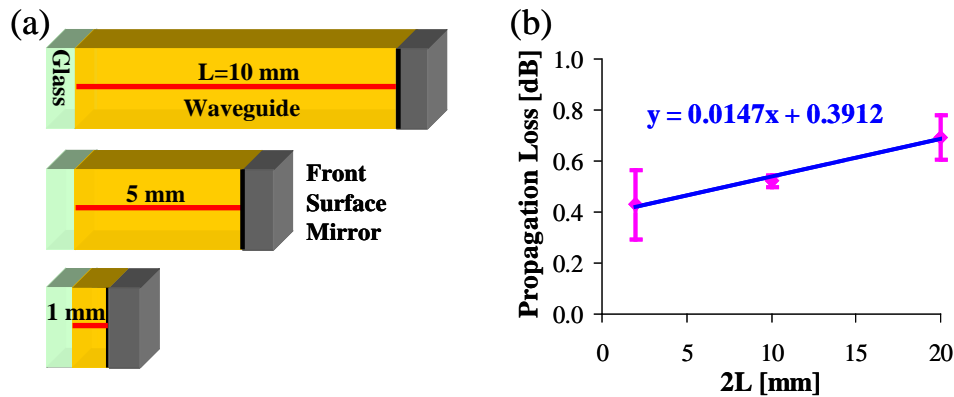


Figure 5.12. Experimental layout and results of loss measurement for the uniform single-mode waveguides. (a) is modified cutback method for the loss measurement. Couple the incident laser beam into the waveguide and capture the maximum power in the guided mode on the mode profiler. By comparing the power in the guided mode to the measured power when the incident laser beam is focused at the front surface mirror, the material

absorption and loss at the reflection surfaces are calibrated out. (b) Loss versus guide length.

This accuracy enables propagation loss measurement from a sample of a single length by subtracting the coupling loss calculated from the mode measurement from the total loss. For a 10-mm waveguide, the calibrated total round trip loss is 0.692dB. The calculated coupling loss due to mode mismatch is 0.413dB. Thus the excess propagation loss of the 10mm waveguides is  $0.140 \pm 0.043$  dB/cm, which agrees with the loss measured from the linear fit. Since the calibrated total round trip loss excludes bulk material absorption, an independently measured material absorption of  $0.141 \pm 0.038$  dB/cm needs to be added back to get a propagation loss of 0.28 dB/cm. This bulk material absorption is primarily due to incomplete initiator bleaching, which reflects on the yellowish color of the sample even after the flood cure. A new polymer material (the LBR polymer) is developed in our group to reduce the bulk material absorption at visible spectrum to a level that the absorption after the flood cure is mainly due to material scatter. This new diffusive photopolymer is initiated at the wavelength of 405nm. The formulation and other advantages compared to the HDS 3000 polymer are demonstrated in chapter 3.

The characterization of mode size and single-mode condition versus length enables precise understanding of the coupling loss even for tapered guides, which in turn permits measurement of propagation loss from a single sample length and avoids the need for cutback loss measurement.

## **5.6 Two extensions of uniform single mode waveguides**

So far, I have shown that it is feasible to make single mode uniform 3D waveguides in diffusive photopolymers with excess propagation loss less than 0.15dB and symmetrical waveguide tapers up to 1:2.5, which are very useful for optical interconnection for hybrid integrated photonics. Optical interconnection is a ubiquitous problem in the fabrication of nearly all single-mode optoelectronic devices, because, unlike purely electronic circuits, the majority of

optical systems demand multiple materials that cannot be fabricated in a single process. These materials include drawn glass fiber, lithographically patterned semiconductors, deposited dielectric films, grown crystals, replicated diffractive elements and ground lenses [148]. Surfaces are cleaved, diced or polished, resulting in dimensional tolerances incompatible with passive registration of single-mode interconnects, even when the initial fabrication is lithographically precise. The active search for a solution to this problem is documented in journals [149], conferences [150] and textbooks [151]. A representative problem is interconnection of single-mode waveguides. Examples include chip-to-chip communication, pig-tailing of lasers and fiber micro-optic components. Micro-machined V-grooves have been used to passively align fibers to on-chip waveguides [152] but cannot match dissimilar modes, while on-chip grating couplers can couple from a near-normal fiber into a smaller waveguide but must be actively aligned and adhered to the chip [153]. Although such solutions are employed in niche applications, the method first formalized for telescopes [154] remains the one that is universally used. Specifically, the first of this step matches the two modes via waveguide tapers and/or micro-optics. The second step aligns the component to within several hundred nm to maximize performance of the active circuit. Then, attach the components to a mechanical scaffold using an adhesive. Finally, seal the enclosure to isolate the optical surfaces from the environment. The resulting device is (1) expensive and limited to small quantities due to active alignment, (2) large due to the scaffold and (3) delicate because of the nanometer tolerances held only by adhesive. These features are acceptable in high-value applications but not high-volume applications that demand the opposite characteristics.

The unique characteristics of the diffusive photopolymer provide an alternative way to integrate a variety of thin transmission, reflective optics with single mode waveguides, making the diffusive photopolymer a highly preferable material platform for hybrid integrated optics applications. The optical components are encapsulated in an initially-liquid diffusive polymer

that protects against contaminants. The encapsulant hardens at room temperature, permanently fixing the component positions. The lithography system uses the microscopes [7] to determine the 3D locations of the subcomponents to sub-100 nm precision. These coordinates and the known mode profiles are used to directly write a custom mode-matching interconnect.

This section demonstrates two extensions of this 3D optical wire bonding in diffusive photopolymers. Waveguides fabricated by the parallel direct-write can naturally go through thin transmission optical elements or bounce back at the reflective optical elements to form sharp waveguide bends. The uniform single mode waveguide and these two extensions are essential for hybrid integrated optics applications.

### 5.6.1 Waveguides through thin optics

When demonstrating waveguides through thin optics, I used thin glass sheet instead of thin optics for simplicity. One 5mm bare photopolymer slab is laminated to each side of a thin glass sheet. A 1mm microscope slide is laminated to the front of the sample to provide a writing window and a front surface mirror to the back for waveguide characterization. The sample geometry is shown in Fig. 5.13. I used three thin glass sheets with thickness of 30um, 50um and 100um respectively.

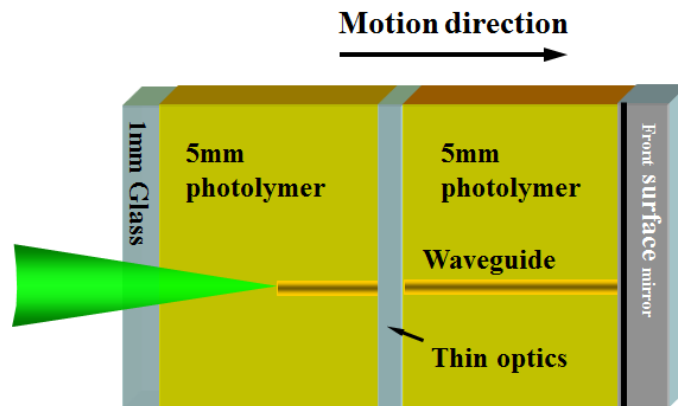


Figure 5.13. Sample geometry for direct-writing a waveguide through thin optics.

Waveguides are written into the sample by dragging the incident laser focus through the polymer sample. The exposure condition is the same as the uniform single mode waveguides demonstrated in Fig. 5.11. After the waveguides are formed, the sample is flood cured under an incoherent uniform light source. Then the waveguides are tested under the active mode imaging system to get the mode performance and the coupling loss through the thin optics. When the incident laser focuses at the front glass slide and polymer surface, without waveguides, the beam diffracts, shown in Fig. 5.14-(a). With waveguides, the incident light couples into the guided mode, which propagates through the waveguide, diffracts at the thin glass, and couples back to the waveguide, as shown in Fig. 5.14-(b).

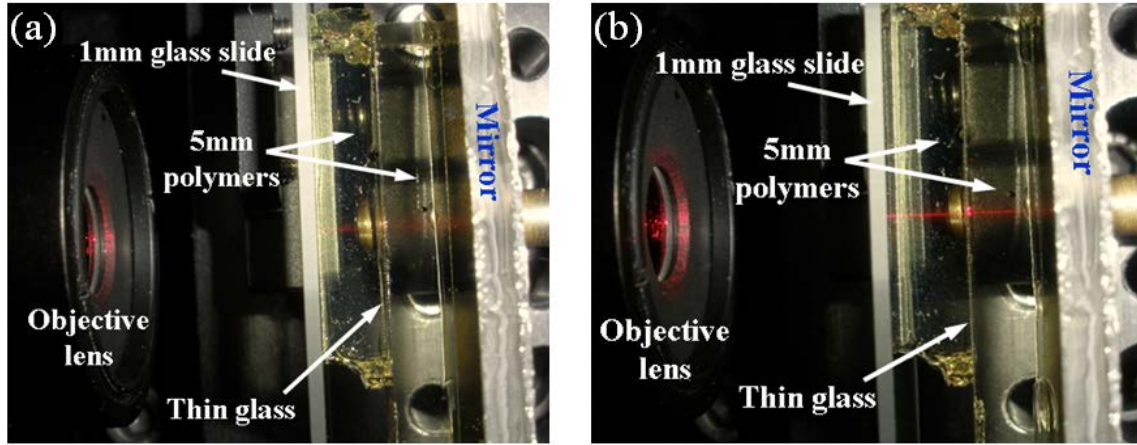


Figure 5.14. Demonstration of the light guided in the waveguide through thin glass. (a) The incident laser focus diffracts without waveguide. (b) The incident laser focus couples into the waveguide.

Given that the waveguides before and after the thin glass are identical, the coupling loss through the thin glass, demonstrated in Fig. 5.15, can be theoretically calculated as

$$\eta(\Delta z, w_0) = \frac{1}{1 + \left( \frac{\Delta z}{2z_0} \right)^2}, \quad (5.9)$$

where  $w_0$  is the mode radius of the uniform single mode waveguide at 635nm,  $\Delta z$  is the thickness of the thin glass sheet,  $z_0 = \frac{n\pi w_0^2}{\lambda}$  is the Rayleigh range of the diffracted mode in the thin glass and  $n$  is the refractive index of the thin glass.

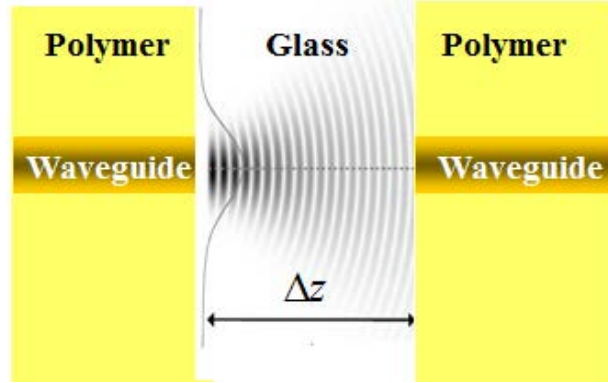


Figure 5.15. The coupling loss through the thin glass due to the shife in z.

The measured mode field diameters and coupling loss of waveguides through thin glass sheets with different thickness are shown in Table 5.2. The mode field diameter is the mean of six measured data points for each sample. The coupling loss is the mean of six measured data points for each sample.

Table 5.2: Experiment results of mode profiles and loss measurement for waveguides through thin glass with different thickness

Glass thickness ( $\mu\text{m}$ )	Mode field diameter ( $\mu\text{m}$ )	Standard Deviation ( $\mu\text{m}$ )	Coupling loss through glass (dB)	Standard Deviation (dB)
30	4.83	0.07	0.837	0.043
50	5.13	0.04	1.353	0.041
100	5.05	0.08	5.413	0.014



The comparison of the measured coupling loss to the theoretical calculated ones is shown in Fig. 5.16. The mismatch between theoretical calculation and experiment measurement are 0.2881dB, 0.2908dB and 0.1084dB respectively for 30 $\mu$ m, 50 $\mu$ m and 100 $\mu$ m thin glass. Such differences, all of which are within 0.3dB, may be attributed to shift between the two layers, which might be caused by the material shrinkage during the flood-cure step and/or different thermal expansion coefficient between the polymer and the glass.

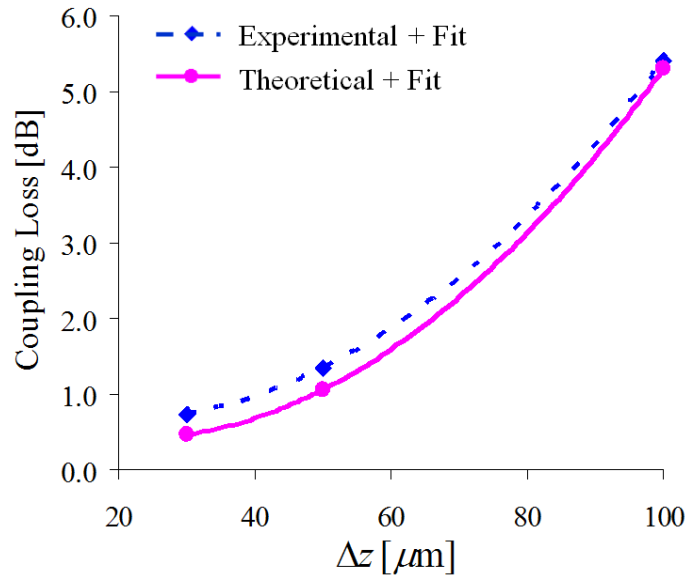


Figure 5.16. The comparison of the measured coupling loss to the theoretical calculated ones through thin glasses at the thickness 30 $\mu$ m, 50 $\mu$ m and 100 $\mu$ m. A polynomial fitting is applied to both the measured and theoretical calculated coupling losses.

### 5.6.2 Sharp waveguide bends

Sharp waveguide bends make integrated optical circuit compact [155] and provide convenient vertical coupling for optical circuits [156,157]. The size of sharp waveguide bends typically limits the degree of the integration, because the propagation loss at the waveguide bends increases exponentially with the inverse bend radius [158]. Also, this bend radius is determined by the index contrast of the waveguide. Therefore, high-index-contrast waveguides, such as silicon (Si) and polycrystalline silicon (poly-Si) embedded in a low index cladding of SiO<sub>2</sub>[159, 160], gain some advantages over low-index-contrasts waveguides, such as silica and

polymer waveguides [161, 162]. First, high-index-contrast waveguides will confine the light by total internal reflection even when the bend radius is at the order of microns [163,164], while low-index-contrast waveguides typically have a minimum radius of multiple millimeters [165,166]. Secondly, the size of a sharp waveguide bends can be reduced furthermore by using resonant cavities [167,168] or corner mirrors [169,170] in the bending region. While the high-index-contrast waveguides offers dense integration, they also bear several disadvantages. The interface roughness of waveguide with such high index contrast ( $\Delta n \approx 2$ ) results scatter loss, which is proportional to  $(\Delta n)^3$  [171]. Also it poses challenges for fiber-to-chip interconnection because of high insertion loss due to mode shape mismatch, tight tolerance for misalignment and sensitivity to fabrication defects.

Alternatively, materials with a large refractive index can be arranged to form waveguides with low refractive index contrast, for example, SiGe on Si waveguides [172] and silicon-on-insulator (SOI) rib waveguides [173]. Vertically etched faces can be functioned as mirror to realize sharp waveguide bends [174,175,176].

However, both the silica waveguide and polymer waveguides have low refractive index contrast as well as low refractive index. Silica waveguides are most commercial available planar lightwave circuits (PLCs). Polymer waveguides continue to receive attention as an attractive candidate for lightwave circuits. Reducing the size of waveguide bends for this type of waveguides has been an active research area in the past decade. One solution is to introduce an etch region that defines a high index contrast bend with tapers on both ends to couple light into and out of the bend region [177,178], thereby reducing the size of the silica waveguides to microns. However this method increases fabrication complexity and is impractical for polymer waveguides. Alternatively, corner mirror and air trenches have been applied in planar silica and polymer waveguides to form compact sharp waveguide bends [179,180].

Here I demonstrate a single-mode  $90^\circ$  waveguide bend in diffusive photopolymers by using a corner mirror. The polymer sample geometry for fabricating and characterizing  $90^\circ$  sharp waveguide bends is shown in Fig. 5.17. The isosceles right triangle polymer sample is made by casting the material into a glass mold. Then the bare photopolymer is dissembled from the triangular glass mold. A front surface mirror is laminated to the hypotenuse of the triangle sample to provide  $90^\circ$  bending. A standard microscope cover glass is laminated to one side of the right triangle sample to provide a writing window and a front surface mirror is laminated to the other side for mode imaging and loss measurement.

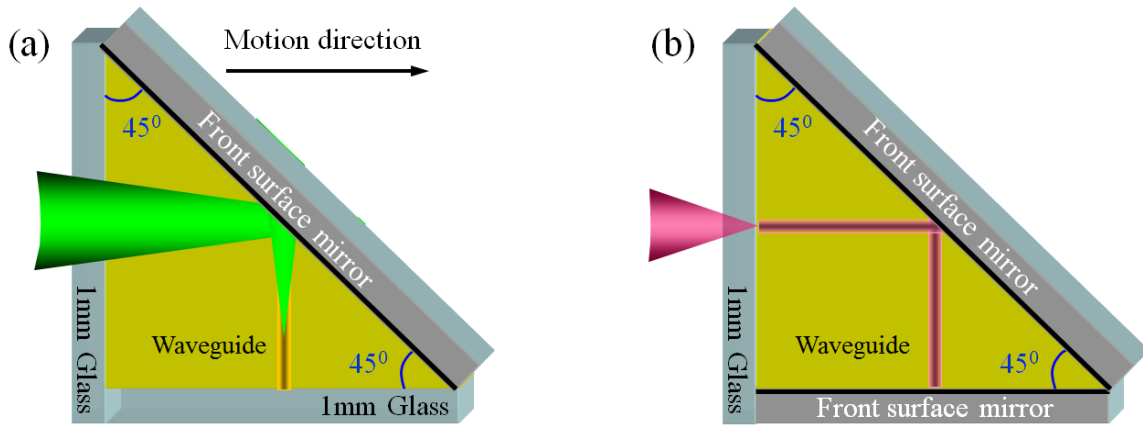


Figure 5.17. Sample geometry for  $90^\circ$  sharp waveguide bend: (a) waveguide bends fabrication through parallel writing and (b) waveguide bends characterization through the active mode imaging.

The sharp waveguide bend is naturally formed when the incident laser focus is moved through material and reflected  $90^\circ$  at the front surface mirror. After the sharp waveguide bend is formed and the sample is flood cured, the waveguide bend is tested using the active mode imaging setup. The incident 660 nm diode laser beam focus spot at the front glass and photopolymer interface is  $2.56\text{ }\mu\text{m}$ . The measured mode diameter of the polymer waveguide is  $5.28\text{ }\mu\text{m}$ . The total length of the waveguide is 10 mm. The calibrated total round trip loss is 5.78dB, which includes a mode coupling loss, an excess propagation loss and the loss at the  $90^\circ$  sharp waveguide bend. The coupling loss is due to mode size mismatch and the angle misalignment.

The angular misalignment is caused by the imperfection of the isosceles right triangle polymer sample I made. Due to the limited availability of high quality isosceles right triangle glass mold, the isosceles right triangle polymer samples are made from commercial square glass cuvettes with size of 10mm×10mm×50mm. A piece of glass slide with thickness of 1mm is dropped into a glass cuvette, which separates the cuvette into two isosceles right triangle regions. Thus, after casting the liquid polymer material into this cuvette, two isosceles right triangle polymer samples are formed after the polymer is thermally cured. Then, isosceles right triangle bare polymer samples are delaminated from the glass mold for experimental use, shown in Fig. 5.17. However the location of the glass slide deviates from the actual diagonal plane of the square cuvette. Therefore the bare polymer sample is not perfect isosceles right triangle, shown in Fig. 5.18.

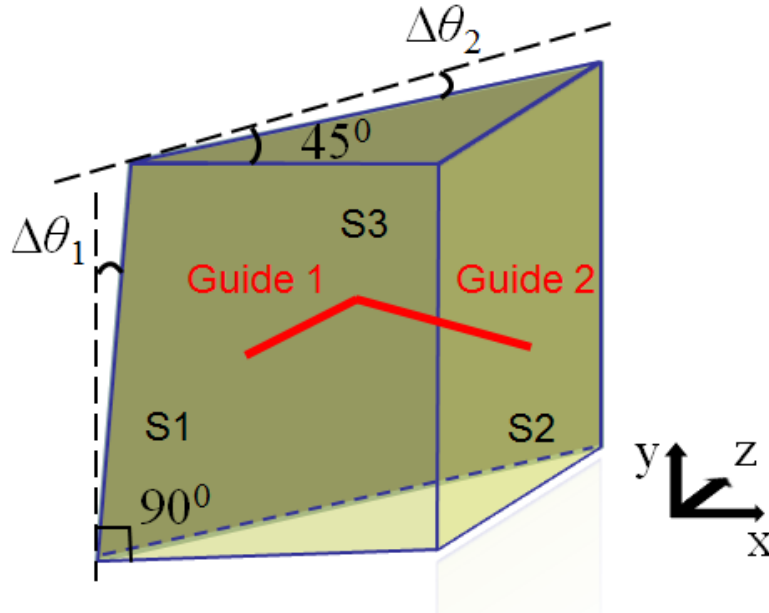


Figure 5.18. Demonstration of the deviation of the polymer sample from a perfect isosceles right the triangle.  $\Delta\theta_1$  shows the deviation of the angle between the diagonal plane of the sample and the x-y plane from  $45^\circ$ .  $\Delta\theta_2$  is the angle that diagonal plane of the sample deviates from perpendicular to x-z plane. S1 is the x-y plane, S2 is the y-z plane, and S3 is the diagonal plane of the triangle sample. Guide 1 is the front portion of the waveguide bend, while Guide 2 is the back portion of the waveguide bend.

During the waveguide bend fabrication, the polymer sample is precisely aligned so the front surface (S1 in Fig. 5.18) of the sample is perpendicular to the incident laser beam. The waveguide bend is formed by the reflecting of the laser beam at the corner mirror. The front portion of the waveguide bend (Guide 1 in Fig. 5.18) is perpendicular to Surface 1. However, the back portion of the waveguide bend (Guide 2 in Fig. 5.18) is not perpendicular to back surface of the sample (S2), because of the two deviation angles. Even worse, the reflection of laser beam at the corner mirror during the waveguide fabrication doubles the effect of the two deviation angles  $\Delta\theta_1$  and  $\Delta\theta_2$  for Guide 2.

During the waveguide test, a front surface mirror is laminated to the front surface of the sample (S1), so that the guided mode in the waveguide reflects at the front surface mirror and automatically couples into the waveguide with minimum loss, since the formed waveguide is perpendicular to the front surface mirror. A diode laser beam at the wavelength of 660nm is aligned perpendicularly to back surface of the sample (S2) and is coupled into the guided mode in the waveguide. The deviate angle in y-z plane for Guide 2 from perpendicular to S2 is  $2\Delta\theta_1$ , while the deviate angle in x-y plane for Guide 2 from perpendicular to S2 is  $2\Delta\theta_2$ , shown in Fig. 5.19. The coupling efficiency from the incident laser beam to the fundamental mode of the Guide 2 is express as:

$$\eta(2\Delta\theta_1, 2\Delta\theta_2) = \left( \frac{w_1 w_2}{w_{0eff}^2} \right)^2 \exp \left( - \left( \frac{w_1 w_2}{w_{0eff}^2} \right)^2 \left( \frac{2\Delta\theta_1 + 2\Delta\theta_2}{\theta_{0eff}} \right)^2 \right), \quad (5.10)$$

where  $\theta_{0eff} = \frac{\lambda}{\pi w_{0eff}}$ , and  $w_{0eff} = \sqrt{\frac{w_1^2 + w_2^2}{2}}$ .

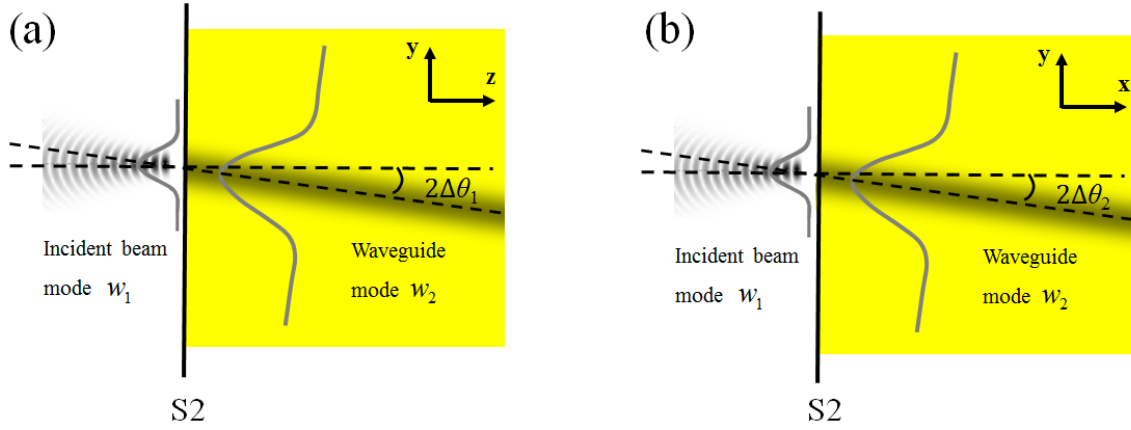


Figure 5.19. Demonstration of the waveguide coupling loss, which is due to angular misalignment in (a) y-z plane and (b) x-y plane.

The angle  $2\Delta\theta_1$  is measured to be 0.045rad and  $2\Delta\theta_2$  is 0.069rad. The coupling loss is calculated to be 3.745 dB. Given the excess propagation loss is previous measured to be 0.140 dB/cm, the excess loss at the  $90^\circ$  sharp waveguide bend is 0.868dB/bend. This excess loss at the bend is potentially due to the complicated index formation at the bending area, which is caused by exposure beam overlapping due to mirror reflection. The experimental measured  $90^\circ$  sharp waveguide bend reported in the literature is in the range of 0.5~3 dB/bend [181,182,183]. The lowest measured  $90^\circ$  bend loss, to my best knowledge in the literature, is 0.32dB/bend in a SOI rib  $90^\circ$  waveguide bend [165]. A 0.74 dB per bend loss is reported for a polymer multimode waveguide  $90^\circ$  bend with a bend radius of 13.5mm and peak index change of 0.0296[184]. Thus, the  $90^\circ$  sharp waveguide bend I fabricated has satisfactory loss performance. The ability to make sharp waveguide bends in diffusive polymers with a satisfactory loss performance is meaningful for the hybrid integrated optical circuits, such as making the circuits compact and being able to integrated reflective optics.

## 5.7 Conclusions

I have demonstrated uniform and parabolically tapered single-mode 3D waveguides in diffusive photopolymers and introduced methods to accurately measure mode profile and propagation loss along the guide length. Single-photon holographic photopolymers developed for data storage are shown to be an attractive platform for 3D photonics due to their high sensitivity and self-developing index change. A logarithmic ND filter synchronized to the sample motion is shown to be a natural external modulator to compensate for the Beer-Lambert absorption in order to fabricate uniform and tapered single-mode waveguides. A laminated sample fabrication method is shown to provide optical-quality surfaces for direct measurement of the evolution of the single-mode profile along the taper length. This precise and repeatable characterization enables coupling loss to be accurately calculated to find propagation loss from single sample measurements. The accuracy and repeatability of both the fabrication procedure and testing methods are verified by loss measurements for guides of 1 to 10 mm length which show excellent agreements. These results demonstrate single-mode waveguides with 0.147 dB/cm excess propagation loss and symmetrical tapers up to 1:2.5 using 1.5  $\mu\text{W}$  of continuous write power. Two extensions of this 3D optical wire bonding in diffusive photopolymers are also demonstrated. Waveguides fabricated by the parallel direct-write can naturally go through thin transmission optical elements or bounce back at the reflective optical elements to form sharp waveguide bends. The uniform single mode waveguide and these two extensions are essential for hybrid integrated optics applications.

# Conclusion and Future Work

### 6.1 Summary

This thesis demonstrated three-dimensional gradient index (GRIN) optics fabricated in diffusive photopolymers. These polymer optical components have localized index structures, which are self-developed in the diffusive photopolymers by introducing localized illuminations. Several quantitative characterization methods for the index structures are also demonstrated in this thesis. Based on the size of the formed index structures, the photopolymer optics studied in this thesis can be divided into two categories: GRIN lens based optics and waveguide based optics. GRIN lenses and lens arrays with parabolic index profiles are created through Gaussian beam exposure, while GRIN lenses with arbitrary index profiles are formed through a dual-axis galvo scanning exposure. Waveguide based optics, on the other hand, are fabricated through the parallel direct-write lithography, and includes uniform waveguides, waveguide tapers, waveguides through thin optics and  $90^\circ$  sharp waveguide bends.

Chapter 2 introduced a single convenient method to make GRIN micro lenses and GRIN lens arrays in the *Tapestry*<sup>TM</sup> HDS 3000 photopolymer. At its core, this method exposes the photopolymer under a defocused Gaussian beam from a low-power CW laser. This fabrication method has the following advantages. First, the exposure dose distribution can be controlled by changing the exposure power, the exposure time and the defocus distance thus the exposure beam size. These variables are sufficient to explore a wide range of GRIN lenses in single convenient exposure geometry. Second, the GRIN lens arrays can be fabricated by a simple step-and-repeat process, where the lens position and properties can be flexibly changed on demand. Third, I use a revised scanning phase microscope [7] to quantitatively measure the index profile of the



fabricated GRIN lens. This revised differential transmission phase microscope is conveniently integrated into the lens exposure system, which facilitates monitoring of index formation during the fabrication. Furthermore, the Gaussian, when truncated by  $O_2$  threshold, yields a generally parabolic shape. Since the Gaussian exposure is convenient and the parabolic index profile is a standard GRIN profile, this motivates why Gaussian exposure is actually a useful way of making lenses. I have demonstrated the capability to create GRIN lenses with NA between 0.05 and 0.13 and diameter from 40 to 1000  $\mu\text{m}$ .

Chapter 3 extended to a more general GRIN lens fabrication method with arbitrary index profiles in a new diffusive polymer, named *Light Blue Resin*. This method utilizes a galvo scanning system to rapidly draw a two dimensional dose distribution in the polymers. Thus, it is analogous to an instantaneous exposure to the material instead of a sequential exposure. The index profiles of the fabricated lenses are characterized in transmission by a Shack-Hatmann wavefront sensor, which is convenient to use and provides a two dimensional index profile within a second. The LBR polymer is developed in our group. Thus we can study this polymer based on the formulation and alter the formation to suit different applications. A preliminary index formation study reveals several useful characteristics of the LBR polymer. First, the profile of the introduced index structures is determined linearly by the photoinitiator consumption distribution. Second, oxygen narrows structures by locally suppressing polymerization below a threshold dose. Third, baking the sample at  $60^\circ\text{C}$  after exposure increases the index change without changing the index shape, which provides a convenient way to fabricate high index structures with controlled profiles. And last, the index change is linear to radical generation, which is not typical of most radical systems that undergo bimolecular termination and sublinear initiation kinetics. This linear response also simplifies design. This index formation model provides a meaningful guidance to fabricate arbitrary index structures with high fidelity in the LBR polymer.

Chapter 4 demonstrated the design, fabrication and testing process for a hybrid GRIN axicon lens. This hybrid GRIN axicon includes an on-shelf GRIN rod lens to provide the offset of the focus and a polymer GRIN phase plate to extend the depth of the focus. A radial BPM MATLAB simulation program is used to directly search the optimal index profile of the GRIN phase plate. An 8-step fabrication procedure is established to make the designed index in a polymer metal tube sample. This 8-step fabrication procedure solves various problems that emerged during the index fabrication process, such as clear oxygen effect and accommodate material shrinkage. The fabricated index profile of the GRIN phase plate is measured by a Shack-Hartman wavefront sensor. The measured index profile of the GRIN phase plate shows a good fidelity with the design. And the DOF of the hybrid GRIN axicon lens I made shows 10 times improvement compared to the DOF from the off-the-shelf GRIN rod lens at the testing wavelength of 532 $\mu\text{m}$ .

Chapter 5 has demonstrated uniform and parabolically tapered single-mode 3D waveguides in diffusive photopolymers and introduced methods to accurately measure mode profile and propagation loss along the guide length. Single-photon holographic photopolymers developed for data storage are shown to be an attractive material platform for 3D photonics due to their high sensitivity and self-developed index structures. A logarithmic ND filter synchronized to the sample motion is shown to be a natural external modulator to compensate for Beer-Lambert absorption in order to fabricate uniform and tapered single-mode waveguides. A laminated sample fabrication method is shown to provide optical-quality surfaces for direct measurement of the evolution of the single-mode profile along the taper length. This precise and repeatable characterization enables coupling loss to be accurately calculated to find propagation loss from single sample measurements. The accuracy and repeatability of both the fabrication procedure and testing methods are verified by loss measurements for single mode uniform waveguides. These results demonstrate single-mode waveguides with 0.147 dB/cm excess propagation loss

and symmetrical tapers up to 1:2.5 using 1.5 mW of continuous write power. This chapter also demonstrated two extensions of this 3D optical wire bonding in diffusive photopolymers. Waveguides fabricated by the parallel direct-write can naturally go through thin transmission optical elements or bounce back at the reflective optical elements to form sharp waveguide bends. The uniform single mode waveguide and these two extensions are essential for hybrid integrated optics applications.

## **6.2 Future research directions**

The future research about fabricating 3D GRIN optics in diffusive photopolymers has two main directions. The first direction is to make new forms optical components in the diffusive polymers and to apply these polymer optical elements to create functional devices. The second direction is to continuously characterize the diffusive polymer materials and engineer the materials to suit different needs.

### **6.2.1 Future studies for 3D index structure fabrication**

I have demonstrated our ability to fabricate and quantitatively characterize GRIN lens based polymer optics and waveguide based optics. Thus, the future work on one hand will continue exploiting current methods or developing new methods to fabricate new forms of polymer optics. On the other hand, continuous efforts are needed to apply the individual polymer optics to make functional devices. For example, a 3D waveguide taper can be used to connect an on-chip SiN ridge waveguide to an off-chip fiber, which is essential for silicon chip package, shown in Fig. 6.1.

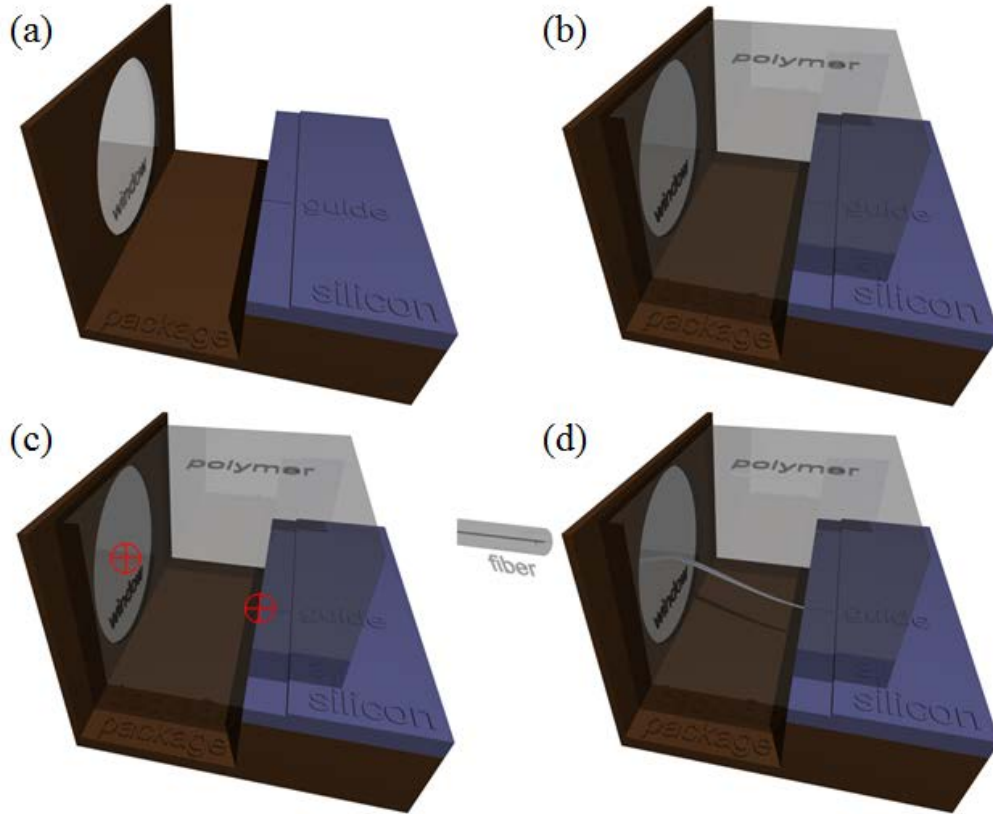


Figure 6.1. Process for on-chip rib waveguide to off-chip fiber connector packaging. (a): The chip is hard-mounted within a package which includes a thin ( $\sim 25$  micron) window centered on an external fiber connector. (b): The edge of the chip is encapsulated with polymer which fills the chip-window gap. (c): The optical bond, working through the package window, identifies the waveguide and window center coordinates. (d): The written waveguide tapers for asymmetry and mode-mismatch of the waveguide and bends from the uncontrolled position of the chip to the center of the connector ferrule. A fiber later inserted into the connector is efficiently connected to the waveguide.

After electrical and physical bonding of the chip, the encapsulating polymer is injected into the package between the edge of the chip containing the waveguide facet and the package wall containing a fiber-optic connector with a thin window. This is a typical hybrid single-mode interconnect in that the relative 3D offset between the center of the fiber connector and the waveguide facet are unknown due to the tolerances of the chip location. Additionally, at 1550 nm the modes mismatch by a typical factor of 2.5 if an on-chip taper is utilized. Conveniently, if component location and waveguide writing are performed through the side of the package, as illustrated, this application can use the symmetric SM waveguides investigated in chapter 5.

This problem illustrates why active coupling is impractical as an alignment guide – the silicon ridge behind the SiN taper is opaque at the visible spectrum. Even if a 1550 nm probe laser were employed, the circuit may contain no detectors and is not complete, so cannot be operated electrically. Instead, the position of the SiN ridge is detected through confocal reflection microscopy which is integrated into the parallel direct-write lithography platform as shown in Fig. 5.6. A 3D S-bend waveguide path combined with a 1:2.5 taper can be fabricated by the parallel direct-write lithography. Then, the polymer is flood-cured to remove all active chemical species and crosslink the remaining monomers. An external fiber can now be inserted into the external ferrule to efficiently and robustly communicate with the on-chip integrated optics.

And finally, significant further efforts are needed to make a functional hybrid integrated optical circuit in the diffusive photopolymer. One example is implementing a 1550nm mode-locked laser into an integrated circuit, which is more compact, stable and less expensive through potential mass production, shown in Fig. 6.2.

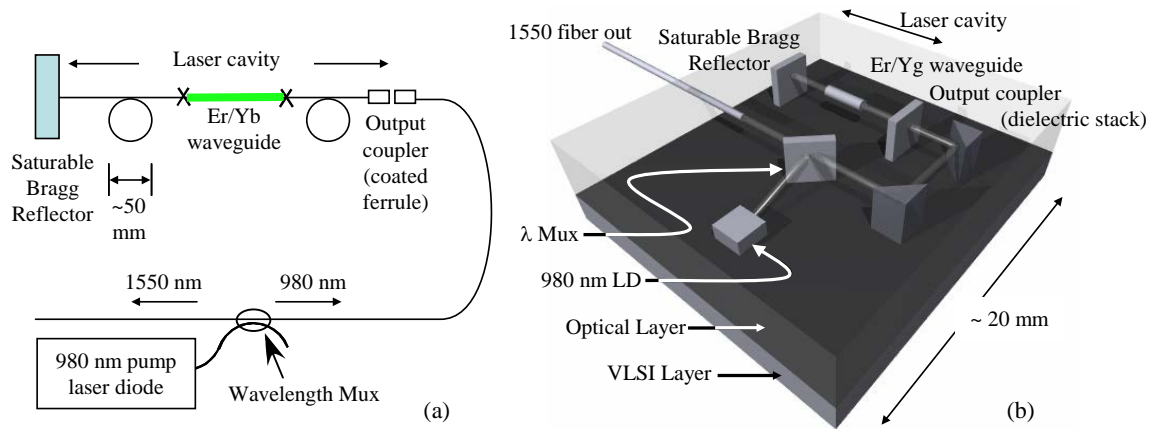


Figure 6.2. A 1550 nm mode-locked laser that is implemented (a) in fiber and (b) in a hybrid optical integrated circuit via 3D-routed waveguides in an encapsulating photopolymer. Note the 90° bends implemented with embedded prisms, the integrated fiber connection and complete hybridization on VLSI.

### 6.2.2 Future studies for characterizing and engineering polymer materials

I have derived an index formation model for the LBR polymer. This index formation model provides a fundamental guidance to fabricate custom design GRIN optics in the polymer. However this model is based the finalized index structures of large scale exposures with a diameter of couple hundred micrometers. Research work done by other two group members has shown that the size of the exposure feature affects the dynamic interaction of the chemical reactions during the index formation process, which includes initiation, polymerization, termination process and diffusion of all the active species in the polymer. Therefore, a more general and correspondingly more complicated model is needed to fully capture the dynamic of the chemical reactions in the polymer. A complete understanding the chemical reactions in the polymer during the index formation is essential.

The monomer diffusion speed limits the turnaround time for fabricating large scale index structures in the polymer, which may become the main obstacle to commercial applications. One potential solution is to use a liquid system to significantly increase the monomer diffusion. An alternative solution is to design sample geometry to reduce the required monomer diffusion distance. One example is to coat a layer of liquid monomers to the bare thin polymer layer. Now the monomers can diffuse from the liquid monomer layer directly into the polymer layer, potentially remove the limitation for fabricating large scale structures in the polymer.

The rubbery and permeable polymer matrix is required for monomer diffusion to form the localized index structures in the diffusive polymer. Also the rubbery matrix has the advantages to encapsulate various optoelectronic components in the polymer. However, as described in chapter 4, the rubbery polymer is not mechanically strong enough, requiring a high modulus material to seal the polymer element, thus complicating the polymer packaging process. One potential solution is to develop a polymer material with controlled material properties during the polymer optics fabrication process. For example, the polymer is rubbery to form localized

index structures, then turns into a high modulus solid through a final flood cure process. A two-stage network forming polymer [185] has been reported recently to achieve material properties at different stages of the material processing.

## Appendix A

# Calibration of the modified differential transmission phase microscope

This section briefly introduces the PSDs and discusses the calibration of the differential transmission phase microscope. PSDs are a type of photo detector used to precisely measure the position of a light spot. PSDs can be classified into two types: isotropic sensors and discrete sensors. The isotropic PSDs have a uniform sensor surface that supplies continuous position data, while discrete PSDs have multiple isolated detectors on the sensor surface and return position data through differences of the individual photocurrents. The PSD used in my experiment is an isotropic duo-lateral silicon photo detector that provides an analog output directly proportional to the position of a light spot on the active area of the detector. The PSD consists of an n-type silicon substrate with two uniform resistive layers separated by a p-n junction, shown in Fig. A.1-(a). The front side has a p-type resistive layer with two contacts at opposite ends. The back side has an ion implanted n-type resistive layer with two contacts at opposite ends placed orthogonally to the contacts on the front side. A light spot within the spectral range of silicon will generate a photocurrent that flows from the incident light location through the resistive layers to the electrodes. The resistivity of the ion implanted layer is extremely uniform. Therefore, the photo-generated current at each electrode is inversely proportional to the distance between the incident spot of light and electrodes. The PSD outputs track the motion of the centroid of power density to a resolution up to  $1.25\text{ }\mu\text{m}$  independent of light intensity and the linearity is better than 0.3%. The linearity here is defined as geometric position error divided by the detector length and is measured within 80% of the detector length [186]. The photoelectric current generated by the



incident light flows through the device and is seen as two input currents and two output currents, shown in Fig. A.1-(b).

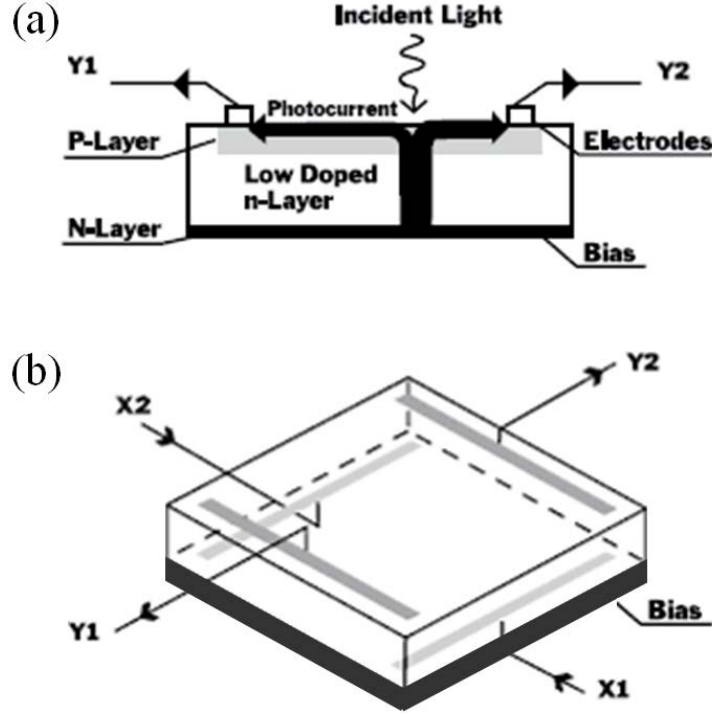


Figure A.3. Theory of operation of a duolateral isotropic position sensitive detector [186]. (a) shows the layout and working principle of an isotropic PSD. (b) shows the photocurrent that flows in a duo-lateral PSD.

The distribution of the output currents directly reflects the light position in the Y dimension, and the distribution of the input currents reflects the light position in the X dimension. Thus, the location of the centroid of the incident light can be expressed as [187]:

$$\begin{aligned} p_x &= L \frac{I_{x1} - I_{x2}}{I_{x1} + I_{x2}}, \\ p_y &= L \frac{I_{y1} - I_{y2}}{I_{y1} + I_{y2}}, \end{aligned} \quad (A.1)$$

where  $p_x$ ,  $p_y$  are the x and y position of the light spot centroid,  $I_{x1}$ ,  $I_{x2}$ ,  $I_{y1}$ ,  $I_{y2}$  are the four currents respectively and  $L$  is the length of the resistor layer. These four currents are amplified, digitized and processed to capture a single data set  $I_x$  for the x channel of the PSD data

acquisition device and a single data set  $I_y$  for the y channel, which are then captured by the LabVIEW program in the PC. Therefore, the transformation from these two data sets into coordinates of the PSD detector surface can be express as:

$$\begin{aligned} P_x &= k_x I_x + bias_x \\ P_y &= k_y I_y + bias_y \end{aligned} \quad (A.2)$$

where  $k_x, k_y$  are the scaling factors for the x, y channels respectively. The PSD is calibrated by recording the x and y channel data after placing the PSD on a three dimensional PM500 stage and then moving the PSD in the x and y directions. The recorded data sets for the x and y channels vs. movement in x and y directions respectively are shown in Fig. A.2. By fitting the raw data using a linear model, I got the scaling factors and biases for x, y channels. The transform equation becomes

$$\begin{aligned} P_x &= 8.9286 I_x + 15.3036 \\ P_y &= -9.1075 I_y + 16.0128 \end{aligned} \quad (A.3)$$

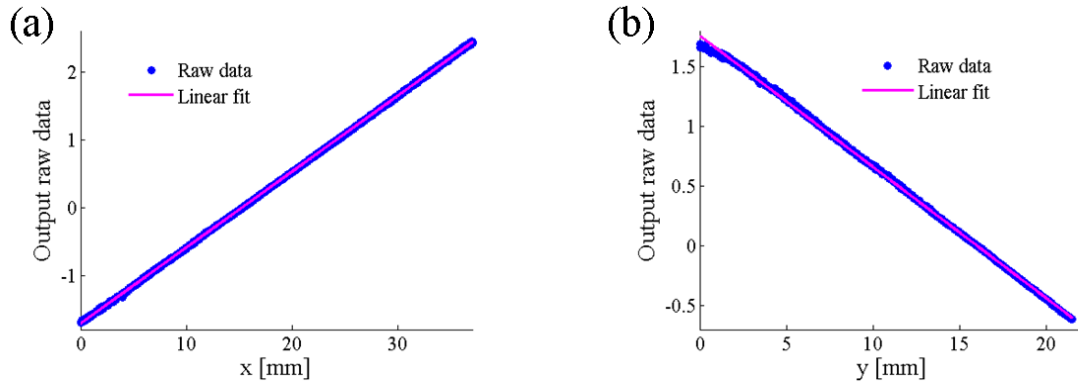


Figure A.4. Calibration of the ON-TRAK PSD detector model PSM2-45 for (a) the x channel and (b) the y channel.

The accuracy of the measurement using the modified differential transmission phase microscope is characterized by measuring several off-the-shelf plano-convex singlet lenses. For example, one plano-convex lens I used has a clear aperture of 22.4mm, a thickness of 2.7mm and the index of refraction of 1.5151 at the wavelength of 632.8nm. The radius curvature of the

convex surface is 104.41mm. The measured lens surface shape is shown in Fig. A.3-(a). The cross section of measured surface shape is compared to the calculated one from the lens parameters, shown in Fig. A.3-(b). The measured optical path delay profiles agree well with the known surface profiles and are within an experimental error of about 1%. The experimental error is the standard deviation between the actual and measured lens surface profile. Generally, this phase microscope is slower than an imaging interferometer or a Shack-Hartmann wavefront sensor, which I will discuss in chapter 3 for GRIN lens measurement. However, it is easily integrated into the fabrication setup for convenient process monitoring and can be optimized for small parts which are often difficult on commercial interferometers.

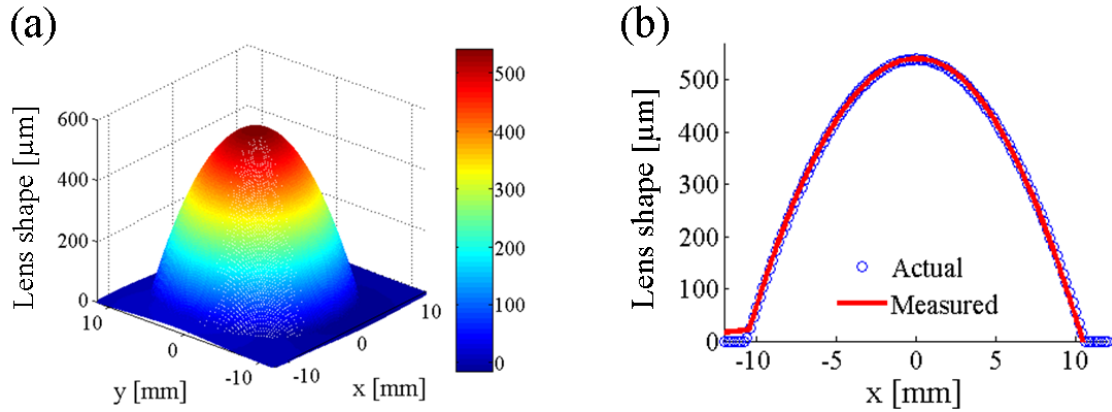


Figure A.5. Validation of the differential transmission phase microscope metrology by measuring an off-the-shelf plano-convex singlet lenses. (a) Measured shape profile of the lens. (b) Comparison of the x cross section of the measured lens shape to the actual one, indicating an experimental error of about 1%.

## Appendix B

# Calibration of the galvo scanning system

This appendix describes the calibration process so that the exposure light dose distribution from the galvo system is consistent with the one from the designed parameter file and vector file. Both the parameter and vector files are designed through MATLAB and are downloaded to the galvo control board.

First, the relationship between the driving current and the output power from the diode laser after the collimation lens is calibrated. While the driving current varies, the output powers from the diode laser after the collimation lens are recorded, as shown in Fig B.1. The linear fitting shows the threshold current for lasing is approximately 15.35mA. The output power can be expressed as  $P = 0.2066(i - 15.35)$ , where  $i$  is the driving current.

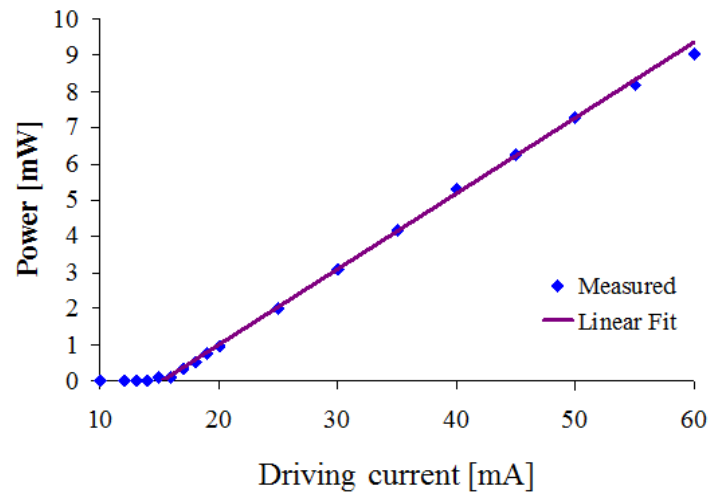


Figure B.6. The output powers from the laser diode vs. driving currents.

Next, calibrate the laser target power command in the parameter file vs. the laser modulation voltage sent to the diode laser controller. The parameter file sets the key control parameters of the system, which contains six four-digit hexadecimal values. The first parameter is

the minimum acceptable power, measured in  $\mu\text{W}$ . The second one is the target power in  $\mu\text{W}$ . The third one is the maximum acceptable power  $\mu\text{W}$ . The fourth one is the scaling factor for the galvo mirror. The fifth one is the mode of drawing, which is either 1 when the image will be drawn repeatedly and continuously or 0 when the image will only be drawn once. The last one is an ASCII value that indicates two characters, which describes the drawing method that corresponds to a software function. The second parameter determines the voltage that is sent to the laser diode controller and ultimately the output power from the laser diode. Now by giving different values to the target power in the parameter file, the output voltage to the laser diode driver is measured correspondingly. The relationship is shown in Fig. B.2. The target power parameter is set so that output laser modulation voltage from the PCB is saturated at 4.34V. This setting gives two advantages: (1) the laser output is stable and (2) the maximum output power is used so that the duration for each scan point is minimum, thus fast to fabricate each lens. The driving current from the controller is 60.84mA given the input voltage is 4.34V.

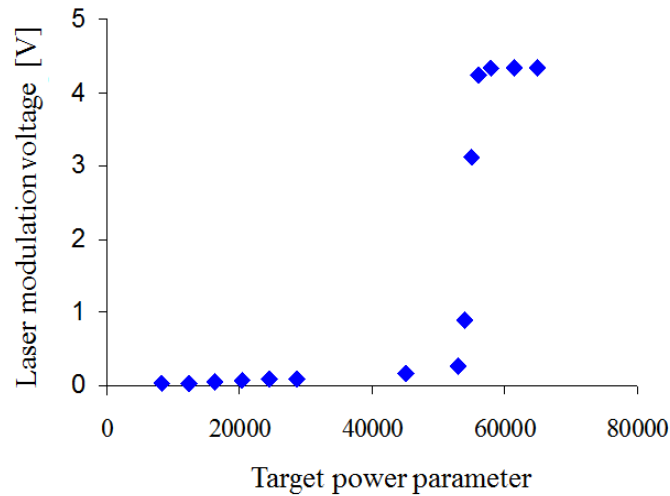


Figure B.7. The laser modulation voltage vs. target power command in the parameter file. The laser modulation voltage saturates at 4.34V.

Then, the time command in the vector file is calibrated. The vector files consist of the x, y coordinates for the two dimensional laser scanning spots and the time command for laser “on”

duration at each spot. While the time command in the vector file varies, the laser “on” time is recorded by an oscilloscope. The measured results are shown in Fig. B.3. By linear fitting, the laser duration time vs. the time command in vector file is expressed as  $t = 42.572 + 10.284N_{Loop}$ , where  $N_{Loop}$  is the time command for laser “on” duration in vector file.

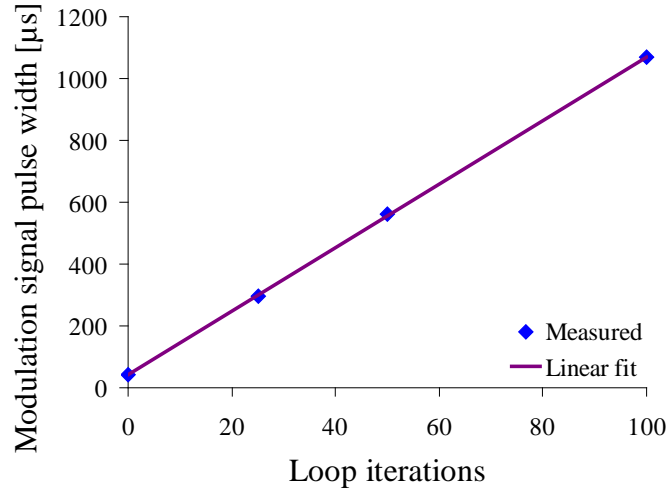


Figure B.8. The modulation pulse width vs. time duration command in the vector file.

Now the energy dose at the each scanning point is given by the equation

$$E = \frac{2TPt}{\pi w_{spot}^2}, \quad (B.1)$$

where  $t$  is the duration time of laser,  $P$  is the output power from the diode laser,  $T$  is the transmittance of the laser beam after the collimated lens to the sample plan and  $w_{spot}$  is the radius of the Gaussian exposure spot in the polymer sample. Given the driving current is set to be 60.84 mA, the output power is 9.40 mW. The total transmittance is 29.2% primarily due to the loss at the mirrors at the wavelength of 405nm.

The last step of calibration is to make sure the size of the exposed index structure is as same as the design. I used a square to calibrate and adjust the maximum exposure area. Recall that the x, y coordinates in the vector file are 0 to  $2^{16}-1$  integers. The four corner x, y coordinates in the vector file for the maximum exposure area are (0, 0), ( $2^{16}-1$ , 0), (0,  $2^{16}-1$ ) and ( $2^{16}-1$ ,  $2^{16}-1$ ).

During the calibration, I used a doublet lens with a focal length of 20mm as the writing objective lens. The maximum exposure area is targeted to be  $250 \times 250 \mu\text{m}^2$ . The designed exposure pattern for the square is shown in Fig. B.4. The dark spots are the locations of each scan spot, while the dark lines trace the laser spot movement. The four bright spots with color scale indicate the exposure intensity of the laser focus.

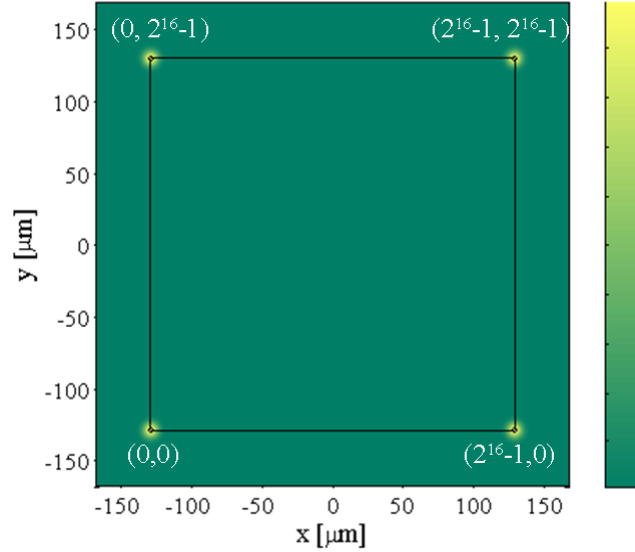


Figure B.9. The calibration pattern. The dark spot is the exposure laser focus spot position. The dark line traces the movement of the laser focus spot. The color bar represents the exposure dose distribution.

The exposure pattern is captured by a camera. As mentioned earlier, a summer and inverter op-amp circuit is placed on the PCB to translate and scale the exposure pattern. Adjust the scale knob while watching the exposure pattern on the camera until the size of the captured square is  $250 \mu\text{m} \times 250 \mu\text{m}$ . Then the square pattern is exposed into a polymer slide sample with thickness of  $200 \mu\text{m}$ . The DIC microscope image for the exposed square pattern is shown in Fig. B.5, demonstrating that the exposed pattern is the replicate of the designed one.

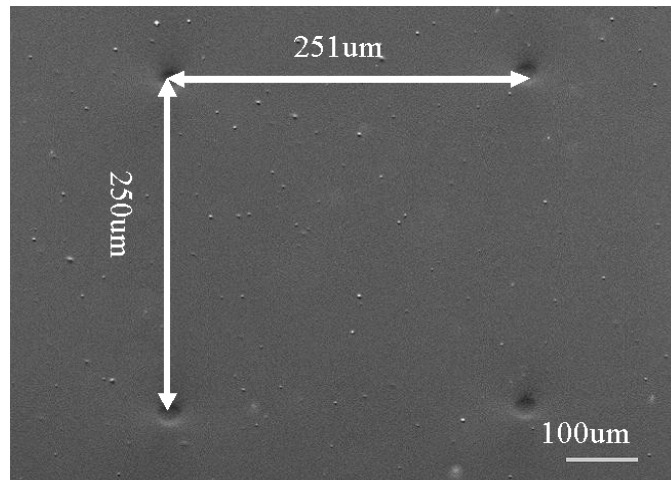


Figure B.10. The measured phase image from a DIC microscope for the calibration square pattern.



## Appendix C

# Introduction to the Shark-Hartmann wavefront sensor

A Shack-Hartmann wavefront sensor has three main optoelectronic components, which are lenslet arrays, a CCD detector and data analysis software, shown in Fig. C.1. The lenslet arrays dissect the incident wavefront into a large number of small segments. The light from each of these segments is collected by the lenslet and focused onto the detector. Since the size of each segment is small, a well-formed focal spot is recorded by the CCD detector. The position of those focal spots corresponds to the average wavefront slope cross each lenslet aperture. Therefore the distribution pattern of those focal spots provides the information about the spatially-resolved wavefront slopes, which can be integrated to reconstruct the incoming wavefront.

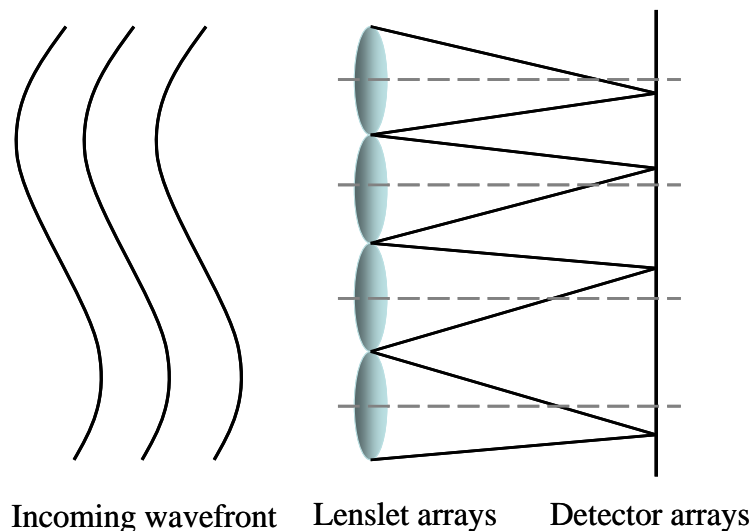


Figure C.11. The basic elements of a Shack-Hartmann sensor.

Compared to other wavefront test methods, such as shearing interferometer, the Shack-Hartmann wavefront sensor is simpler and less expensive to implement. It does not need tight

alignment, and is insensitive to vibration due to the fact that the wavefront information is captured rapidly by a single frame. These advantages make the Shack-Hartmann wavefront sensor favorable in a variety of applications. The Shack-Hartmann technique is originally developed to improve distorted images from ground-based telescopes due to atmosphere turbulence. Later, this technique has been applied to high-energy laser application [188,189], retinal imaging [190,191], measuring optical component quality during manufacture and testing [192], optical system calibration and alignment [193], fluid mechanics [194] and other areas [195,196].

The data analysis software takes three main steps to reconstruct the shape of the incoming wavefront from the raw image captured by the detector, shown in Fig. B.2. First, locate the focal spots from the lenslet arrays to get the centroids of focal spots. Second, calculate the wavefront slope by comparing the centroids of focal spots to the reference centroids. Finally, use reconstruction algorithm to estimate the wavefront profile from the wavefront slope.

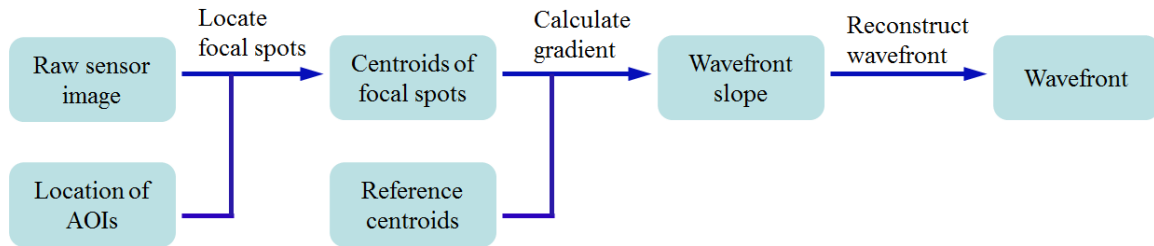


Figure C.12. The data flow diagram for the wavefront analysis.

During the detector calibration process, the detector surface is divided into a number of small areas-of-interest (AOIs), where the focal spot for a given lenslet is expected to fall onto. The locations of each focal spot are determined by the light distribution within the each AOI. A center-of-mass algorithm is used to calculate the centroid of each focal spot, whose x, y coordinates is expressed as

$$\begin{aligned}\rho_{x,k} &= \frac{\sum_{(i,j) \in AOI_k} I_{ij} x_{ij}}{\sum_{(i,j) \in AOI_k} I_{ij}} \\ \rho_{y,k} &= \frac{\sum_{(i,j) \in AOI_k} I_{ij} y_{ij}}{\sum_{(i,j) \in AOI_k} I_{ij}},\end{aligned}\tag{C.1}$$

where  $I_{ij}$  is the measured pixel intensity,  $x_{ij}$ ,  $y_{ij}$  are the coordinates of each pixel within the AOI.

The wavefront slope distribution is determined by the comparison of the measured centroids to the centroids of a reference wavefront. A reference wavefront can be provided by the manufacturer of the sensor or captured by a calibration step. During the calibration process, a reference set of centroids is also computed. Therefore the wavefront slopes can be calculated:

$$\begin{aligned}\theta_{x,k} &= \left. \frac{\partial \varphi}{\partial x} \right|_k = \frac{\rho_{x,k} - \rho_{x,k}|_{ref}}{L}, \\ \theta_{y,k} &= \left. \frac{\partial \varphi}{\partial y} \right|_k = \frac{\rho_{y,k} - \rho_{y,k}|_{ref}}{L},\end{aligned}\tag{C.2}$$

where  $\rho_{x,l}|_{ref}$ ,  $\rho_{y,l}|_{ref}$  are the reference centroid coordinates,  $L$  is the distance from the lenslet array to the detector, which is normally set to be the focal length of the lenslet. Therefore, absolute accuracy of the sensor is largely dependent on creating an accurate reference beam. There are several methods for creating very good reference sources, including high quality beam expanders, pinhole diffraction and single mode fibers.

Finally, the wavefront is reconstructed by solving the gradient equation:

$$\nabla \varphi(x, y) = \theta_x(x, y) \hat{i} + \theta_y(x, y) \hat{j}.\tag{C.3}$$

A variety of approaches have been developed to reconstruct the wavefront phase profile from a set of discrete phase slope measurements. These estimation approaches can be categorized into two basic types [197,198], modal reconstruction and zonal reconstruction, depending on whether the estimated phase is a set of value in local zones or a set of coefficients of a polynomial

expansion. Both types of phase reconstructions use least-squares algorithm. In modal method, the measured wavefront slope data is fit to the derivative of an analytical surface described by a polynomial expansion, which provides a very compact notation for describing the wavefront. Since Zernike polynomials are closely related to the aberration introduced in the optical systems, the reconstructed wavefront phase is often fit into Zernike polynomials,

$$\varphi(x, y) = a_{00} + a_{10}Z_{10}(x, y) + a_{11}Z_{11}(x, y) + a_{20}Z_{20}(x, y) + \dots + a_{mn}Z_{mn}(x, y) + \dots, \quad (C.4)$$

where  $Z_{mn}(x, y)$  is the  $m^{\text{th}}$  Zernike polynomial of  $n^{\text{th}}$  order. The derivatives of the phase in x and y direction respectively can be expressed as:

$$\begin{aligned} \frac{\partial \varphi}{\partial x} &= a_{10} \frac{\partial Z_{10}}{\partial x} + a_{11} \frac{\partial Z_{11}}{\partial x} + a_{20} \frac{\partial Z_{20}}{\partial x} + \dots + a_{mn} \frac{\partial Z_{mn}}{\partial x} + \dots \\ \frac{\partial \varphi}{\partial y} &= a_{10} \frac{\partial Z_{10}}{\partial y} + a_{11} \frac{\partial Z_{11}}{\partial y} + a_{20} \frac{\partial Z_{20}}{\partial y} + \dots + a_{mn} \frac{\partial Z_{mn}}{\partial y} + \dots \end{aligned} \quad (C.5)$$

Equation C.5 is then fit to the measured wavefront slope data using a least-square method to get these coefficients  $a_{mn}$ . These individual polynomials describe parameters such as defocus, astigmatism, coma and spherical aberration.

Although the Zernike approximation is effective for describing the individual aberrations, they also have a smoothing effect over the high frequency components in the wavefront. Alternatively, zonal reconstruction gains a unique description of the wavefront surface at every measurement point. The zonal reconstruction supports point-by-point variation in the wavefront surface and thus provides a high resolution wavefront description. However it does not provide for a direct interpretation in optical terms. Therefore, an additional calculation step is required to determine defocus, spherical, astigmatism, or other aberration terms from zonal reconstruction.

The Zonal reconstruction method implemented in the software of the SHWFS I use is iterative matrix implicit. In principle this method follows the formulation of Southwell [198] to derive a set of relations for the phase given a number of slope measurements. The phase at a given point is predicted from the four adjacent points. An iterative technique is used to solve for a

set of phase that are both internally consistent with the adjacent slope measurements. Generally, most of zonal reconstructors do not include the irradiance in the analysis, which is acceptable for astronomical or other adaptive optics systems, when the irradiance is usually uniform over the aperture. However, when the irradiance of the incoming light varies strongly across the aperture, such as a laser beam, the irradiance must be considered to obtain accurate wavefront results. In the matrix interactive method, the irradiance is used to weight the distribution of the slope measurements in order to prevent low light level portion of the measurement from having too strong influence the resulting phase. The matrix iterative reconstructor thus is faster and more accurate than other zonal reconstruction methods.

## Bibliography

---

1. M. J. Madou, *Fundamentals of Microfabrication*, 2nd edition (CRC Press, 2002).
2. A. Himeno, K. Kato, and T. Miya, "Silica-based planar lightwave circuits," *IEEE J. Sel. Topics Quantum Electron.*, vol. 4, 913-924(1998).
3. T. Miya, "Silica-based planar lightwave circuits: passive and thermally active devices," *IEEE J. Sel. Topics Quantum Electron.*, vol. 6, 38-45(2000).
4. J. Goodrich, "A silicon optical bench approach to low cost high speed transceivers," in *Electronic Components and Technology Conference*, 238 -241(2001).
5. J. V. Gates, G. Henein, J. Shmulovich, D. J. Muehlner, W. M. MacDonald and R. E. Scotti, "Uncooled laser packaging based on silicon optical bench technology," *Proc. SPIE*, vol. 2610, 127-137(1996).
6. C.J.R. Sheppard and D.M. Shotton, *Confocal laser scanning microscopy*, (Oxford, New York, 1997).
7. M. R. Ayres, and R. R. McLeod, "Scanning transmission microscopy using a position-sensitive detector," *Appl. Opt.*, vol. 45, 8410-8418 (2006).
8. Personal experience of Dr. Robert. R. McLeod while at JDS Uniphase.
9. A. C. Sullivan, M. W. Grabowski, R. R. McLeod, "Three-dimensional direct-write lithography into photopolymer," *Appl. Opt.*, vol. 46, 295-301 (2007).
10. C. D. Anderson, "Photopolymer waveguide to fiber coupling via 3D direct-write lithography," thesis (M.S. E.E.), University of Colorado at Boulder (2006).
11. R. H. Wopschall, "Dry photopolymer film for recording holograms", *Appl. Opt.*, vol. 11, 2096-2097 (1972) (first presented at OSA annual meeting, Tucson AZ, April 1971).
12. B.L. Booth, "Photopolymer material for holography," *Appl. Opt.*, vol. 14, 593-601(1975).

- 
13. W. J. Gambogi, A. M. Weber and T. J. Trout, "Advances and applications of DuPont holographic photopolymers," *Proc. SPIE*, vol. 2043, 2-13(1993).
  14. D. A. Waldman, R. T. Ingwall, P. K. Dhal, M. G. Horner, E. S. Kolb, H.-Y. S. Li, R. A. Minns, and H. G. Schild. "Cationic ring-opening photopolymerization methods for volume hologram recording," *Proc. SPIE*, vol. 2689, 127-141 (1996).
  15. <http://www.aprilisinc.com/home.htm>
  16. L. Dhar, A. Hale, H. E. Katz, M. L. Schilling, M. G. Schnoes, and F. C. Schilling, "Recording media that exhibit high dynamic range for digital holographic data storage," *Opt. Lett.*, vol.24, 487-489(1999).
  17. H. Thienpont, C. Debaes, V. Baukens, H. Ottevaera, P. Vynck , P. Tuteleers , G. Verschaffelt, B. Volkaerts, A. Hermanne, and M. Hanney , "Plastic microoptical interconnection modules for parallel free-space inter- and intra-MCM datacommunication," *Proc. IEEE*, vol. 88, 69–79 (2000).
  18. W. J. Tomlinson, "Applications of GRIN-rod lenses in optical fiber communication systems," *Appl. Opt.*, vol. 19, 1127-1138 (1980).
  19. J. Arai, F. Okano, H. Hoshino, and I. Yuyama, "Gradient-index lens-array method based on real-time integral photography for three-dimensional images," *APPL. OPT.*, vol. 37, 2035-2045(1998).
  20. T. Xie, S. Guo, and Z. Chen, "GRIN lens rod based probe for endoscopic spectral domain optical coherence tomography with fast dynamic focus tracking," *Opt. Express*, vol. 14, 3238-3246 (2006).
  21. J. Knittel, L. Schnieder, G. Buess, B. Messerschmidt, and T. Possner, "Endoscope-compatible confocal microscope using a gradient index-lens system," *Opt. Commun.*, vol. 188, 267-273(2001).
  22. M.-H. Wu, and G. M. Whitesides, "Fabrication of two-dimensional arrays of microlenses and their applications in photolithography," *J. Micromech. Microeng.*, vol. 12, 747–758(2002).

- 
23. S. Möller and S. R. Forrest, "Improved light out-coupling in organic light emitting diodes employing ordered microlens arrays," *J. Appl. Phys.*, vol. 91, 3324-3328 (2002).
  24. N Morton, "Gradient refractive index lenses," *Phys. Educ.*, vol. 19, 86-90 (1984)
  25. W. J. Tomlinson, "Applications of GRIN-rod lenses in optical fiber communication systems," *Appl. Opt.*, vol. 19, 1127-1138 (1980).
  26. G. J. Tearney, S. A. Boppart, B. E. Bouma, M. E. Brezinski, N. J. Weissman, J. F. Southern and J. G. Fujimoto, "Scanning single-mode fiber optic catheter–endoscope for optical coherence tomography," *Opt. Lett.*, vol. 21, 543-545(1996).
  27. Y. Koike, Y. Sumi, and Y. Ohtsuka, "Spherical gradient-index sphere lens," *Appl. Opt.*, vol. 25, 3356-3363(1986).
  28. J. Jin, H. Tai, A. Hiltner, E. Baer, and J. S. Shirk, "New class of bioinspired lenses with a Gradient refractive index," *J. of Appl. Poly. Sci.*, vol. 103, 1834-1841(2007).
  29. D. T. Moore, "Gradient-index optics – a review," *Appl. Opt.*, vol. 19, 1035-1038 (1980).
  30. P. Sinai, "Correction of optical aberration by neutron irradiation," *Appl. Opt.*, vol. 10, 99-104 (1971).
  31. M. A. Pickering, R. L. Taylor, and D. T. Moore, "Gradient infrared optical material prepared by a chemical vapor deposition process," *Appl. Opt.*, vol. 25, 3364-3372 (1986).
  32. S. Ohmi, "Gradient-index rod lens made by a double ion-exchange process," *Appl. Opt.*, vol. **27**, 496-499 (1988).
  33. R. K. Mohr, J. A. Wilder, P. B. Macedo, and P. K. Gupta, in Digest of Topical Meeting on Gradient-Index Optical Imaging Systems (Optical Society of America, Washington, D.C., 1979), paper WAL.



- 
34. J. Liu, J.-L. Chen, H.-Y. Wang, F.-R. Tsai, "Fabrication of a gradient refractive index (GRIN) plastic rod using the novel process of centrifugal diffusing polymerization," *Macromol. Chem. Phys.*, vol. 201, 126–131 (2000)
  35. M. J. N. Jahromi, J.-H. Liu, "Gel effects on the fabrication of gradient refractive index plastic rods via energy-controlled polymerization," *J. of the Taiwan Inst. of Chem. Eng.*, vol. 43, 301-305(2012).
  36. J. Bähr, K.-H. Brenner, "Realization of refractive continuous phase elements with high design freedom by mask structured ion exchange," *Proc. SPIE*, vol. 4437, 50-60(2001).
  37. F. Hudelist, R. Buczynski, A.J.Waddie, M.R.Taghizadeh, "Design and fabrication of nano-structured gradient index microlenses," *Opt. Express*, vol. 17, 3255-3263(2009).
  38. F. Luan, A. K. George, T. D. Hedley, G. J. Pearce, D. M. Bird, J. C. Knight, and P. S. J. Russell, "All-solid photonic bandgap fiber," *Opt. Lett.*, vol. 29, 2369–2371 (2004)
  39. K. Totsu, K. Fujishiro, S. Tanaka, and M. Esashi, "Fabrication of three-dimensional microstructure using maskless gray-scale lithography," *Sensors and Actuators A*, vol. 130-131, 387-392(2006).
  40. K. Naessens, H. Ottevaere, P. Van Daele, R. Bates, "Flexible fabrication of microlenses in polymers with excimer laser ablation," *Appl. surface science*, vol. 208-209, 159-164(2003).
  41. Mangirdas Malinauskas, Holger Gilbergs, Albertas Žukauskas, Vytautas Purlys, Domas Paipulas and Roaldas Gadonas, "A femtosecond laser-induced two-photon photopolymerization technique for structuring microlenses", *J. Opt.* **12** , 035204(2010).
  42. P. Nussbaum, "Design, fabrication and testing of microlens arrays for sensors and microsystems," *Pure Appl. Opt.*, vol. 6, 617-636 (1997).
  43. F. Beinhorn, "Micro-lens arrays generated by UV laser irradiation of doped PMMA," *Appl. Phys. A*, vol. 68, 709-713(1999).

- 
44. N. F. Borrelli, "Photolytic technique for producing microlenses in photosensitive glass," *Appl. Opt.*, vol. 24, 2520-2525(1985).
  45. Y. L. Li, "Research on micro-optical lenses fabrication technology," *Optik.*, vol. 118, 395-401 (2007).
  46. T. Huang, B. Chan, J. Ciou, and S. Yang, "CO<sub>2</sub> assisted embossing (Fabrication of microlens arrays using a CO<sub>2</sub>-assisted embossing technique," *J. Micromech. Microeng.*, vol. 19, 015018(2009).
  47. N.S. Ong, Y.H. Koh, Y.Q. Fu, "Microlens array produced using hot embossing process," *Microelectron. Eng.*, vol. 60, 365-379(2002).
  48. H.H. Yang, M.C. Chou, A. Yang, C.K. Mu, R.F. Shyu, "Realization of fabrication microlens array in mass production," *Proc. SPIE*, vol. 3739, 178-185(1999).
  49. K. A. Berchtold, T. M. Lovestead, and C.N Bowman, "Coupling chain length dependent and reaction diffuse controlled termination in the free radical polymerization of multivinyl(meth)acrylates," *Macromolecules*, vol. 35, 7968-7975 (2002).
  50. A. S. Kewitsch and A. Yariv, "Self-focusing and self-trapping of optical beams upon photopolymerization," *Opt.Lett.*, vol. 21, 24-26 (1996).
  51. K. Curtis, L. Dhar, A. J. Hill, W. L. Wilson, and M. R. Ayres, *Holographic Data Storage from Theory to Practical Systems*, Wiley (2010).
  52. K. Morishita, "Index profiling of three-dimensional optical waveguides by the propagation-mode near-field method", *J. lightwave technol.*, vol. 4, 1120-1124(1986).
  53. F.M.E. Sladen, D.N. Payne, and M. J. Adams, "Determination of optical fiber refractive index profiles by a near-field scanning technique," *Appl. Phys. Lett.*, vol. 28, 255-258(1976).

- 
54. C. J. Cogswell and C. J. R. Sheppard, "Confocal differential interference contrast (DIC) microscopy: including a theoretical analysis of conventional and confocal DIC imaging," *J. Microsc.*, vol.165, 81-101 (1992).
  55. S. V. King, A. Libertun, R. Piestun, and C. J. Cogswell, "Quantitative phase microscopy through differential interference imaging," *J. Biomed. Opt.*, vol. 13(2), 024020 (2008).
  56. M. Ikeda, M. Tateda, and H. Yoshikiyo, "Refractive index profile of a graded index fiber: measurement by a reflection method," *Appl. Opt.*, vol. 14, 814-815(1975).
  57. Y. Youk, and D. Kim, "A simple reflection-type two-dimensional refractive index profile measurement technique for optical waveguides", *Opt. Commun.*, vol. 262, 206-210(2006).
  58. E. D. Moore, R. R. McLeod, "Index contrast measurement using Scanning optical frequency domain reflectometry", *Frontiers in Optics/Laser Science*, JWA38 (2010).
  59. M. Tateda, "Single-mode-fiber refractive-index profile measurement by reflection method," *Appl. Opt.*, vol. 17, 475~478(1978).
  60. T. Wilson, J.N. Gannaway, and C. J. R. Sheppard, "Optical fiber profiling using a scanning optical microscope," *Opt. Quant. Electro.*, vol. 12, 341-345(1980).
  61. T. Okoshi and K. Hotate, "Refractive-index profile of an optical fiber: its measurement by the scattering-pattern method," *Appl. Opt.*, vol.15, 2756-2764(1976)
  62. C. D. Anderson, "Photopolymer waveguide to fiber coupling via 3D direct-write lithography," thesis (M.S. E.E.), University of Colorado at Boulder (2006).
  63. 'Gradient Index (GRIN) Lenses', <http://www.grintech.de>.
  64. S. Piazzolla and B. K. Jenkins, "Holographic grating formation in photopolymers," *Opt. Lett.*, vol. 21, 1075-1077(1996).

- 
65. J. V. Kelly, M. R. Gleeson, C. E. Close, F. T. O' Neill, and J. T. Sheridan, "Temporal analysis of grating formation in photopolymer using the nonlocal polymerization-driven diffusion model," *Opt. Express*, vol. 13, 6990-7004(2005).
  66. J. G. Kloosterboer, G. F. C. M. Lijten, and H. M. J. Boots, "Network formation by chain crosslinking photopolymerization and some applications in electronics," *Polym. Mater. Sci. and Eng.*, vol. 24, 223-230 (1989).
  67. K. S. Anseth, S. M. Newman, and C. N. Bowman, "Polymeric dental composites: properties and reaction behavior of multimethacrylate dental restoration," *Advances in Polymer Science*, vol.122, 176-217(1995).
  68. F. H. Mok, G. W. Burr, and D. Psaltis, "System metric for holographic memory systems," *Opt. Lett.*, vol. 21, 896-898(1996).
  69. W. Däschner, R. Stein, P. Long, C. Wu and S. H. Lee, "One-step lithography for mass production of multilevel diffractive optical elements using high energy beam sensitive (HEBS) gray-level mask," *Proc. SPIE*, vol. 2689, 153-5 (1996).
  70. C. Wu, "Method of making High Energy Beam Sensitive Glasses" U.S. Patent No. 5,078,771, Jan. 7<sup>th</sup>, 1992.
  71. <sup>71</sup> C.M. Waits, M. Kastantin, R. Ghodssi, "Investigation of gray-scale technology for large area 3D silicon MEMS structures," *J. Micromech. Microeng.*, vol. 13, 170-177 (2003).
  72. C.M. Waits, B. Morgan, M. Kastantin, R. Ghodssi, "Microfabrication of 3D silicon MEMS structures using gray-scale lithography and deep reactive ion etching," *Sensors and Actuators A*. vol. 119, 245-253(2005).
  73. Y. Opplinger, P. Sixt, J.M. Stauffer, J.M. Mayor, P. Regnault, G. Voirin. "One-step 3D shaping using a gray-tone mask for optical and microelectronic applications," *Microelectron. Eng.*, vol. 23, 449-454(1994).
  74. T.J. Suleski, D.C. O'Shea, "Gray-scale masks for diffractive-optics fabrication. I. Commercial slide images," *Appl. Opt.*, vol. 34, 7507-7517(1995).

- 
75. M. H. Wu, C. Park, G.M. Whitesides, "Fabrication of arrays of microlenses with controlled profiles using gray-scale microlens projection photolithography," *Langmuir*, vol. 18, 9312- 9318(2002).
  76. C. Sun, N. Fang, D.M. Wu, and X. Zhang, "Projection micro-stereolithography using digital micro-mirror dynamic mask," *Sensor and Actuator A*, vol. 121, 113-120(2005).
  77. A. Bertsch, S. Zissi, J.Y. J ézéquel, S. Corbel, J.C. André, "Micro stereophotolithography using a liquid crystal display as dynamic mask-generator," *Microsystem Technol.*, 42-47(1997).
  78. L.J. Hornbeck, "Deformable-Mirror Spatial Light Modulators," *Spatial Light Modulators and Applications III, SPIE Critical Reviews*, vol. 1150, 86-102 (1989).
  79. [http://focus.ti.com/download/dlpdmd/141\\_hornbeck.pdf](http://focus.ti.com/download/dlpdmd/141_hornbeck.pdf).
  80. L.J. Hornbeck, "Digital light processing and MEMS: timely convergence for a bright future," *Proc. SPIE*, vol. 2639, 2(1995).
  81. D. Sabol, M. R. Gleeson, S. Liu, J. T. Sheridan, "Photoinitiation study of Irgacure 784 in an epoxy resin photopolymer," *J. Appl. Phys.*, vol. 107, 053113 (2010).
  82. M. G. Neumann, W. G. Miranda Jr., C. C. Schmitt, F. A. Rueggeberg, and I. C. Correa, "Molar extinction coefficients and the photon absorption efficiency of dental photoinitiators and light curing units," *J. Dentistry*, vol. 33, 525-532(2005).
  83. <http://www.sigmaaldrich.com/MSDS/MSDS/DisplayMSDSPage.do?country=US&language=en&productNumber=415952&brand=ALDRICH&PageToGoToURL=http%3A%2F%2Fwww.sigmaaldrich.com%2Fcatalog%2Fproduct%2Faldrich%2F415952%3Flang%3Den>
  84. J. G. Kloosterboer, G. F. C. M. Lijten, and H. M. J. Boots, "Network formation by chain crosslinking photopolymerization and some applications in electronics," *Polym. Mater. Sci. and Eng.*, vol. 24, 223-230 (1989).

- 
85. K. S. Anseth, S. M. Newman, and C. N. Bowman, "Polymeric dental composites: properties and reaction behavior of multimethacrylate dental restoration," *Advances in Polymer Science*, vol. 122, 176-217(1995).
86. C. Decker and A.D. Jenkins, "Kinetic Approach of O<sub>2</sub> Inhibition in Ultraviolet- and Laser-Induced Polymerizations," *Macromolecules*, vol. 18, 1241-1244(1985).
87. W. D. Cook, Q. Nghiem, Q. Chen, F. Chen, and M. Sangermano, "Simultaneous photoinduced silver nanoparticles formation and cationic polymerization of Divinyl Ethers," *Macromolecules*, vol. 44, 4065–4071(2011).
88. Willfried Heller, "Remarks on refractive index mixture rules," *J. Phys. Chem.*, vol. 69, 1123-1129(1965).
89. P. R. Griffiths, and J. A. de Haseth, *Fourier transform infrared spectroscopy*, Wiley-Blackwell , 2007.
90. L. Liu, J. A. Gardecki, S. K. Nadkarni, J. D. Toussaint, Y. Yagi, B. E. Bouma, and G. J. Tearney, "Imaging the subcellular structure of human coronary atherosclerosis using micro-optical coherence tomography", *Nature Medicine*, vol. 17, 1010-1014(2011).
91. D. Huang, E. A. Swanson, C. P. Lin, J. S. Schuman, W. G. Stinson, W. Chang, M. R. Hee, T. Flotte, K. Gregory, C. A. Puliafito, and J. G. Fujimoto, "Optical coherence tomography" *Science*, vol. 254, 1178 (1991).
92. W. Drexler, U. Morgner, F. X. Kärtner, C. Pitris, S. A. Boppart, X. D. Li, E. P. Ippen, and J. G. Fujimoto, "In vivo ultrahigh-resolution optical coherence tomography," *Opt. Lett.*, vol. 24, 1221-1223 (1999)
93. T. Xie, S. Guo, Z. Chen, D. Mukai, and M. Brenner, "GRIN lens rod based probe for endoscopic spectral domain optical coherence tomography with fast dynamic focus tracking," *Opt. Express*, vol. 14, 3238-3246 (2006).

- 
94. Z. Ding, H. Ren, Y. Zhao, J. S. Nelson, and Z. Chen, "High-resolution optical coherence tomography over a large depth range with an axicon lens," *Opt. Lett.*, vol. 27, 243-245(2002)
  95. L. Liu, C. Liu, W.C. Howe, C. J. R. Sheppard, and N. Chen, "Binary-phase spatial filter for real-time swept-source optical coherence microscopy," *Opt. Lett.*, vol. 32, 2375-2377(2007).
  96. E. R. Dowski, Jr. and W. T. Cathey, "Extended depth of field through wavefront coding," *Appl. Opt.*, vol. 34, 1859-1866 (1995).
  97. S. Bradburn, W.T. Cathey, and E. R. Dowski, "Realizations of focus invariance in optical/digital systems with wavefront coding," *Appl. Opt.*, vol.36, 9157-9166(1997).
  98. Z. Ding, H. Ren, Y. Zhao, J. S. Nelson, and Z. Chen, "High-resolution optical coherence tomography over a large depth range with an axicon lens," *Opt. Lett.*, vol. 27, 243-245(2002)
  99. R. A. Leitgeb, M. Villiger, A. H. Bachmann, L. Steinmann, and T. Lasser, "Extended focus depth for Fourier domain optical coherence microscopy," *Opt. Lett.*, vol. 31, 2450-2452(2006)
  100. Kye-Sung Lee and Jannick P. Rolland, "Bessel beam spectral-domain high-resolution optical coherence tomography with micro-optic axicon providing extended focusing range," *Opt. Lett.*, vol. 33, 1696-1698 (2008)
  101. J. H. McLeod, "The axicon: a new type of optical element," *J. Opt. Soc. Am.*, vol. 44, 592-597 (1954)
  102. J. Durnin, "Exact solutions for non-diffracting beams. I. The scalar theory," *J. Opt. Soc. Am. A*, vol. 4, 651-654 (1987).
  103. R. M. Herman and T.A. Wiggins, "Production and uses of diffraction less beams", *JOSA A* vol.8, 932-942 (1991).
  104. J. H. McLeod, "Axicons and their uses," *J. Opt. Soc. Am.*, vol. 50, 166-169(1960).

- 
105. Z. Jaroszewicz, A. Burvall, and A. T. Friberg, "Axicon - the Most Important Optical Element," *Optics and Photonics News*, vol. 16, 34-39 (2005).
  106. R. Arimoto, C. Saloma, T. Tanaka and S. Kawata, "Imaging properties of axicon in a scanning optical system," *App. Opt.*, vol. 31, 6653- 6657 (1992).
  107. P. Bélanger and M. Rioux, "Ring pattern of a lens-axicon doublet illuminated by a Gaussian beam," *App. Opt.*, vol. 17, 1080-1088(1978).
  108. M. Rioux and P. A. Belanger, "Linear, annular, and radial focusing with axicons and application to laser machining," *Appl. Opt.*, vol. 17, 1532–1536 (1978).
  109. J. A. Kim, K. I. Lee, H. R. Noh, W. Jhe and M. Ohtsu, "Atom trap in an axicon mirror," *Opt. Lett.*, vol. 22, 117-119 (1997).
  110. V. I. Balykin, V. S. Letokhov, V. G. Minogin, Y. V. Rozbdestvenskyt, and A. L. Sidorov, "Radiative collimation of atomic beams through two-dimensional cooling of atoms by laser-radiation pressure," *J. Opt. Soc. Am. B*, vol. 2, 1776-1783(1985).
  111. T. Wulle and S. Herminghaus, "Nolinear optics of Bessel beams," *Phys. Rev. lett.*, vol. 70, 1401-1405(1993).
  112. M. Villiger, J. Goulley, M. Friedrich, A. Grapin-Botton, P. Meda, T. Lasser, and R. A. Leitgeb, "In vivo imaging of murine endocrine islets of Langerhans with extended-focus optical coherence microscopy," *Diabetologia*, vol. 52, 1599–1607(2009).
  113. X. Lin, Q. Chen, L. Niu, T. Jiang, W. Wang, and H. Sun, "Mask-free production of integratable monolithic micro logarithmic axicon lenses," *J. lightwave technol.*, vol. 28, 1256-1260(2010).
  114. W. Chi and N. George, "Electronic imaging using a logarithmic asphere," *Opt. Lett.*, vol.26, 875-877(2001)
  115. J. Sochacki, A. Kotodziejczyk, Z. Jaroszewicz, and S. Barc, "Nonparaxial design of generalized axicons," *Appl. Opt.*, vol. 31, 5326- 5330 (1992).



- 
116. I. Golub, B. Chebbi, D. Shaw, and D. Nowacki, "Characterization of a refractive logarithmic axicon," *Opt. Lett.*, vol. 35, 2828-2830(2010).
  117. X. Yuan, B.P.S. Ahluwalia, W.C. Cheong, J. Bu, H.B. Niu and X. Peng, "Direct electron beam writing of kinoform micro-axicon for generation of propagation-invariant beams with long non-diffracting distance," *J. Opt. A: Pure Appl. Opt.*, vol. 9, 329-334(2007).
  118. Kevin Gourley, Ilya Golub, and Brahim Chebbi, "Demonstration of a Fresnel axicon," *Appl. Opt.*, vol. 50, 303-306(2011).
  119. S. K. Mohanty, K. S. Mohanty, and M. W. Berns, "Organization of microscale objects using a microfabricated optical fiber," *Opt. Lett.*, vol. 33, 2155-2157 (2008).
  120. Y. Yu, H. Noh, M. Hong, H. Noh, Y. Arakawa, and W. Jhe, "Focusing characteristics of optical fiber axicon microlens for near-field spectroscopy: Dependence of tip apex angle," *Opt. Commun.*, vol. 267, 264–270(2006).
  121. J. M. González-Leal and J. A. Angel, "Fabrication of axicons by cw laser effusion," *Opt. Lett.*, vol. 32, 2384-2386(2007).
  122. W. N. Charman, "Theoretical aspects of concentric varifocal lenses," *Ophthalmic Physiol. Opt.*, vol. 2, 75–86 (1982)
  123. D. Fisher, C. J. Harkrider, and D. T. Moore, "Design and manufacture of a gradient-index axicon," *Appl. Opt.*, vol. 39, 2687-2694(2000).
  124. Z. Jaroszewicz and T. Morales, "Lens axicons: systems composed of a diverging aberrated lens and a perfect converging lens," *J. Opt. Soc. Am. A*, vol. 15, 2383–2390 (1998).
  125. M. Guizar-Sicairos and J. C. Gutierrez-Vega, "Computation of quasi-discrete Hankel transforms of integer order for propagating optical wave fields," *J. Opt. Soc. Am. A*, vol. 21, 53-58 (2004).

- 
126. K. M. Davis, K. Miura, N. Sugimoto, and K. Hirao, "Writing waveguides in glass with a femtosecond laser," *Opt. Lett.*, vol. 21, 1729-1731 (1996).
  127. S. Sowa, W. Watanabe, T. Tamaki, J. Nishii, and K. Itoh, "Symmetric waveguides in poly (methyl methacrylate) fabricated by femtosecond laser pulses," *Opt. Express*, vol. 14, 291-297 (2005).
  128. J. Ishihara, K. Komatsu, O. Sugihara, and T. Kaino, "Fabrication of three-dimensional calixarene polymer waveguides using two-photon assisted polymerization," *Appl. Phys. Lett.*, vol. 90, 033511 (2007).
  129. K. Dorkenoo, O. Crégut, L. Mager, F. Gillot, C. Carre, and A. Fort, "Quasi-solitonic behavior of self-written waveguides created by photopolymerization," *Opt. Lett.*, vol. 27, 1782-1784 (2002).
  130. K. L. Deng, T. Gorczyca, B. K. Lee, H. Xia, R. Guida, and T. Karras, "Self-aligned single-mode polymer waveguide interconnections for efficient chip-to-chip optical coupling," *IEEE J. Sel. Topics Quantum Electron.*, vol. 12, 923-930 (2006)
  131. O. Sugihara, H. Tsuchie, H. Endo, N. Okamoto, T. Yamashita, M. Kagami, and T. Kaino, "Light-induced self-written polymeric optical waveguides for single-mode propagation and for optical interconnections," *IEEE Photo. Tech. Lett.*, vol. 16, 804-806 (2004)
  132. R. S. Fan and R. B. Hooker, "Tapered polymer single-mode waveguides for mode transformation," *J. lightwave Technol.*, vol. 17, 466-474 (1999).
  133. R. Inada, M. Kato, M. Sagawa, and H. Akahoshi, "Two-dimensional mode size transformation by  $\Delta n$ -controlled polymer waveguides," *J. Lightwave Technol.*, vol. 16, 620-624 (1998).
  134. S. J. Frisken, "Light-induced optical waveguide uptapers," *Opt. Lett.*, vol. 18, 1035-1037 (1993).
  135. A. C. Sullivan and R. R. McLeod, "Tomographic reconstruction of weak, replicated index structures embedded in a volume," *Opt. Express*, vol. 15, 14202-14212 (2007)

- 
136. T. Wilson, J. N. Gannaway, and C. J. R. Sheppard, "Optical fiber profiling using a scanning optical microscope," *Opt. Quantum Electron.*, vol. 12, 341-345 (1980)
  137. K. Curtis, L. Dhar, A. J. Hill, W. L. Wilson, and M. R. Ayres, *Holographic Data Storage: From Theory to Practical Systems* (John Wiley & Sons, 2010)
  138. B. Cai, K. Komatsu, O. Sugihara, M. Kagami, M. Tsuchimori, T. Matsui and T. Kaino, "A three-dimensional polymeric optical circuit fabrication using a femtosecond laser-assisted self-written waveguide technique," *Appl. Phys. Lett.*, vol. 92, 253302 (2008).
  139. M. Ams, G. D. Marshall, D. J. Spence, and M. J. Withford, "Slit beam shaping method for femtosecond laser direct-write fabrication of symmetric waveguides in bulk glasses," *Opt. Express*, vol. 13, 5676-5681 (2005).
  140. T. F. Scott, B. A. Kowalski, A. C. Sullivan, C. N. Bowman, and R. R. McLeod, "Two-color single-photon photoinitiation and photoinhibition for subdiffraction photolithography," *Science*, vol. 324, 913-917(2009).
  141. R. S. Fan and R. B. Hooker, "Tapered polymer single-mode waveguides for mode transformation," *J Lightwave technol.*, vol. 17, 466-474(1999).
  142. T. Bakke, C. T. Sullivan, and S. D. Mukherjee, "Polymeric optical spot-size transformer with vertical and lateral tapers," *J. Lightwave technol.*, vol. 20, 1188-1197(2002).
  143. L. Vivien, X. Le Roux, S. Laval, E. Cassan, and D. Marris-Morini, "Design, realization, and characterization of 3-D taper for fiber/micro-waveguide coupling," *IEEE J. Sel. Topics Quantum Electron.*, vol. 12, 1354-1358(2006).
  144. DataRay Incorporated, WinCamDTM Series CCD/CMOS Beam Imagers User Manual, Rev. 1007b, page 42, DataRay Incorporated, Bella Vista CA (2010)
  145. D. Sabol, M. R. Gleeson, S. Liu, J. T. Sheridan, "Photoinitiation study of Irgacure 784 in an epoxy resin photopolymer," *J. Appl. Phys.*, vol. 107 053113 (2010)

- 
146. A. W. Snyder and J. D. Love, *Optical Waveguide Theory*, (Chapman and Hall, 1983), pp. 337-342.
  147. K. A. Berchtold, T. M. Lovestead, and C. N. Bowman, "Coupling chain length dependent and reaction diffusion controlled termination in the free radical polymerization of multifunctional(meth)acrylates, " *Macromolecules*, vol. 35, 7968-7975 (2002).
  148. L. Eldada, "Advances in telecom and datacom optical components," *Opt. Eng.*, vo. 40, 1165 (2001).
  149. See for example: IEEE Transactions on Advanced Packaging
  150. See for example: SPIE Photonics Packaging, Integration and Interconnects, SPIE Laser-based Micro- and Nanopackaging and Assembly.
  151. A. R. Mickelson, N. R. Basavanahally, Y-C Lee Editors, *Optoelectronic Packaging*, (Wiley-Interscience, New York, 1997).
  152. J. T. Boyd and S. Sriram, "Optical coupling from fibers to channel waveguides formed on silicon," *Appl. Opt.*, vo. 17, 895-898 (1978).
  153. Dirk Taillaert, Peter Bienstman, and Roel Baets, "Compact efficient broadband grating coupler for silicon-on-insulator waveguides," *Opt. Lett.*, vol. 29, 2749-2751 (2004)
  154. P R. Yoder Jr., P. Yoder, D. Vukobratovich, R. A. Paquin, in *Opto-Mechanical Systems Design*, (CRC Press, New York, 2005).
  155. Y. Z. Tang, W. H. Wang, T. Li, and Y. L. Wang, "Integrated waveguide turning mirror in silicon-on-insulator," *IEEE Photo. Technol. Lett.*, vol. 14, 68-70 (2002).
  156. J. S. Kim and J. J. Kim, "Stacked polymer multimode waveguides arrays for two-dimensional optical interconnects," *J. Lightwave Technol.*, vol. 22, 840-844 (2004).
  157. S. Hiramatsu, K. Miura, and K. Hirao, "Optical backplane connectors using three-dimensional waveguide arrays *J. Lightwave Technol.*, vol. 25, 2776-2782(2007).

- 
158. H. Nishihara, M. Haruna, and T. Suhara, *Optical Integrated Circuits*, (McGraw Hill, New York, 1989).
  159. K. K. Lee, D. R. Lim, L. C. Kimmerling, J. Shin, and F. Cerrina, "Fabrication of ultralow-loss Si/SiO<sub>2</sub> waveguides by roughness reduction," *Opt. Lett.*, vol. 26, 1888 - 1890(2001).
  160. A. M. Agarwal, L. Liao, J. S. Foresi, M. R. Black, X. Duan, and L. C. Kimmerling, "Low-loss polycrystalline silicon waveguides for silicon photonics," *J. Appl. Phys.*, vol. 80, 6120 (1996).
  161. Akira Himeno, Kuniharu Kato, and Tetsuo Miya, "Silica-based planar lightwave circuits," *IEEE J. Sel. Topics Quantum Electron.*, vol. 4, 913-924 (1998).
  162. K. Chiang, "Development of optical polymer waveguide devices," *Proc. SPIE*, vol. 7605, 760507 (2010).
  163. K. Yamada, T. Shoji, T. Tsuchizawa, T. Watanabe, J. Takahashi, and S. Itabashi, "Silicon-wire-based ultrasmall lattice filters with wide free spectral ranges," *Opt. Lett.*, vol. 28, 1663-1664 (2003).
  164. R. U. Ahmad, F. Pizzuto, G. S. Camarda, R. L. Espinola, H. Rao, and R. M. Osgood, "Ultracompact corner-mirrors and T-branches in silicon-on-insolutor," *IEEE Photo. Technol. Lett.*, vol. 14, 65-67(2002).
  165. Y. Qian, J. Song, S. Kim, and G. P. Nordin, "Compact 90° bends and splitters for silicon rib waveguides ", *Integrated Photonics and Nanophotonics Research and Applications* (IPNRA), IMC3(2007)
  166. L. Li, G. P. Nordin, J. M. English, and J. Jiang, "Small-area bends and beamsplitters for low-index-contrast waveguides," *Opt. Express*, vol. 11, 282-290 ( 2003)
  167. C. Manolatou, S.G. Johnson, S. Fan, P.R. Villeneuve, H. A. Haus, and J. D. Joannopoulos, "High-DensityIntegrated Optics," *J. Lightwave Technol.*, vol. 17, 1682-1692 (1999).

- 
168. R.L. Espinola, R.U. Ahmad, F. Pizzuto, M.J. Steel and R.M. Osgood, Jr., "A study of high-index-contrast 90o waveguide bend structures," *Opt. Express*, vol. 8, 517-528 (2001).
  169. Y. Chung and N. Dagli, "Experimental and theoretical study of turning mirrors and beam splitters with optimized waveguide structures," *Opt. and Quantum Electron.*, vol. 27, 395-403 (1995).
  170. C. Ma, Q. Zhang and E.V. Keuren, "Right-angle slot waveguide bends with high bending efficiency," *Opt. Express*, vol. 16, 14330-14334 (2008).
  171. S. Suzuki, M. Yanagisawa, Y. Hibino, and K. Oda, "High-density integrated planar lightwave circuits using SiO<sub>2</sub> GeO<sub>2</sub> waveguides with a high refractive index difference," *J. Lightwave Technol.*, vol. 12, 790-796 (1994).
  172. R. A. Soref, J. Schmidtchen, and K. Petermann, "Large single-mode rib waveguides in GeSi-Si and Si-on-SiO<sub>2</sub>," *J. Quantum Electron.*, vol. 27, 1971 (1991).
  173. U. Fischer, T. Zinke, J.-R. Kropp, F. Arndt, and K. Petermann, "0.1 dB/cm waveguide losses in single mode SOI rib waveguides," *Phot. Techn. Lett.*, vol. 8, 647 (1996).
  174. Y. Z. Tang, W. H. Wang, T. Li and Y.L. Wang, "Integrated waveguide turning mirror in silicon-on insulator," *Phot. Techn. Lett.*, vol. 14, 68-70 (2002).
  175. R. Orobtcchouk, S. Laval, D. Pascal, A. Koster, "Analysis of Integrated Optical Waveguide Mirrors," *J. Lightwave Technol.*, vol. 15, 815-820 (1997).
  176. P. D. Swanson, D. B. Shire, C. L. Tang, M. A. Parker, J. S. Kimmert and R. J. Michlak, "Electron-cyclotron resonance etching of mirrors for ridge-guided lasers," *Phot. Techn. Lett.*, vol. 7, 605-607 (1995).
  177. K. Wada, M. Popovic, S. Akiyama, H. A. Haus, J. Michel, "Micron-size bending radii in silica-based waveguides," *Advanced Semiconductor Lasers and Applications*, (Copper Mountain, CO USA, 2001), pp.13-14.

- 
178. M. Popovic, Kazumi Wada, Shoji Akiyama, Hermann A. Haus, Jürgen Michel, “Air trenches for sharp silica waveguide bends,” *J. Lightwave Technol.*, vol. 20, 1762-1772 (2002).
179. L. Li, G. P. Nordin, J. M. English, and J. Jiang, “Small-area bends and beamsplitters for low-index-contrast waveguides,” *Opt. Express*, vol. 11, 282-290 (2003).
180. Y. Lin, N. Rahmanian, S. Kim, and G. P. Nordin, “Compact and high efficiency polymer air-trench waveguide bends and splitter,” *Proc. SPIE*, vol. 6462, 64620V (2007).
181. Y. Chung and N. Dagli, “Experimental and theoretical study of turning mirrors and beam splitters with optimized waveguide structures,” *Opt. and Quantum Electron.*, vol. 27, 395-403 (1995).
182. S. Hiramatsu, K. Miura, and K. Hirao, “Optical backplane connectors using three-dimensional waveguide arrays,” *J. Lightwave Technol.*, vol. 25, 2776-2782 (2007).
183. R. U. Ahmad, F. Pizzuto, G. S. Camarda, R. L. Espinola, H. Rao, and R. M. Osgood, “Ultracompact Corner-Mirrors and T-Branched in Silicon-on-Insulator,” *IEEE Photo. Technol.*, vol. 14, 65-67 (2002).
184. I. Papakonstantinou, K. Wang, D. R. Selviah, and F. A. Fernández, “Transition, radiation and propagation loss in polymer multimode waveguide bends,” *Opt. Express*, vol. 15, 669-679 (2007).
185. D. P. Nair , N. B. Cramer, J. C. Gaipa, M. K. McBride , E. M. Matherly, Robert R. McLeod , Robin Shandas , and Christopher N. Bowman, “Two-stage reactive polymer network forming systems,” *Adv. Funct. Mater.*, vol. 22, 1502-1510(2012).
186. <http://www.on-trak.com/theory.html>
187. H. Liu, Y. Xiao, and Z. Chen, “A high precision optical position detector based on duo-lateral PSD”, *International Forum on Computer Science-Technology and Applications* (2009), pp. 90-92.

- 
188. B D. Greenwood and C. A. Primmerman, "The history of adaptive-optics development and the MIT Lincoln Laboratory," *Proc. SPIE*, vol. 1920, 220-234 (1993).
  189. B. A. Horwitz, "Comparison approach for wavefront sensors," *Proc. SPIE*, vol. 1920, 186-192 (1993).
  190. J. Liang , D.R. Williams, D.T. Miller, "Supernormal vision and high-resolution retinal imaging through adaptive optics," *J Opt. Soc. Am. A*, vol. 14, 2884-2892(1997).
  191. A. Roorda , and D.R. Williams, "The arrangement of the three cone classes in the living human eye," *Nature*, vol. 397, 520-522(1999).
  192. D. R. Neal, J. K. Gruetzner, and J.P. Roller, "Use of beam parameters in optical component testing", *Proc. SPIE*, vol. 4451, 394-395(2001).
  193. <http://www.wavefrontsciences.com/Application-2.pdf>.
  194. D. R. Neal, T. J. O'Hern, J.R. Torczynski, M. E. Warren, R. Shul and T. S. McKechnie, "Wavefront sensors for optical diagnostics in fluid mechanics: application to heated flow, turbulence and droplet evaporation," *Proc. SPIE*, vol. 2005, 194-203(1993).
  195. D. R. Neal, W. J. Alford, and J. K. Gruetzner, "Amplitude and phase beam characterization using a two-dimensional wavefront sensor," *Proc. SPIE*, vol. 2870, 72-82 (1996).
  196. M. Brown, T. Gong, D. R. Neal, J. Roller, S. Luanava and H. Urey, "Measurement of the dynamic deformation of a high frequency scanning mirror using a Shack-Hartmann wavefront sensor," *Proc. SPIE*, vol. 4551, 480-488(2001).
  197. <http://www.wavefrontsciences.com/Zernike%20vs%20Zonal.pdf>
  198. W. H. Southwell, "Wavefront estimation from wave-front slope measurements," *JOSA*, vol. 70, 998-1006 (1980).